

Electronic Interfaces for Carbon Nanotube Electromechanical Oscillators and Sensors

THÈSE N° 6127 (2014)

PRÉSENTÉE LE 21 MARS 2014

À LA FACULTÉ DES SCIENCES ET TECHNIQUES DE L'INGÉNIEUR
INSTITUT DE GÉNIE ÉLECTRIQUE ET ÉLECTRONIQUE
PROGRAMME DOCTORAL EN MICROSYSTÈMES ET MICROÉLECTRONIQUE

ÉCOLE POLYTECHNIQUE FÉDÉRALE DE LAUSANNE

POUR L'OBTENTION DU GRADE DE DOCTEUR ÈS SCIENCES

PAR

Christian KAUTH

acceptée sur proposition du jury:

Dr C. Dehollain, présidente du jury
Prof. M. Kayal, Dr M. Pastre, directeurs de thèse
Prof. A. Kaiser, rapporteur
Prof. C. Lallement, rapporteur
Dr J.-M. Sallese, rapporteur



ÉCOLE POLYTECHNIQUE
FÉDÉRALE DE LAUSANNE

Suisse
2014

What we know is a drop,
what we don't know is an ocean.
— Isaac Newton

To my parents...

*You can do anything,
but not everything.*

— David Allen

Acknowledgements

Dear actors of my doctoral life span, it is with great pleasure that I express my deepest gratitude for your share in my contribution to science. This page is about you and for you!

First and foremost I warmly thank all of you, my colleagues of the electronics lab, for making my workdays here not only bearable, but enjoyable! Thank you Maher for your management and trust in my doings, a successful combination. Marc and Jean-Michel, thank you for all your valuable time and inexhaustible interest in our scientific discussions. You are the inspiration behind some of my favourite ideas. Cédric and Eric, I give you props for your precious help on the hardware design. There was no administrative or logistic obstacle which Isabelle, Karin, Marie, Joseph or Raymond could not circumvent. Dear colleagues of the *CabTuRes* project, I enjoyed striving with you to a common goal. Thank you all!

Research

Serendipitously there is more to doctoral studies than just research. Teaching was always a very welcome change, especially in front of motivated and friendly students. I ascribe the faultlessly pleasant atmosphere in the classroom and labs to our humorous gang of teaching assistants. Andrea, Ira, Sylvain, François, Naser, Pietro and Camillo, thank you for having shared this experience, here at EPFL, in Oxford, Seville and Mons.

Teaching

And then there was this little something, which made these years in academia special. Pierluca, Robert, Jonas and Jean-Paul, it was a sublime satisfaction to see grow our brainchild, PolyProg, into the now so popular Helvetic Coding Contest. Peter and Titus, your dedicated contribution to our algorithmic seminars was unprecedented. It was my pleasure working with you! I'd also like to thank the team of the *Flash Informatique*, especially Jaqueline and Appoline. PolyProg always benefited from your support. I gladly sowed throughout the present document some relicts of a memorable era.

PolyProg

At moments when the neurons refused service and the soul called for freedom, then it was time to set out with you, sports fan(atic)s: Dania, Sam, Alain, Joël and Philippe, I will always remember our literally breathtaking cycling and running trips. Hornists of the *Orchestre Symphonique et Universitaire de Lausanne*, I enjoyed the numerous years we played together! The homemade pizzas were the best far and wide, thank you Massimo and Francesco. I now close the door of my office for good, with a wink from the whiteboard smiley, thank you Annick.

Friends

Last but not least, I want to express my heartiest thanks to my parents, my brother Dan and my girlfriend Blandine. I so highly appreciate your faith in me, your indefatigable support and continuous encouragements. Every moment with you floods me with happiness and enthusiasm. My gratefulness to you is beyond words!

My dearest

*There's plenty of room
at the bottom.*

— Richard Feynman

Preface

Dear reader, be welcome to this PhD dissertation! If you resemble me, you generally do not read prefaces. This one, however, contains useful information that will help you to efficiently manage your way through this document. So I hope you will make an exception.

What can I
do for you?

Research, as you might know since ages, or are just about to discover, may be structured as a search tree. Innocently ambling along its branches, without having a clear goal in mind, almost certainly gets you lost. Research trees are infinite and in steady growth. While you start off exploring them to build up expertise, you eventually end up extending them with your own great findings! Your professional time to do so is limited however, and you need a strategy. Planning to search infinitely profound trees in depth seems vain, because an enthralling vortex will absorb you, and you will virtually learn so much about so little that in the end, you know everything about nothing. A breadth-first-search isn't any better in trees with infinite branching factor, as you will not make it to any depth and will in the end know nothing about everything.

Infinite re-
search trees

Personally, I tried to combine both approaches into a diagonal search, during which I used some kind of heuristics that helped me to branch into the directions that looked most promising, while leaving less viable subtrees unfortunately unexplored. A good dose of open-mindedness further lead to some quantum jumps towards seemingly random locations in the tree, and I finally bobbed up with as much expertise and contribution as I could within time. Now this dissertation will not lead you along the exact same trajectory, but it forms a concise summary of my experience gained within the PhD. Especially do I intend to tell you the story of why I cared more about certain research directions than others, what I understood from them, and finally how I contributed, sometimes nested into fractal patterns.

Branch
and bound
mindset

Such a structure entails that some sections require in-depth understanding of domain-specific phenomena, while others can be easily digested by a larger public. So I sowed some chilies throughout the document, which indicate the specificity or complexity of each section. Whether you are new (🌶) to the fields of carbon nanotubes, control system design and analog electronics, have some knowledge (🌶🌶), or are an expert (🌶🌶🌶), feel free to compose your personal diet by skipping sections that lie out of your interest, or on the contrary, get in touch with them. A comprehensive summary, necessary to move on, concludes each chapter.

Your chili
tolerance

I wish you an inspiring and insightful reading, enjoy!

Lausanne, January 2014

C. K.

Somewhere, something incredible is waiting to be known.

— Carl Sagan

Abstract

While microelectromechanical systems cavort in compact volumes within cell phones, automated transport systems and medical equipment, to name but a few, their smaller fellows have a hard time breaking into these applications. Carbon nanotubes, micrometer-long and nanometer-thin hollow cylinders, are in this unpropitious situation. Operated as suspended CNT-NEMS, they offer tunable resonance frequencies up to gigahertz and high environmental sensitivity, but still lack popularity and applicability. The lurking potential of making capital of their marvelous properties remains unexploited for want of appropriate electronic interfaces.

Interfaces
are key

This thesis presents investigations on CNT-NEMS and interface circuits, leading to a system which is prone to becoming the world's fastest, high-precision mass balance.

Overview

Modelled as oscillating Euler-Bernoulli beams with von Kármán strains, discretized by a Galerkin procedure, CNT-NEMS experience potential fluctuations (capacitive effect), carrier state repopulation (field effect) and density of state variations (piezoresistive effect). Doubly-clamped, single-walled CNT-NEMS yield maximal, circuit compliant, signal-to-noise ratio when biased to diffusive saturation of several microamperes DC. Motion is inferred via the 100nA strong field effect for two thirds of the tubes, the moderate 1nA piezoresistive effect for a sixth, and the capacitive effect otherwise. These values form an upper bound, achieved by optimal CNT-NEMS selection, resulting from maximisation of the electromechanical transduction efficiency under state-of-the-art process constraints. Narrow, possibly prestrained tubes of lengths between 100nm to 1 μ m, cover eigenfrequencies from tens of mega- to gigahertz.

Pushing the
envelope of
CNT-NEMS

All current modulation effects in CNT-NEMS are categorized, for the first time ever, by their strength, frequency and phase, and instructions for experimental validation by mixing are provided. A novel 4ω detection leads the way to mass sensors with adsorbate configuration recognition. High-speed readout is achieved via multi-stage common source MOS front-ends, outperforming common emitter BJT interfaces up to hundreds of megahertz. They are projected to offer a full bandwidth SNR of up to 30dB for on-chip interfaces.

Prospective
motion
detection

A robust and debug-capable feedback system embeds the NEMS into a phase-locked loop, allowing open-loop characterization and closed-loop high-speed operation of NEMS with *a priori* unknown characteristics. Tensile straining enables frequency tuning for VCOs. Fastest settling, within hundreds of nanoseconds, is obtained for type two, slightly underdamped PLLs with maximal, sub-eigenfrequency (100MHz) bandwidth. Integrated in a 180nm technology, the 4.5mm² PLL could operate on NEMS with eigenfrequencies from 37.5MHz to 770MHz.

Conceiving
NEMS-
VCOs

In combination with a novel calibration system, unprecedented high-speed mass sensitivity is claimed. Observed through a non-linearity, the unknown NEMS phase is corrected via a third-order feedback. The IC's noise predicts zeptogram resolution within a microsecond, thereby undercutting the world's fastest equally precise balance by orders of magnitude.

Precise &
fast sensing

The results presented in this thesis may lead the CNT-NEMS out of their promising-property-investigating ivory tower, towards beneficial system applications.

Carbon nanotubes – Electromechanical systems – Electronics – Modelling – Oscillators – Sensors

On ne perçoit du monde que ce qu'on est préparé à en percevoir.

— Bernard Werber

Résumé

Alors que les systèmes microélectromécaniques (MEMS) envahissent les portables, les systèmes de transport automatisés et des équipements médicaux, leurs petits congénères, les NEMS, ont du mal à percer. Telle est la situation actuelle des nanotubes de carbone (CNT), cylindres creux de quelques micromètres de long et nanomètres d'épais. Opérés comme CNT-NEMS suspendus, ils offrent des fréquences de résonance accordables jusqu'au gigahertz et une sensibilité environnementale marquée. Malgré ces merveilleuses propriétés, peu d'applications autour des CNT-NEMS ont émergé, faute d'interfaces électroniques appropriées.

Le potentiel des interfaces

Cette thèse combine les CNT-NEMS et des circuits d'interface en un système prôné de devenir la balance haute-précision la plus rapide au monde.

Vue d'ensemble

La théorie des poutres d'Euler-Bernoulli, les tensions de von Kármán et une discrétisation selon Galerkin, décrivent la mécanique du CNT-NEMS, tandis que leur propriétés électriques sont ramenées à des fluctuations de potentiel (effet capacitif), la repopulation des états (effet de champ) et des variations de densité d'états électroniques (effet piezorésistif). Le meilleur rapport signal-sur-bruit (SNR) pour des CNTS-NEMS interfacés par un circuit, est obtenu en saturation, sous une polarisation de quelques microampères. L'oscillation des deux tiers des tubes est observable par l'effet de champ, fort de 100nA, par l'effet piezo modéré, de 1nA, et l'effet capacitif, dans un sixième des cas respectivement. Cette limite supérieure est atteinte pour une sélection minutieuse du CNT-NEMS, selon les critères résultant d'un processus d'optimisation de l'efficacité de transduction sous les contraintes de fabrication actuelles.

Les CNT-NEMS à la limite du possible

Tous les effets de modulation du courant sont classifiés, pour la première fois, par leur amplitude, fréquence et phase. Des instructions pour leur validation expérimentale, par mixage, sont fournies. Une nouvelle détection 4ω ouvre la voie à des capteurs de masse avec reconnaissance de la configuration d'adsorption. Des interfaces source commune MOS et émetteur commun BJT, opérables jusqu'à des centaines de mégahertz, sont propices d'offrir des SNR de 30dB sous pleine bande passant pour des interfaces intégrées (IC).

Détection de mouvement

Une rétroaction robuste encastre le NEMS dans une boucle à verrouillage de phase (PLL), permettant une caractérisation séparée, tout comme l'adaptation au NEMS pour une opération à haute vitesse en boucle fermée. Un MEMS de traction permet l'accordage en fréquence pour des VCOs. Une convergence en quelques centaines de nanosecondes est obtenue pour des PLLs pseudo-périodiques de type deux avec bande passante maximale. La PLL, intégrée en 180nm, de 4.5mm^2 peut asservir des NEMS aux fréquences propres de 37.5MHz à 770MHz.

Conception de NEMS-VCOs

Combiné à une calibration inédite, une résolution et vitesse sans paires sont obtenues. Observée à travers une non-linéarité, la phase du NEMS est corrigée par un réglage d'ordre trois. Le bruit de l'IC permet une résolution du zeptogramme en une microseconde, rendant ce système des ordres de grandeur plus rapide que toute autre balance à précision similaire.

Détection précise & rapide

Les résultats présentés dans cette thèse ont le potentiel d'ouvrir la voie aux CNT-NEMS depuis leur tour d'ivoire des caractérisations, vers des applications bénéfiques au niveau système.

Nanotubes de carbone – Systèmes électromécaniques – Electronique – Oscillateurs – Capteurs

Es irrt der Mensch, solange er strebt.

— Johann Wolfgang von Goethe

Zusammenfassung

Während sich elektromechanische Mikrosysteme (MEMS) auf engstem Raum in Mobiltelefonen, automatisierten Transportsystemen und medizinischer Infrastruktur tummeln, gelingt es ihren kleineren Artgenossen, den NEMS, nicht so richtig Fuß zu fassen. So ergeht es derzeit den Mikrometerkurzen und Nanometerschmalen Kohlenstoffnanoröhren (CNT). Im Gebrauch als schwingende CNT-NEMS, offenbaren diese höchste Sensorempfindlichkeit und stimbare, bis zu Gigahertz hohe Resonanzfrequenzen. Mangels geeigneter Schnittstellen wurde sofern jedoch wenig Kapital aus diesen fabelhaften Eigenschaften geschlagen.

Schnittstelle
zum Erfolg

Diese Dissertation flechtet CNT-NEMS und elektronische Schnittstellen zu einem System, welches die vielleicht schnellste Präzisionswaage der Welt werden könnte.

Übersicht

Euler-Bernoulli Balkentheorie, von Kármán Spannung und die Galerkin Prozedur dienen der mechanischen Beschreibung von CNT-NEMS, während Potentialfluktuationen (kapazitiver Effekt), Elektronenneuverteilung (Feldeffekt) und Zustandsdichteveränderungen (piezoresistiver Effekt) den Elektronenfluss kontrollieren. Gekoppelt an eine elektronische Schaltung, weisen vorgespannte einwandige CNT-NEMS ein maximales Signal-Rausch-Verhältnis (SNR) bei einer Diffusionssättigung von mehreren Mikroampere auf. Die Schwingung kann in zwei Drittel der Fälle dank des 100nA starken Feldeffekts, und in je einem Sechstel durch den moderaten 1nA Piezoeffekt oder schwachen Kapazitätseffekt, ausgelesen werden. Diese Oberwerte sind unter optimaler CNT-NEMS Auswahl erreichbar, entsprechend maximaler Transduktionseffizienz unter den Randbedingungen modernster Herstellverfahren.

CNT-NEMS
Das ist
drin...

Zum ersten Mal werden alle Modulationseffekte in CNT-NEMS nach Intensität, Frequenz und Phase kategorisiert. Anleitungen zur experimentellen Validierung dank einer Mischtechnik stehen bereit. Eine neuentdeckte 4ω Erkennung entpuppt ihr Potential zu einer Molekülwaage mit Adsorbat Konfigurationserkennung. Signalauslese im hohen Eigenfrequenzbereich wird mit mehrstufigen MOS und BJT Frontends erreicht. Ein 30dB SNR über eine 100MHz Bandbreite ist für integrierte Schaltkreise (IC) möglich.

Aussichtsreiche
Bewegungs-
erkennung

Ein robustes und testfähiges Feedbacksystem bettet das NEMS in eine Phasenregelschleife (PLL) ein, ermöglicht eine separate Charakterisierung und passt sich automatisch dem NEMS an. Zugspannung ermöglicht Frequenzabstimmung für VCOs. Leicht unterdämpfte Typ zwei PLLs mit hoher Bandbreite rasten bereits nach möglichst kurzen Hunderten von Nanosekunden ein. Die integrierte $4,5\text{ mm}^2$ PLL kann NEMS im 37,5-770 MHz Frequenzbereich handhaben.

Konzeption
von NEMS-
VCOs

In Kombination mit einem neuartigen Kalibrierungssystem wird eine beispiellos schnelle Masseempfindlichkeit erreicht. Die NEMS Phase wird durch eine Nichtlinearität gemessen und dank einer Regelung dritter Ordnung korrigiert. Das Rauschen des IC prognostiziert eine Zeptogramm Auflösung innerhalb einer Mikrosekunde, und wäre damit mehrere Größenordnungen schneller als jede bekannte ebenso präzise Waage.

Schnelles
& präzises
Messen

Die Ergebnisse dieser Dissertation könnten das CNT-NEMS aus dem Elfenbeinturm der Charakterisierung hinaus zu vorteilhaften Systemanwendungen führen.

Kohlenstoffnanoröhren – Mikrosysteme – Elektronik – Modellierung – Oszillatoren – Sensoren

*Never memorize something
that you can look up.*

— Albert Einstein

Contents

Acknowledgements	v
Preface	vii
Abstract (English)	ix
Résumé (Français)	xi
Zusammenfassung (Deutsch)	xiii
Contents	xv
List of figures	xix
List of tables	xxv
1 Introduction	1
1.1 Shaping the Smart Dust Utopia	1
1.2 This work in a nutshell	2
1.3 Enabling Autonomous Sensor Nodes	4
1.3.1 Motivation and qualitative rationale	5
1.3.2 A contextual technological platform	6
1.4 Identifying the Challenges	8
1.4.1 Handling interconnects and contact parasitics	8
1.4.2 Relating modes of operation to device bias	9
1.4.3 Efficiently actuating the CNT-NEMS	11
1.4.4 Robust signal readout	11
1.4.5 Conceiving tunable self-regulating CNT-NEMS oscillators	12
1.4.6 High-speed high-resolution mass balances	13
1.5 Inventing the Solutions	15
	xv

2	Carbon Nanotube Electromechanical Resonators at System Level	17
2.1	CNT-NEMS – an Electromechanical Multiport	18
2.2	Setting the NEMS to Motion	20
2.2.1	Forcing the tube to motion	20
	From a continuum to a lumped model	21
	The constrained harmonic oscillator model	25
	The mechanical transfer function	32
2.2.2	The electrostatic force – an upper bound	35
2.2.3	A quantum of solid states physics	37
2.2.4	The electrostatic force - revisited	44
2.2.5	Electromechanical actuation summary	47
2.3	Decrypting the NEMS Response	49
2.3.1	Capacitive Effect	50
2.3.2	Field effect	52
2.3.3	Piezoresistive effect	55
2.3.4	A brief comment on contacts and sensing	57
2.4	CNT-NEMS Resonators in a Nutshell	58
3	Electrical Detection of Mechanical Motion in Carbon Nanotubes	63
3.1	The Front-end’s Mission	64
3.2	CNT-NEMS Sensor in a Nutshell	65
3.3	The Dementia and Latency of Mixers	68
3.3.1	State-of-the-art mixing	69
3.3.2	Stepping onto the virgin soil of mixers	70
3.4	The Versatility of Direct Readout	72
3.4.1	Eliminating spurious signals	73
3.4.2	Low-noise front-end design	75
3.5	Implementation & Characterization	81
3.6	Summary	85
4	Electromechanical Oscillators and Sensors	89
4.1	Ingredients to Electromechanical VCOs and Sensors	90
4.1.1	Frequency tunability for VCOs	91
4.1.2	Strain sensitivity for force and pressure sensors	91
4.1.3	Adsorption sensitivity for particle detectors & mass balances	92
4.2	The Quest of the Ideal Oscillator Topology	95
4.2.1	The sobriety of self-sustained oscillation	95
4.2.2	The indefatigability of forced actuation	98
4.2.3	The memory effect of phase-locked loops	99
4.3	Closed-loop System Optimisation	105
4.3.1	Models and system design	105
4.3.2	From open- to closed-loop	107
4.3.3	Robustness to circuit noise and delays	109

4.3.4	Optimal PLL design under limited bandwidth	111
4.4	Merging High-Speed & High-Resolution Mass Sensing	113
4.4.1	Fast and precise oscillators	113
4.4.2	The nonlinear physical phenomenon	116
4.4.3	Controllability & observability	117
4.4.4	NEMS mass balance system	118
4.5	Microelectromechanical VCOs & Sensors in a Nutshell	119
5	Implementation, Characterization & Assessment	123
5.1	Functional Proof of Concept on PCB	124
5.2	Performance on IC	126
5.3	NEMS versus Circuit Compatibility	132
5.4	Mass Resolution & Sensor Speed	133
5.5	Summary	135
	Conclusion	137
	Bibliography	141
	Publications	149
	Curriculum Vitae	153

List of Figures

1.1	Suspended carbon nanotubes (<i>top</i>) can be set to resonance by application of an electrical signal. They are highly sensitive to their environment, and a binding molecule alters the resonance frequency. This change in frequency can be tracked by an electronic loop (<i>right</i>), that reads the current flowing through the tube, and steadily corrects the actuation signal, so to keep the tube oscillating. The tube and electronics can be integrated into a compact 1mm ³ sensor node (<i>left</i>).	3
1.2	Graphene (left) is a flat sheet of carbon atoms arranged in a honeycomb lattice. Rolling such a sheet up into a cylinder, yields a carbon nanotube (right), which is a high aspect-ratio hollow molecular wire 50'000 times thinner than a human hair. [drawn with Wolfram Carbon Nanotube online project]	5
1.3	Contextual system architecture for CNT-NEMS oscillators and sensors [CabTuRes - Nanotera.ch]	7
1.4	CNT-NEMS operated as a mixer. The low-frequency signal $\Delta\omega$ seamlessly flows through the lowpass filter formed by the CNT-NEMS contact impedance and the track capacitance. It peaks in amplitude and inflects in phase when $\omega \in \{\omega_0, \frac{\omega_0}{2}\}$, where ω_0 is the NEMS eigenfrequency and $n=1$ [1], $n=2$ [2] or $n=4$ (new).	9
1.5	Impact of source drain and gate voltage on current through SWNT	10
1.6	The capacitive, field-effect and piezoresistive transduction mechanisms generate peaks at different spectral positions that allow to separate motional and purely electrical information under direct readout.	11
1.7	In its linear dynamic range, the CNT-NEMS may be modelled as an harmonic oscillator with mechanical eigenfrequency ω_0 and quality factor Q . The frequency response peaks in amplitude (–) and inflects in phase (···) close to ω_0 . Outside this range, the NEMS presents hysteretic behaviour and is inappropriate for closed-loop operation.	13
1.8	Binding of a particle onto the oscillating CNT-NEMS entails a change in eigenfrequency that holds quantitative information on the particle nature. This shift is to be detected as fast and as precisely as possible.	14
2.1	The gate voltage sets the NEMS into motion, which can be inferred from the drain current.	18

List of Figures

2.2	Cantilever (left) and clamped-clamped (right) CNT-NEMS with capacitive actuation. Capacitive current into and out of the NEMS is detectable in both topologies, field- and piezoresistive effects on the other hand become observable only through doubly-clamped NEMS.	19
2.3	Suspended carbon nanotube clamped between drain (D) and movable source (S) electrodes. A nearby gate (G) electrode controls the current flow. The motion is observable at the drain terminal as current or voltage.	20
2.4	(left) Molecular representation of a single walled (10,10) armchair carbon nanotube. Their shape may be approximated as a hollow cylinder of length L , average diameter d and thickness τ . (right) The optical microscope view of the suspended CNT reveals the high $\frac{L}{d}$ aspect ratio. [by courtesy of [3]]	21
2.5	Anchored CNT shapes: Bending dominated bending CNTs and stress dominated tensioned CNTs may be modelled by lumped elements	23
2.6	Small-amplitude CNT eigenfrequency as a function of tube length L and diameter d for bending dominated (left) and tension dominated (right) tubes.	25
2.7	[Left] Displacement-by-force $\frac{y(\bar{x},t)}{F_0}$ gain in the small-displacement limit imposed by equation (2.10) [Right] Onset of nonlinearity causes hysteretic amplitude and phase jumps	26
2.8	The Duffing response presents a rich harmonic content. The fundamental component does not peak around ω_0 anymore and presents hysteresis. The three-fold component remains hysteresis-free for relatively small amplitudes.	27
2.9	Tensile strain is found to increase the linear dynamic range of CNTs (c&d) at the cost of a lower transduction gain (b). The eigenfrequency can be tuned over decades without tube destruction (a). 28	
2.10	The maximum obtainable average deflection (a), strain (b) and transduction gains (c&d) at resonance over the length, diameter and prestrain space, as a function of actuation force and eigenfrequency. The maxima of each graph correspond to one and the same design point of Figure 2.11. (hyp. $Q = 100$)	29
2.11	Maximum linear-regime oscillation-induced strain and amplitude are obtained for the following NEMS parameters within the $L \times d \times s_0 \equiv [100\text{nm}..1\mu\text{m}] \times [1\text{nm}..5\text{nm}] \times [0\%..1\%]$ design space. .	30
2.12	The maximum obtainable average deflection (a), strain (b) and transduction gains (c&d) at resonance, optimized over the length, diameter and prestrain space, as a function of actuation force and eigenfrequency. Every entry to each of the 4 graphs corresponds to one and the same optimal design point, given by Figure 2.11. (hyp. $Q = 100$)	32
2.13	Force to average displacement transfer gain and constraints, optimized over the available NEMS parameter space (length, diameter and prestrain). The linear regression norms of residuals are respectively $\ r_{\text{gain}}\ = 0.0495$, $\ r_{F^+}\ = 0.0692$ and $\ r_{F^-}\ = 0.0367$ (hyp. $Q = 100$, $\omega = \omega_0$)	33
2.14	Force to strain transfer gain and constraints, optimized over the available NEMS parameter space (length, diameter and prestrain). The linear regression norms of residuals are respectively $\ r_{\text{gain}}\ = 0.0245$, $\ r_{F^+}\ = 0.0971$ and $\ r_{F^-}\ = 0.0914$ (hyp. $Q = 100$, $\omega = \omega_0$)	34
2.15	The lineic electrical gate to CNT capacitance and its derivative are relatively insensitive to the suspension height h and tube diameter d . Zero-order approximations would be $C_e' \approx 10 \text{ aF}/\mu\text{m}$ and $\partial_y C_e' \approx 6 \text{ pN}/(\mu\text{mV}^2)$	36

2.16 The electrical C'_e and quantum C'_q capacitance share the same through variable and appear in series. While a voltage on C'_e will exert an attractive electrostatic force onto the tube, this is not the case for C'_q 37

2.17 The dispersion relation for graphene is a hexagonal lattice with energies from $-3\gamma_0=-8.1\text{eV}$ to $+3\gamma_0=8.1\text{eV}$. The bandgap is closed at the six K-points which define the Brillouine zone corners. 38

2.18 The (n,m) -CNT unit cell is defined by its circumferential $\mathbf{C} = n \cdot \mathbf{a}_1 + m \cdot \mathbf{a}_2$ and translational $\mathbf{T} = \frac{2m+n}{\text{GCD}} \mathbf{a}_1 - \frac{2n+m}{\text{GCD}} \mathbf{a}_2$ vectors in the direct space and contains $N_c = 4 \frac{n^2+nm+m^2}{\text{GCD}}$ carbon atoms, where GCD is the greatest common divisor of $2n + m$ and $2m + n$ 39

2.19 (7,7) armchair nanotubes are metallic (eq. (2.35)) because their dispersion relation intersects the K-points of the graphene Brillouine zone. The bandstructure presents no gap and a finite non-zero density of states prevails around the neutrality level. 41

2.20 (13,0) zigzag nanotubes are semi-conducting (eq. (2.35)) because their dispersion relation does not intersect the K-points of the graphene Brillouine zone. The bandstructure presents a gap and no states are available around the neutrality level. 41

2.21 (10,5) nanotubes are semi-conducting (eq. (2.35)) because their dispersion relation does not intersect the K-points of the graphene Brillouine zone. The bandstructure presents a gap and no states are available around the neutrality level. 41

2.22 (left) Density of available states of a (13,0) semiconducting zigzag SWNT and the excess carriers' state occupation probability at $\mu = 1\text{eV}$. (right) Number of excess carriers per μm as a function of the tube potential for three wrapping angles. The point's y-value at $\mu = 1\text{eV}$ corresponds to the coloured area of the left graph 42

2.23 The quantum capacitance C'_q exceeds the electrical capacitance C'_e if the tube potential ϕ_{CNT} lies in the valence and conduction band, while the opposite is true inside the bandgap. This implies that the tube potential equals the gate voltage until it saturates at the band edges. 43

2.24 The force spectrum for metallic SWNTs reveals the components at DC, once and twice the actuation voltage frequency. For semiconductive SWNTs, the force drops considerably inside the bandgap, leading to higher harmonic nonlinearities for biases in the bandgap vicinity. (the colour-scale is logarithmic) 45

2.25 A sinusoidal drive at $\tilde{v} \sin(\omega_{in} t)$ creates force components at DC, $1 \cdot \omega_{in}$ and $2 \cdot \omega_{in}$. Metallic tubes are represented in red, semiconducting tubes in blue. Equation (2.51) (—) is found to nicely approximate the quantum equation (2.30) (o). The ratio $\frac{(2.51)}{(2.30)}$ is indeed generally close to unity whenever the force is large. 46

2.26 Electromechanical actuation input and output dynamic ranges for $\omega_{in} = \frac{\omega_0}{2}$ (red) and $\omega_{in} = \omega_0$ actuation schemes. (hyp. Q=100) 49

2.27 The capacitive current for both actuation schemes has a mechanical component (black) below the nanoampere floor and a relatively stronger electrical background signal (gray). Both signals fortunately come with distinct phase ($\omega = \omega_0$) and distinct frequency ($\omega = \frac{\omega_0}{2}$). (hyp. Q = 100) . 51

2.28 Simulations (left, taken from [4]) and measurements (right, taken from [5]) show that tubes longer than 100nm suffer scattering at source-drain voltages above 100mV. Transport may be appropriately described by a diffusive Drude model. 52

2.29 Drain current as a function of the drain-source bias (left) and gate bias (right) for an SWNT with diameter $d = 1\text{nm}$, as given by equation (2.64). 53

List of Figures

2.30	(left) Motional transconductance in saturation regime as a function of the gate bias. (right) Motional Field effect current for half (red) and full (blue) actuation. Both curves overlap. (hyp. $Q=100$)	54
2.31	(left) Electrical transconductance in saturation regime as a function of the gate bias. (right) Electrical Field effect current for half (red) and full (blue) actuation.	55
2.32	(left) Piezoresistive transconductance in saturation regime as a function of the gate bias. (right) Piezoresistive current for half (red) and full (blue) actuation. Both curves overlap.	57
2.33	CNT output spectrum for $\omega_{\text{gate}} = \omega_0$	60
2.34	CNT output spectrum for $\omega_{\text{gate}} = \frac{\omega_0}{2}$	60
3.1	Small signal equivalent circuit from CNT-NEMS to front-end	64
3.2	CNT-NEMS operated as a mixer. The low-frequency signal $\Delta\omega$ seamlessly flows through the lowpass filter formed by the CNT-NEMS contact impedance and the track capacitance. It peaks in amplitude and inflects in phase when $\omega \in \{\omega_0, \frac{\omega_0}{2}\}$, where ω_0 is the NEMS eigenfrequency and $n=1$ [1], $n=2$ [2] or $n=4$ (new).	69
3.3	Chemisorption of oxygen on CNTs is more likely to happen in ether (ET) configurations, than in epoxy (EP) configurations. Hence no perturbing effect on the bandgap may be expected. Simultaneous observation of the electrical and mechanical implications of oxygen adsorption may be monitored by the ($\omega_g = \omega_0, n = 1$) mixing technique. [by courtesy of [6]]	72
3.4	CNT-NEMS connected to a 3-stage biased CE low-noise amplifier. The interconnect parasitics of Figure 3.1 are not represented and the noise contributions of the base bias resistors is negligible for sufficiently large resistors.	76
3.5	3-stage (simulated with ADS) and 1-stage (analytical expression of equation (3.4)) NF of CE front-end with $C=2\text{pF}$, $R_{\text{CNT}}=1\text{M}\Omega$, $R_L=1\text{k}\Omega$. The inset shows the base and collector white noise sources along with the load noise. Flicker noise may be neglected for operation above the corner frequency. 77	77
3.6	Noise figure for front-ends with $C=2\text{pF}$ (—) and $C=200\text{fF}$ (- - -), $R_{\text{CNT}}=1\text{M}\Omega$, $R_L=1\text{k}\Omega$	79
3.7	Minimum detectable current from CNT with $R_{\text{CNT}} = 1\text{M}\Omega$, by an optimally biased CE ($\beta = 100$) and CS front-end at ambient temperature for $\text{SNR}_{\text{out}} = 1$. The represented curves may be pessimistic in the sense that the noise integration has been approximated conservatively.	80
3.8	Gain-constrained minimum NF as a function of frequency and number of stages for real CE front-end with bias-dependent current gain and transition frequency. (hyp. $\text{SNR}_{\text{out}}=1$).	82
3.9	3-stage discrete component CE front-end	83
3.10	4-stage discrete component CS front-end interfaced with CNT-NEMS. The 27.72dB SNR, achieved over a 1Hz bandwidth, requires the use of a selective filter under direct readout. The test-conditions with the CNT biased to the linear regime, however, where not optimal.	84
4.1	Suspended carbon nanotubes (<i>top</i>) can be set to resonance by application of an electrical signal. They are highly sensitive to their environment, and a binding molecule alters the resonance frequency. This change in frequency can be tracked by an electronic loop (<i>right</i>), that reads the current flowing through the tube, and steadily corrects the actuation signal, so to keep the tube oscillating. The tube and electronics can be integrated into a compact 1mm^3 sensor node (<i>left</i>). 90	90
4.2	NEMS eigenfrequency tunability and strain sensitivity.	91
4.3	NEMS-VCO extension to force and pressure sensing.	92

4.4 Sensitivity of NEMS eigenfrequency to adsorption. 93

4.5 Closed-loop systems enable unbiased quantitative mass sensing if they lock precisely onto the NEMS eigenfrequency. Failure of doing so leads to a bias in the measurement and a relative error, increasing with the frequency offset from the eigenfrequency, expressed here as an error in phase with respect to Table 3.1. 94

4.6 Self-sustained single-feedback oscillation loops offer minimal component count. They need to be augmented by a starter circuit, to ensure the loop locks onto the NEMS's motion and not on a spurious signal. The NEMS signal is amplified and relieved from noise and spurious signals. Frequency division reverses the optional frequency multiplication of the NEMS, while gain and phase regulators ensure loop-lock on the NEMS eigenfrequency. 96

4.7 Forced actuation ensures incessant oscillation of the NEMS. The actuation efficiency depends on the distance between the forced frequency and the NEMS eigenfrequency. A feedback-loop adjusts the NEMS eigenfrequency accordingly via tensile stiffening. For this adjustment to converge towards the eigenfrequency, the phase delay must complement the NEMS and circuit delays to π . 98

4.8 NEMS operated within a PLL. Oscillation is forced at a frequency that corresponds to a NEMS phase delay of $\Delta\Phi$. A tensile actuator allows to adjust oscillation frequency by tuning the NEMS eigenfrequency. Although open-loop start-up is necessary, this topology comes with built-in amplitude control. Phase control (of $\Delta\Phi$) can be added via a second feedback loop, as shown in section 4.4. 100

4.9 PLL tracking of random frequency jumps in open-loop configuration, for loop parameters $\omega_n = 1\text{MHz}$ and $Q_n = \frac{1}{2}$. This simulation uses the parameterset of the PCB implementation of section 5.1.102

4.10 CNT-NEMS operated within a PLL with peripheral control and start-up blocks, and NEMS emulator.103

4.11 In closed-loop, the PLL tracks the NEMS signal, and the NEMS is stimulated by the PLL. The system's transient response depends on the PLL's reactivity (section 4.3), while the system's steady state is defined by the loop phase delay (section 4.4). 104

4.12 Closed-loop interplay between NEMS and PLL 106

4.13 Loop closure system transients with type 1 (left) and type 2 (right) second order PLLs with $\omega_n = \frac{\omega_0}{100}$ and $Q_n = 1$ 108

4.14 Lock-in time as a function of Q_n for several ω_n for type 2 PLLs. The minimal time a PLL needs to observe an oscillating NEMS in open-loop, before the loop can be closed successfully, decreases with the PLL speed ω_n and is minimal for slightly underdamped $Q_n \approx 1$. Loop closure is defined as successful when no transient signal fallback below the 50% threshold occurs. This arbitrary criterion causes discontinuities in the result graph, because the memory effect of PLLs could revive a signal which temporarily dived below the threshold. 109

4.15 Loop delays and their compensation by memorization. 110

4.16 System dynamics for noisy type 1 PLL without (left) and with (right) delay correction, with $\omega_n = \frac{\omega_0}{100}$ and $Q_n = 1$ 111

4.17 Auto-calibrating mass balance, derived from the NEMS-embedding PLL of Figure 4.8. 115

List of Figures

4.18	The calibration technique, proposed in Figure 4.17a, introduces small variations onto the loop phase $\Delta\Phi$, and hence the NEMS phase ϕ . The NEMS's nonlinear phase-frequency relation translates the variation of ϕ into a variation of ω , which gives away the loop's oscillation frequency with respect to the NEMS eigenfrequency. The impact of the phase shift on ω is illustrated for a sinusoidal phase variation, centered in $\tilde{\phi} \in \{\phi_i \pm \frac{\pi}{8}, \phi_i\}$ and of amplitude $\Delta\phi = \frac{\pi}{5}$	116
4.19	Phase modulation for controllability and signal differentiation for observability	117
4.20	An all-in-one system for circuit and NEMS characterization, VCO and mass balance operation.	120
5.1	Partially integrated NEMS oscillator for VCO and mass balance applications	124
5.2	Oscillator feedback loop topology and PCB implementation (shaded area)	125
5.3	Printed circuit board PLL performance	126
5.4	PLL trackig of emulator	126
5.5	NEMS oscillator for VCO and mass balance	127
5.6	Topology of the implemented fully differential programmable VCO with common mode feedback	128
5.7	5V to 1.8V level-shifter for saturated full-swing signals	128
5.8	TSPC flip-flop based frequency division circuit	129
5.9	Phase frequency detector and charge pump	129
5.10	Measured chip characteristics	130
5.11	Compatibility between the designed IC and CNT-NEMS, in terms of frequency.	132
5.12	Tensile MEMS actuator and its driver electronics	133
5.13	CNT-NEMS sensor sensitivity and 3σ -detection speed limits imposed by the integrated PLL. The indicated mass-time resolution is obtained once the PLL has settled. Once Flicker noise starts, the slope smoothens.	134

List of Tables

2.1	Temporal and spectral description of the actuation voltage and resulting electrostatic force. Sinusoidal actuation has the beneficial effect of yielding force frequency components that are not present in the voltage spectrum.	45
2.2	Approximation of the electrostatic force as a function of the time varying gate voltage with amplitude \tilde{v} and frequency ω_{in} . To be independent of the nature of the tube, the DC bias \tilde{V} shall exceed 1V. The numerical values suppose $\tilde{V} \sim 2V$ and NEMS dimensions as suggested in section 2.2.2.	47
3.1	@ $\omega_0 = 100MHz$: Strength, frequency and phase of the current modulation through the nanotube, at resonance, in the linear dynamic range and for optimal CNT design. All values are based on chapter 2 with its summarizing Figure 2.33 and 2.34, and drive voltages of Figure 2.26, larger for the $\omega_g = \frac{\omega_0}{2}$ scenario.	67
3.2	@ $\omega_0 = 1GHz$: Strength, frequency and phase of the current modulation through the nanotube, at resonance, in the linear dynamic range and for optimal CNT design. All values are based on chapter 2 with its summarizing Figure 2.33 and 2.34, and drive voltages of Figure 2.26, larger for the $\omega_g = \frac{\omega_0}{2}$ scenario.	67
3.3	Observable mixing phenomena at $\Delta\omega$ for full frequency actuation (left) and half frequency actuation (right). (hyp. $\Phi = 0$)	71
3.4	@ $\omega_0 = 100MHz$: Direct comparison between the motional effects, occurring at frequency ω_e , and competing effects at surrounding frequencies. Positive SBR entries reflect dominance of the desired motional effect.	74
3.5	@ $\omega_0 = 1GHz$: Direct comparison between the motional effects, occurring at frequency ω_e , and competing effects at surrounding frequencies. Positive SBR entries reflect dominance of the desired motional effect.	74
4.1	PLL phase error as a function of the NEMS sensor event and the PLL type.	101
4.2	Type 1 (left) and type 2 (right) second order PLL open $G(s)$ and closed-loop $H(s)$ transfer functions. 107	
4.3	Second order type 2 PLL design limitations and optimal sizing	112

List of Tables

5.1	Performance summary of the integrated PLL. The most important figures of merit for fast sensor operation are Settling time : It defines the minimal time it takes the PLL to lock onto the NEMS frequency and corresponds consequently to the earliest time a quantitative assessment can be made. Frequency range : The PLL frequency range determines which CNT-NEMS can be used in combination with it (see Table 5.11a for details). High-frequency NEMS improve sensor resolution faster (see equation (4.4)). Jitter : The lower the jitter, the better the sensor resolution (for a fixed integration time) (see equation (4.7)).	131
-----	---	-----

*The best way to predict the future,
is to invent it.*

— Alan Kay

1

Introduction

Let me start by describing my personal motivation to put stout-hearted efforts into the field of electronic interface design for nanoelectromechanical applications. In a nutshell, I provide an outlook on the major contributions of this work. The technological context for the studied system is then presented in more depth, major challenges are identified and the related state of the art is reviewed. A presentation of the aspirations and novel contributions of this document follows, before the outline of the dissertation concludes the chapter.

Outline

1.1 Shaping the Smart Dust Utopia



I have two questions for you. The first goes, “How is the weather tomorrow?” Depending on your location, the season, today’s weather and your experience, you will probably formulate a quite accurate forecast about a complex phenomenon impacted by the hundred tredecillion (10^{44}) molecules within the Earth’s atmosphere. That’s absolutely fantastic! The second is “How is your health tomorrow?” Based on your health status today and your plans until tomorrow, you may formulate a prediction. In addition, you might be cautious and shield yourself from unintentional injuries. However, you cannot foresee whether you start developing a cancer or will suffer a heart attack. After some thinking you will reach the unfortunate conclusion that we can’t foretell what happens to our octillion (10^{27}) molecules. Though this second problem directly impacts our daily life and should be at least a quadrillion times easier to solve, today we cannot predict our health with ease.

Provocative
Fermi
estimate

Weather forecast is made possible thanks to environmental sensors, ranging from thermo- or hygrometers to satellite Earth observers, which communicate their data and feed complex models, then evaluated by powerful computers. Based on the result, you may make decisions

Sense,
compute,
actuate

and plan for tomorrow.

Miniaturization paradigm When it comes to your health and activities within your body, the scales change, gravity fades and surface forces dominate. Operations similar to what your eyes observe, your brain processes and your hands accomplish, shall be performed by sensors, microprocessors and actuators at micro- (10^{-6}) and nanoscales (10^{-9}) and high speed. The miniaturization progress has been tremendous: nowadays, that is in 2013, sensors reach atomic-scale detection, commercial integrated processors scratch the teraflop level (10^{12} floating point operations per second) and fine tweezers can displace single atoms.

Automated decision-making at the nanoscale Such miniaturized and high speed sensing, computation and actuation at nanoscale, raises hope for unprecedented environmental and healthcare applications, to name but a few. One of the major challenges that still protracts these achievements from turning into life changing applications, is the difficulty to interface phenomena happening in different energy domains. Similarly to the nervous system and muscles, which interfaces our eyes, brain and hands into part of a reactive human, does this dissertation connect a carbon nanotube, some transistors and a spring into a minuscule and high-speed sensor system. Combined to functionalities from the realms of telecommunications, biology and medicine, such systems may further evolve into tiny intelligent nodes.

Impact potential As such, this work contributes to the development of a concept called smart dust: Devices, small in size and large in number, autonomously perform unimaginable feats. The future might see systems that kill cancerous cells right after their mutation or instantly remove deposits of white blood cells, cholesterol and fat from arteries to prevent heart attacks.

The journey is the reward During my PhD I descried and addressed fundamental challenges in electronic carbon nanotube resonator interfaces. Some I could solve, others subsist. It would simultaneously be myopic and magniloquent to expect the here presented oscillating sensor to revolutionize the world as such. But then some of the here-presented beads of expertise on nanoelectromechanical interfaces make this dissertation valuable for the designers of the future.

1.2 This work in a nutshell



Sensor & interface In the context of enabling compact sensor nodes, it was the aim of this thesis to develop electronic interfaces that would allow to operate single carbon nanotubes as electromechanical oscillators and dynamic sensors. To get you started smoothly, let us first look at an analogy at the macroscopic scale.

The viola analogy Simplistically speaking, a viola is formed by four tensioned strings that may be brought to oscillation over a wooden cavity. To do so, the violist uses a bow to draw sound from the strings. The friction of the bow on the strings transmits the necessary energy to make the string oscillate at audible frequencies. The wooden cavity amplifies the signal from the string and adds further harmonics, which altogether result in the peaceful warm sound known for

1.2. This work in a nutshell

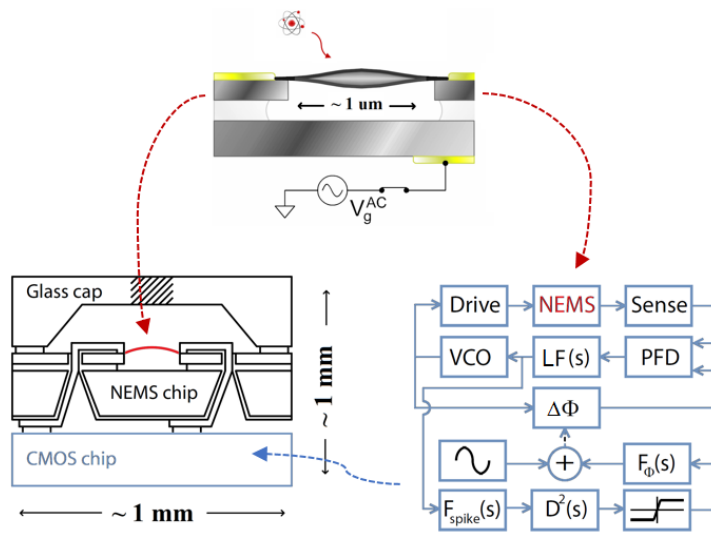


Figure 1.1: Suspended carbon nanotubes (*top*) can be set to resonance by application of an electrical signal. They are highly sensitive to their environment, and a binding molecule alters the resonance frequency. This change in frequency can be tracked by an electronic loop (*right*), that reads the current flowing through the tube, and steadily corrects the actuation signal, so to keep the tube oscillating. The tube and electronics can be integrated into a compact 1mm^3 sensor node (*left*).

violins. If the musician hears that the produced note is slightly detuned, she can adjust the tension of the strings and hence shift their resonance frequency. Four strings are certainly not enough to cover the whole spectrum of notes composing a symphony, but infinitely many tones can be produced by placing the finger at a carefully chosen location along the string. This has as an effect to reduce its apparent length and shift the oscillation to a higher frequency.

Scaling down the viola a million times per dimension, brings us to the dimensions this document will cope with. The viola string becomes a suspended carbon nanotube, a micrometer-long hollow cylindrical single molecule, composed of a few thousands of carbon atoms. Such a suspended and tensioned carbon nanotube oscillates at higher frequencies, around gigahertz. The electrostatic force between the tube and a nearby electrode, plays the role of the bow. Detectable tube oscillation amplitude builds up only if the force's periodicity is close to the tube's eigenfrequency. Transistors are then necessary to amplify the feeble signal, a flow of electrons in and out the tube, similarly to the wooden viola body. An electronic feedback circuit detects whether the received signal corresponds to the tube's eigenfrequency, and adjusts the electrostatic actuation force if necessary, just as violinists do. A small tensile actuator allows to tune the tube's eigenfrequency by strain. Not fingers, but surrounding molecules, may bind to the tube and alter its eigenfrequency. If the feedback circuit is able to find the new eigenfrequency, then sensing becomes possible, and the binding molecule's nature might be inferred for example. Such a sensor may fit into a 1mm^3 cube, and become part of future health sensors.

Scale-down

Beyond this point, your reading will become more technical. To put you into the appropriate mindset, you will be guided forthright through a brief outlook of what this document encompasses. Advanced explanations have been omitted for the sake of clarity. Simply let the tour affect you, and the following chapters will touch the essence of these highlights.

Technical warm-up

First and foremost, the electromechanical resonator, shown in Figure 1.1-top, earns some

CNT-NEMS

attention, because all the circuit design is about how to interface these carbon nanotubes (CNT). Until today, suspended electromechanical carbon nanotube resonators (CNT NEMS) remain a rare article, and no electromechanical black box models, ready for simulations at system level, exist yet. By lumping the NEMS' continuum equations of motion and diving into solid state physics, the useful linear dynamic range of CNT-NEMS operation is identified. Optimisation over the complete CNT design space (tube length, diameter, chirality, prestrain, ...), yields an upper bound on the achievable CNT-NEMS performance. Most notably, are orders of magnitude of the actuation force, capacitive, field- and piezoresistive- effects evaluated in terms of signal strength, frequency and phase.

- Front-end** Biasing of the NEMS and the choice of the first gain stage, are extremely delicate, because this is where the feeble signal out of the one-dimensional CNT meets the noisy three-dimensional world. Aggressive filtering is generally used to observe a relatively clear NEMS signal. But such an approach would obstruct the prospects of achieving fast and high resolution sensing. This is why a broadband approach is adopted, and the adequacy for readout of bipolar junction (BJT) and metal oxide semiconductor (MOS) transistors is assessed.
- Feedback** To sustain CNT oscillation and allow rapid adaptation to environmental changes, part of the CNT output signal must be coupled back to its input, so to correct for errors before the NEMS signal is lost. Figure 1.1-right shows the NEMS, embedded into such a feedback loop. Electronic blocks like a voltage controlled oscillator (VCO), phase-frequency detector (PFD) and loop filter, form a phase-locked loop (PLL) that tracks the NEMS motion. Traditional PLL design encounters here a novel challenge, as it must be fast enough for its external signal, which is the CNT motion, not to cease. An additional phase correcting loop is necessary to lock onto the NEMS independently of the signal delay, necessary for quantitative high-speed sensing.
- Implementation** The final sensor node could look like the 1mm^3 cube of Figure 1.1-left, which contains the NEMS, integrated atop a CMOS chip holding the feedback electronics. Printed circuit board (PCB) realizations of the front-end and feedback loop have been implemented, and partial integration has been performed, with a lower priority. Working CNT-NEMS are an not easy to create rare and hence precious article, which is difficult to spy out. So an electronic CNT-NEMS emulator was the best possible option to verify the functionality of the implementations.
- Ready?** Now that you got a rough idea of what this document holds in readiness, the sequel of the introduction provides a more detailed description of the technological context, visualizes part of the major challenges and highlights the document's structure.

1.3 Enabling Autonomous Sensor Nodes



- Why** The motivation and a qualitative rationale, for why electronic interfaces for carbon nanotube
How electromechanical oscillators and sensors merit attention in the quest for ambitious smart
What dust applications, are presented next. A technological platform, providing a realistic context

1.3. Enabling Autonomous Sensor Nodes

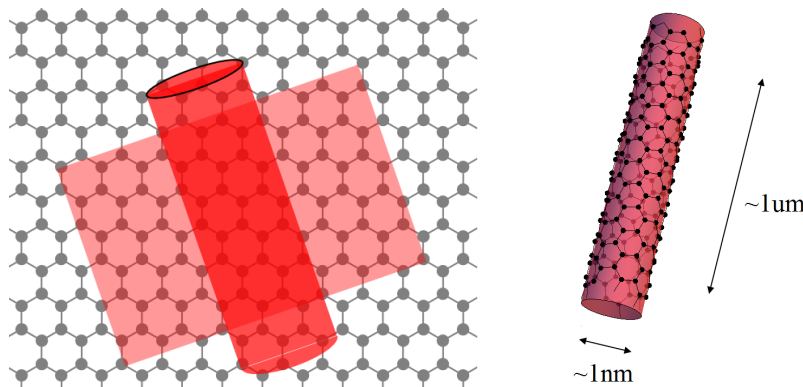


Figure 1.2: Graphene (left) is a flat sheet of carbon atoms arranged in a honeycomb lattice. Rolling such a sheet up into a cylinder, yields a carbon nanotube (right), which is a high aspect-ratio hollow molecular wire 50'000 times thinner than a human hair. [drawn with Wolfram Carbon Nanotube online project]

for such a contribution, is sketched and will show what role electronic interfaces play in there.

1.3.1 Motivation and qualitative rationale



What miniaturization of electronics was to computation and integrated intelligence (*savoir*), miniaturization of mechanics will be to detection, actuation and integrated action (*faire*). The combination of both domains gives rise to micro- and nanoelectromechanical systems (MEMS/NEMS) that enable autonomous know-how (*savoir-faire*) at microscopic scales.

Savoir-faire at micro- and nanoscales

The duty of a sensor is to make a physical phenomenon observable. And observability of the environment is the very first step towards interactive decision making. Environments may be subtle and damageable, requiring high sensor sensitivity and noninvasive small device size. Such microsensors further benefit from higher speed, less inertia, increased functionality density and reduced cost, compared to their macroscale versions. Given that the semiconductor industry is mainstream for information processing, large scale economic viability requires the sensed information to be converted into an electronic signal. Mechanical detection of the physical phenomenon turns out to allow versatile grafting of complementary detection mechanisms, as presented in section 1.3.2.

Microelectromechanical sensors

Purely electrical oscillators are ubiquitous in electronic circuit design and may be found among others in clock generators, signal transmitters and receivers. The benefit of electromechanical oscillators comes with the high mechanical quality factor of such structures, which would primordially translate into enhanced signal purity and selectivity in electronics design. An end in itself, electromechanical oscillators are also a means towards micromechanical sensor design. Oscillating sensors experience indeed a beneficial boost in signal strength by the quality factor at resonance and facilitate readout of the sensed data.

Electromechanical oscillators

When looking at the electromechanical sensing device itself, silicon, gallium-arsenide, silicon-nitride, silicon-carbide and aluminum-nitride NEMS are mainstream, due to the established lithographic and surface micromachining techniques. Reproducible carbon nanotube NEMS growth, yielding well controlled device properties, on the other hand, is still in its fledgling stages. Given the promising feats of carbon nanotube resonators though, one might expect

Carbon nanotube NEMS

the technology to experience a boost in the near future, and it is probably not too early to explore their full potential. Carbon nanotubes, high aspect-ratio hollow molecular wires, are grown from catalytic particles and possess nanometer diameters. They may be thought of as a rolled-up sheet of graphene, as suggested by Figure 1.2. This bottom-up approach allows sizing down NEMS to dimensions simply inaccessible to batch photo-lithography top-down approaches. The smaller dimensions enable higher spatial resolution and entail higher eigenfrequencies, which translate into better temporal resolution. Mass decreases as well, requiring less driving force for a same acceleration, and lowers the power budget. Simultaneously do carbon nanotubes show unprecedented sensitivity to strain and mass loading, making them suitable for fine sensor operation. They also tolerate large strains and may be widely tuned over frequency. Their round shape suggests potentially high quality factors and the absence of dangling bonds. Finally, functionalization via grafting of molecules is possible and might lead to very selective sensors.

Electronic interfaces The previously presented electromechanical carbon nanotubes have the potential to become outstanding oscillators or sensors. Now an appropriate interface is indispensable to activate the device, operate it as oscillator or sensor and read the sensed information to carry it towards a computational unit or evaluate it in place. Electronic circuits are mainstream, as has been mentioned before, and they are very practical and scalable, compared to other techniques, like interferometric optics. Fast operation of NEMS requires reactive electronics, which steadily drive the former, read out the sensed data, and process part of it in place in order to ensure stable operation. The electronic interface consequently forms a feedback loop around the NEMS and must control it seamlessly in order to operate it as an oscillator or sensor. The challenges awaiting such an interface for oscillator or sensor operation of electromechanical carbon nanotubes are tremendous and will be exhibited in section 1.5.

1.3.2 A contextual technological platform

System-in-Package A versatile platform for nanoelectromechanical oscillators and sensors is shown in Figure 1.3. The packaged die of a few cubic millimeters consists of a stack of three layers: a NEMS chip, a CMOS integrated circuit (IC) and a glass cap. A three-dimensional integration process assembles the silicon CMOS and silicon-on-insulator NEMS chips by a stud bump technology, while the glass cap is eutectically bonded to the latter. The inter-wafer electronic connection may be ensured by through-silicon vias (TSV).

The NEMS chip hosts a tunable carbon nanotube (CNT) electromechanical resonator. Structurally, the device consists of a suspended single-walled carbon nanotube, which bridges the gap between two anchor tips. One of the tips is mobile and coupled to a tensile MEMS actuator, enabling control of the tube strain and consequently its mechanical eigenfrequency. Electronically, the device allows to transport charges between the two tips and its transport properties are controllable by a movable nearby electrode. All in all, a controllable and operational electromechanical resonator, with environmental

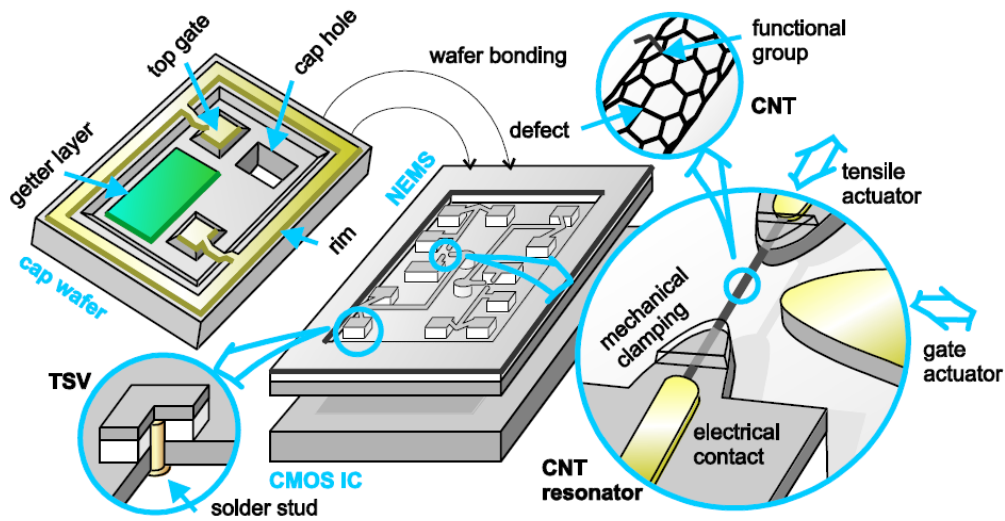


Figure 1.3: Contextual system architecture for CNT-NEMS oscillators and sensors [CabTuRes - Nanotera.ch]

sensitivity, results.

The CMOS IC hosts the electronics that accomplish diverse operations with the above carbon nanotube nanoelectromechanical system (CNT-NEMS) and actuator MEMS. This is the core business of the present dissertation. We will dive deep into these electronic interface challenges in the coming chapters.

The glass cap mediates the interaction of the CNT-NEMS with the environment. It is hermetically sealed at low pressure and equipped with a purification getter when realizing purely electronic functions and perforated for gas inlet onto the surface of the functionalized CNT-NEMS when sensor operation is desired.

In combination with energy harvesters for power supply and a communication layer for in-vivo or remote sensing, this system-in-package platform constitutes a milestone towards autonomous smart dust applications and forms a tangible context for electronic CNT-NEMS sensor interface design.

The presented platform leads straightforwardly to diverse applications that have the potential to establish new performance records.

Application
outlook

Mass balances and particle detectors: Quantitative mass determination can be inferred from shifts in the NEMS eigenfrequency. Selectivity may be obtained via tube functionalization and the low-mass CNT-NEMS may yield atomic scale mass sensitivity, beneficial to biological, chemical and medical applications in health care and environmental monitoring.

Force and pressure sensors: Frequency tuning can be achieved by straining the tube via a tensile MEMS, similarly to the tuning of a viola string, which makes the system extend-

able to a force sensor. In combination with a diaphragm, pressure sensing also becomes possible. The application spectrum of such sensors is immense, ranging from personal mobile phones over the automobile industry to aerospace.

Voltage controlled oscillators and clocks: With higher quality factors than integrated LC tanks and wider tuning ranges than quartz crystals, tunable CNT-NEMS would complement these omnipresent electronic blocks in their roles as oscillators and system clocks.

Filters: Electromechanical signal purification would benefit from the high NEMS quality factors at high frequencies.

The common denominator of all these applications is the ability to continuously operate the CNT-NEMS as a quantitatively controllable oscillator. The present dissertation will focus on this aspect, while regularly relating the implications of the findings to the applications.

1.4 Identifying the Challenges

Veni, vidi, ... Now that the context has been set, time is ripe to identify the potential challenges awaiting
composui the "design of electronic interfaces" for carbon nanotube electromechanical resonators. CNT history started roughly two decades back and the even younger field of CNT-NEMS emerged only a single decennium ago. This left research with more time for bringing up new challenges than it actually could solve. The presentation of the state-of-the-art may consequently look a bit wide-ranging at first sight, but this effort is inalienable to get a good idea of the issues and opportunities, before diving deep down (the wrong branch of) the research tree.

1.4.1 Handling interconnects and contact parasitics

Ideally Signal flux between the CNT-NEMS and the CMOS chip should be lossless. Excessive attenuation may indeed plunge the feeble NEMS signal into the noise and make it invisible to the interface electronics.

Challenge Though CNTs possess excellent intrinsic electrical conductivity [7], the contact resistance at the CNT-metal interface, where the three-dimensional world clashes with the one-dimensional tube, is large [8], especially for single walled carbon nanotubes (SWNT). In combination with capacitive through-silicon vias [9], a lowpass filter forms and complicates signal readout at high frequencies in the megahertz (10^6 Hz) to gigahertz (10^9 Hz) bands, where the CNT-NEMS eigenfrequency ω_0 ranges.

State-of-the-art Ingenious tricks to minimize or circumvent signal loss evolved along two orthogonal axes and may be categorized into *process techniques* and *circuit techniques*:
Process techniques take advantage of the insight that CNT-metal interface states are not strong enough to pin the Fermi level [10], leading to Schottky barriers with heights, and consequently

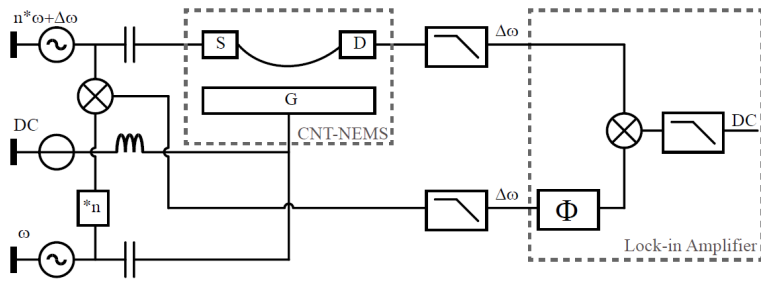


Figure 1.4: CNT-NEMS operated as a mixer. The low-frequency signal $\Delta\omega$ seamlessly flows through the lowpass filter formed by the CNT-NEMS contact impedance and the track capacitance. It peaks in amplitude and inflects in phase when $\omega \in \{\omega_0, \frac{\omega_0}{2}\}$, where ω_0 is the NEMS eigenfrequency and $n=1$ [1], $n=2$ [2] or $n=4$ (new).

transmissivity, depending on the metal work function [11] and the CNT diameter [8], creating an interval for ohmic contacts. Rapid thermal annealing [12], grafitic interfacial layers [13] or the introduction of topological defects [14] were recently shown to lower the contact resistance. TSVs and flip-chip packaging present lower RLC parasitics than traditional wire bonding techniques and their resistance and inductance are negligible with respect to the CNT-metal contact [9], while their capacitance contributes to the lowpass filter.

Circuit techniques, as shown by Figure 1.4, consist in shifting the information towards lower frequencies $\Delta\omega$, at which signals flow seamlessly. This may be achieved by operating the CNT-NEMS as a mixer [1] or by averaging [15]. Direct readout [16] has not yet successfully been demonstrated, although graphene sheet resonators [17] and nanowires [18] may already enjoy the advantages of high-speed readout. The actual trend is to make mixers faster in order to advance to high-speed applications. Mixer bandwidth has been enhanced from kHz to MHz very recently [19].

Today's low-frequency readout techniques doubtlessly allow to experimentally prove CNT-NEMS properties that are fundamental for sensing, such as capacitive, field effect and piezoresistive conductance modulation, but obstruct its passage towards the full spectrum of high-speed sensing applications that may open new windows on in-vivo biology and disease mechanisms [20]. The feasibility of direct large bandwidth signal readout needs to be reassessed in the frame of the latest technological advances and a quantitative comparison between readout mechanisms is to be established.

Assessment

1.4.2 Relating modes of operation to device bias

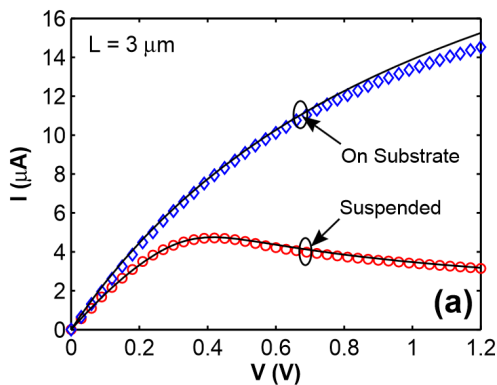


Motion of the CNT-NEMS may be inferred through electrical detection of the mechanical motion. Capacitive, field effect and piezoresistive current modulation may serve as such detection mechanisms. Unfortunately purely electrical, motion-independent, background signals also appear, as well as noise. The CNT-NEMS shall be biased towards a mode of operation with favourable relative strength of signal versus background, in a way that makes it operational by the interface electronics under minimal addition of noise.

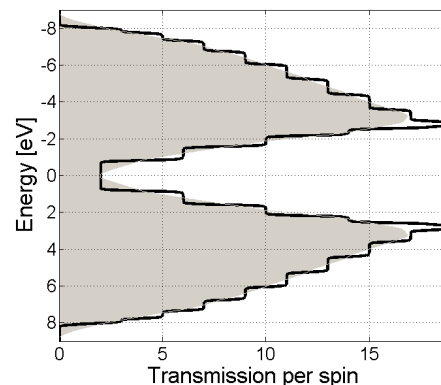
Ideally

The strength of the electromechanical transduction mechanisms roots in solid state physics and is highly sensitive to the device bias. Profound understanding of the transduction mecha-

Challenge



(a) Source-drain current through a SWNT as a function of the source-drain voltage (published by [21]). Scattering saturates the current under high bias and reduced evacuation of hot phonons generates a negative differential resistance in suspended tubes.



(b) Transmission per spin for a (10,10) armchair SWNT, under ballistic transport at 300K (–) and averaged over a linear 1V potential drop along the tube (shaded area). No bandgap exists and the CNT is metallic. Its conductance depends, however, on the gate potential.

Figure 1.5: Impact of source drain and gate voltage on current through SWNT

nisms seems of paramount importance for optimal device biasing.

State-of-the-art Carbon nanotubes are one-dimensional constrictions that exhibit quantized conductance under ballistic transport [22], as illustrated by Figure 1.5b. This non-dissipative property persists when elastic scattering in long tubes or under high bias sets in, but with reduced transmission coefficient, which entails that the conductance is no longer precisely quantized [23]. As a matter of fact, however, no prominent quantization is generally observed for room temperature transistors [24], which are often considered as semi-conducting band-gap materials with controllable channel band bending and contacted either ohmically or through a Schottky barrier. Today’s hall of fame of CNT-NEMS with successful resonance detection, operating the CNT-NEMS exclusively in a mixer setup, is only sparsely populated and shows no clear progress from early [1] [2] to late [25] entries. If large potential differences contact the extremes of long tubes, then optical and zone boundary scattering saturate the current [26], and the CNT behaves as a current source, with possibly negative differential conductance for suspended tubes [21], as can be seen from Figure 1.5a.

Assessment An optimal bias in the context of quantified conductance would be an operation point with conductance insensitive to electrical phenomena, while motion would succeed to change it by a quantum. Relating the conductance modulation in resonating NEMS merely to changes in the tube-gate capacitance, as is done systematically in state-of-the-art articles, supports the observed phenomena qualitatively, but lacks any quantitative evaluation, which may have in store novel insights. It definitely seems worth displaying the solid state physics of CNT-NEMS from a circuit design point of view, in order to make the NEMS designer community aware of the potential and issues of biasing, especially when electrostatic frequency tuning may shift the operation point without the necessary awareness [1]. In addition to this, it is worth

Quantity	Frequency	Effect
drive ↓ $(+)^2$		→ capacitive
position ↓ $(+x)^2$		→ field-effect
elongation		→ piezoresistive

Figure 1.6: The capacitive, field-effect and piezoresistive transduction mechanisms generate peaks at different spectral positions that allow to separate motional and purely electrical information under direct readout.

considering new, non-mixing topologies for CNT-NEMS oscillators, which have the potential for new applications, and which analyse the impact of circuit noise.

1.4.3 Efficiently actuating the CNT-NEMS



The electrostatic force, sufficiently strong to keep the CNT-NEMS in motion, is provided by the gate electrode voltage and shall create only minimal undesired electrical coupling. Ideally

Given the suspended CNT, electrostatic force may induce motion upon the NEMS, but comes at the cost of a parasitic capacitive coupling that complicates motion detection. While the electrical coupling to the CNT may be minimized by optimal biasing, the coupling to the source and drain electrodes depend on the device geometry, driving technique, scales with increasing operating frequency and may overshadow the motional information. Challenge

To date, electrode placement seems not to follow any clear design trend and wide bottom electrodes [1], providing controllability along the entire tube length at the cost of stronger parasitical coupling to the source and drain electrodes, are as frequent as slender side-electrodes, with reduced coupling [25]. The reason for the little interest in electrode shaping may be the fact that CNT-NEMS are operated as mixers and readout is performed at an intermediate frequency. This technique simultaneously circumvents the lowpass filtering interconnects, as well as it allows to spectrally separate the signal from the capacitive coupling. State-of-the-art

With the goal of enabling direct readout, necessary for high-speed closed-loop operation, interest raised in devising strategies that reduce the spurious coupling. Process techniques such as electrode design, and circuit techniques such as temporal multiplexing, frequency multiplexing by sinusoidal or square actuating signals, as well as the potential of filtering, will be addressed. Assessment

1.4.4 Robust signal readout



The readout should allow to extract the instantaneous motion out of any CNT-NEMS. This supposes that the motional information must be made observable with respect to the electrical background and noise, and that information on instantaneous phase must be conserved. Enabling such a readout would definitively put the highly sensitive CNT-NEMS resonators into a privileged situation for ubiquitous sensor design. Ideally

- Challenge** Electronically, CNTs can be semiconducting or metallic, but only characterization may tell. For some, potential fields and strain change their conductance, but rarely in the same way. The signals are rather feeble and the mechanical quality factors lower than theoretically predicted. This makes it challenging to observe the CNT full-time, while controlling it only part-time. While optimal biasing and actuation techniques may cater maximal signal strength, readout should enable spectral separation of the motional and electrical information, without bandwidth reduction.
- State-of-the-art** Given the tremendous challenges in CNT-NEMS growth processes, localization and chirality control [27], the potential one third yield loss is negligible and circuit-level solutions have not yet been addressed. Four circuit tricks have been proposed on the other hand for spectral separation of signal and background. Mixing the signal to an intermediate frequency to circumvent noise and background signals [1], is the workhorse. It has further been discovered that the NEMS may be actuated at half its eigenfrequency [28], which spectrally separates the motional information from the capacitive gate-drain coupling. Averaging the signal response over time also allows to see the resonance peak due to the tube's piezoresistivity [15]. Finally, a frequency modulated mixing technique possesses no electrical background signal at all at the intermediate lock-in frequency [29].
- Assessment** All previous techniques have in common that they infer the motional information from an intermediate frequency, which makes them suffer instant phase information loss. Given that the theoretic background on mixing techniques does not account for the CNT band structure, but bases merely on a macroscopic capacitance model, a deeper analysis is required to assess the ubiquity of this method. MEMS motion has traditionally been inferred via capacitive sensing. But the drastic scale-down to NEMS dimensions makes it challenging to read changes in capacitance that are orders of magnitude smaller than the parasitic track capacitance. Orders of magnitude for signal strength and process invariance of capacitive, field effect and piezoresistivity need to be established, and may lead to novel readout concepts that steer electronic interface design. Figure 1.6 suggests that actuation, oscillation and tube elongation may appear at distinct frequencies, depending on the choice of actuation technique. This means that the capacitive, field- and piezoresistive signal modulation appear at a frequency that is distinct from the actuation frequency. Spectral separation of the motional signal from the electrical feedthrough is possible and is put under investigation in chapter 2.

1.4.5 Conceiving tunable self-regulating CNT-NEMS oscillators



- Ideally** Voltage controllable oscillators find wide uses in electronics, but an electromechanical equivalent would provide a higher quality factor than inductor-capacitor (LC) tanks and offer tunability over quartz crystals. The NEMS eigenfrequency should further be adjustable to match the circuit bandwidth. The circuit should automatically operate the NEMS close to its eigenfrequency, where signal strength is maximal.
- Challenge** In order to conceive versatile oscillators that can adapt to a large portion of the CNT-NEMS

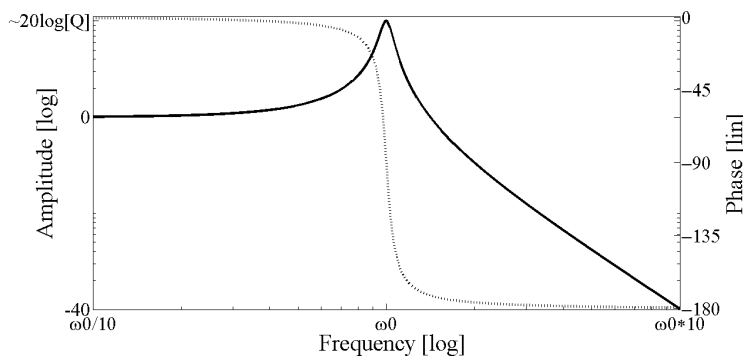


Figure 1.7: In its linear dynamic range, the CNT-NEMS may be modelled as an harmonic oscillator with mechanical eigenfrequency ω_0 and quality factor Q . The frequency response peaks in amplitude (—) and inflects in phase (···) close to ω_0 . Outside this range, the NEMS presents hysteretic behaviour and is inappropriate for closed-loop operation.

design space in terms of resonance frequency, either the circuit blocks must be tunable or wideband, or the NEMS eigenfrequency has to be made controllable. While wideband operation stands for larger noise, circuit tunability is a serious design overhead. NEMS frequency tuning, on the other hand, needs an additional degree of freedom in order to adjust the eigenfrequency independently from the operating point.

Resonance gives itself away against frequency, as a peak in amplitude and an inflection in phase, as can be seen from Figure 1.7. Making the NEMS operate close to resonance yields stronger signals and better signal to noise ratios. To date, only frequency sweeps allow to detect either of these phenomena [1], [29]. Once the resonance frequency has been found, the signal out of the mixing NEMS appears however at a low frequency and the benefits of the electromechanical high-frequency high quality factor resonator fade away. This situation is different for silicon based NEMS, that yield stronger signals and have already been embedded into self-adjusting closed loops [30] that make the intrinsic NEMS signal available. Given the low frequency readout, circuit bandwidth has rarely been an issue, and tuning was less relevant. No viable tuning solution exists so far, given that the electrostatic tuning through the gate potential [1] changes the operating point.

State-of-the-art

Searching for the eigenfrequency by sweeping through the spectrum hazards the consequences of temporarily losing control of the NEMS, which seems unacceptable in the prospect of critical in vivo applications. So a self-regulating closed-loop system needs to be conceived. Frequency tuning, without changing the NEMS operation point, cannot be performed by the gate electrode and an extra mechanical degree of freedom is necessary.

Assessment

1.4.6 High-speed high-resolution mass balances



A particle that binds onto the CNT-NEMS changes the latter's eigenfrequency and quality factor. This shift in eigenfrequency, illustrated by Figure 1.8, shall be detected as precisely as possible and as fast as possible in order to enable high-speed high-resolution mass sensing.

Ideally

The absolutely fastest way to extract the frequency of any periodic signal is to measure the time of its period. Given the presence of noise and finite resolution of the time measurement, averaging over several periods enhances the precision of the observed frequency at the cost of

Challenge

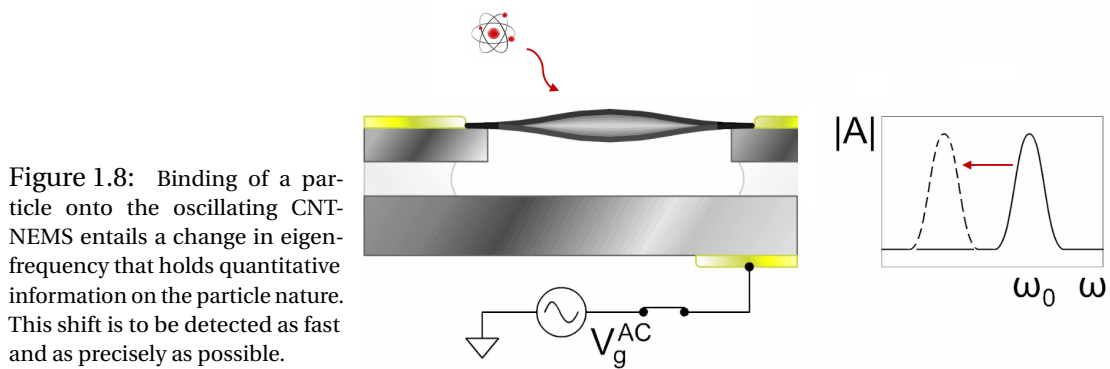


Figure 1.8: Binding of a particle onto the oscillating CNT-NEMS entails a change in eigenfrequency that holds quantitative information on the particle nature. This shift is to be detected as fast and as precisely as possible.

a longer observation time. Fixing the observation time and counting the periods may do as well. As a matter of fact, the confidence on the estimated period increases over time and with the signal's frequency. High-speed high resolution mass sensing hence requires fast signal detection. Additionally must the signal occur precisely at the eigenfrequency, or the offset be correctable. The CNT-NEMS must consequently be brought to resonance at its eigenfrequency as fast as possible.

State-of-the-art The advent of ultra-light ultra-sensitive MEMS improved the record of mass detectability down to zeptograms (10^{-21} g), the weight of a small protein [30]. CNT-NEMS further enhanced this down to yoctograms (10^{-24} g), the weight of a single proton [31]. Below that, there is not much more to weigh and progress seems to have reached the useful limits in terms of detectability. From a point of view of speed, things look different, however. Initial approaches that sweep through the entire frequency spectrum in order to detect the resonance peak of phase inflection [1], have been replaced by microcontroller- [30] and computer-controlled feedback loops [31] that track the resonance frequency with a feedback time of tens of milliseconds. The latency of these systems roots in the mixer operation of the CNT-NEMS, which makes the eigenfrequency observable only indirectly at a much lower frequency of the order of kHz. A breakthrough was the very recent microsecond mixer readout [19], which has the potential to lead in the future to frequency tracking in the order of microseconds.

Assessment Binary detection or qualitative assessment of sensed phenomena can be achieved by detecting a shift in the oscillation frequency. Quantitative evaluation, however, requires tracking of the NEMS eigenfrequency. Frequency sweeping allows to find this eigenfrequency precisely, but slowly. Speed has been enhanced to milliseconds and the latest findings raise hope for microsecond resolution, while direct readout would be the best possible scenario. Closed-loop operation has admittedly to deal with circuit block delays, and the theoretical $\frac{\pi}{2}$ phase shift hypothesis (see Figure 1.7) becomes inapplicable in systems where the NEMS is only observable through a cascade of several electronic blocks, each contributing with its own delay. A system-level solution to this would be desirable in order to enable quantitative high-speed high-resolution mass sensing.

1.5 Inventing the Solutions



By the day this thesis started, the world has seen only a fistful of resonating CNT-NEMS. Context
 A first demonstration emerged in 2004 [1] and slack could be removed in 2006 [32]. This allowed to cross the GHz barrier [2] and interest in CNT-based mass sensors started in 2008 [33]. High quality factors at cryogenic temperatures were first confirmed in 2009 [34]. All these demonstrators shared the common characteristics that they operated the NEMS as a mixer. Although the field took off (reference [1] counts 654 citations on ISI WoK today), this fact remained unchanged during the years of this thesis - frequency-modulated mixing [29] emerged in 2010 and two-source mixing [19] saw a speed-up from kilo- to megahertz at the end of 2013. CNT-NEMS mass balances reached atomic scale resolution in 2012 [31] and enhanced speed would be the next milestone. But even today, batch CNT-NEMS fabrication methods are not yet mature and individual manipulation is a tedious art. Consequently few devices exist, fewer are operational, and even less frequent are those that exhibit the desirable properties and appear in literature. The situation excludes statistical evaluation and makes reported conclusions skate on thin ice. This context immersed the four years of research on electronic CNT-NEMS interfaces into an amalgam of hope to be offered one day an operational CNT-NEMS for testing, and suspiciousness that this day will not come before completion. The latter turned out to be the case. This explains why the work of this thesis is nicely diversified, reaching from CNT-NEMS modelling over circuit implementations towards system-level contributions. The following chapters lead in a bottom-up approach from CNT-NEMS modelling over the front-end design towards system-level conception. Circuit implementations and characterization are saved for the final chapter.

Carbon nanotubes in general and their operation as suspended electromechanical resonators Chapter 2
 in particular, are analysed from a system-level point of view. A review of the physical origins of their electrical and mechanical properties allows to systematically categorize the signals that an electronic interface will have to handle. Orders of magnitude and ubiquity of the capacitive, field-effect and piezoresistive signal components are established and linked to state-of-the-art measurements that express the observed phenomena by a deprecate capacity model. A novel mixing method with fourfold frequency separation between motional and capacitive coupling naturally crystalizes and becomes the second known method (after [29] in 2010) that completely dissociates mechanical from electrical information. The chapter concludes in a circuit-level model of suspended carbon nanotube resonators with associated orders of magnitude as well as bias and frequency dependence of its component values.

Different actuation and detection schemes for the CNT-NEMS are assessed subsequently Chapter3
 in a circuit context, where electrical component noise enters the game. Selective but low-bandwidth mixers are categorized and completed by a novel mixing technique with a 4-fold frequency ratio between actuation and detection. From here it is just a few steps towards a dual mixing technique, allowing to monitor electrical and mechanical characteristics simultaneously, and having application potential in the characterization of adsorbate configuration states. The chapter's focus sweeps then to direct readout topologies, which have the

potential to enable unprecedented high-speed high-resolution sensing and can operate as microelectromechanical voltage controlled oscillators. The readout topologies are evaluated analytically in terms of signal-to-noise and signal-to-background (motional versus purely electrical information) ratios. The optimal interface choice within today's library of electronic components, is found to be a function of the CNT-NEMS eigenfrequency, favouring the use of metal-oxide-semiconductor (MOS) transistors at low or moderate frequencies, and bipolar junction transistors (BJT) at high frequencies. Simulations support this conclusion and a circuit implementation gives rise to a direct readout demonstration on a CNT-NEMS device.

- Chapter 4 Once the signal can be extracted, an electronic feedback loop is designed in order to create an electromechanical oscillator. Different topologies are investigated and one that embeds the NEMS into a phase-locked loop (PLL) is retained as a good compromise for its flexibility and utility: on the one hand it can be tested without CNT-NEMS and on the other hand it allows to characterize CNT-NEMS in terms of capacitive, field-effect and piezoresistive signal strength. It has additionally the potential to operate CNT-NEMS in a high-speed closed-loop configuration as oscillators, in a very similar way to self-sustained oscillators. Mixing topologies would miss the speed factor here, making them less attractive for the high-speed target applications. Optimal feedback design guidelines are established. The utility of the electromechanical oscillator for sensor applications in general, and as a mass balance in particular, is discussed next. The benefits of closed-loop oscillator operation of the CNT-NEMS over frequency sweeping and mixing, is the better temporal resolution. Closed-loop sensing techniques are found to be susceptible to offsets and a novel calibration system is proposed. This system brings sweeping and closed-loop sensing on a par in terms of resolution and offers substantially higher sensing speed.
- Chapter 5 The previously developed systems are partially implemented, on a printed circuit board to prove the concepts, and in a 180nm CMOS technology to strive for performance. A VCO as emulator of the CNT-NEMS, was added in prevision of the likely case that no operable NEMS would be available. Sufficient for illustration of the principles, a big chunk on NEMS related dynamics is thereby neglected, reason to make the implementation and characterization parts a lesser priority. The circuit's compatibility with the CNT characteristics is nevertheless assessed in the context of mechanical frequency tunability of CNT-NEMS. Its settling time and noise figures allow to conclude on the expected speed and resolution performance, outperforming state-of-the-art mass balances by several orders of magnitude.

*Everything should be made as simple as possible,
but not simpler.*

— Albert Einstein

2

Carbon Nanotube Electromechanical Resonators at System Level

A successful strategy towards electronic interface design for carbon nanotube electromechanical oscillators and sensors, requires a basic understanding of CNT-NEMS operation principles. Crafty solutions necessitate furthermore subtle insights. Therefore this chapter aims at establishing a system level view of the suspended carbon nanotube NEMS. Although it is concerned rather about orders of magnitude than precise values, attention is paid to some details that will lead to unprecedented insights of primordial importance for readout design. Electromechanical transduction mechanisms are assessed in terms of signal strength, frequency and phase delay. This information is necessary for adequate design of the electronic interfaces, which are the topic of the following chapters. The approach is kept at high level wherever possible, but to truly harness the potential and limitations of CNT-NEMS, occasional descents to the basic physics are necessary to develop a fundamental understanding of the electromechanical transduction mechanisms. As soon as the piece of information has been found, the chapter recurses back to the high level.

Top-down approach

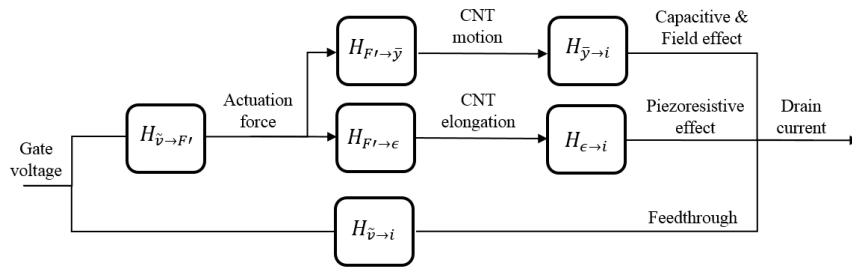
State-of-the-art single-source [35] and two-source [1] mixing techniques have successfully demonstrated observability of CNT-NEMS motion. The provided theoretical justification however merely treats the NEMS as a variable capacitor. Such an analysis is questionable given the one-dimensionality of CNTs and does not reveal the full potential of CNTs with respect to high-speed direct readout. This chapter is therefore devoted to the analysis of capacitive, field-effect and piezoresistive phenomena, and their impact on the conductance of CNTs and will indeed display yet unexplored techniques of motion detection.

Rationale

The outcome of this chapter will be the quantification of the current modulation through

Overview

Figure 2.1: The gate voltage sets the NEMS into motion, which can be inferred from the drain current.



the tube, caused by electrical and mechanical phenomena. These orders of magnitude will serve as reference for the subsequent circuit design. The signal path is decomposed into the partial transfer functions of Figure 2.1, describing the electromechanical actuation and mechano-electrical detection mechanisms. Foremost the NEMS is formally described as an electromechanical multiport. Then the mechanical dynamics are established: Starting from a general continuum model, a lumped Duffing type equation crystallizes. Hysteresis under large amplitude motion and the thermomechanical noise floor are shown to define the useful dynamic range. Transduction gain is then maximized over all available CNT parameters and the optimal solution is interpolated to yield an upper bound on the signal strength that can be expected from CNTs up to gigahertz frequencies. The capacitive, field effect and piezoresistive contributions to the signal can then finally be quantified.

2.1 CNT-NEMS – an Electromechanical Multiport

SWNTs & MWNTs Carbon nanotubes are long hollow cylinders formed of hexagonally arranged carbon atoms, that may be thought of as rolled up sheets of graphene (see Figure 2.18) and can be synthesized by arc discharge [36], laser ablation [37], plasma torch [38] or be catalytically grown by chemical vapor deposition [39]. The number of walls may be one or more, and the respective tubes are designated as single-walled CNT (SWNTs) and multi-walled CNTs (MWNTs). The electromechanical properties of MWNTs are a combination of the individual ones of their co-cylindrical SWNTs plus their interaction. In contrast to MWNTs, are all the atoms of SWNTs part of their surface. In combination with the lower mass of SWNTs, does this feat make them highly sensitive to the environment. This makes SWNTs the NEMS of choice for sensing applications. In this prospect will the present chapter focus exclusively on SWNTs.

Cantilever & clamped-clamped CNTs SWNTs may find themselves operated as cantilever beams [40] with a fixed and a free end, or as doubly-clamped beams [1]. Both topologies are presented in Figure 2.2. To preserve their environmental sensitivity and intrinsic properties, their surface may not be coated by a piezoelectric material, which leaves the electrostatic force, between the tube and a nearby electrode, as the only electrical actuation mechanism for both topologies. The free end topology moreover grants only capacitive readout: Motion of the CNT modulates the capacitance between itself and the nearby electrode and may thus cause current flowing in and out of the tube. These changes are on the order of the parasitical track capacitance or smaller however, which makes them hardly detectable, except by transmission electron

2.1. CNT-NEMS – an Electromechanical Multiport

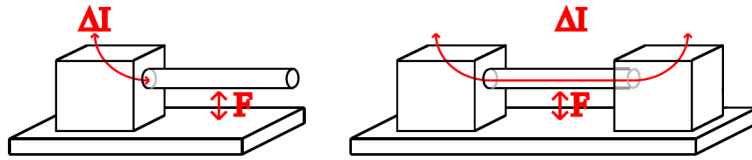


Figure 2.2: Cantilever (left) and clamped-clamped (right) CNT-NEMS with capacitive actuation. Capacitive current into and out of the NEMS is detectable in both topologies, field- and piezoresistive effects on the other hand become observable only through doubly-clamped NEMS.

microscopy (TEM). The doubly-clamped topology, however, presents the CNT in a suspended transistor configuration, which opens the possibility to further sense the current through the device, modulated via the NEMS' motion by field- and piezoresistive effects. They also present the benefits of a higher and tunable resonance frequency over the cantilever beams, which motivates this chapter's focus on clamped-clamped topologies.

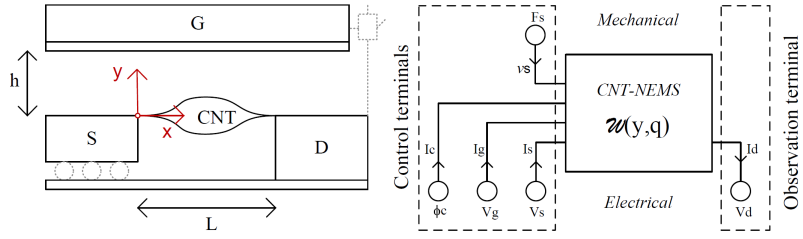
SWNTs are single molecular wires of carbon atoms with sp^2 hybridization. Their mechanical properties are primarily defined by these strong in-plane σ -bonds, while the electronic properties depend almost exclusively on the remaining delocalized π -states. The proposed clamped-clamped topology operates the SWNT as channel material, contacted in a transistor configuration, with source (S), drain (D) and gate (G) electrodes, as shown in Figure 2.3. Mechanical degrees of freedom occur when the channel is suspended and allow for frequency tuning via straining. With force and voltage (potential difference) as across-variables, velocity and current as through-variables, in the mechanical and electrical energy domains respectively, this electromechanical system presents two electrical (gate V_G and source V_S potential) and two mechanical (source and channel positions) degrees of freedom to steer inter-domain energy transfer. The drain is chosen to be the electrical observation terminal. This decision roots in the fact that the movable, frequency tuning, electrode (source) presents an elevated parasitic capacitance, which hampers high frequency readout. Figure 2.3 also lists the CNT potential ϕ_C , which is only indirectly controllable through V_G and V_S , but forms a useful auxiliary variable when establishing the equations. The CNT is actuated via an electrostatic force pulling from the gate electrode and its motion modulates the current flowing through it by nanoamperes, as shall be seen. Molecules, binding to the tube, or strain, induced via the movable source terminal, may alter the CNT's resonance frequency, entailing sensor and voltage controlled oscillator (VCO) applications.

Electro-
mechanical
multiport

Orders of magnitude of the geometrical parameters of the NEMS are given subsequently. Typical suspension heights h range from 100nm to $1\mu\text{m}$ and, by construction, often equal the buried oxide (BOX) thickness of silicon on insulator (SOI) wafers. The suspended tube segment length L spans from 100nm to $1\mu\text{m}$ and is limited downwards by lithography or electrode movability, and upwards by process yield for long tubes. The tube radius r strongly depends on the synthesis method. State-of-the art methods yield diameters d from 0.5nm to 5nm [41].

NEMS
geometry

Figure 2.3: Suspended carbon nanotube clamped between drain (D) and movable source (S) electrodes. A nearby gate (G) electrode controls the current flow. The motion is observable at the drain terminal as current or voltage.



2.2 Setting the NEMS to Motion

Outlook The introductory chapter alluded to CNTs that could be operated as electromechanical oscillators and clocks, as dynamic particle detectors and force sensors. The common denominator of these applications is that the CNT oscillates, and the very first mission consists therefore in bringing the suspended CNT to motion. First the tube motion is traced back to an homogeneously distributed actuation force in subsection 2.2.1, before the following subsections show how the gate potential may induce this force. Here it is worth to antedate that the capacitive (section 2.3.1) and field-effect readout (section 2.3.2) scale with the average oscillation amplitude \bar{y} of the tube, while the piezoresistive one (section 2.3.3) scales with the oscillation-induced strain ϵ . In this prospect, section 2.2.1 establishes the force to amplitude $H_{F' \rightarrow \bar{y}}(j\omega)$ and force to strain $H_{F' \rightarrow \epsilon}(j\omega)$ transfer functions, and the voltage to force $H_{\bar{v} \rightarrow F'}(j\omega)$ relation is obtained in section 2.2.4. The composed functions $H_{F' \rightarrow \bar{y}} \circ H_{\bar{v} \rightarrow F'}$ and $H_{F' \rightarrow \epsilon} \circ H_{\bar{v} \rightarrow F'}$ finally form the pertinent actuation transfer functions.

2.2.1 Forcing the tube to motion

Need for a mechanical model The sum of all incoherent stochastic noise processes is not strong enough to bring the tube into spontaneous detectable motion. So a well-engineered force needs to be designed, in order to control the tube's movement. The prediction of the relation between force and motion can only be as accurate as the model reflects reality truthfully. While the use of advanced mechanical models may seem disproportionate, too simplistic approximations may not catch the essence. A semi-empirical approach, that fits a relatively simple, but still sufficiently accurate, model to measured data, sounds then like an acceptable compromise. Even this approach is not straightforward nowadays, because yet the simplest models present more parameters than single-machine measurements yield data point dimensions. Take the minimalistic lumped model of a damped driven harmonic oscillator (pictured in Figure 2.5c), which relates a driving force F to effective displacement \tilde{y} via the resonator's mass m , stiffness k and damping c

$$m \cdot \frac{\partial^2 \tilde{y}}{\partial t^2} + c \cdot \frac{\partial \tilde{y}}{\partial t} + k \cdot \tilde{y} = F \quad [\text{N}] \quad (2.1)$$

These three model parameters (m, c, k) face the two parameters obtainable by resonance measurements, which are the resonance frequency $\omega_0 = \sqrt{\frac{k}{m}}$ and quality factor $Q = \frac{\sqrt{mk}}{c}$.

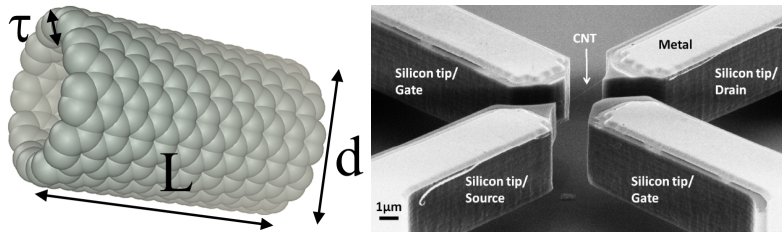


Figure 2.4: (left) Molecular representation of a single walled (10,10) armchair carbon nanotube. Their shape may be approximated as a hollow cylinder of length L , average diameter d and thickness τ . (right) The optical microscope view of the suspended CNT reveals the high $\frac{L}{d}$ aspect ratio. [by courtesy of [3]]

The third measured parameter, the absolute signal amplitude, however is not directly usable, because it is not a direct observation of the NEMS position \tilde{y} , but an image of this information, that is scaled by a variety of electrical properties, which will be investigated in section 2.3. The state-of-the-art solution to this problem is the hypothesis that the measured NEMS signal can entirely be traced back to the variation of the tube to gate capacitance [1]. Such an hypothesis needs a proof, or shall be disproven, as it turns out in section 2.4. An alternative third measurable parameter could be the tube's mass. Direct weighing is not possible, given the featherweight of such tubes, but the weight may be inferred from the tube's geometry. The suspension length is known from lithography, while the radius can be determined either by atomic force microscopy (AFM) [42], or Raman spectroscopy [43]. Scanning (SEM) and transmission electron microscopy (TEM) on the other hand would be destructive measurement techniques for CNTs [44]. All in all, three parameters - the eigenfrequency, quality factor and mass - can indeed be determined, at the price of bringing the NEMS into the different measurement machines, which is a tedious process and certainly not a viable approach at large scale. Some representative statistics would be very valuable though, because the measured data presents large spreads. Mechanical resonance frequencies span from low MHz [1] to low GHz [2] and quality factors range from 10^5 at cryogenic temperatures [34], down to 100 at room temperature [1]. Further do structural defects and chemical functionalization, necessary for sensing, impact the electronic [45] [46] and mechanical [47] properties. So an approximate understanding of these phenomena is crucial in the planning of sensitive and robust interface design, and error estimations must absolutely accompany simplifications.

From a continuum to a lumped model



Proper model selection is the key to accurate results. As the wavelength of the lowest vibrational modes ($\sim L \sim 1\mu\text{m}$) are long compared to the carbon-carbon interatomic spacing ($a_{cc} = 1.42\text{\AA}$), continuum models provide an accurate description of mode structures and dynamics. It has indeed been shown [48] that nonlinear continuum models yield good match with the more complicated molecular dynamics models. So the suspended CNT may be satisfactorily described by a hollow cylindrical Euler-Bernoulli beam model, valid for small displacements of high aspect ratio beams. Being a simplification of the Timoshenko beam theory, it covers the case of small deflections of a beam that is subjected to lateral loads only.

Euler,
Bernoulli
& von
Kármán

Additionally introduced von Kármán strains account for the geometric nonlinearity at large amplitude motion. The displacements remain too small for buckling to occur, and slack is not taken into account either. This undesirable NEMS imperfection can be eliminated by tube straining at the source electrode. The tube is considered to be a homogeneous hollow cylinder of length L , mean radius r (diameter $d = 2r$) and wall thickness τ , illustrated in Figure 2.4. The extended Euler-Bernoulli differential equation of motion writes

$$EI \frac{\partial^4 y}{\partial x^4} + \rho A \frac{\partial^2 y}{\partial t^2} + \rho A \frac{\omega_0}{Q} \frac{\partial y}{\partial t} - \left(T_0 + \frac{EA}{2L} \int_0^L \left(\frac{\partial y}{\partial x} \right)^2 dx \right) \frac{\partial^2 y}{\partial x^2} = F' \quad \left[\frac{\text{N}}{\text{m}} \right] \quad (2.2)$$

- The first term represents the potential energy due to internal forces, scaling with the tube's Young modulus $E \approx 1\text{TPa}$ [49] and areal moment of inertia $I = 2\pi r\tau (r^2 + \tau^2) \approx 2\pi r^3\tau \left[\frac{\text{N}}{\text{m}} \right]$. The wall thickness may be approximated by the carbon-carbon spacing $\tau \approx a_{cc} = 1.42\text{\AA}$ [50].
- The second term represents the kinetic energy, where $\rho \approx 2300 \left[\frac{\text{kg}}{\text{m}^3} \right]$ is the mass density of graphene and $A = 4\pi r\tau$ its cross sectional tube area.
- The third term represents the damping losses, scaling with the mode eigenfrequency $\omega_0 \in [10^6, 10^9]$ Hz and inversely to a phenomenological mechanical quality factor $Q \in [10^2, 10^5]$.
- The fourth term represents the stress-strain energy due to mid-plane stretching, which may be caused by an externally applied tensional force T_0 [N] or oscillation-induced von Kármán stress.
- Gravity is not taken into account and can safely be neglected at the NEMS scale.
- The external lineic driving force F' is uniformly applied all along the beam length.

The partial differential equation (2.2) has to be solved for $y(x, t)$ under the boundary conditions of the mechanical clamping, as illustrated by Figure 2.5a, with zero displacement and zero angle at the clamps. This imposes a bending beam shape to the tube under application of a uniformly distributed force. Once nonlinearity sets in, the tube becomes however stress dominated and behaves as a tensioned string. Modified boundary conditions are then zero deflection and zero curvature at the clamps.

$$\begin{array}{l|l} y(0, t) = y(L, t) = 0 & y(0, t) = y(L, t) = 0 \\ \frac{\partial y(0, t)}{\partial x} = \frac{\partial y(L, t)}{\partial x} = 0 & \frac{\partial y^2(0, t)}{\partial x^2} = \frac{\partial^2 y(L, t)}{\partial x^2} = 0 \end{array} \quad (2.3)$$

Both cases are analysed subsequently, and the lefthand side of the equations refers to the bending mode (Figure 2.5a), while the righthand side refers to the tensioned mode of Figure 2.5b. It will occur that the exact clamping conditions and mode shape, have no drastic implications on the oscillation amplitude and frequency orders of magnitude.

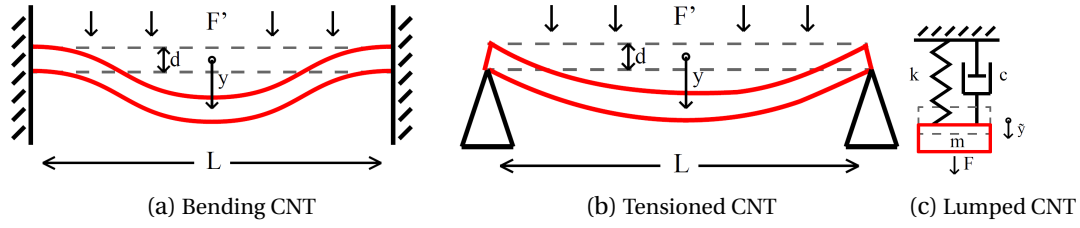


Figure 2.5: Anchored CNT shapes: Bending dominated bending CNTs and stress dominated tensioned CNTs may be modelled by lumped elements

Since this problem has no analytical solution, a variational method is adopted, which expresses the tube motion $y(x, t)$ as the product of a quasi-static shape function $\psi(x)$, weighted by a time-dependent coefficient $u(t)$. The shape being unknown, it may be expressed as a weighted sum of basis functions $\psi_i(x)$. So the Galerkin procedure is used to discretize equation (2.2) and transform it into a system of equations, spanning a reduced order model (ROM). The solution is expressed as the weighted $u_i(t)$ sum of orthogonal basis functions $\psi_i(x)$

Variational method & Galerkin procedure

$$y(x, t) = \sum_{i=1}^n u_i(t) \cdot \psi_i(x) \quad [\text{m}] \quad (2.4)$$

each respecting the boundary conditions of equation (2.3). The closer the basis functions $\psi_i(x)$ approximate the real tube shape, and the higher the order n of the model, the more accurate the predictions will be. A general property of variational solutions is: The more precise the shape function, the larger are the deflections y , the smaller is the stiffness k and the lower turns the resonance frequency ω_0 [51]. An arbitrary guess of the shape function will generally overestimate the resonance frequency and underestimate the deflection.

Keeping the existence of these estimation errors in mind, the problem is further simplified by approximating the shape function by a first order ROM ($n = 1$) $y(x, t) = \psi(x) \cdot u(t)$. The proposed shape functions, verifying the boundary conditions of equation (2.3), are

Lumped Duffing model

$$\psi(x) = \sqrt{\frac{2}{3}} \cdot [1 - \cos(\frac{2\pi}{L}x)] \quad | \quad \sqrt{2} \cdot \sin(\frac{\pi}{L}x) \quad (2.5)$$

Both functions have been chosen such that the root mean square displacement, averaged over the length of the CNT, equals $\psi(\tilde{x}) \equiv \tilde{\psi} = \sqrt{\langle \psi^2 \rangle} = 1$. In both cases the deflection is maximal at the middle of the CNT $\hat{x} = \frac{L}{2}$ and equals $\hat{\psi} = \sqrt{\frac{8}{3}}$ and $\hat{\psi} = \sqrt{2}$ for the bending and tensioned models respectively. Now that the mode shape is frozen, the tube motion may be expressed by a single point on the tube. Given that the system's energy scales with the square of displacement and velocity, the natural choice is to make $\tilde{y} = \tilde{\psi} \cdot u(t) = \psi(\tilde{x}) \cdot u(t)$ this reference point. The spatial derivatives of the shape function, necessary to solve the

dynamic beam equation, are

$$\begin{array}{l}
 \psi(\tilde{x}) = \quad \quad \quad 1 \quad \quad \quad \left| \quad \quad \quad 1 \\
 \frac{\partial^2 \psi}{\partial x^2}(\tilde{x}) = \quad -2\left(\frac{\pi}{L}\right)^2 \quad \left| \quad -\left(\frac{\pi}{L}\right)^2 \\
 \frac{\partial^4 \psi}{\partial x^4}(\tilde{x}) = \quad \quad \quad 8\left(\frac{\pi}{L}\right)^4 \quad \left| \quad \left(\frac{\pi}{L}\right)^4 \\
 \int_0^L \left(\frac{\partial \psi}{\partial x}\right)^2 dx = \quad \quad \quad \frac{4\pi^2}{3L} \quad \left| \quad \frac{\pi^2}{L}
 \end{array} \quad (2.6)$$

Substituting the spatial parts of equation (2.6) into the Euler-Bernoulli equation (2.2), yields the lineic lumped ordinary Duffing-type differential equation of motion

$$m' \cdot \frac{\partial^2 y(\tilde{x}, t)}{\partial t^2} + c' \cdot \frac{\partial y(\tilde{x}, t)}{\partial t} + k' \cdot y(\tilde{x}, t) + k'_3 \cdot y^3(\tilde{x}, t) = F' \quad \left[\frac{\text{N}}{\text{m}} \right] \quad (2.7)$$

where the parameters are given by

$$\begin{array}{l}
 m' = \quad \quad \quad \rho A \quad \quad \quad \left| \quad \quad \quad \rho A \\
 c' = \quad \quad \quad \rho A \frac{\omega_0}{Q} \quad \quad \quad \left| \quad \quad \quad \rho A \frac{\omega_0}{Q} \\
 k' = \quad \left(\frac{\pi^2}{L^2}\right)^2 8EI \left(1 + \frac{T_0 L^2}{4\pi^2 EI}\right) \quad \left| \quad \left(\frac{\pi^2}{L^2}\right)^2 EI \left(1 + \frac{T_0 L^2}{\pi^2 EI}\right) \\
 k'_3 = \quad \left(\frac{\pi^2}{L^2}\right)^2 8EI \frac{A}{6I} \quad \quad \quad \left| \quad \left(\frac{\pi^2}{L^2}\right)^2 EI \frac{A}{2I}
 \end{array} \quad (2.8)$$

Clamping invariance Comparing the parameter mappings of equation (2.8) for the bending and tensioned beam respectively, and remembering the shape functions of equation (2.5), makes it clear that an order of magnitude estimation of the NEMS dynamics can be obtained without precise knowledge on the exact clamping conditions. The subsequent twofold expressions of the eigenfrequency and dynamic range serve as an illustration of this claim. Focus is henceforth set on the bending beam hypothesis, keeping in mind that the results would be little off, if the resonating SWNT happened to be clamped as a tensioned beam.

Eigenfrequency For small displacements ($k'_3 \cdot y^3(\tilde{x}, t) \ll k' \cdot y(\tilde{x}, t)$), the Duffing equation (2.7) reduces to the driven harmonic oscillator equation (2.1) and the low-amplitude eigenfrequency expresses as

$$\omega_0 = \sqrt{\frac{k'}{m'}} = \left(\frac{\pi^2}{L^2}\right) \sqrt{\frac{8EI}{\rho A} \left(1 + \frac{T_0 L^2}{4\pi^2 EI}\right)} \quad \left| \quad \left(\frac{\pi^2}{L^2}\right) \sqrt{\frac{EI}{\rho A} \left(1 + \frac{T_0 L^2}{\pi^2 EI}\right)} \quad (2.9)$$

2.2. Setting the NEMS to Motion

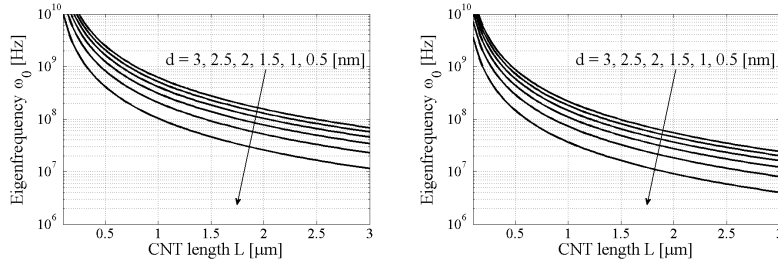


Figure 2.6: Small-amplitude CNT eigenfrequency as a function of tube length L and diameter d for bending dominated (left) and tension dominated (right) tubes.

From equation (2.9) it becomes clear that an order of magnitude estimation of the eigenfrequency can be obtained without precise knowledge on the exact clamping conditions, as both expressions diverge by less than a factor 3. Given its variational method nature, expression (2.9) slightly overestimates the real eigenfrequency in any case. This small-amplitude eigenfrequency is plotted in Figure 2.6 for suspended tubes without prestrain ($T_0 = 0$). The eigenfrequencies are much more sensitive to the tube length than they are to the diameter. This is good news, as the suspension length can be controlled by lithography, while the tube diameter depends on the catalytic particle size. It is observed that the eigenfrequencies for common lengths and diameters range from megahertz (MHz) to low gigahertz (GHz). This information is crucial for the upcoming electronic interface design. The other important information is the signal strength, which scales with oscillation amplitude, and is analysed subsequently.

The constrained harmonic oscillator model



Under the condition that the oscillation amplitude is small enough for the nonlinear cubic term of equation (2.7) to be negligible $k_3' y^3(\tilde{x}, t) \ll k' y(\tilde{x}, t)$

Linear regime limit

$$y(\tilde{x}, t) \ll y_{\text{cubic-limit}}(\tilde{x}, t) = r \sqrt{3 \left(1 + \frac{T_0 L^2}{4\pi^2 EI} \right)} \left| r \sqrt{1 + \frac{T_0 L^2}{\pi^2 EI}} \right. \quad (2.10)$$

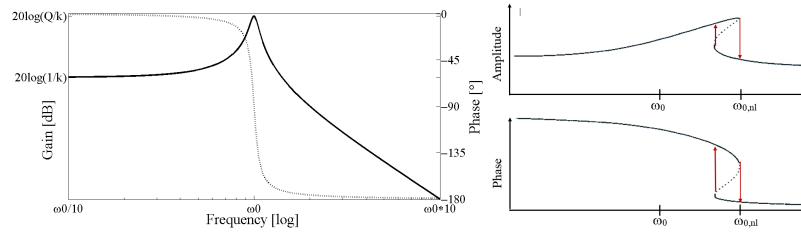
the Duffing type equation turns into the one of a driven damped harmonic oscillator. This limit, solely dependent on the tube diameter if no prestrain is applied, is rather stringent, as it is on the order to the radius r . So nonlinearity roughly sets in at root mean square (RMS) oscillation amplitudes exceeding 1nm. Below this limit, the nonlinear term may be neglected and equation (2.7) can be reduced to the forced harmonic oscillator of equation (2.1).

An analytical solution exists in this case for a sinusoidal driving force $F' = F_0' \sin(\omega_0 t)$, and writes

Analytical solution

$$y(\tilde{x}, t) = \frac{F_0'}{m'} \frac{1}{\sqrt{\frac{\omega^2 \omega_0^2}{Q^2} + (\omega^2 - \omega_0^2)^2}} \sin(\omega_0 t + \varphi) \quad [\text{m}] \quad (2.11)$$

Figure 2.7: [Left] Displacement-by-force $\frac{y(\bar{x},t)}{F_0}$ gain in the small-displacement limit imposed by equation (2.10) [Right] Onset of nonlinearity causes hysteretic amplitude and phase jumps



$$\text{with } \varphi = \arctan\left(\frac{\omega\omega_0}{Q(\omega^2 - \omega_0^2)}\right)$$

The low frequency gain is $\left|\frac{y(\bar{x},t)}{F_0}\right|_{DC} = \frac{1}{k'}$, in accord with Hook's law. At the eigenfrequency the gain reaches $\left|\frac{y(\bar{x},t)}{F_0}\right|_{\omega_0} = \frac{Q}{k'}$ and decays at $-40 \frac{dB}{dec}$ at high frequencies. Two special frequencies are $\omega_p = \omega_0\sqrt{1 - \frac{1}{2Q^2}}$ and $\omega_i\sqrt{\sqrt{4 - \frac{1}{Q^2}} - 1}$, where the gain peaks and the phase inflects respectively. Both frequencies can be considered equal to ω_0 for sufficiently large quality factors Q .

The Bode plots of the transfer function are given in Figure 2.7. The amplitude peak with quality factor Q and the 180° phase inflection are attractive and easy to track properties of CNT resonators, which may lead to oscillator applications.

Cubic non-linearity & hysteresis

If the oscillation amplitude turns large enough to exceed the linear limit $y_{cubic-limit}$, then the cubic term of equation (2.7) considerably changes the NEMS's dynamics. Mathematically speaking, the system converges towards chaotic behaviour, and loses all its interest from an engineering point of view. The CNT motion spectrum under large driving forces is shown in Figure 2.8a. First, it is observed that the response contains higher harmonics at odd multiples of the driving frequency. The 1ω linear response component henceforth peaks at a frequency $\omega_{0,nl}$ above ω_0 , as can be seen from Figure 2.8b. The peak is followed by an abrupt jump, which is accompanied by a jump in the phase response as well, as Figure 2.8c reveals. The right part of Figure 2.7 gives the complete picture, including the unstable solutions to the Duffing equation. Increasing and decreasing frequency sweeps will quit the two stable curves at different points, and the sweep shows hysteretic behaviour. While this is acceptable for frequency sweeping characterization, parameter extraction, such as ω_0 and Q , becomes extremely difficult or impracticable [52]. Closed-loop operation, on the other hand, tries to stabilize the drive frequency around a desired point of operation, which generally is the eigenfrequency-peak. The quality of such a stabilization process would considerably suffer under the presence of hysteresis, and result in considerable steady-state oscillation around the equilibrium point.

Benefits of the 3rd harmonic

Among the higher order components, the 3ω component is most prominent. Driving the NEMS at a third its nonlinear peak frequency, reestablishes a lorentzian shaped and hysteresis-free response around $\omega_{0,nl}$, as can be seen from Figure 2.8b and 2.8c. This holds only until the driving force also causes this peak to distort, bringing the system even closer to chaos.

2.2. Setting the NEMS to Motion

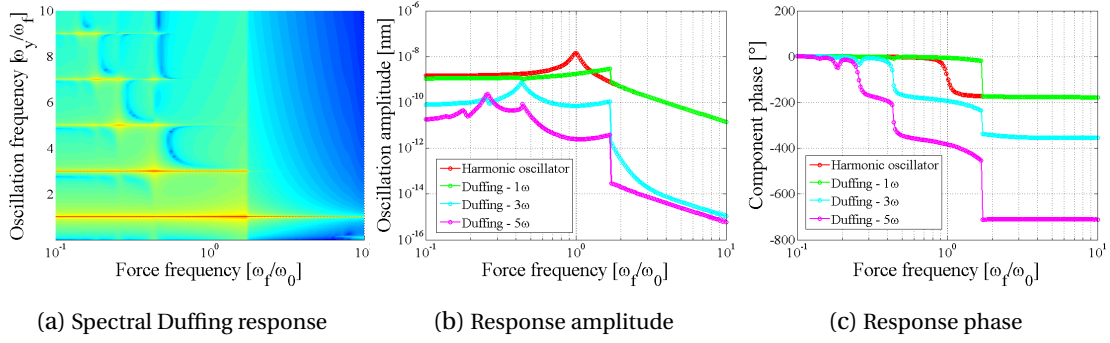


Figure 2.8: The Duffing response presents a rich harmonic content. The fundamental component does not peak around ω_0 anymore and presents hysteresis. The three-fold component remains hysteresis-free for relatively small amplitudes.

But driving forces, which cause already hysteresis, if applied at frequency $\omega_{0,nl}$, do not cause any such nonlinearity yet if applied at $\frac{\omega_{0,nl}}{3}$. Arises then the natural question in how far this phenomenon may be exploited for applications. The first observation on the way to an answer is that $\omega_{0,nl}$ depends on the force amplitude, and so would thus $\frac{\omega_{0,nl}}{3}$. If steady amplitude can be guaranteed, then the third harmonic Duffing oscillator has indeed the potential to be used as a voltage controlled oscillator (VCO) for instance, especially as frequency tuning is as easy as increasing the driving force. On the other side of the coin, such a resonator would be very sensitive to amplitude noise. Given that the motion of the tube occurs at a threefold superharmonic frequency with respect to the actuation, bandpass filtering would allow to isolate the motional component. If there was no other finesse in our bag of tricks, this approach would merit further investigations. Given the relatively lower superharmonic transduction gain, feeble signal strength might become an obstacle though, and quantitative sensing seems difficult, given the strong correlation between the oscillation amplitude and frequency.

Desiring to restrain a quasi-chaotic system is ambitious, even more when the exploitable linear oscillation amplitude is weak and on the order of the tube diameter. This upper bound is to be compared with the thermomechanical noise limit. By the fluctuation-dissipation theorem and regardless of the origin of the dissipation mechanism, the motion of the NEMS ultimately thermalizes into heat. Given that quantum fluctuations are negligible at ambient temperature and radiofrequencies ($k_B T \gg \hbar \omega_0$), the classical equipartition law predicts an average energy of $k_B T$ per mode, with T being the physical temperature of the NEMS and $k_B = 1.38 \cdot 10^{-23} [\frac{J}{K}]$ the Boltzmann constant. This established thermomechanical noise energy [53] may infer an upper bound on the thermal fluctuations \tilde{y}_{noise}

Thermo-
mechanical
noise limit

$$\sqrt{\langle y_{\text{noise}}^2 \rangle} \leq \sqrt{\frac{k_B T}{k' \cdot L}} \quad [\text{m}] \quad (2.12)$$

This value is certainly an upper bound on the thermomechanically induced fluctuations, but it is nevertheless instructive to observe that it scales inversely to the lumped spring constant

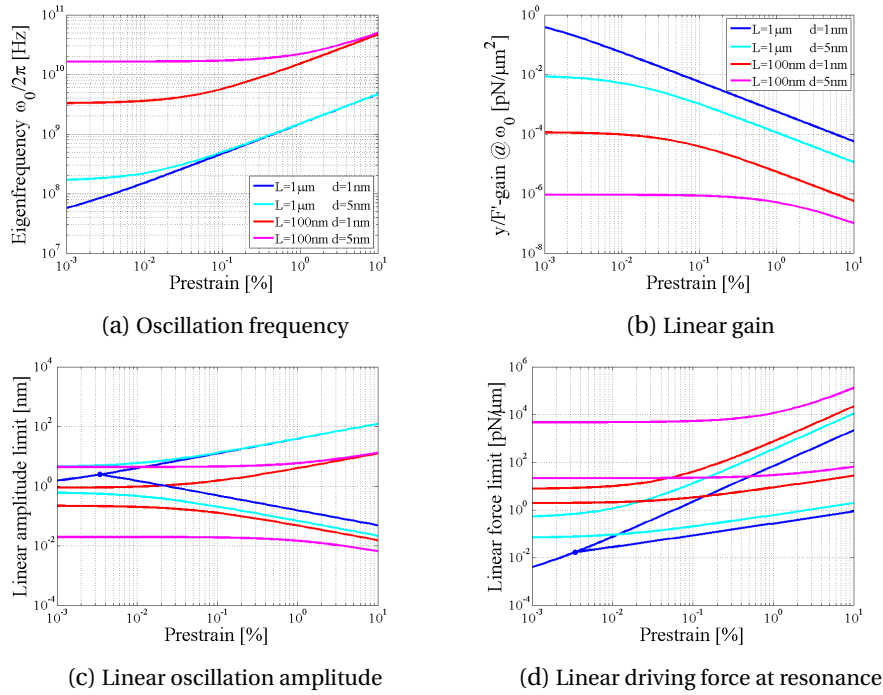


Figure 2.9: Tensile strain is found to increase the linear dynamic range of CNTs (c&d) at the cost of a lower transduction gain (b). The eigenfrequency can be tuned over decades without tube destruction (a).

$k' \cdot L$. Combining the insights from equations (2.10) and (2.12), it becomes clear that stiffer tubes present a larger linear dynamic range.

Tensile strain The source electrode is movable and allows to tension the suspended SWNT. SWNTs may support up to 5% tensile strain [54], more is tolerated by MWNTs. To induce strains from $10^{-3}\%$ to 1%, electrode displacements of pico- to nanometer and forces on order from pico- to micronewton are necessary. This lies well within the range of piezoelectric MEMS, but other systems may be appropriate as well [55]. The effects of tensile strain are manifold. First of all do they allow to tune the NEMS eigenfrequency, as suggested by equation (2.9) and shown in Figure 2.9a for thin ($d = 1\text{nm}$), thick ($d = 5\text{nm}$), long ($L = 1\mu\text{m}$) and short ($L = 100\text{nm}$) tubes. The eigenfrequency of thin long tubes is sensible to very small strains already, while thick short tubes require rather large strains to be tuned. The tensile force that indwells the tube upon tuning, makes it harder for the lateral actuation force to cause displacement and reduces the transduction gain, as can be seen from Figure 2.9b. Physically the tensile force renders the tube stiffer. This increased stiffness translates into an increase of the linear dynamic range, which is bounded to the top by the onset of the cubic nonlinearity (equation (2.10)) and to the bottom by the thermodynamic noise (equation (2.12)). Both limits are presented in Figure 2.9c for the amplitude and 2.9d for the force.

Quality factor Although quality factors in the broad range from 10 [2] to almost 10^5 [56] (at 100mK) have been observed, most room temperature experiments report quality factors around 100 [1] [2]

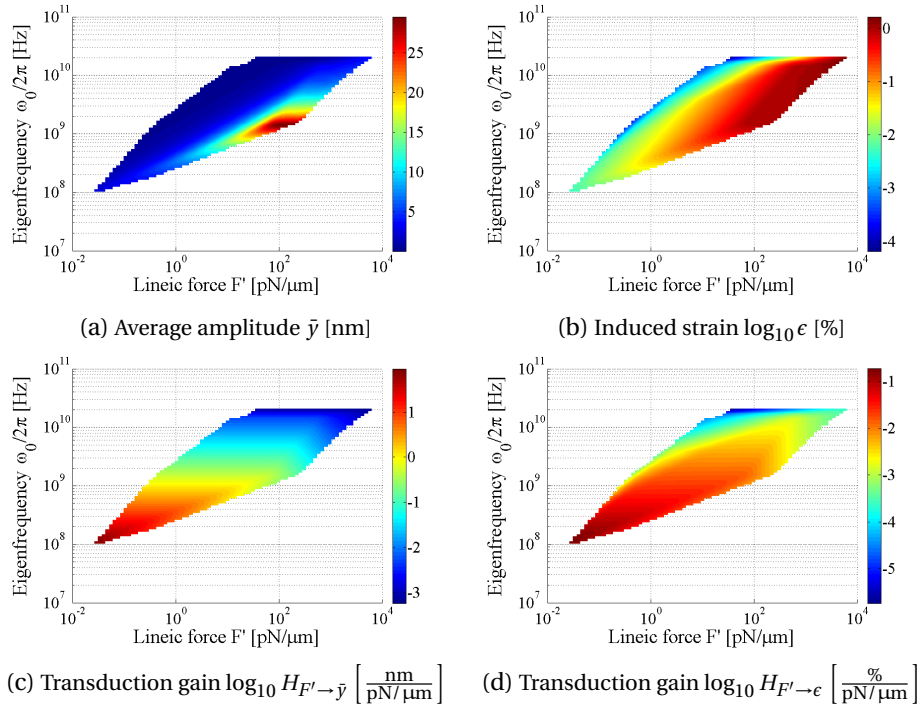


Figure 2.10: The maximum obtainable average deflection (a), strain (b) and transduction gains (c&d) at resonance over the length, diameter and prestrain space, as a function of actuation force and eigenfrequency. The maxima of each graph correspond to one and the same design point of Figure 2.11. (hyp. $Q = 100$)

[32]. This fact supports the decision that the following paragraphs suppose $Q = 100$ in order to provide conceptional estimates on orders of magnitudes. Generalization to arbitrary Q is then performed in the next subsection.

The question that ultimately interests system designers is how much oscillation amplitude one can expect for a given actuation force, and at which frequency. Relevant displacement quantities are the tube's (spatial-) average displacement, Important quantities

$$\bar{y}(x, t) = y(\bar{x}, t) = \sqrt{\frac{2}{3}} \cdot y(\bar{x}, t) \quad [\text{m}] \quad (2.13)$$

found by integrating equation (2.5) along the tube length, and the oscillation-induced strain

$$\begin{aligned} \epsilon(t) &= \frac{1}{L} \left(\int_0^L \sqrt{1 + \partial_x (\psi(x) \cdot y(\bar{x}, t))^2} dx - 1 \right) \\ &\approx \frac{2}{3} \pi^2 \left(\frac{y(\bar{x}, t)}{L} \right)^2 \end{aligned} \quad (2.14)$$

that is found by a Taylor expansion of the elliptic integral of the second kind to evaluate the arc length.

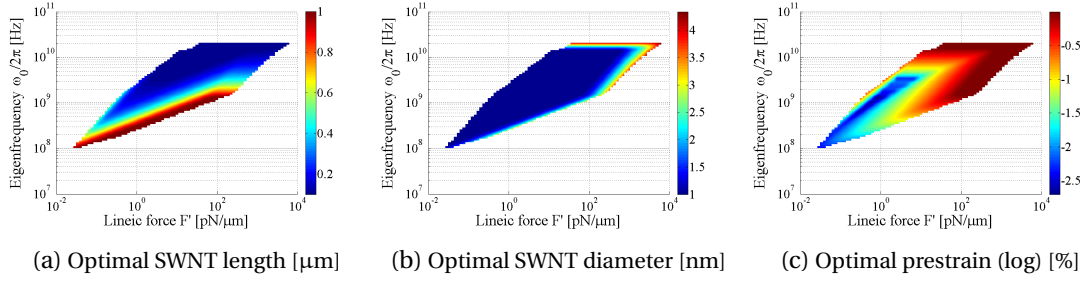


Figure 2.11: Maximum linear-regime oscillation-induced strain and amplitude are obtained for the following NEMS parameters within the $L \times d \times s_0 \equiv [100\text{nm}..1\mu\text{m}] \times [1\text{nm}..5\text{nm}] \times [0\%..1\%]$ design space.

Ultimate bounds For optimal signal detectability, these two quantities, \bar{y} and ϵ , are to be maximized over the available tubes with lengths from 100nm to 1 μm , diameters from 1 to 5nm and prestrains up to 1%, and this within the linear regime limits imposed by equations (2.10) and (2.12). Solving this nonlinear constrained optimisation problem leads to the valuable Figure 2.10, showing the optimisation problem's solution. Figure 2.11 unveils the optimal parameter set, and the following qualitative insights follow:

On the force and frequency ranges

- Linear oscillation above the thermomechanical noise level can be achieved only above 100MHz and starting from lineic forces of $0.1 \frac{\text{pN}}{\mu\text{m}}$. The frequency and noise floor might be slightly overestimated, as has been announced previously. So it happens that [32] found a 50MHz resonance frequency for their device. Lower observed resonances [1] have been attributed to slack in the tube.
- Thick and short tubes can present eigenfrequencies up to 20GHz and forces must not exceed $10 \frac{\text{nN}}{\mu\text{m}}$ for the NEMS to stay in the linear regime.

On the parameter set

- Both quantities, the average displacement \bar{y} and the induced strain ϵ are maximal for one and the same parameter set. From equation (2.13), Hook's law and equation (2.8), $\bar{y} \sim \mathcal{O}(L^4 \cdot r^3 |L^2 \cdot 1)$ is observed to scale with positive powers of the tube length and radius in the bending and tensioned regimes. Combining equations (2.13) and (2.14) shows that the dependence stays positive also for $\epsilon \sim \left(\frac{\bar{y}}{L}\right)^2 \sim \mathcal{O}(L^6 \cdot r^6 |L^2 \cdot 1)$. So this result was previsible.
- Maximum \bar{y} and ϵ along the minimum frequency edge, are obtained by long and rather thin tubes, prestrained as required by the frequency. Only when the 1% tensile tuning range of these tubes has served out, progressively shorter and thicker tubes serve as back-up plan for maximum amplitude under maximum prestrain.

- Maximum \bar{y} and ϵ along the minimum force edge, are obtained for the thinnest tubes and under minimal prestrain. The tube length decreases as required by the frequency. Only when the minimum length has been reached, tubes need to be prestrained to reach even higher frequencies, but stay shallow up to the ultimate prestrain limits, above which thick tubes remain the only choice.

On the optimal \bar{y} and ϵ

- The maximum average displacement \bar{y} ranges from 1nm to 30nm, depending on the force and frequency (Figure 2.10a). The transduction efficiency $H_{F' \rightarrow \bar{y}}$ may be considered independent of the force, but decays rapidly with frequency (Figure 2.10c). This rapid decay will set an upper bound on the frequency range observable through capacitive and field effect readout.
- The maximum oscillation-induced strain ϵ spans over several decades and is maximal for the highest tolerable driving forces. The maximum transduction efficiency $H_{F' \rightarrow \epsilon}$ on the other hand, is obtained at the low-frequency low-force corner, just as for $H_{F' \rightarrow \bar{y}}$.

It is worth to anticipate the fact that the electrostatic force, assessed in section 2.2.2, will not exceed tens of $\frac{\text{pN}}{\mu\text{m}}$. Furthermore can MHz circuit design be easily based on lumped component models, whereas GHz design must take into account the wave nature of currents. It is a fact that electronic interface design approaches will considerably change throughout the force-frequency space represented in Figure 2.10 and 2.11. So a choice had to be made here, and the decision was to focus on sub-GHz frequency ranges. The choice is motivated by the following facts:

Design space

- The maximum transduction efficiency appears at low frequencies (see Figure 2.10c and 2.10d).
- The best signal strength in this subspace still approaches the global maximum asymptotically (see Figure 2.10a and 2.10b).
- Circuit design and characterization below GHz are considerably more convenient, flexible and robust than beyond GHz. Remembering that one of the targets of the present work is to integrate CNT-NEMS into large bandwidth closed-loop systems, lower frequencies are beneficial for noise rejection and definitely the way to go. Bringing CNT-NEMS to higher frequencies is an all different challenge and not our primary concern here.

The optimal average displacement and induced strain values, as well as the gains, have a very convenient structure below the GHz barrier, that is visualized by Figure 2.12. Here presented are horizontal slices through the graphs of Figure 2.10, spaced by 100MHz. The best achievable average amplitude \bar{y} (Figure 2.12a) and strain ϵ (Figure 2.12b) saturate above a critical force

Sub-GHz optimisation

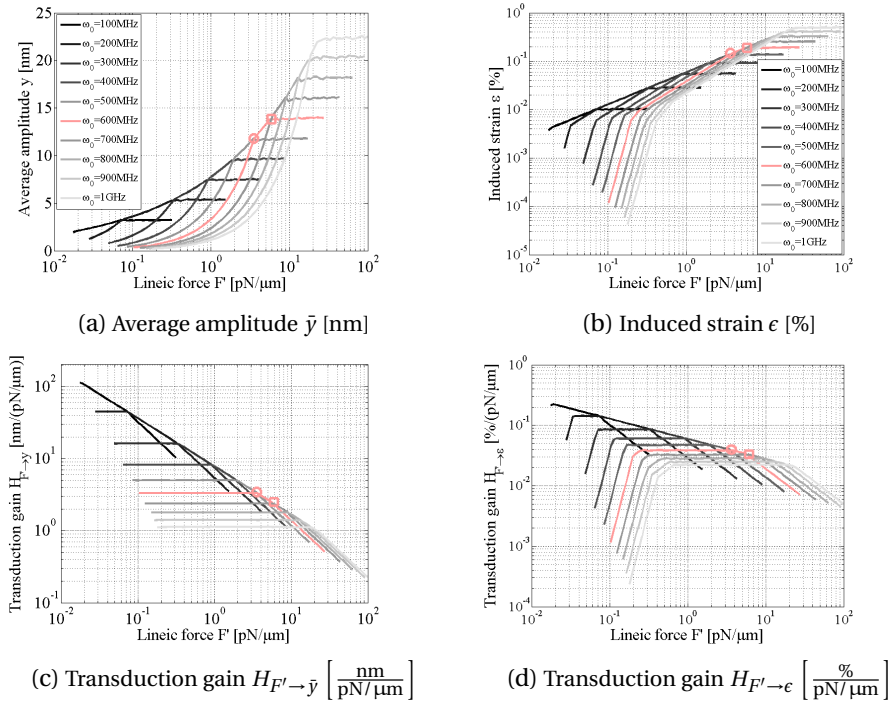


Figure 2.12: The maximum obtainable average deflection (a), strain (b) and transduction gains (c&d) at resonance, optimized over the length, diameter and prestrain space, as a function of actuation force and eigenfrequency. Every entry to each of the 4 graphs corresponds to one and the same optimal design point, given by Figure 2.11. (hyp. $Q = 100$)

value F'_{\square} , while the transduction gains $H_{F' \rightarrow \bar{y}}$ (Figure 2.12c) and $H_{F' \rightarrow \epsilon}$ (Figure 2.12d) are constant below the critical force value F'_c . This means that F'_{\square} offers the best gain at maximal signal strength, while F'_c offers the best signal strength at maximal gain. Any force $F' \in [F'_c, F'_{\square}]$ is pareto-optimal in the gain versus strength trade-off, while any force outside this interval would be a miss. From Figure 2.12 it appears that strength and gain at F'_c and F'_{\square} lie rather close together, and even converge towards the GHz limit. Hence choosing one or the other will not change performance significantly. Here preference is given to F'_c , which maximizes the transduction gain. The minor sub-optimality in terms of signal strength (less than a factor three) sees itself compensated by an enhanced linearity. The critical force range $[F'_{\text{lim}^-}, F'_{\text{lim}^+}]$ is then defined as the interval where the gain is maximum and independent of the force. Its dependence on frequency is to be detected next, while the dependence on the geometrical tube parameters and prestrain is complex and has been identified as the optimal parameter set shown in Figure 2.11. It will henceforth form the numerical part of the gain transfer function.

The mechanical transfer function



Transfer function @ ω_0 & $Q = 100$ From the previous insights follows that the optimal gain transfer function at resonance can be uniquely represented by the maximum gain and the critical force limits. These two are plotted against the eigenfrequency in Figure 2.13 and 2.14 in logarithmic scales. The points are found

2.2. Setting the NEMS to Motion

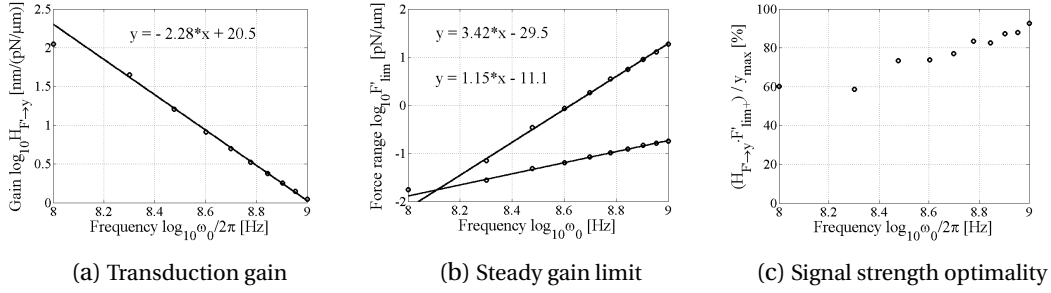


Figure 2.13: Force to average displacement transfer gain and constraints, optimized over the available NEMS parameter space (length, diameter and prestrain). The linear regression norms of residuals are respectively $\|r_{\text{gain}}\| = 0.0495$, $\|r_{F'_+}\| = 0.0692$ and $\|r_{F'_-}\| = 0.0367$ (hyp. $Q = 100$, $\omega = \omega_0$)

to nicely align on a linear regression straight line, and the interpolation equation is provided as an inset. This means that an optimal choice of L , d and T_0 (see Figure 2.11) leads to the following gain transfer functions

$$|H_{F' \rightarrow \bar{y}}|_{Q=100, \omega=\omega_0} \equiv \left| \frac{\bar{y}}{F'} \right| = 10^{20.5} \cdot \left(\frac{\omega_0}{2\pi} \right)^{-2.28} \quad \left[\frac{\text{nm}}{\text{pN}/\mu\text{m}} \right] \quad (2.15)$$

$$|H_{F' \rightarrow \epsilon}|_{Q=100, \omega=\omega_0} \equiv \left| \frac{\epsilon}{F'} \right| = 10^{8.59} \cdot \left(\frac{\omega_0}{2\pi} \right)^{-1.14} \quad \left[\frac{\%}{\text{pN}/\mu\text{m}} \right] \quad (2.16)$$

which validity in the respective force ranges

$$10^{-11.1} \cdot \left(\frac{\omega_0}{2\pi} \right)^{1.15} \leq |F'_{H_{F' \rightarrow \bar{y}}}|_{Q=100, \omega=\omega_0} \leq 10^{-29.5} \cdot \left(\frac{\omega_0}{2\pi} \right)^{3.42} \quad \left[\frac{\text{pN}}{\mu\text{m}} \right] \quad (2.17)$$

$$10^{-17.0} \cdot \left(\frac{\omega_0}{2\pi} \right)^{1.87} \leq |F'_{H_{F' \rightarrow \epsilon}}|_{Q=100, \omega=\omega_0} \leq 10^{-29.4} \cdot \left(\frac{\omega_0}{2\pi} \right)^{3.42} \quad \left[\frac{\text{pN}}{\mu\text{m}} \right] \quad (2.18)$$

The upper force bounds are identical for strain and displacement. The apparent numerical difference comes from finite resolution simulations and is amplified by rounding. Figure 2.13c and 2.14c illustrate that the signal strength obtained for forces at the upper limit of the maximum gain intervals reach at least a third of the best possible value, which could be obtained by F'_{\square} .

So far the quality factor had been pinned to the commonly observed value 100. Generalization to arbitrary Q is admittedly straightforward by noticing that at resonance Hook's law writes $F' = \frac{k'}{Q} \bar{y}$. So the horizontal axes of Figure 2.10, 2.11 and 2.12 can be reinterpreted as $F' \mapsto \frac{F'}{Q}$ and the gain and boundary equations have to be rescaled as

$$|H_{F' \rightarrow \bar{y}}|_{\omega=\omega_0} \equiv \left| \frac{\bar{y}}{F'} \right| = Q \cdot 10^{18.5} \cdot \left(\frac{\omega_0}{2\pi} \right)^{-2.28} \quad \left[\frac{\text{nm}}{\text{pN}/\mu\text{m}} \right] \quad (2.19)$$

Generalization to arbitrary Q

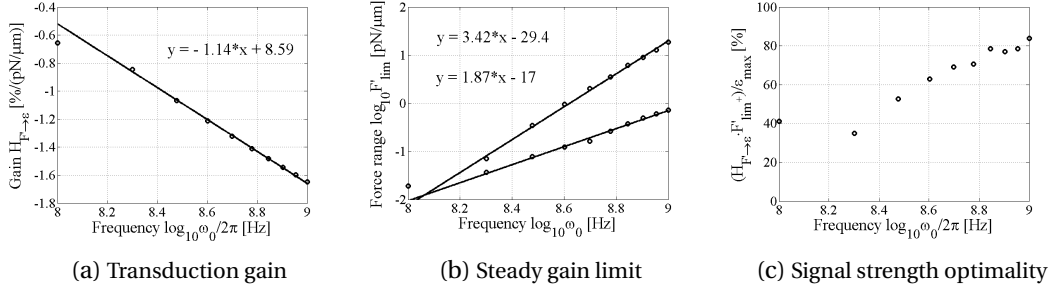


Figure 2.14: Force to strain transfer gain and constraints, optimized over the available NEMS parameter space (length, diameter and prestrain). The linear regression norms of residuals are respectively $\|r_{\text{gain}}\| = 0.0245$, $\|r_{F'_+}\| = 0.0971$ and $\|r_{F'_-}\| = 0.0914$ (hyp. $Q = 100$, $\omega = \omega_0$)

$$|H_{F' \rightarrow \epsilon}|_{\omega=\omega_0} \equiv \left| \frac{\epsilon}{F'} \right| = Q \cdot 10^{6.59} \cdot \left(\frac{\omega_0}{2\pi} \right)^{-1.14} \quad \left[\frac{\%}{\text{pN}/\mu\text{m}} \right] \quad (2.20)$$

with validity in the respective force ranges

$$Q^{-1} \cdot 10^{-9.1} \cdot \left(\frac{\omega_0}{2\pi} \right)^{1.15} \leq |F'_{H_{F' \rightarrow \bar{y}}}|_{\omega=\omega_0} \leq Q^{-1} \cdot 10^{-27.5} \cdot \left(\frac{\omega_0}{2\pi} \right)^{3.42} \quad \left[\frac{\text{pN}}{\mu\text{m}} \right] \quad (2.21)$$

$$Q^{-1} \cdot 10^{-15.0} \cdot \left(\frac{\omega_0}{2\pi} \right)^{1.87} \leq |F'_{H_{F' \rightarrow \epsilon}}|_{\omega=\omega_0} \leq Q^{-1} \cdot 10^{-27.5} \cdot \left(\frac{\omega_0}{2\pi} \right)^{3.42} \quad \left[\frac{\text{pN}}{\mu\text{m}} \right] \quad (2.22)$$

Generalization to arbitrary ω Previous sections showed that SWNTs shall be operated within their linear regime limits for closed loop applications to become conceivable. Within these limits they behave as driven damped harmonic oscillators (equation (2.1)), which show a lorentzian harmonic response (equation (2.11)). So the foregoing equations can be generalized to off-resonance frequencies as well

$$\begin{aligned}
 H_{F' \rightarrow \bar{y}}(j\omega) : |F'| \cdot e^{j(\omega t + \varphi)} &\mapsto |\bar{y}| \cdot e^{j(\omega \bar{y} t + \varphi_{\bar{y}})} && \left[\frac{\text{pN}}{\mu\text{m}} \rightarrow \text{nm} \right] \\
 |F'| &\rightarrow |F'| \cdot \frac{10^{18.5} \cdot \left(\frac{\omega_0}{2\pi} \right)^{-2.28}}{\sqrt{Q^2 \omega^2 + \left(\frac{\omega^2}{\omega_0^2} - 1 \right)^2}} \\
 \omega &\rightarrow \omega \\
 \varphi &\rightarrow \varphi + \arctan \left(\frac{\omega \omega_0}{Q(\omega^2 - \omega_0^2)} \right)
 \end{aligned} \quad (2.23)$$

$$\begin{aligned}
 H_{F' \rightarrow c}(j\omega) : |F'| \cdot e^{j(\omega t + \varphi)} &\longmapsto |\epsilon| \cdot e^{j(\omega_c t + \varphi_c)} && \left[\frac{\text{pN}}{\mu\text{m}} \rightarrow \% \right] \\
 |F'| &\rightarrow \frac{|F'|}{2} \cdot \frac{10^{6.59} \cdot \left(\frac{\omega_0}{2\pi}\right)^{-1.14}}{\sqrt{Q^2 \omega_0^2 + (\omega_0^2 - \omega^2)^2}} \\
 \omega &\rightarrow 2\omega \\
 \varphi &\rightarrow 2\varphi + 2 \arctan\left(\frac{\omega \omega_0}{Q(\omega^2 - \omega_0^2)}\right) - \frac{\pi}{2}
 \end{aligned} \tag{2.24}$$

The above transfer functions stand for the most efficient force to displacement and strain conversions that carbon nanotubes can provide in the linear regime limits. These limits are given by equations (2.21) and (2.22) and the optimal CNT parameters are shown by Figure 2.11. The frequency doubling in the strain response comes from the square in equation (2.14).

Now that the force to motion transfer functions $H_{F' \rightarrow \bar{y}}(j\omega)$ and $H_{F' \rightarrow c}(j\omega)$ have been established, the next step is to create the actuation force electrically by application of a gate voltage. The coming three sections will evaluate the relation between voltage and force $H_{\bar{v} \rightarrow F'}(j\omega)$. Section 2.2.5 will finally summarize the complete electromechanical actuation $H_{\bar{v} \rightarrow \bar{y}}(j\omega)$ and $H_{\bar{v} \rightarrow c}(j\omega)$. Coming soon

2.2.2 The electrostatic force – an upper bound

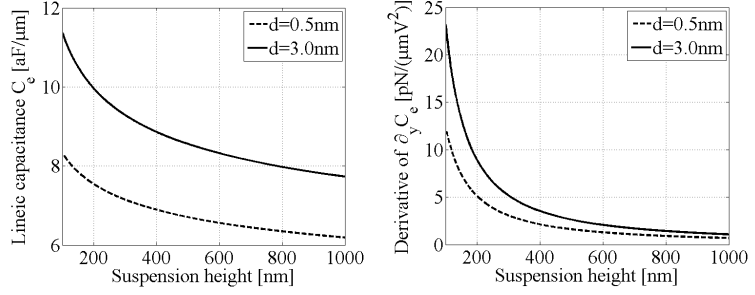
The roots of actuation lie in the two-port capacitor C_e , formed by the gate electrode and the CNT itself. As the energy stored in this capacitor can be modulated via the induced charge Q_{CNT} in the electrical domain and the gate to tube distance $h + y(x)$ in the mechanical domain, transdomain signal flow becomes possible. Given that electrical biasing naturally imposes potentials and consequently controls rather the gate-tube voltage than the charge, the reasoning shall be based on the system's co-energy. Without loss of generality, one may take the source terminal as electrical reference ($V_S = 0$). The system's co-energy density writes then as a function of the directly controllable gate potential V_G , the indirectly controllable tube potential ϕ_{CNT} and the local tube deflection $y(x)$ Virtual work

$$\mathcal{W}^*(V_{\text{GS}}, y(x)) = \frac{1}{2} \cdot C'_e(y(x)) \cdot (V_G - \phi_{\text{CNT}})^2 \tag{2.25} \quad \left[\frac{\text{J}}{\text{m}} \right]$$

where ϕ_{CNT} is the tube potential that is determined in the subsequent sections. This entails the expression of the force density along the tube

$$F'(V_{\text{GS}}, x) = - \frac{\partial \mathcal{W}^*(V_{\text{GS}}, y(x))}{\partial y(x)} \tag{2.26} \quad \left[\frac{\text{N}}{\text{m}} \right]$$

Figure 2.15: The lineic electrical gate to CNT capacitance and its derivative are relatively insensitive to the suspension height h and tube diameter d . Zero-order approximations would be $C'_e \approx 10 \text{ aF}/\mu\text{m}$ and $\partial_y C'_e \approx 6 \text{ pN}/(\mu\text{mV}^2)$.



Integrating equation (2.26) along the tube length $x \in [0..L]$, yields the total electrostatic force, which is non-negative and may consequently attract the tube, but never repel it.

Electric capacitance Neglecting the contribution of the density of states (DOS) in the CNT, (hyp. $\phi_{\text{CNT}} = V_S = 0$) and approximating the device as a long conductive equipotential cylinder above an infinite metallic plate, the electrical gate to tube capacitance is found by the method of image charges and writes

$$C'_e(x) = \frac{2\pi\epsilon}{\text{acosh}\left(\frac{h-y(x)}{r}\right)} \quad \left[\frac{\text{F}}{\text{m}}\right] \quad (2.27)$$

where $y(x)$ is the transversal tube motion as a function of the position along the tube, and ϵ the gap permittivity, which may be approximated by the vacuum permittivity $\epsilon_0 = 8.854 \cdot 10^{-12} \frac{\text{F}}{\text{m}}$. Differentiating C'_e with respect to the displacement $y(x)$, leads to

$$\begin{aligned} \partial_y C'_e(x) &= \frac{2\pi\epsilon}{\sqrt{h-y(x)}\sqrt{h-y(x)+2r} \cdot \text{acosh}^2\left(\frac{h+r-y(x)}{r}\right)} \quad \left[\frac{\text{N}}{\text{m} \cdot \text{V}^2}\right] \quad (2.28) \\ &\approx \frac{2\pi\epsilon}{h \cdot \text{acosh}^2\left(\frac{h}{r}\right)} \quad \left[\frac{\text{N}}{\text{m} \cdot \text{V}^2}\right] \end{aligned}$$

which sets an upper bound to the electrostatic force of equation (2.26) if multiplied by $\frac{V_{\text{GS}}^2}{2}$. For small oscillation amplitudes ($y(x) \ll h$) and to first order, the lineic capacitance scales inversely to the suspension height. Its derivative is relatively insensitive to the tube radius, given that $r \ll h$. Equation (2.27) and its derivative are plotted in Figure 2.15 and show that C_e is on the order of $10 \frac{\text{aF}}{\mu\text{m}}$ and a good order of magnitude of $\partial_y C_e$ would be $6 \frac{\text{pN}}{\mu\text{m} \cdot \text{V}^2}$.

Quantum capacitance Given the possibility that SWNTs may possess an energy gap and in consideration of their reduced charge density of states as one dimensional conductors, injection of charge carriers onto the tube may affect the latter's potential ($\phi_{\text{CNT}} \neq 0$). This results in a decrease of the tube to gate voltage $V_G - \phi_{\text{CNT}}$, that would multiply the electrical capacitance C'_e to define the charges that create the electrostatic actuation force. This phenomenon may be modelled by a lineic quantum capacitance C'_q that appears in series with C'_e , as illustrated by Figure 2.16.

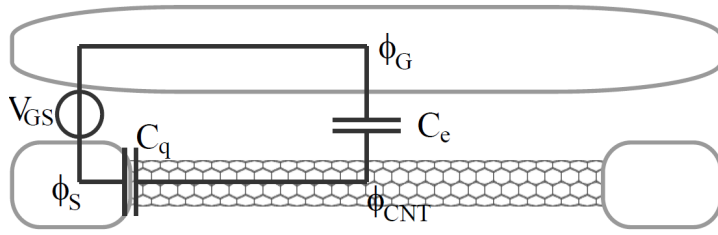


Figure 2.16: The electrical C'_e and quantum C'_q capacitance share the same through variable and appear in series. While a voltage on C'_e will exert an attractive electrostatic force onto the tube, this is not the case for C'_q

The resulting tube potential writes

$$\phi_{CNT} = \frac{1}{1 + \frac{C'_q}{C'_e}} V_G \quad [V] \quad (2.29)$$

The effective capacitance, that defines the electrostatic force as a function of the controllable gate to source voltage,

$$F'(V_{GS}, x) = \frac{1}{2} \cdot \partial_y \left(\frac{C'_e(y)}{\left(1 + \frac{C'_q(y)}{C'_q(V_{GS})}\right)^2} \right) \cdot V_{GS}^2 \quad \left[\frac{N}{m}\right] \quad (2.30)$$

depends indeed on the relative ratio between quantum and electrical capacitance. It becomes apparent that this effective capacitance corresponds to the electrical capacitance if C'_q is large, as it is the case for 3D metals. On the other hand does the electrostatic force of equation (2.30) decay to zero if the position-independent quantum capacitance approaches zero, as for insulators.

The expression of C'_q is established by linking the charges in the tube to its potential. This is done in the following section that contains a teaspoon of solid state physics. Care has been taken to illustrate the ingredients sufficiently to make them smoothly accessible to high-level circuit designers, who are rarely confronted to these fundamental physical phenomena. The section will also serve as a backbone for the upcoming evaluation of the field- and piezoresistive effects. A succinct summary, presenting the major findings, is provided at the subsection's end.

Three chilis ahead

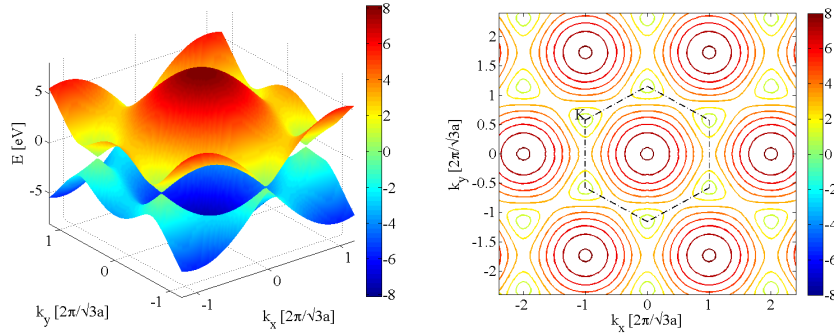
2.2.3 A quantum of solid states physics



Electrons, having half-integer spins, are fermions and must respect the Pauli exclusion principle. This quantum mechanical principle states that, in a system, no two fermions may occupy the same quantum state simultaneously. While the number of electrons defines the charge, the energy states they occupy define the tube's potential ϕ_{CNT} , which leads to the expression of the quantum capacitance C'_q . The following paragraphs first identify the density of available energy states per unit volume and energy level (DOS), and show then how these states are occupied according to the Fermi-Dirac distribution.

Pauli exclusion principle

Figure 2.17: The dispersion relation for graphene is a hexagonal lattice with energies from $-3\gamma_0 = -8.1\text{eV}$ to $+3\gamma_0 = 8.1\text{eV}$. The bandgap is closed at the six K-points which define the Brillouine zone corners.



Dispersion relation of graphene

Given the CNTs' cognation to graphene, they inherit part of the electronic properties of this semi-metal. As has been mentioned previously do the electronic properties of graphene predominantly depend on the delocalized π -states that occupy a wide range of energies around the Fermi energy E_F . The tight binding approximation [57] takes into account only the overlap of direct neighbouring atoms' electronic clouds and still leads to an accurate estimate of the dispersion relation. The eigenstates (Bloch waves) of the Hamiltonian to the Schrödinger equation of an infinite 2D graphene sheet are of energies

$$E^\pm = \pm\gamma_0 \sqrt{1 + 4 \cos\left(\frac{\sqrt{3}a}{2}k_x\right) \cos\left(\frac{a}{2}k_y\right) + 4 \cos^2\left(\frac{a}{2}k_y\right)} \quad [\text{eV}] \quad (2.31)$$

where the hopping integral between first neighbours γ_0 is of 2.7eV , $a = \sqrt{3}a_{cc}$ is the graphene lattice parameter, $a_{cc} = 1.42\text{\AA}$ is the carbon-carbon bond length, and $\mathbf{k}(k_x, k_y)$ is the momentum vector in the reciprocal space, which is formed by hexagonally-shaped Brillouine zones for the honeycomb arrangement of carbon atoms in graphene. The positive (E^+) and negative (E^-) energy levels give the conduction (upper surface) and valence (lower surface) band respectively and are represented in Figure 2.17. At zero potential ($E_F = 0$) and zero temperature, the valence band is fully populated, while the conduction band is empty. In any other situation, some electrons possess energies in the conduction band and current may flow. The fact that the conduction and valence bands touch at the six Fermi K-points of the first Brillouine zone, makes graphene a semi-metal: A bandgap exists for all electron momenta (just as in semiconductors or insulators), except for the K-points, where no energy gap exists (just as in metals).

Direct & reciprocal space quantization

By their one-dimensionality, the dispersion relation of CNTs must be a one-dimensional subspace of the two-dimensional dispersion relation of graphene. This dispersion relation informs about the energy E of carriers that screw through the tube with different momenta \mathbf{k} and leads to the density of available states, which gives the number of carriers available as a function of potential. Structurally CNTs are described by two parameters n and m that define the CNT's roll-up in a circumferential $\mathbf{C} = n \cdot \mathbf{a}_1 + m \cdot \mathbf{a}_2$ and translational $\mathbf{T} = \frac{2m+n}{\text{GCD}} \mathbf{a}_1 - \frac{2n+m}{\text{GCD}} \mathbf{a}_2$

2.2. Setting the NEMS to Motion

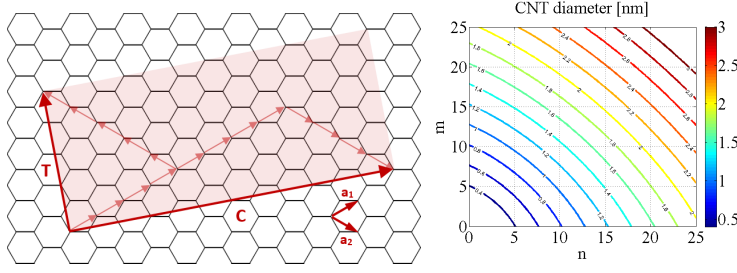


Figure 2.18: The (n,m) -CNT unit cell is defined by its circumferential $\mathbf{C} = n \cdot \mathbf{a}_1 + m \cdot \mathbf{a}_2$ and translational $\mathbf{T} = \frac{2m+n}{\text{GCD}} \mathbf{a}_1 - \frac{2n+m}{\text{GCD}} \mathbf{a}_2$ vectors in the direct space and contains $N_c = 4 \frac{n^2 + nm + m^2}{\text{GCD}}$ carbon atoms, where GCD is the greatest common divisor of $2n + m$ and $2m + n$.

direction, as shown in Figure 2.18. The resulting tube diameter is

$$d = \frac{|\mathbf{C}|}{\pi} = \frac{a}{\pi} \sqrt{n^2 + nm + m^2} \quad [\text{m}] \quad (2.32)$$

The basis vectors of this direct space are $\mathbf{a}_1 = \left(\frac{\sqrt{3}}{2}, \frac{1}{2}\right) a$ and $\mathbf{a}_2 = \left(\frac{\sqrt{3}}{2}, -\frac{1}{2}\right) a$ and GCD is the greatest common divisor of $2n + m$ and $2m + n$. The dispersion relation of equation (2.31) has been defined for the reciprocal space however, that is defined by the basis vectors $\mathbf{b}_1 = 2\pi \frac{(\hat{x} \otimes \hat{y} - \hat{y} \otimes \hat{x}) \mathbf{a}_2}{\mathbf{a}_1 \cdot (\hat{x} \otimes \hat{y} - \hat{y} \otimes \hat{x}) \mathbf{a}_2}$ and $\mathbf{b}_2 = 2\pi \frac{(\hat{y} \otimes \hat{x} - \hat{x} \otimes \hat{y}) \mathbf{a}_1}{\mathbf{a}_2 \cdot (\hat{y} \otimes \hat{x} - \hat{x} \otimes \hat{y}) \mathbf{a}_1}$, where \otimes designates the tensor product. In this reciprocal space \mathbf{k}_{\parallel} and \mathbf{k}_{\perp} give the translational and circumferential directions of the electron momenta, similarly to \mathbf{T} and \mathbf{C} respectively in the direct space. In a row-vector convention, this leads, by construction of the reciprocal space, to the equations

$$\begin{bmatrix} \mathbf{k}_{\perp} \\ \mathbf{k}_{\parallel} \end{bmatrix} = 2\pi \mathbb{I}_2 \begin{bmatrix} \mathbf{C}^{\text{tr}} & \mathbf{T}^{\text{tr}} \end{bmatrix}^{-1} \quad \left[\frac{1}{\text{m}}\right] \quad (2.33)$$

For infinitely long tubes, \mathbf{k}_{\parallel} is continuous. The rolling up of the graphene strip, however imposes a cyclic boundary condition on \mathbf{k}_{\perp} , which quantizes \mathbf{k}_{\perp} according to

$$\mathbf{k}_{\perp} \cdot \mathbf{C} \in 2\pi \mathbb{N}^* \quad (2.34)$$

The dispersion relation of SWNTs is consequently defined by substituting the solutions of equation (2.33) into the graphene dispersion relation of equation (2.31). This substitution is graphically illustrated for three SWNTs of similar diameter $1\text{nm} \pm 5\%$, but different roll-up angles (n, m) in Figure 2.19a, 2.20a and 2.21a. Projected onto k_{\perp} , the SWNTs' band structure results in Figure 2.19b, 2.20b and 2.21b, that reveal the valence sub-bands ($E < 0$) and conduction sub-bands ($E > 0$). It is observed that the valence and conduction band overlap if the Fermi K -points belong to the discretized momentum vectors, as it is the case for Figure 2.19b and any other (n, m) -SWNT satisfying the congruence

$$n \equiv m \pmod{3} \quad (2.35)$$

Such tubes are metallic and have a non-zero density of states around the Fermi level, where semi-conducting tubes present a band gap. This Fermi-level density of states can be derived

CNT band-structure and DOS

by observing that the derivative of the graphene dispersion relation around the K-points writes

$$\left. \frac{\partial E}{\partial k_{\parallel}} \right|_{\mathbf{k} \in \text{K-points}} = \frac{\sqrt{3}a\gamma_0}{2} \quad \left[\frac{1}{\text{eV}} \right] \quad (2.36)$$

and multiplying the inverted quantity by $\frac{1}{\pi}$ times the number of open sub-bands, as suggested by the upcoming equation (2.37). The graph 2.19c reveals this $g(E_F) = 0.22 \cdot 10^{-10} \left[\frac{1}{\text{eV} \cdot \text{m}} \right]$ density, while graphs 2.20c and 2.21c finally give away the resulting number of available states $g(E)$ per energy level E and unit length $\frac{1}{L}$ of the 1D SWNTs.

$$\begin{aligned} g(E) &= 2 \cdot \frac{1}{L} \cdot \left| \frac{\partial N}{\partial E} \right| \\ &= 2 \cdot \frac{1}{L} \cdot \sum_{k_{\perp}} \frac{\partial N}{\partial k_{\parallel}} \cdot \left| \frac{\partial k_{\parallel}}{\partial E} \right| \\ &= 2 \cdot \frac{1}{L} \cdot \sum_{k_{\perp}} \frac{L}{2\pi} \cdot \int_{k_{\parallel}} \left| \frac{\partial E}{\partial k_{\parallel}} \right|^{-1} \delta(E - E(k_{\parallel}, k_{\perp})) dk_{\parallel} \\ &= \frac{1}{\pi} \cdot \sum_{k_{\perp}} \int_{k_{\parallel}} \left| \frac{\partial E}{\partial k_{\parallel}} \right|^{-1} \delta(E - E(k_{\parallel}, k_{\perp})) dk_{\parallel} \quad \left[\frac{1}{\text{eV} \cdot \text{m}} \right] \quad (2.37) \end{aligned}$$

The factor 2 accounts for spin degeneracy. Two fermions of opposite spin can indeed occupy the same energy level, in accord with the Pauli exclusion principle. $\frac{\partial E}{\partial k_{\parallel}}$ needs to be evaluated for every k_{\parallel} with energy equal to E , which is achieved by sampling the integration of the continuous k_{\parallel} variable with a Kronecker delta at E , with $k_{\parallel} \in \left[0; \frac{2\pi}{|T|} \right]$. This procedure is to be repeated for every discrete $k_{\perp} \in \frac{2\pi}{|C|} \cdot \left\{ 0, 1, \dots, \frac{N_c}{2} \right\}$, with $N_c = 4 \frac{n^2 + nm + m^2}{\text{GCD}}$ the number of carbon atoms per unit cell. The number of carriers per momentum has been implicitly derived from the construction of the reciprocal space.

Fermi-Dirac distribution The probability that a state at energy E is occupied, is given by the Fermi distribution

$$f(E, \mu) = \frac{1}{e^{\frac{E-\mu}{k_B T}} + 1} \quad (2.38)$$

as a function of the electrochemical potential $\mu = q \cdot \phi_{\text{CNT}}$, $q = 1.6 \cdot 10^{-19}$ [C] being the unit charge, $k_B = 8.6 \cdot 10^{-5} \left[\frac{\text{eV}}{\text{K}} \right]$ the Boltzmann constant and T [K] the absolute temperature. The total number N of π -electrons per unit length in the SWNT is then given by

$$N(\mu) = L \cdot \int_{E=-\infty}^{\infty} g(E) \cdot f(E, \mu) dE \quad (2.39)$$

2.2. Setting the NEMS to Motion

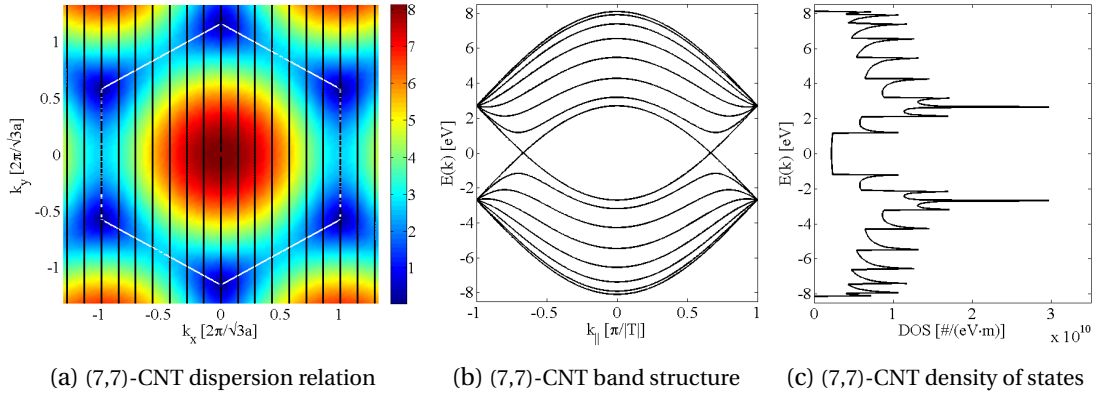


Figure 2.19: (7,7) armchair nanotubes are metallic (eq. (2.35)) because their dispersion relation intersects the K-points of the graphene Brillouine zone. The bandstructure presents no gap and a finite non-zero density of states prevails around the neutrality level.

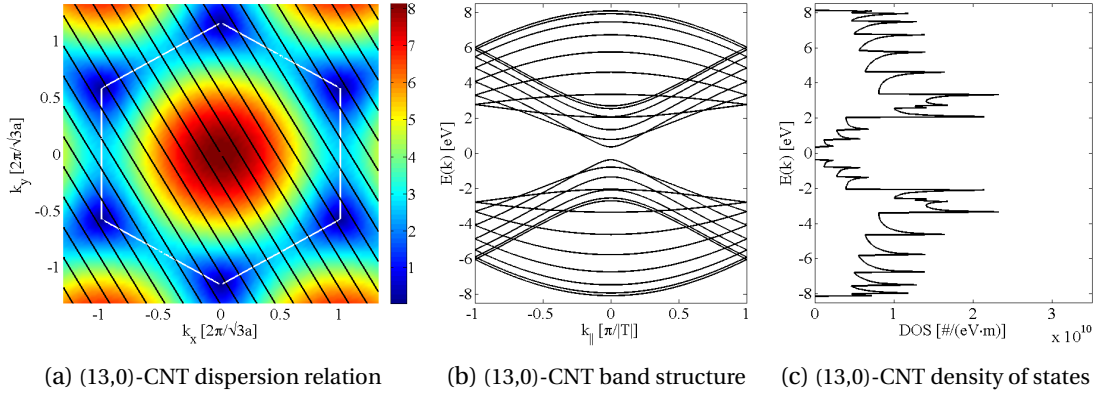


Figure 2.20: (13,0) zigzag nanotubes are semi-conducting (eq. (2.35)) because their dispersion relation does not intersect the K-points of the graphene Brillouine zone. The bandstructure presents a gap and no states are available around the neutrality level.

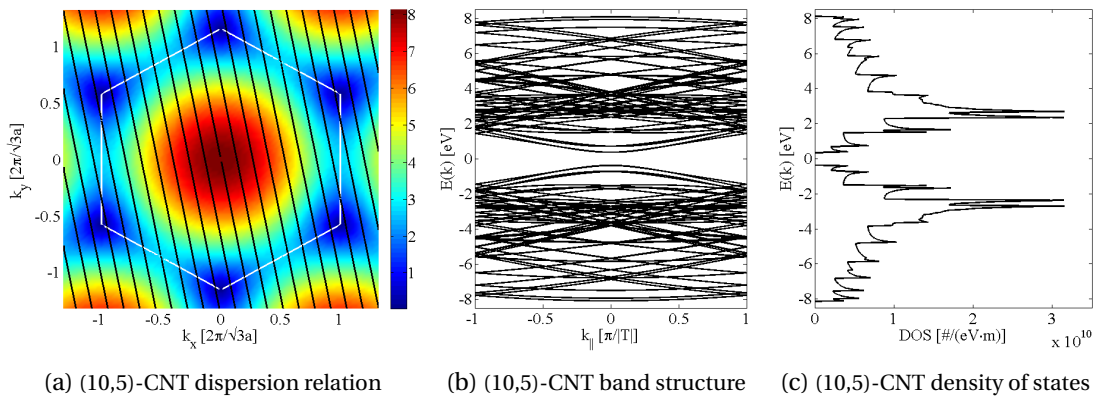
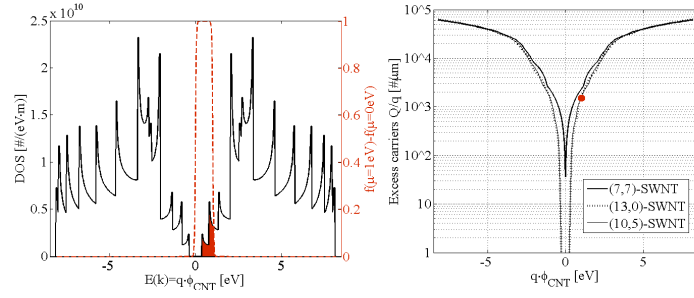


Figure 2.21: (10,5) nanotubes are semi-conducting (eq. (2.35)) because their dispersion relation does not intersect the K-points of the graphene Brillouine zone. The bandstructure presents a gap and no states are available around the neutrality level.

Figure 2.22: (left) Density of available states of a (13,0) semiconducting zigzag SWNT and the excess carriers' state occupation probability at $\mu = 1\text{eV}$.

(right) Number of excess carriers per μm as a function of the tube potential for three wrapping angles. The point's y-value at $\mu = 1\text{eV}$ corresponds to the coloured area of the left graph



Which, given the SWNT's neutrality at $\mu = 0$, caters a net charge of

$$Q(\phi_{\text{CNT}}) = q \cdot (N(q\phi_{\text{CNT}}) - N(0)) \quad [\text{C}] \quad (2.40)$$

This net charge is close to zero if the tube potential ϕ_{CNT} falls into the bandgap and monotonically increases in the valence and conduction bands, as emanates from Figure 2.22.

Quantum capacitance The lineic quantum capacitance C'_q and the differential quantum capacitance $\delta C'_q$ may be now defined as

$$C'_q(V_{\text{GS}}) = \frac{1}{L} \cdot \frac{Q_{\text{CNT}}}{\phi_{\text{CNT}}} \quad \left[\frac{\text{F}}{\text{m}} \right] \quad (2.41)$$

$$\delta C'_q(\delta V_{\text{GS}}) \Big|_{V_{\text{GS}}} = \frac{1}{L} \cdot \frac{\delta Q_{\text{CNT}}}{\delta \phi_{\text{CNT}}} \quad \left[\frac{\text{F}}{\text{m}} \right] \quad (2.42)$$

and can be derived from equation (2.40). Numerical values are provided in Figure 2.23b and 2.23c, which offer the precious insight that the quantum capacitance exceeds the electrical one by an order of magnitude if at least one sub-band is open. So the electrical capacitance happens to dominate the events if the tube potential ϕ_{CNT} lies in the valence or conduction band, while the quasi-zero quantum capacitance dominates if ϕ_{CNT} falls into the band gap. Catching a glimpse of Figure 2.23a reveals that the tube potential does not increase much within the gate voltage range available in integrated technologies. In this range, the quantum capacitance is observed to have little relative variation. In addition is it improbable that other bands open, given the feeble potential slope and the non-negligible sub-band spacing of equations (2.34) and (2.31). $C'_q(V_{\text{GS}})$ may hence be approximated by the quantum capacitance at the Fermi points, which is deduced from the work required to add a single electron to the

2.2. Setting the NEMS to Motion

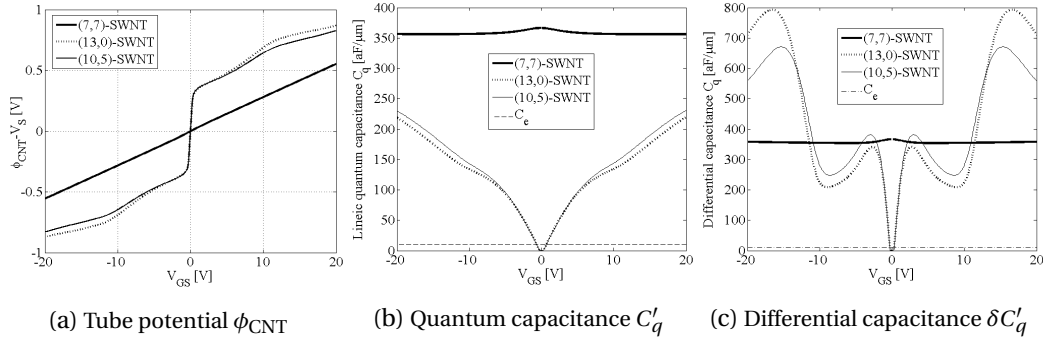


Figure 2.23: The quantum capacitance C'_q exceeds the electrical capacitance C'_e if the tube potential ϕ_{CNT} lies in the valence and conduction band, while the opposite is true inside the bandgap. This implies that the tube potential equals the gate voltage until it saturates at the band edges.

system

$$\begin{aligned}
 C'_q(E_F) &\approx \frac{1}{L} \cdot \frac{\partial Q_{\text{CNT}}}{\partial \phi_{\text{CNT}}} = \frac{1}{L} \cdot \frac{q \partial N}{\frac{1}{q} \partial E} = \frac{q^2}{2} \cdot g(E) \\
 &= \frac{q^2}{2} \cdot \frac{4}{\pi} \cdot \left(\frac{\sqrt{3} a \gamma_0}{2} \right)^{-1} = \frac{4q^2}{\sqrt{3} \pi a \gamma_0} \\
 &\approx 300 \quad \left[\frac{\text{aF}}{\mu\text{m}} \right] \quad (2.43)
 \end{aligned}$$

Based on Figure 2.23b and 2.23c and equation (2.29), the tube potential may be approximated by the piecewise linear function Tube potential

$$\phi_{\text{CNT}}(V_{\text{GS}}, y(x)) = \begin{cases} V_{\text{GS}} & \text{if } |V_{\text{GS}}| < \frac{E_g}{2q} \\ \pm \frac{E_g}{2q} + \frac{C'_e}{C'_q} \cdot V_{\text{GS}} & \text{else} \end{cases} \quad [\text{V}] \quad (2.44)$$

where E_g is the bandgap and Fermi-level alignment at half-gap has been hypothesized, as it is the case for undoped SWNTs up to roughly several nm close to the junction with the contacting drain and source metals [10]. The expected bandgap E_g may be found by observing that the k-lines are spaced by $\Delta k_{\perp} = \frac{2}{d}$ from equations (2.32) and (2.34), multiplying by equation (2.36) and weighing by the fact that two third of the SWNTs possess a bandgap, leads to

$$\begin{aligned}
 E_g &= \frac{2}{d} \cdot \frac{\sqrt{3} a \gamma_0}{2} \cdot \frac{2}{3} = \frac{2 a_{cc} \gamma_0}{d} \\
 &\approx \frac{0.77}{d [\text{nm}]} \quad [\text{eV}] \quad (2.45)
 \end{aligned}$$

The tube potential of equation (2.44) scales linearly with the gate voltage until a first sub-band opens. Then the rate of increase drops to the ratio of the electrical to quantum capacitance, which is negligible.

Summary This excursion to solid state physics closes by providing orders of magnitudes and approximations of several NEMS parameters that will be amply used throughout this document.

The gate to tube capacitance of equation (2.27) is relatively insensitive to the tube diameter, deflection and suspension height and approximately of

$$C'_e(y(x)) = 10 \quad \left[\frac{\text{aF}}{\mu\text{m}} \right] \quad (2.46)$$

and changes with gate tube distance $y(x)$ as

$$\partial C'_e(y(x)) = 6 \quad \left[\frac{\text{pN}}{\mu\text{m} \cdot \text{V}^2} \right] \quad (2.47)$$

The quantum capacitance may be approximated by

$$C'_q(\phi_{\text{CNT}}(V_{\text{GS}})) = 300 \quad \left[\frac{\text{aF}}{\mu\text{m}} \right] \quad (2.48)$$

The tube potential piecewise linear approximation is obtained by substituting $C'_e = 10 \frac{\text{aF}}{\mu\text{m}}$ and $C'_q = 300 \frac{\text{aF}}{\mu\text{m}}$ into equation (2.44)

$$\phi_{\text{CNT}}(V_{\text{GS}}, y(x)) = \begin{cases} V_{\text{GS}} & \text{if } |V_{\text{GS}}| < \frac{E_g}{2q} \\ \pm \frac{E_g}{2q} + \frac{V_{\text{GS}}}{30} & \text{else} \end{cases} \quad [\text{V}] \quad (2.49)$$

where the bandgap may be related to the tube diameter d by

$$E_g = \begin{cases} \frac{0.77}{d[\text{nm}]} & \text{if SWNT is semiconducting} \\ 0 & \text{if SWNT is metallic} \end{cases} \quad [\text{eV}] \quad (2.50)$$

2.2.4 The electrostatic force - revisited

Actuation force Following the insights from the previous subsections, the electrostatic force of equation (2.30) may approximately be expressed by the device geometry as

$$F'(V_{\text{GS}}, x) = \begin{cases} \frac{\pi\epsilon}{h \cdot \text{acosh}^2(\frac{h}{r})} \cdot V_{\text{GS}}^2 & \text{if SWNT is metallic} \\ \frac{\pi\epsilon}{h \cdot \text{acosh}^2(\frac{h}{r})} \cdot \left(V_{\text{GS}} - \frac{0.77}{2d[\text{nm}]} \right)^2 & \text{else if } |V_{\text{GS}}| > \frac{0.77}{2d[\text{nm}]} \\ 0 & \text{else} \end{cases} \quad \left[\frac{\text{N}}{\text{m}} \right] \quad (2.51)$$

where $\frac{1}{2} \partial C'_e = \frac{\pi\epsilon}{h \cdot \text{acosh}^2(\frac{h}{r})}$ has been found by equation (2.47) to be on the order of $\sim 3 \left[\frac{\text{pN}}{\mu\text{m} \cdot \text{V}^2} \right]$. While a steady DC (direct current) bias outside the energy gap is necessary to obtain any force at all, oscillatory tube motion additionally requires the gate voltage to possess a time-varying component.

Sinus vs. square Simple periodic time-varying signals are sine (analog) and rectangular (digital) signals, where

2.2. Setting the NEMS to Motion

	Voltage V_{GS}	Force $F \times \frac{2}{\partial C_e}$
Temporal	$\bar{V} + \tilde{v} \sin(\omega_{in} t)$	$\left(\bar{V}^2 + \frac{\tilde{v}^2}{2}\right) + 2\bar{V}\tilde{v} \sin(\omega_{in} t) + \frac{\tilde{v}^2}{2} \sin\left(2\omega_{in} t - \frac{\pi}{2}\right)$
Spectral	$\{0, 1\} \cdot \omega_{in}$	$\{0, 1, 2\} \cdot \omega_{in}$
Temporal	$\bar{V} + \tilde{v} \text{rect}(\omega_{in} t)$	$(\bar{V}^2 + \tilde{v}^2) + 2\bar{V}\tilde{v} \text{rect}(\omega_{in} t)$
Spectral	$\{0\} \cup \{2N + 1\} \cdot \omega_{in}$	$\{0\} \cup \{2N + 1\} \cdot \omega_{in}$

Table 2.1: Temporal and spectral description of the actuation voltage and resulting electrostatic force. Sinusoidal actuation has the beneficial effect of yielding force frequency components that are not present in the voltage spectrum.

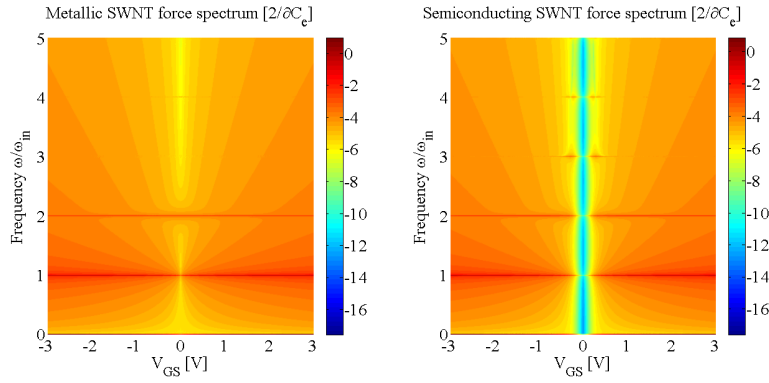


Figure 2.24: The force spectrum for metallic SWNTs reveals the components at DC, once and twice the actuation voltage frequency. For semiconducting SWNTs, the force drops considerably inside the bandgap, leading to higher harmonic nonlinearities for biases in the bandgap vicinity. (the colour-scale is logarithmic)

the latter pose higher exigencies in terms of circuit bandwidth due to their harmonic content. The spectral content of the force, scaling with the square of the voltage, is given by Table 2.1, where the signal is composed of a steady DC component (\bar{V}) superposed to a time-varying signal (\tilde{v}). The square of the sinusoidal drive creates a force component at twice the drive frequency. This is valuable information, as it would allow to drive the NEMS at a frequency that is not polluted by direct capacitive coupling between the gate actuation and drain readout electrodes, facilitating detection of the motion. A similar convenience does unfortunately not hold for a square wave actuation, where the voltage and force spectra are identical and comprise all odd harmonics of the base frequency.

The appearance of the second harmonic component in the force spectrum for sinusoidal drives is certified by Figure 2.24, where \bar{V} is scanned from -3V to 3V with \tilde{v} being 100mV. The absence of force within the bandgap of semiconducting SWNTs becomes visible. This force non-linearity is observed to yield even higher order harmonic force components for DC bias voltages near the band edge. Those components are weak though and gambling on their

Approx-
imation
validation

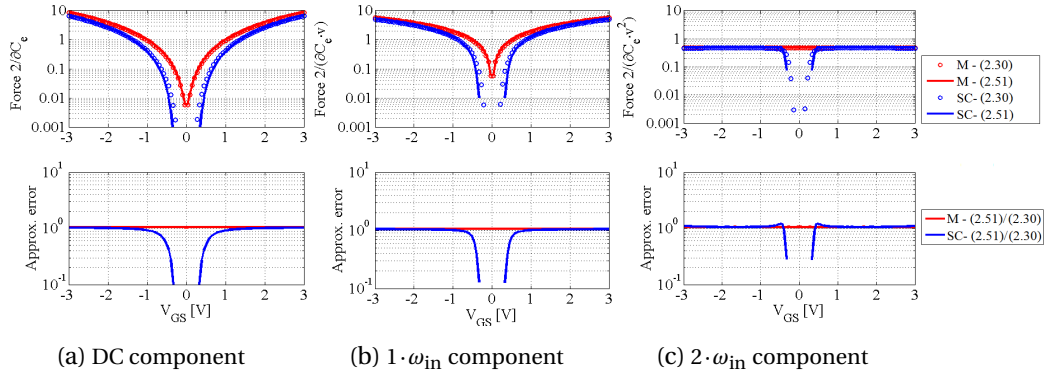


Figure 2.25: A sinusoidal drive at $\tilde{v} \sin(\omega_{in} t)$ creates force components at DC, $1 \cdot \omega_{in}$ and $2 \cdot \omega_{in}$. Metallic tubes are represented in red, semiconducting tubes in blue. Equation (2.51) (—) is found to nicely approximate the quantum equation (2.30) (o). The ratio $\frac{(2.51)}{(2.30)}$ is indeed generally close to unity whenever the force is large.

presence for readout would be unrealistic. Figure 2.24 has been obtained by simulating all the previously mentioned quantum effects. The DC, $1\omega_{in}$ and $2\omega_{in}$ spectra are extracted and reported to Figure 2.25, so to compare them with the approximation made by equation (2.51). It is concluded that equation (2.51) approximates the actuation force sufficiently well for order of magnitude estimations.

Aspiring to robustness

The electrostatic force amplitude has been found to be ratable by the geometrical NEMS dimensions (see equation (2.51)), and graph 2.15 unveiled the fact that this force is rather insensitive to parameter fluctuations, leading to equation (2.47). Moreover will the force difference between metallic and semiconducting tubes vanish under high bias, that is if $V_{GS} \gg \frac{E_g}{2q}$, as emanates from equation (2.51). For this discrepancy to be less than a factor 4, it is sufficient to guarantee a gate to source bias equal to the tube bandgap, which is slightly above 1V for narrow tubes, and even less for large diameter tubes. Finally, the electrostatic force is found to possess three frequency components at DC, once and twice the drive voltage frequency, listed in Table 2.1 and scaling with \tilde{V}^2 , $\tilde{V} \tilde{v}$ and \tilde{v}^2 respectively. The DC force is of little interest in actuation and has been used for frequency tuning [1]. Tuning can also be achieved via mechanical straining, as has been seen previously. This makes the DC force component obsolete, and biasing two gate electrodes, placed symmetrically around the tube (see Figure 2.4), to identical DC voltage, would cancel the major part of this force component. The $1\omega_{in}$ component scales linearly with \tilde{V} , which will not vary by an order of magnitude, but rather stay in the 1V to 5V range, which is sufficient for proper device operation. The $2\omega_{in}$ component is even entirely independent of the bias and tube nature, provided that $\tilde{V} > 1V$.

Summary

At the intersection of all these approximations, appears the solid conclusion, that good estimations of the electrostatic force can be established and will hold through a considerable range of SWNTs and bias conditions. These orders of magnitude are summarized in Table 2.2 and will serve as a reference in the following. Combining the values of Table 2.2 and the

2.2. Setting the NEMS to Motion

Frequency	Expression	Value $\left[\frac{\text{pN}}{\mu\text{m}} \right]$
DC	$\frac{\pi\epsilon}{h \cdot \text{acosh}^2\left(\frac{h}{r}\right)} \cdot \left(\tilde{V}^2 + \frac{\tilde{v}^2}{2} \right)$	10
$1 \cdot \omega_{\text{in}}$	$\frac{\pi\epsilon}{h \cdot \text{acosh}^2\left(\frac{h}{r}\right)} \cdot 2\tilde{V}\tilde{v}$	$10 \cdot \tilde{v}$
$2 \cdot \omega_{\text{in}}$	$\frac{\pi\epsilon}{h \cdot \text{acosh}^2\left(\frac{h}{r}\right)} \cdot \frac{\tilde{v}^2}{2}$	$1 \cdot \tilde{v}^2$

Table 2.2: Approximation of the electrostatic force as a function of the time varying gate voltage with amplitude \tilde{v} and frequency ω_{in} . To be independent of the nature of the tube, the DC bias \tilde{V} shall exceed 1V. The numerical values suppose $\tilde{V} \sim 2\text{V}$ and NEMS dimensions as suggested in section 2.2.2.

insights from Table 2.1, the voltage to force transfer function can be approximated by

$$H_{\tilde{v} \rightarrow F'}(j\omega) : |\tilde{v}| \cdot e^{j(\omega t)} \longmapsto 10\tilde{v} \cdot e^{j(\omega t)} + \tilde{v}^2 \cdot e^{j(2\omega t - \frac{\pi}{2})} \quad \left[\text{V} \rightarrow \frac{\text{pN}}{\mu\text{m}} \right] \quad (2.52)$$

2.2.5 Electromechanical actuation summary

The voltage to motion transfer function results as a combination of the voltage to force transfer function (equation (2.52)) and the force to displacement/strain transfer functions of section 2.2.1

Voltage-induced motion

$$H_{\tilde{v} \rightarrow \tilde{y}}(j\omega) = H_{F' \rightarrow \tilde{y}}(H_{\tilde{v} \rightarrow F'}(j\omega)) \quad [\text{V} \rightarrow \text{nm}] \quad (2.53)$$

$$H_{\tilde{v} \rightarrow \epsilon}(j\omega) = H_{F' \rightarrow \epsilon}(H_{\tilde{v} \rightarrow F'}(j\omega)) \quad [\text{V} \rightarrow \text{\%}] \quad (2.54)$$

Given the single transfer functions, their composition will present lorentzian peaks around two particular frequencies, which are half and full the NEMS eigenfrequency. In the following discussion, the resonant response is hypothesized to dominate any off-resonance contribution. This is in practice the case for sufficiently large quality factors. The voltage to displacement and strain conversion around these peaks is of particular interest and is provided subsequently.

Average displacement at ω_0 for half-frequency actuation $\frac{\omega_0}{2}$

$$\begin{aligned}
 H_{\tilde{v} \rightarrow \bar{y}}\left(\frac{\omega_0}{2}\right): \\
 \left[Q^{-0.5} \cdot 10^{-4.55} \cdot \left(\frac{\omega_0}{2\pi}\right)^{0.575}; Q^{-0.5} \cdot 10^{-13.75} \cdot \left(\frac{\omega_0}{2\pi}\right)^{1.71} \right] &\longrightarrow \left[10^{9.4} \cdot \left(\frac{\omega_0}{2\pi}\right)^{-1.13}; 10^{-9.0} \cdot \left(\frac{\omega_0}{2\pi}\right)^{1.14} \right] \\
 \tilde{v} \cdot \sin\left(\frac{\omega_0}{2}t\right) &\longrightarrow \tilde{v}^2 \cdot Q \cdot 10^{18.5} \cdot \left(\frac{\omega_0}{2\pi}\right)^{-2.28} \cdot \sin(\omega_0 t + 0)
 \end{aligned} \tag{2.55}$$

Average displacement at ω_0 for full-frequency actuation ω_0

$$\begin{aligned}
 H_{\tilde{v} \rightarrow \bar{y}}(\omega_0): \\
 \left[Q^{-1} \cdot 10^{-10.1} \cdot \left(\frac{\omega_0}{2\pi}\right)^{1.15}; Q^{-1} \cdot 10^{-28.5} \cdot \left(\frac{\omega_0}{2\pi}\right)^{3.42} \right] &\longrightarrow \left[10^{9.4} \cdot \left(\frac{\omega_0}{2\pi}\right)^{-1.13}; 10^{-9.0} \cdot \left(\frac{\omega_0}{2\pi}\right)^{1.14} \right] \\
 \tilde{v} \cdot \sin(\omega_0 t) &\longrightarrow \tilde{v} \cdot Q \cdot 10^{19.5} \cdot \left(\frac{\omega_0}{2\pi}\right)^{-2.28} \cdot \sin\left(\omega_0 t + \frac{\pi}{2}\right)
 \end{aligned} \tag{2.56}$$

Oscillation-induced strain at $2\omega_0$ for half-frequency actuation $\frac{\omega_0}{2}$

$$\begin{aligned}
 H_{\tilde{v} \rightarrow \epsilon}\left(\frac{\omega_0}{2}\right): \\
 \left[Q^{-0.5} \cdot 10^{-7.5} \cdot \left(\frac{\omega_0}{2\pi}\right)^{0.935}; Q^{-0.5} \cdot 10^{-13.75} \cdot \left(\frac{\omega_0}{2\pi}\right)^{1.71} \right] &\longrightarrow \left[10^{-8.41} \cdot \left(\frac{\omega_0}{2\pi}\right)^{0.73}; 10^{-20.91} \cdot \left(\frac{\omega_0}{2\pi}\right)^{2.28} \right] \\
 \tilde{v} \cdot \sin\left(\frac{\omega_0}{2}t\right) &\longrightarrow \frac{\tilde{v}^2}{2} \cdot Q \cdot 10^{6.59} \cdot \left(\frac{\omega_0}{2\pi}\right)^{-1.14} \cdot \sin\left(2\omega_0 t - \frac{\pi}{2}\right)
 \end{aligned} \tag{2.57}$$

Oscillation-induced strain at $2\omega_0$ for full-frequency actuation ω_0

$$\begin{aligned}
 H_{\tilde{v} \rightarrow \epsilon}(\omega_0): \\
 \left[Q^{-1} \cdot 10^{-16.0} \cdot \left(\frac{\omega_0}{2\pi}\right)^{1.87}; Q^{-1} \cdot 10^{-28.5} \cdot \left(\frac{\omega_0}{2\pi}\right)^{3.42} \right] &\longrightarrow \left[10^{-8.41} \cdot \left(\frac{\omega_0}{2\pi}\right)^{-0.73}; 10^{-20.91} \cdot \left(\frac{\omega_0}{2\pi}\right)^{2.28} \right] \\
 \tilde{v} \cdot \sin(\omega_0 t) &\longrightarrow \frac{\tilde{v}}{2} \cdot Q \cdot 10^{7.59} \cdot \left(\frac{\omega_0}{2\pi}\right)^{-1.14} \cdot \sin\left(2\omega_0 t + \frac{\pi}{2}\right)
 \end{aligned} \tag{2.58}$$

From these four transfer functions, it becomes already clear that the choice of the electrical driving frequency will impose the output to input frequency ratio. This one can be 1 or 2 for capacitive and field-effect readout, that are based on the average tube displacement, and 2 or 4 for piezoresistive readout, based on the oscillation-induced strain. The acceptable driving voltage and achievable displacements and amplitudes are illustrated by Figure 2.26 for $Q = 100$. While the output range is independent of the quality factor, higher Q allow to obtain these

2.3. Decrypting the NEMS Response

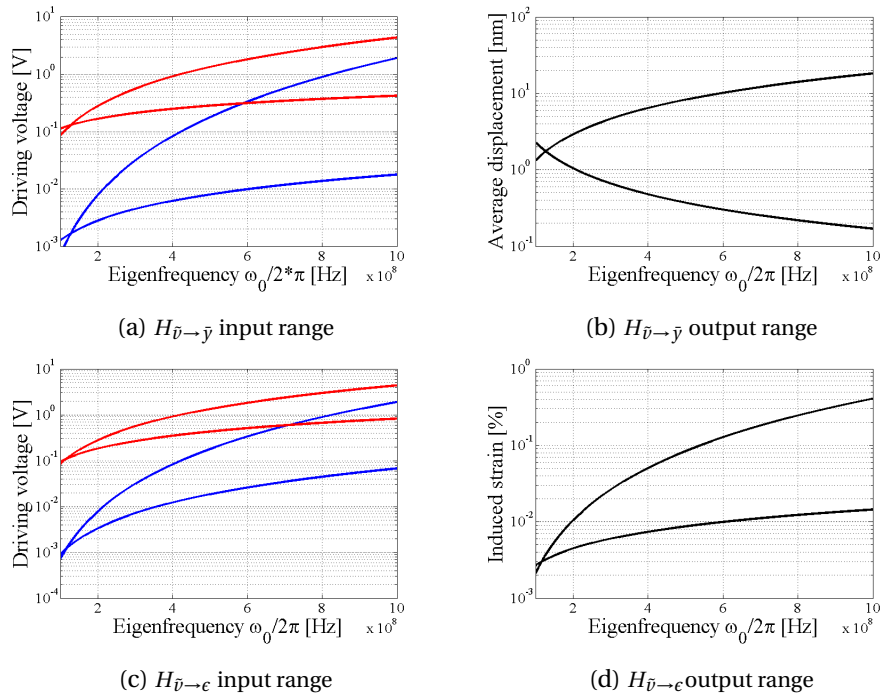


Figure 2.26: Electromechanical actuation input and output dynamic ranges for $\omega_{in} = \frac{\omega_0}{2}$ (red) and $\omega_{in} = \omega_0$ actuation schemes. (hyp. $Q=100$)

displacements for lower driving voltages. Noticeable are also the phase delays that vary from one transfer function to another and that will play a major role in closed-loop operation, as shall be seen in this chapter's summary and especially in chapters 3 and 4.

2.3 Decrypting the NEMS Response



For a circuit to sense the motion of the NEMS, it needs to detect changes in the NEMS's Overview electrical characteristics. Those may be induced by three phenomena, which are:

Capacitive: Tube motion or gate voltage variation \bar{v} modulate the static charge on the electrical-quantum capacitive divider of Figure 2.16. The related charge flow can be measured at the source and drain terminals in form of a current flowing into and out of the tube.

Field effect: The tube potential changes under the influence of the tube motion or a gate voltage variation \bar{v} , which causes a repopulation of the electronic states and a change in tube conductance (at constant state density) and hence in the current flow through the tube.

Piezoresistive effect: As the tube oscillates and elongates under the influence of the gate voltage modulation \bar{v} , the graphene and CNT Brillouine zones stretch and modify the density of available states. This results in a modification of the tube conductance (at

constant tube potential) and hence in the current flow through the tube.

Each of these phenomena is subsequently quantified and finds its place in the chapter concluding Figure 2.33 and 2.34.

2.3.1 Capacitive Effect

Effect description It has been shown in the first part of this chapter, that a modulation of the gate voltage $\bar{V} + \tilde{v} \sin(\omega t)$ pulls charges onto the capacitive divider, formed by the electrical gate to tube C'_e and the quantum CNT C'_q capacitors. The attraction between charges on the tube and the gate then causes the force that allows to set the tube into motion. The nature of this motion reversely impacts the charges on the tube, a quantity that can be measured in form of a current \tilde{i}'_{capa} , flowing into and out of the CNT, given by

$$\begin{aligned} \tilde{i}'_{\text{capa}} &= \frac{\partial q'}{\partial t} = \partial_t (C'_e \cdot (\bar{V} + \tilde{v} \sin(\omega t))) \\ &= \tilde{i}'_{\text{capa,mech}} + \tilde{i}'_{\text{capa,elec}} \quad \left[\frac{\text{A}}{\mu\text{m}} \right] \end{aligned} \quad (2.59)$$

Mechanical component where the equivalent series of capacitors $C' = \frac{C'_e C'_q}{C'_e + C'_q} \approx C'_e$, seen by the voltage, has been simplified in virtue of the fact that $C'_q \gg C'_e$ (see equations (2.46) and (2.48)). The mechanical and purely electrical contributions write

$$\begin{aligned} \tilde{i}'_{\text{capa,mech}} &= \frac{\partial C'_e}{\partial \bar{y}} \left[\frac{\text{pN}}{\mu\text{m} \cdot \text{V}^2} \right] \cdot \frac{\partial \bar{y}}{\partial t} \left[\frac{\text{nm}}{\text{s}} \right] \cdot \bar{V} [\text{V}] \cdot 10^{-12} \quad \left[\frac{\text{nA}}{\mu\text{m}} \right] \\ &= \begin{cases} 10^{9.4} \cdot Q \cdot \omega_0^{-1.28} \cdot \tilde{v}^2 \cdot \sin(\omega_0 t + \frac{\pi}{2}) & \text{if } \omega = \frac{\omega_0}{2} \\ 10^{10.4} \cdot Q \cdot \omega_0^{-1.28} \cdot \tilde{v} \cdot \sin(\omega_0 t + \pi) & \text{if } \omega = \omega_0 \end{cases} \end{aligned} \quad (2.60)$$

$$\begin{aligned} \tilde{i}'_{\text{capa,elec}} &= C'_e \left[\frac{\text{aF}}{\mu\text{m}} \right] \cdot \tilde{v} [\text{V}] \cdot \omega \left[\frac{\text{rad}}{\text{s}} \right] \cdot \cos(\omega t) \cdot 10^{-9} \quad \left[\frac{\text{nA}}{\mu\text{m}} \right] \\ &= \begin{cases} 10^{-8.3} \cdot \omega_0 \cdot \tilde{v} \cdot \sin\left(\frac{\omega_0}{2} t + \frac{\pi}{2}\right) & \text{if } \omega = \frac{\omega_0}{2} \\ 10^{-8.0} \cdot \omega_0 \cdot \tilde{v} \cdot \sin\left(\omega_0 t + \frac{\pi}{2}\right) & \text{if } \omega = \omega_0 \end{cases} \end{aligned} \quad (2.61)$$

where the factors 10^{-12} and 10^{-9} correct for the unit prefix-scaling, $\partial_{\bar{y}} C'_e = 6 \frac{\text{pN}}{\mu\text{m} \cdot \text{V}^2}$ according to equation (2.47), $C'_e = 10 \frac{\text{aF}}{\mu\text{m}}$ and $\partial_t \bar{y}$ is derived from $H_{\tilde{v} \rightarrow \bar{y}}$ for the half (equation (2.55)) and full (equation (2.56)) actuation strategies. The DC bias $\bar{V} = 2\text{V}$ has been chosen identically as in Table 2.2 so to guarantee a bias outside the bandgap. Numerical values have been regrouped and basic trigonometric identities were used to determine the phase delay. The driving voltage \tilde{v} is bound to the domains of equations (2.55) and (2.56) respectively, drawn in Figure 2.26a.

Signal and background The capacitive \tilde{i}'_{capa} current's mechanical (black) and electrical (gray) components are plotted in Figure 2.27 for half and full frequency actuation within the linear dynamic range. First, the

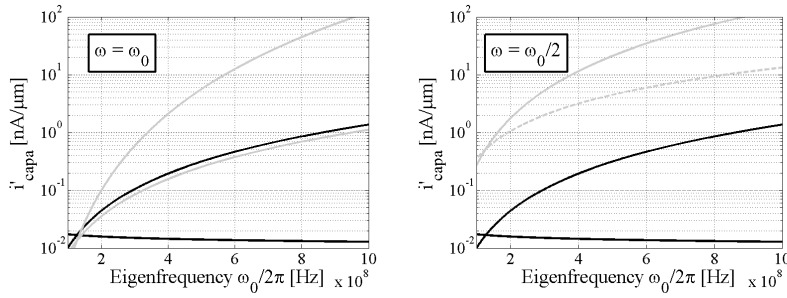


Figure 2.27: The capacitive current for both actuation schemes has a mechanical component (black) below the nanoampere floor and a relatively stronger electrical background signal (gray). Both signals fortunately come with distinct phase ($\omega = \omega_0$) and distinct frequency ($\omega = \frac{\omega_0}{2}$). (hyp. $Q = 100$)

mechanical component is observed not to exceed the nanoampere floor. Additionally it is overshadowed by the purely electrical component, which carries no motional information. This means that the bare capacitive current, flowing in and out the tube, does not unveil any motional information at first sight. Motion could be retrieved in both cases nevertheless as follows:

In the half frequency drive case, the mechanical signal has twice the frequency of the electrical signal, as can be seen from equations (2.60) and (2.61). So an electrical filter could attenuate the electrical component to isolate the mechanical one.

Filtering

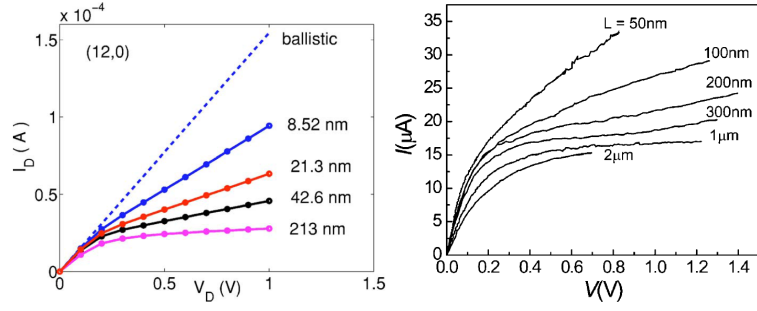
In the case of the full frequency drive, both components appear at an identical frequency, and filtering will not do the trick. This time, both signals distinguish themselves by their phase delay nevertheless. The key observation to distinguish the signals, is that the integral of the product of two periodic orthogonal functions is periodic as well, while the integral shows an increasing or decreasing trend, if the two functions are not orthogonal. Two sine waves are orthogonal if they are dephased by $\pm \frac{\pi}{2}$. So multiplying (mixing) \tilde{i}'_{capa} with the actuation signal $\tilde{v} \cdot \sin(\omega_0 t)$ and averaging (integrating) their product, yields a signal whose average value only increases with the non-orthogonal motional component, but not with the orthogonal purely electrical component. Such a technique is capable of demonstrating that the CNTs move [1], but it cannot provide instant information on the actual motion. Note that sines with different periods are orthogonal as well, so this mixing and integrating technique would also get rid of the electrical contribution to the signal in the half frequency case: \tilde{i}'_{capa} needs to be multiplied by $\tilde{v} \cdot \sin(\omega_0 t + \frac{\pi}{2})$ then.

Mixing

Another, yet unspoken, component to the drain current, is the feedthrough due to the capacitive coupling between the gate and drain electrodes. This capacitance may geometrically be evaluated to $C_{\text{gd}} \sim 100\text{aF}$ for an electrode setup like in Figure 2.4 ([58] estimates it to 30aF), and causes an even stronger electrical signal on the drain than the gate's coupling via the CNT

Feedthrough

Figure 2.28: Simulations (left, taken from [4]) and measurements (right, taken from [5]) show that tubes longer than 100nm suffer scattering at source-drain voltages above 100mV. Transport may be appropriately described by a diffusive Drude model.



of equation (2.61), namely

$$\begin{aligned} \tilde{i}'_{\text{capa,feed}} &= C_{\text{gd}} [\text{aF}] \cdot \tilde{v} [\text{V}] \cdot \omega \left[\frac{\text{rad}}{\text{s}} \right] \cdot \cos(\omega t) \cdot 10^{-9} & [\text{nA}] \\ &= \begin{cases} 10^{-7.3} \cdot \omega_0 \cdot \tilde{v} \cdot \sin\left(\frac{\omega_0}{2} t + \frac{\pi}{2}\right) & \text{if } \omega = \frac{\omega_0}{2} \\ 10^{-7.0} \cdot \omega_0 \cdot \tilde{v} \cdot \sin\left(\omega_0 t + \frac{\pi}{2}\right) & \text{if } \omega = \omega_0 \end{cases} & (2.62) \end{aligned}$$

2.3.2 Field effect



Ballistic or
diffusive

To stand out of the noise floor, caused by the electronic circuit, especially in broadband applications, maximal signal strength out of the CNT is priceless. So rather high biases will be applied to the CNTs, to have them operate in their on-state (imposed by V_g) and in the saturation regime (imposed by V_{ds}). To quantify the strength of the field- and piezoresistive current modulations, an equation for the drain current under high bias is needed. Their one-dimensional nature confers electronic transport properties to CNTs that differ from the ones observed in bulk materials. Ballistic transport has for instance been observed at room temperature in metallic CNTs under low bias [59]. Consequently arises the legitimate question whether current flow through CNTs follows a ballistic Landauer-Büttiker formalism or rather a diffusive model. Ballistic transport at room temperature has been attributed to the fact that acoustic phonons possess micrometer mean free paths, and do not hinder electrons travelling through sub-micrometer long tubes under low bias [5]. Under higher bias, optical and zone boundary phonon scattering set in and drastically reduce the mean free path to tens of nanometers only [5], which translates into current saturation. The observed mean free path is further roughly five times lower than the theoretical prediction. One explanation may be that phonons cannot dissipate fast enough, which generates hot phonons. This is especially the case for suspended CNTs without contact to the substrate, and may even lead to negative differential conductance as shown in Figure 1.5a. Given that the optical phonons have energies around 160meV [60], high bias scattering limits the maximal current in long tubes to roughly

$$I_d = \frac{4q^2}{h} \cdot 160 [\text{mV}] \approx 25 \quad [\mu\text{A}] \quad (2.63)$$

2.3. Decrypting the NEMS Response

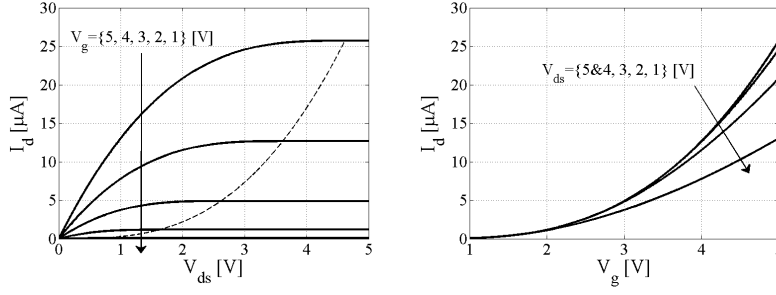


Figure 2.29: Drain current as a function of the drain-source bias (left) and gate bias (right) for an SWNT with diameter $d = 1\text{nm}$, as given by equation (2.64).

where $G_0 = \frac{4q^2}{h} \approx 155\mu\text{S}$ is the Landauer-Büttiker quantum conductance. Shown in Figure 2.28 are simulated [4] and measured [5] current-voltage characteristics of SWNTs. It is apparent that tubes with lengths considered in the previous sections (100nm-1 μm) exceed the ballistic regime already for relatively low drain to source biases. This fact motivates the decision to describe the drain current by a diffusive model [61], based on Fermi's Golden rule [62] and accounting for the CNT's one-dimensional band structure when combining the quantum and diffusive resistances. The drain current then writes as a function of the bias [63]

$$I_d = \begin{cases} G_0 \cdot V_{ds} \cdot \left(1 + \frac{\arctan\left(\frac{V_g - \frac{E_g}{2q} - V_{ds}}{\alpha}\right) - \arctan\left(\frac{V_g - \frac{E_g}{2q}}{\alpha}\right)}{\frac{V_{ds}}{\alpha}} \right) & \text{if } V_{ds} < V_g - \frac{E_g}{2q} \\ G_0 \left(V_g - \frac{E_g}{2q} \right) \left(1 - \frac{\arctan\left(\frac{V_g - \frac{E_g}{2q}}{\alpha}\right)}{\frac{V_g - \frac{E_g}{2q}}{\alpha}} \right) & \text{else} \end{cases} \quad [\text{A}] \quad (2.64)$$

where the tube potential is hypothesized to follow the gate voltage with an offset of half the bandgap, according to equation (2.49) and $\alpha = \frac{8q}{3\pi d C'_e} = \frac{8q \frac{E_g}{2}}{3\pi a_{cc} \gamma_0 C'_e}$. Equation (2.64) is plotted in Figure 2.29 for narrow diameter tubes ($d = 1\text{nm}$), which provide the highest oscillation amplitudes, as it had been shown by Figure 2.11b.

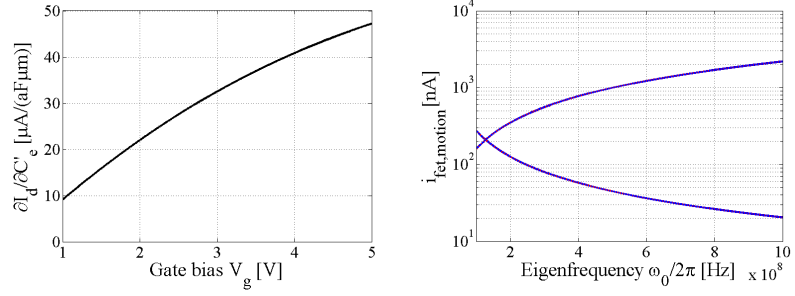
It is observed that drain and gate bias voltages in the 0V to 5V range respect the saturation limits imposed by optical phonon scattering, which means that equation (2.64) provides a valid analytical expression of the drain current within this voltage range for narrow tubes. Differentiation of the saturated equation (2.64) with respect to the gate voltage (V_g), the gate to tube capacitance (C'_e) and the bandgap (E_g) will respectively lead to the electrical field effect, mechanical field effect and the piezoresistive current modulations.

Saturation regime

The motion of the CNT in the potential field modulates the current flowing through it as

Motional field effect

Figure 2.30: (left) Motional transconductance in saturation regime as a function of the gate bias. (right) Motional Field effect current for half (red) and full (blue) actuation. Both curves overlap. (hyp. $Q=100$)



follows

$$\begin{aligned}
 \tilde{i}'_{\text{fet,motion}} &= \frac{\partial I_d}{\partial C'_e} \left[\frac{\mu\text{A}}{\text{aF}/\mu\text{m}} \right] \cdot \frac{\partial C'_e}{\partial \tilde{y}} \left[\frac{\text{aF}/\mu\text{m}}{\mu\text{m}} \right] \cdot H_{\tilde{v} \rightarrow \tilde{y}} (\tilde{v} \cdot \sin(\omega t)) \quad [\text{nA}] \\
 &= G_0 \cdot \frac{\alpha}{C'_e} \cdot \left(\arctan \left(\frac{V_g - \frac{E_g}{2q}}{\alpha} \right) - \frac{\left(\frac{V_g - \frac{E_g}{2q}}{\alpha} \right)^2}{1 + \left(\frac{V_g - \frac{E_g}{2q}}{\alpha} \right)^2} \right) \cdot \frac{\partial C'_e}{\partial \tilde{y}} \cdot H_{\tilde{v} \rightarrow \tilde{y}} (\tilde{v} \cdot \sin(\omega t)) \\
 &= \begin{cases} 10^{22.4} \cdot Q \cdot \omega_0^{-2.28} \cdot \tilde{v}^2 \cdot \sin(\omega_0 t + 0) & \text{if } \omega = \frac{\omega_0}{2} \\ 10^{23.4} \cdot Q \cdot \omega_0^{-2.28} \cdot \tilde{v} \cdot \sin(\omega_0 t + \frac{\pi}{2}) & \text{if } \omega = \omega_0 \end{cases} \quad (2.65)
 \end{aligned}$$

where $\frac{\partial C'_e}{\partial \tilde{y}} = 6 \frac{\text{aF}/\mu\text{m}}{\mu\text{m}}$ according to equation (2.47), $C'_e = 10 \frac{\text{aF}}{\mu\text{m}}$ by equation (2.46) and a DC bias of $\tilde{V} = 2\text{V}$ has been used, in consistency with previous equations. The mechanical transconductance is plotted in Figure 2.30 and $\frac{\partial I_d}{\partial C'_e} \Big|_{V_g=2\text{V}} = 22 \frac{\mu\text{A}}{\text{aF}/\mu\text{m}}$ is used for the numerical evaluation in equation (2.65). The motional field effect current modulation is plotted in Figure 2.30 within the linear limits of equations (2.55) and (2.56) and reveals current modulations of ten to hundred nanoamperes at the thermomechanical noise limit. These values are considerably stronger than the capacitive modulation presented in Figure 2.27. This fact justifies section 2.1's claim that doubly-clamped NEMS architectures shall be preferred to cantilever beams, which exhibit solely the capacitive effect, when signal strength is of importance.

Electrical field effect Among the attending ills of the motional field effect current modulation, is the electrical field effect, which modulates the current through the CNT via the gate potential, in a way that does not depend on motion and that is also observed in non-suspended CNTs. The related current modulation is obtained by differentiation of equation (2.64) with respect to the gate voltage

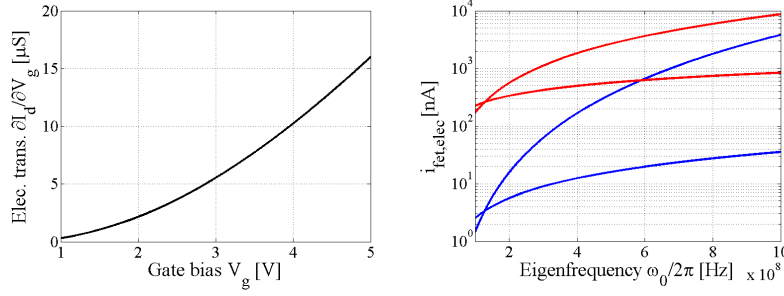


Figure 2.31: (left) Electrical transconductance in saturation regime as a function of the gate bias. (right) Electrical Field effect current for half (red) and full (blue) actuation.

V_g .

$$\begin{aligned}
 \tilde{i}'_{\text{fet,elec}} &= \frac{\partial I_d}{\partial V_g} \left[\frac{\text{A}}{\text{V}} \right] \cdot \delta V_g [\text{V}] \cdot 10^9 && [\text{nA}] \\
 &= 10^9 \cdot G_0 \cdot \left(\frac{\left(\frac{V_g - E_g}{\alpha} \right)^2}{1 + \left(\frac{V_g - E_g}{\alpha} \right)^2} \right) \cdot \tilde{v} \cdot \sin(\omega t) \\
 &= \begin{cases} 10^{3.3} \cdot \tilde{v} \cdot \sin\left(\frac{\omega_0}{2} t + 0\right) & \text{if } \omega = \frac{\omega_0}{2} \\ 10^{3.3} \cdot \tilde{v} \cdot \sin(\omega_0 t + 0) & \text{if } \omega = \omega_0 \end{cases} && (2.66)
 \end{aligned}$$

The electrical transconductance $\frac{\partial I_d}{\partial V_g}$ is plotted in Figure 2.31 for narrow SNWTs ($d = 1\text{nm}$) and is found to be on the order of micro-Siemens. The numerical values of equation (2.66) suppose a DC bias $\bar{V} = 2\text{V}$ so to be coherent with all previous expressions. The obtained transconductance $\left. \frac{\partial I_d}{\partial V_g} \right|_{V_g=2\text{V}} = 2.16\mu\text{S}$ is in accord with the values that have been reported in literature. [58] observed for example frequency independent transconductances of $1.5\mu\text{S}$ and $12\mu\text{S}$ in long and short tubes respectively. The electrical field effect current modulation is presented for half and full frequency actuation, within the linear dynamic range, bounded by equations (2.55) and (2.56) and drawn in Figure 2.26a.

2.3.3 Piezoresistive effect



A third and last transduction principle roots in the CNTs' piezoresistive property. Tensional or rotational strains have indeed an important impact on the SWNT's Brillouine zone, band structure, density of states and electrical transport properties in general.

When oscillating, SWNTs repeatedly elongate with respect to their rest position. This elongation, called strain and denoted ϵ , is zero at rest and symmetrical with respect to either upswing, towards the gate or away from it. Consequently any signal, modulated by the piezoresistive effect, will occur at twice the oscillation frequency, as is stipulated by the actuation transfer functions (2.57) and (2.58). By its construction, shown in Figure 2.18, oscillation of the CNT strains the graphene sheet along its translational T axis by a factor $(1 + \epsilon)$, and Poisson's ratio ν caters for contraction along the perpendicular circumferential C axis by a factor $(1 - \epsilon\nu)$. Intuition

To get a feeling of how this strain physically impacts the transport properties, it is worth to briefly fade in the graphene and CNT Brillouine zones, shown in Figure 2.19, 2.20 and 2.21. The resulting deformation of the graphene lattice entails a reshaping of its Brillouine zone. Most importantly do the Fermi K -points outlive strain in the lattice [64], but those points are shifted with respect to their unstrained position. In addition to the Brillouine zone reshaping, come the slightly modified boundary conditions (see equation (2.34)) due to the contracted CNT circumference and diameter, which translate into an increased spacing between the \mathbf{k}_\perp vectors. The joint combination of these phenomena results in a relative shift between the CNT dispersion relation and the graphene Fermi points, leading to a change in the bandgap and modified transport properties.

Strained bandgap Expressed more formally, applied strain changes the distance between neighbouring carbon atoms, the six-fold symmetry breaks down, and the hopping integral γ_0 between first neighbours becomes dependent on directionality and is to be reevaluated by Harrison's formula [65]. Recalculating the dispersion relation of graphene with the new overlap energies, by eigenvalue $E(k)$ extraction of the π -orbital Hamiltonian, and finding the intersection with the modified wrap-up boundary conditions, finally leads to the expression of the change of the bandgap [66]

$$\Delta E_g(\epsilon) = \text{sgn}(2(n-m)_{\text{mod}3} + 1) \cdot 3\gamma_0 \cdot ((1+\nu)\epsilon \cdot \cos(3\theta)) \quad [\text{eV}] \quad (2.67)$$

Equation (2.67) shows that the piezoresistive modulation is positive, negative or absent for respectively one third of the tubes. The effect is maximal when the chiral angle $\theta = \widehat{\mathbf{a}_1; \mathbf{C}} = 0^\circ$.

Metallic tubes So it happens that strain opens a bandgap in metallic zigzag $(3 \cdot \mathbb{N}, 0)$ SWNTs, for which $\text{sgn}(2(n-m)_{\text{mod}3} + 1) = +1$ and $\theta = 0^\circ$. Motion of these tubes can hence be sensed by the piezoresistive property, although the motional field effect would not inform about their oscillation. The situation is unfortunately different for metallic armchair (n, n) SWNTs, for which $\theta = \frac{\pi}{6}$, and no bandgap opens. These metallic armchair CNTs remain consequently the only ones for which no motion detection other than capacitive, is possible.

Bandgap sensitivity Equation (2.67) predicts a maximal bandgap sensitivity of $\frac{\partial E_g}{\partial \epsilon} = 97.2 \frac{\text{meV}}{\%}$ for a Poisson ratio of $\nu = 0.2$ [67]. The model of equation (2.67) is based on the Cauchy-Born rule, which assumes that the atomic movements under strain follow a homogeneous deformation, not taking into account sub-lattice relaxation. Considering the exact movement of the atoms of the two graphene sub-lattices, leads to a multiplicative correction factor of 0.57 for equation (2.67), which then peaks at $\frac{\partial E_g}{\partial \epsilon} = 55 \frac{\text{meV}}{\%}$ [68] [69]. *Ab initio* calculations lead to $\frac{\partial E_g}{\partial \epsilon} = 115 \frac{\text{meV}}{\%}$ [70]. It may be concluded that, although the exact magnitude of the bandgap sensitivity to strain is still under discussion, equation (2.67) provides a good estimate. Apart from the sign, the average bandgap sensitivity of the two thirds of the nanotubes for which equation (2.67) does not yield zero, is found by averaging over theta and is

$$\frac{\partial E_g}{\partial \epsilon} = \frac{3}{\sqrt{2}} \gamma_0 (1+\nu) \approx 69 \quad \left[\frac{\text{meV}}{\%} \right] \quad (2.68)$$

2.3. Decrypting the NEMS Response

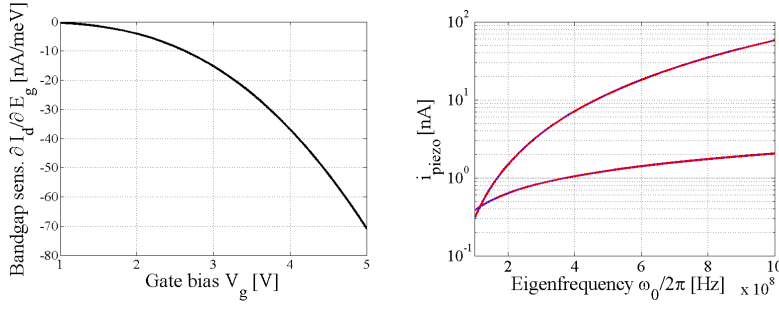


Figure 2.32: (left) Piezoresistive transconductance in saturation regime as a function of the gate bias. (right) Piezoresistive current for half (red) and full (blue) actuation. Both curves overlap.

This average bandgap sensitivity will subsequently be used when evaluating the piezoresistive current modulation

Piezoresistive effect

$$\begin{aligned}
 \tilde{i}_{\text{piezo}} &= \frac{\partial I_d}{\partial E_g} \left[\frac{\text{nA}}{\text{meV}} \right] \cdot \frac{\partial E_g}{\partial \epsilon} \left[\frac{\text{meV}}{\%} \right] \cdot H_{\tilde{v} \rightarrow \epsilon} (\tilde{v} \cdot \sin(\omega t)) [\%] && [nA] \\
 &= \frac{G_0}{2q} \cdot \left(-1 + \frac{1}{\frac{E_g}{2q}} \cdot \left(\frac{V_g}{1 + \left(\frac{V_g - \frac{E_g}{2q}}{\alpha} \right)^2} - \alpha \cdot \arctan \left(\frac{V_g - \frac{E_g}{2q}}{\alpha} \right) \right) \right) \\
 &= \begin{cases} \pm 10^{9.65} \cdot Q \cdot \omega_0^{-1.14} \cdot \tilde{v}^2 \cdot \sin \left(2\omega_0 t - \frac{\pi}{2} \right) & \text{if } \omega = \frac{\omega_0}{2} \\ \pm 10^{10.65} \cdot Q \cdot \omega_0^{-1.14} \cdot \tilde{v} \cdot \sin \left(2\omega_0 t + \frac{\pi}{2} \right) & \text{if } \omega = \omega_0 \end{cases} && (2.69)
 \end{aligned}$$

where $\alpha = \frac{8q^2 E_g}{3\pi a_{cc} \gamma_0 C_e}$ is a function of the bandgap. $\partial_\epsilon E_g = 69 \frac{\text{meV}}{\%}$ according to equation (2.68) and a DC bias $V = 2\text{V}$ has been chosen for consistency. The piezoresistive transconductance $\frac{\partial I_d}{\partial E_g}$ is plotted in Figure 2.32 for narrow SWNTs ($d = 1\text{nm}$) and $\frac{\partial I_d}{\partial E_g} \Big|_{V_g=2\text{V}} = 4.1 \frac{\text{nA}}{\text{meV}}$ is used for the numerical evaluation in equation (2.69). The piezoresistive current modulation is plotted in Figure 2.32 within the linear limit of equations (2.57) and (2.58) and reveals current modulations of several nanoamperes at the thermomechanical noise limit. These values range between the ones of the capacitive (see Figure 2.27) and field (see Figure 2.30) effects. This makes the piezoresistive effect a nice backup plan for motional sensing of zigzag SWNTs, which exhibit no field effect current modulation.

2.3.4 A brief comment on contacts and sensing



The previous results assumed perfect ohmic contacts at the source-tube and drain-tube interfaces, and focused on careful choice of optimal SWNT parameters to obtain strong signals. It is therefore worth to briefly address the impacts of Schottky contacts and assess the likelihood of this to happen. The Schottky or ohmic nature of the contacts is greatly determined by the contact material. Due to the unique 1D structure and a quasi 0D interface of SWNTs, the interface states are not strong enough to pin the Fermi level [10]. The height of the Schottky barrier at the metal-CNT interface therefore depends strongly on the metal work function. Desired ohmic contacts for high device performance can be achieved among others

Ohmic and Schottky contacts

for aluminum (Al), palladium (Pd) and gold (Au) contacts [71]. Smaller bandgaps favour the formation of ohmic contacts for at least one type of carrier. In accord with equation (2.50), a clear diameter and Schottky-barrier height dependence of the apparent on-state resistance was demonstrated [11]. SWNT diameters well below 1nm have bandgaps that approach 1eV, making the formation of Schottky barriers at the interface more likely and boosting the apparent SWNT resistance to MΩ values [8].

Enforcing ohmic contacts Except for circuit designers who are on the quest of Schottky transistors, ohmic contacts are preferred in NEMS applications, where the signal strength shall maximally depend on the CNT (and its motion) rather than on the interface. The CNT-metal contact barrier is well described by [72]

$$\phi_b = \chi_m - \chi_{\text{CNT}} \quad [\text{eV}] \quad (2.70)$$

where ϕ_b is the Schottky barrier height, $\chi_{\text{CNT}} \approx 4.5\text{eV}$ [73] is the CNT midgap distance to the vacuum level and χ_m is the metal work function. Considering that the bandgap of the here considered tubes ($d \in [1\text{nm}; 5\text{nm}]$) is below 0.77eV, by equation (2.50), ohmic contacts are formed for electrons by aluminum ($\chi_{\text{Al}} = 4.1\text{eV}$) [74] and for holes by gold ($\chi_{\text{Au}} = 5.5\text{eV}$) [75] and palladium ($\chi_{\text{Pd}} = 5.1\text{eV}$) [71] source and drain metals. So ohmic contacts to CNTs can be achieved and the previous findings remain valid or may require a trivial sign inversion for p-type CNTs contacted by gold or palladium.

Impact of chemi- & physi-sorption Further did the previous investigations study pristine CNT-NEMS resonators in a controlled microbiotop. But when it comes to sensor operation, the CNTs are to interact with their environment. In this context, chapter 4 treats inertial mass sensing, which is based on the physical property that the NEMS eigenfrequency shifts under mass loading. Binding of a molecule to the CNT, either directly or via a functionalized group, however, may also induce a change in the CNT's electrochemical properties. Functionalization of CNTs with methyl (-CH_n), amine (-NH_n), carboxyl (-COOH) or hydroxyl (-OH) groups is for instance found to cause local sp^2 to sp^3 rehybridization, induce pentagon/heptagon defects into the hexagonal CNT lattice, or introduce impurity bands, which reduce the effective bandgap [76]. Chemisorption of hydrogen atoms is found to induce states within the bandgap with a spatial extension on the order of a few nanometers only, meaning that local tube functionalization or pollution may only have minor impacts on the global CNT conductance [46]. Oxygenic (O₂) environments dope CNTs p-type, while ammonia (NH₃) tends to dope them n-type [77]. The study of such phenomena lies nevertheless outside the scope of this thesis. I here settle by pointing out that these electrical interactions exist and merit some attention when sensors are designed, based on the here presented findings.

2.4 CNT-NEMS Resonators in a Nutshell



Survey The present chapter provided a systematic study of the electromechanical transduction properties of carbon nanotube resonators and condenses in a compact summary of their

sensing properties and related orders of magnitude [78]. The subsequently summarized figures of merit provide an all-you-need-to-know digest of CNT resonators for circuit and system designers and form the cornerstone for electronic interface design. Explanations on the *why* and *how* can be retrieved by recursing through the chapter. The antecedent attention to detail now pays off in an unprecedented systematic categorization of the components in the CNT-NEMS spectrum, which is of primordial importance for readout design.

Suspended CNT resonators are shown to behave as driven damped harmonic oscillators. This conclusion derives from the analysis of Euler-Bernoulli and von Kármán continuum beam models, which simultaneously provide upper- and lower bounds on the validity of this model simplification. The thermomechanical noise has been quantified and forms the lower limit of the linear dynamic range of CNT resonators. The upper range limit comes at the onset of the cubic nonlinearity, leading to a hysteretic CNT transfer function, inappropriate for controllable closed-loop topologies. Within these limits, pull-in is excluded to occur. A glimpse was given at interesting frequency tuning options by amplitude control in the nonlinear Duffing regime, but those were not retained as a robust approach towards oscillator design.

Harmonic oscillator

Least effort maximum oscillation amplitude has been found by optimisation of the choice of tube length, diameter and prestrain, under the constraints of today's technological limits, and an optimal CNT design strategy resulted. Nanometer thin tubes are a good choice in applications ranging from 100MHz to 1GHz, while optimal tube length and prestrain are correlated to the desired operation frequency, as shown in Figure 2.11.

Optimal CNT design

An analytical expression of the maximal transduction gain, achieved for optimal CNT design, is established by interpolation. Findings from solid state physics, translate the mechanical signal back into an electrical one by capacitive-, field- and piezoresistive effects. All three effects modulate the current flowing through the tube, but at various frequencies and different phase delays. This frequency and phase multiplexity is the key to efficient interface design.

Maximal transduction gain

Two actuation strategies, one at half $\omega_{\text{gate}} = \frac{\omega_0}{2}$, the other at full $\omega_{\text{gate}} = \omega_0$ eigenfrequency, crystallized as good ways to operate the CNT as a NEMS. For both strategies, the precise strength of the signals depends on the exact bias and actuation voltages. The chapter provides all necessary equations to compute those values for custom actuation schemes. Here we conclude on the values for mid-range biases ($V_g = 2\text{V}$, $V_{ds} = 1\text{V}$, $I_d = 1\mu\text{A}$), actuation voltages above, but close to the thermomechanical noise limit (equations (2.55), (2.56), (2.57) and (2.58), shown in Figure 2.26c) and hypothesize proper CNT selection, with room-temperature quality factor $Q = 100$, diameter, length and prestrain according to Figure 2.11 and ohmic contacts.

Two actuation strategies

The components to the CNT output spectrum for an $\omega_{\text{gate}} = \omega_0$ actuation scheme are summarized in Figure 2.33, categorized by their frequency ($\frac{\omega_0}{2}$ (left), ω_0 (middle), $2\omega_0$ (right)), and their phase-delay with respect to the actuation signal (in-phase (—), orthogonal (- - -)). First of all, it is noted that the motional field effect (magenta, equation (2.65)) is the overall strongest component and its $\sim 100\text{nA}$ amplitude shall be measurable rather straightforwardly.

CNT spectrum for $\omega_{\text{gate}} = \omega_0$

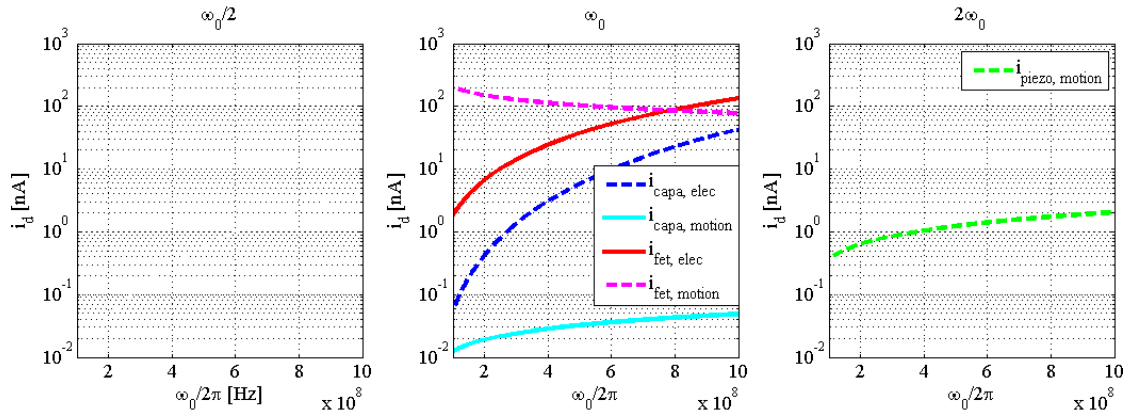


Figure 2.33: CNT output spectrum for $\omega_{\text{gate}} = \omega_0$

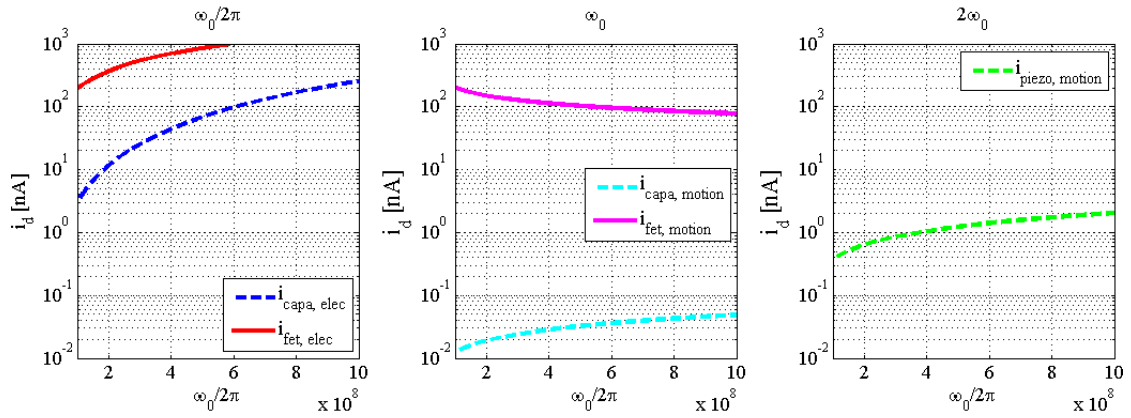


Figure 2.34: CNT output spectrum for $\omega_{\text{gate}} = \frac{\omega_0}{2}$

At GHz frequencies, the electrical field effect (red, equation (2.66)) draws level with its motional counterpart. Both signals occur at ω_0 , but exhibit different shifts in phase, making them distinguishable, as we shall shortly see in chapter 3. The weaker motional capacitive (cyan, equation (2.60)) and electrical capacitive (blue, equation (2.62)) components are unobservable, as they are overshadowed by the equal-frequency equal-phase field-effect components respectively. Out on a limb is the nA-strong purely motional piezoresistive component, which becomes observable by filtering out all other stronger components.

CNT spectrum for $\omega_{\text{gate}} = \frac{\omega_0}{2}$ To maintain an identical motional signal strength under a half frequency actuation scheme, larger driving voltages are necessary. These imply stronger electrical effects, as can be observed from the amplification of the electrical field (red, equation (2.66)) and capacitive (blue, equation (2.62)) components. As a reward, these components now appear at half the oscillation frequency, conferring unique frequency and phase-delay properties to the three motional components, now all observable. A caveat for this actuation strategy is the impressively strong electrical field effect component, caused by the necessary driving voltages of hundreds of millivolts and up to volts (see Figure 2.26c), which may turn off the transistor. While things are

fine around 100MHz, this actuation scheme requires larger ($V_g > 2V$, $I_d \approx 25\mu A$) device bias in order to extend towards GHz.

The above findings are beneficial both to physical CNT-NEMS characterization, as well as to sensor interface design. Knowledge on the frequency and phase occurrence of each component allows to deterministically characterize the strength of the respective effects and convey an experimental validation of the here presented theory. Thitherto the theoretically extracted optimal signal strength shall serve as the golden reference for electronic circuit design. Utility

To date these component strengths, frequencies and delays, have not yet been evidenced experimentally. This is partially due, on the one hand, to the fact that the here reported signal strength is intimately linked to an optimal CNT-NEMS design, as reported by Figure 2.11, and on the other hand, that today's experiments are still rather concerned about proofs of concept, than about their optimisation. Readout is performed through mixing topologies, which happen to filter the capacitive component rather than the field effect [1] [2]. Theoretical explanations widely ignore the field- and piezoresistive effect contributions and boil all explanations down to the capacitive effect. I would be grateful to one of the few privileged research groups around the globe, with sound know-how in CNT-NEMS design, to follow the here indicated tracks and possibly unearth the truth of the presented theoretical findings. State-of-the-art

*To reach the possible,
one must strive for the impossible.*

— Hermann Hesse

3

Electrical Detection of Mechanical Motion in Carbon Nanotubes

Midway between NEMS devices and electronic systems, the present chapter focuses on the design of the front-end interface block. The quality of the NEMS to circuit interface has a decisive impact on the potential and benefits of NEMS as voltage controlled oscillators or electromechanical sensors. The strategic decision on which type of front-end is optimal, is equally impacted by the signals that may be expected out of the NEMS, studied in chapter 2, and the needs of the applications that are given consideration, presented in chapter 1 and investigated in chapter 4. Front-end

A myriad of electronic techniques, to detect the CNT's mechanical motion, has been proposed. Some rely on cryogenic temperature phenomena, others support room-temperature operation. Some keep the motional information at its original frequency, others shift it to lower bands. The spectrum of options is large, and the most popular techniques of today are not good enough for the target applications of tomorrow. This situation partially results from the ignorance of the full survey of CNT-NEMS signals, the ligation on 50Ω lab equipment and RF components, and a certain myopia with respect to future applications. It is true that, operating the NEMS as a mixer, considerably simplifies the interface design and still allows to prove NEMS motion and investigate physical phenomena. Contenting oneself with this approach, nevertheless, leaves unnoticed the opportunities for high-speed sensing and observation of further physical phenomena. A direct readout scheme has not yet been successfully applied for measuring CNT motion, but for graphene [17] and nanowire [18] resonators, it has. Rationale

The mission of the front-end is described in section 3.1. Then, following the categorization and quantification of the electromechanical signals produced by carbon nanotube NEMS, Overview

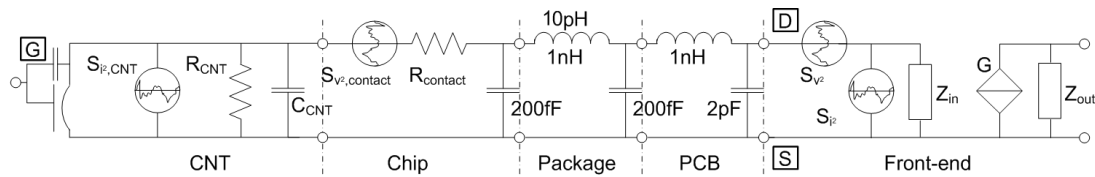


Figure 3.1: Small signal equivalent circuit from CNT-NEMS to front-end

section 3.2 highlights the most important facts and figures in terms of signal strength and frequency. In section 3.3, the use of CNT-NEMS as mixers is then briefly reviewed and discussed. The meticulous CNT-NEMS analysis of chapter 2 leads in section 3.3.2 to the discovery of novel mixing schemes, which allow to separately assess in practice the strength of the motional and electrical capacitive, field effect and piezoresistive phenomena in CNT-NEMS. A convenient characterization technique for molecular adsorbate configurations crystallizes as a corollary of the simultaneous observation of electrical and motional phenomena. Section 3.4 is devoted to the more ambitious high-frequency direct readout, which opens the gate to NEMS oscillator and high-speed high-resolution sensing applications. Different bipolar and metal oxide semiconductor transistor front-end amplifiers are analysed in terms of noise figure and minimal filter selectivity is briefly discussed. The theoretical development is illustrated by two sample front-end implementations in section 3.5. The chapter closes on a summary of the achievable signal to noise and signal to background ratios.

Novelty

3.1 The Front-end's Mission



Interface parasitics

The front-end is an active gain stage, interfacing the CNT-NEMS through some interconnect parasitics, as illustrated by Figure 3.1. Biased to saturation, the NEMS itself may be seen as a noisy current source with an RC output impedance. The resistance is on the order of megaohms and the capacitance is sub-femtofarad, leading to a trans-gigahertz cut-off. The contact resistance, between the CNT and the electrodes, is limited downwards by the quantum resistance of $6.5\text{k}\Omega$, and will not exceed tens of kilohms for proper metal choice. If the NEMS is packaged, wire bonding (1mm) and bonding pads caters for $0.1\Omega - 1\text{nH} - 1\text{pF}$ RLC parasitics, and if TSVs ($100\mu\text{m}$) are used, those parasitics reduce to $0.1\Omega - 10\text{pH} - 100\text{fF}$ [9]. The resistance is negligible, compared to the contact resistance, and has been omitted in Figure 3.1. So is the inductance for frequencies up to several gigahertz. Remains the capacitance, which forms a shunt of a few kilohms at gigahertz frequencies and may drain the CNT-NEMS signal before this one reaches the front-end.

Low noise

First and foremost, must the front-end deliver, at its output, a signal that still contains the motional information. Hence the noise, added by the electrical components, shall be minimal. A filter may be necessary to limit the noise bandwidth. But the price of such a solution might be high, because selective filtering would restrict the tunability bandwidth in electromechanical VCO applications and reduce the sensing range. Further do self-adjusting closed-loops lock on the characteristics of the most frequency sensitive component, which shall be the CNT-NEMS.

A too selective high-Q filter could take over this role, and cause complete loss of the system's environmental sensitivity.

The feeble signal out of the CNT-NEMS must be amplified, before standard circuit blocks may process it. Most critical in the amplification chain, is the very first stage, as it largely decides on the circuit's overall noise performance, as can be seen from Friis' formula for the noise factor of a cascade of stages,

Signal amplification

$$F_{total} = F_1 + \sum_{i=2}^n \frac{F_i - 1}{\prod_{j=1}^{i-1} G_j} \quad (3.1)$$

F_i is the noise factor of stage i and G_i the power gain of that same stage. The first stage's noise contributes entirely to the overall system noise, while the noise contribution of subsequent stages is divided by the cumulative gain up to that stage. A low-noise high-gain first stage forms consequently the ideal case.

Depending on the application, some of the motional information may be sacrificed, especially if it is difficult to obtain the piece of information in question without encasing therefore a weaker or noisier signal. The study of low-frequency physical phenomena, or the proof of resonance, can be extracted at lower frequency by operating the CNT as a mixer. If on the other hand, the plan is to couple the NEMS output signal directly back onto its input, for self-adjusting closed-loop oscillation for instance, then the information on phase delay is crucial, and the signal must absolutely be kept at its original frequency. Only direct readout allows to do so.

Information conservation

The interconnect parasitics, information loss, and signal degradation, render the design of the front-end a decisive step along the road towards applications. Mixer operation of the NEMS demodulates the signal towards lower frequencies and hence trades information loss for signal purity, while direct readout saves all information, but may suffer signal attenuation and is more sensible to noise. Both approaches have merit and shall be examined subsequently. While signal strength can be recovered by amplification, information loss is irremediable, which means that efforts towards direct readout are worthwhile.

Decisive step

3.2 CNT-NEMS Sensor in a Nutshell



A short factual summary of properties and associated orders of magnitude of suspended carbon nanotube NEMS, relevant at circuit-level, is given first. These values find their justification in chapter 2 and serve as reference for the assessment of the readout topologies.

Based on chapter 2

The dynamics of suspended carbon nanotube resonators may be described by a damped harmonic oscillator, if operated within their linear dynamic range, limited downwards by thermomechanical fluctuations and upwards by Duffing-type spring stiffening. CNTs exhibit tunable eigenfrequencies from tens of MHz to low GHz. Their ambient temperature quality

CNT dynamics

factors are rather low, on the scale of 100.

Actuation CNT-NEMS are actuated by application of a sinusoidal voltage on the nearby gate electrode. The suggested amplitude of the signal is strongly correlated to the actuation strategy. Either a full-frequency actuation may be chosen, with the gate frequency equal the eigenfrequency ($\omega_g = \omega_0$) and amplitudes of tens of mV, or a half-frequency actuation can be applied, with $\omega_g = \frac{\omega_0}{2}$ and amplitudes of hundreds of mV. The exact amplitude linear range depends on the frequency and can be looked up in Figure 2.26.

Bias regime CNTs may be biased to the linear regime or towards saturation, reached for several hundreds of millivolt source-drain bias. Maximal mechano-electrical transduction gain is obtained in the saturation regime, and it is highly advisable to operate CNTs in this regime, where they act as current sources of several microamperes DC, and megaohm differential output impedance, up to the gigahertz. Larger DC gate bias enhances the current flow, but values in the realm of integrated technologies are sufficient.

Detection Upon oscillation, several spectral components modulate the current through the CNT. These components result from capacitive (capa), field effect (fet) and piezoresistive (piezo) phenomena and are of various strengths, frequencies and phases, as a function of the eigenfrequency and the actuation strategy.

Capacitive: Tube motion and gate voltage variation modulate the static charge on the CNT. The related charge flow can be measured at the source and drain terminals in form of a current flowing into and out of the tube.

Field effect: The tube potential changes under the influence of the tube motion and gate voltage variation, which cause a repopulation of the electronic states and a change in tube conductance (at constant state density) and modulate the current flow through the tube.

Piezoresistive effect: Tube oscillation and elongation modifies the density of available states. This results in a modification of the tube conductance (at constant tube potential) and hence a change in the current flow through the tube.

All contributions are summarized by Table 3.1 for CNT-NEMS with eigenfrequencies around 100MHz and by Table 3.2 for eigenfrequencies approaching the GHz. Entries are rounded conservatively and a more general picture may be retrieved in Figure 2.33 and 2.34. It is noteworthy to remember that these values are the result of a CNT-NEMS design optimisation procedure, and represent an upper bound on signal strength. This upper bound can be achieved in practice for CNT-NEMS design following the instructions of Figure 2.11.

Strength, frequency & phase A look at Table 3.1, reveals that at 100MHz, CNT motion shall be directly observable through the motional field effect, which outreaches all other components by two orders of magnitude in a full-frequency actuation scheme. This 100nA signal strength is still to be assessed against the

3.2. CNT-NEMS Sensor in a Nutshell

		$\omega_g = \omega_0$			$\omega_g = \frac{\omega_0}{2}$			
Effect	—	Strength	Frequency	Phase	—	Strength	Frequency	Phase
fet	motion	10^2 nA	ω_0	$\frac{\pi}{2}$	—	10^2 nA	ω_0	0
fet	elec	10^0 nA	ω_0	0	—	10^2 nA	$\frac{\omega_0}{2}$	0
piezo	motion	10^0 nA	$2\omega_0$	$\frac{\pi}{2}$	—	10^0 nA	$2\omega_0$	$-\frac{\pi}{2}$
capa	elec	10^{-1} nA	ω_0	$\frac{\pi}{2}$	—	10^1 nA	$\frac{\omega_0}{2}$	$\frac{\pi}{2}$
capa	motion	10^{-2} nA	ω_0	π	—	10^{-2} nA	ω_0	$\frac{\pi}{2}$

Table 3.1: @ $\omega_0 = 100$ MHz: Strength, frequency and phase of the current modulation through the nanotube, at resonance, in the linear dynamic range and for optimal CNT design. All values are based on chapter 2 with its summarizing Figure 2.33 and 2.34, and drive voltages of Figure 2.26, larger for the $\omega_g = \frac{\omega_0}{2}$ scenario.

		$\omega_g = \omega_0$			$\omega_g = \frac{\omega_0}{2}$			
Effect	—	Strength	Frequency	Phase	—	Strength	Frequency	Phase
fet	motion	10^2 nA	ω_0	$\frac{\pi}{2}$	—	n/a	n/a	n/a
fet	elec	10^2 nA	ω_0	0	—	n/a	n/a	n/a
piezo	motion	10^0 nA	$2\omega_0$	$\frac{\pi}{2}$	—	n/a	n/a	n/a
capa	elec	10^2 nA	ω_0	$\frac{\pi}{2}$	—	n/a	n/a	n/a
capa	motion	10^{-1} nA	ω_0	π	—	n/a	n/a	n/a

Table 3.2: @ $\omega_0 = 1$ GHz: Strength, frequency and phase of the current modulation through the nanotube, at resonance, in the linear dynamic range and for optimal CNT design. All values are based on chapter 2 with its summarizing Figure 2.33 and 2.34, and drive voltages of Figure 2.26, larger for the $\omega_g = \frac{\omega_0}{2}$ scenario.

circuit noise. A half-frequency actuation scheme is detrimental, as the motional component is then on a par with the purely electrical contribution. Both signals remain nevertheless distinguishable, as they appear at different frequencies, and filtering may help. The same holds for the nanoampere piezoresistive effect, which appears at twice the resonance frequency. At gigahertz frequencies, the half-frequency actuation scheme fails, because it requires a too strong gate actuation, which entails an overwhelming electrical field effect, switching the CNT entirely from on to off state and making the mechanical components unobservable for part of the time. According to Table 3.2, the options for motion observation are then either to filter out the higher frequency piezoresistive component, or to eliminate the electrical field effect by mixing, and to hope that the motional field effect remains stronger than the electrical capacitive effect. We stop the overview of possibilities for now and will systematically explore all options in the coming sections.

Some statistics Before doing so, it is instructive to recall that not all listed effects appear in each and every nanotube. The presence and strength of the effects depends indeed on the CNT chirality. Two thirds of the CNTs are semiconducting, while one third is metallic. Only semiconducting CNTs exhibit the electrical and mechanical field effects. Metallic CNTs split equally into zigzag or armchair chirality. Zigzag CNTs present maximal piezoresistive current modulation, while this feature is not present at all in armchair tubes. This leaves us with a situation, where $2/3^{\text{rd}}$ of the tubes can be probed with the strong field effect, another $1/6^{\text{th}}$ with the moderate piezoresistive effect, and a final $1/6^{\text{th}}$ of the tubes solely leaves the weak capacitive sensing option.

3.3 The Dementia and Latency of Mixers



Why mixing? A way to circumvent the problems of high-frequency readout, is to operate the CNT-NEMS as a mixer, and extract information at a lower frequency. Although instantaneous information about the NEMS is lost, mixing still allows to locate the eigenfrequency spectrally by its lorentzian peak, and hence analyse some physical properties. One may, for example, detect that the NEMS is currently oscillating at its eigenfrequency, while having no clue about the exact instantaneous NEMS position (phase). Such phase information becomes of interest when closing a direct feedback loop around the NEMS and requires a direct readout scheme. No such scheme has been practically reported yet, which leaves mixing schemes the only viable solution today, and they merit further attention.

In this section This section contributes by enhancing the knowledge on CNT-NEMS signals when it comes to readout. A quick review of the different mixing schemes, reported in literature, will be followed by their systematic categorization, and the proposal of a novel mixing scheme concludes the section.

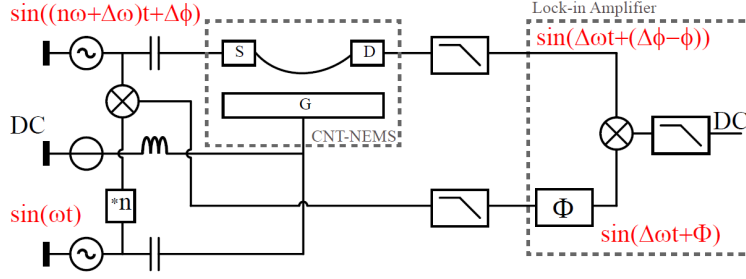


Figure 3.2: CNT-NEMS operated as a mixer. The low-frequency signal $\Delta\omega$ seamlessly flows through the lowpass filter formed by the CNT-NEMS contact impedance and the track capacitance. It peaks in amplitude and inflects in phase when $\omega \in \{\omega_0, \frac{\omega_0}{2}\}$, where ω_0 is the NEMS eigenfrequency and $n=1$ [1], $n=2$ [2] or $n=4$ (new).

3.3.1 State-of-the-art mixing



To get to know the true promise of mixing, the current through CNTs must be made dependent on both, the gate voltage, and the drain-source bias. This requires operation in the linear regime, under low drain-source bias. For small variations of the gate voltage at frequency ω , the tube conductance G may be assumed to scale harmonically, according to Table 3.1 and 3.2, as $G = \bar{G} + \tilde{g} \cdot \sin(n\omega t + \phi)$. Applying an oscillatory signal to the source, with an n -fold frequency, offset by $\Delta\omega$ and phase $\Delta\phi$, leads to a linear regime drain current

Principles
of mixing

$$\begin{aligned} I_{\text{mix}} &= G \cdot V_{\text{ds}} & [\text{A}] \\ &= (\bar{G} + \tilde{g} \cdot \sin(n\omega t + \phi)) \cdot \tilde{v}_{\text{ds}} \cdot \sin((n\omega + \Delta\omega)t + \Delta\phi) & (3.2) \end{aligned}$$

This current presents a component at low frequency,

$$\tilde{i}_{\text{mix}} = \frac{1}{2} \cdot \tilde{g} \cdot \tilde{v}_{\text{ds}} \cdot \sin(\Delta\omega t + (\Delta\phi - \phi)) \quad [\text{A}] \quad (3.3)$$

The current modulation's proportionality to the conductance change allows to detect the resonance peak. \tilde{i}_{mix} peaks indeed at the same frequency as \tilde{g} does, which occurs at resonance. The current's dependence on the relative phase of the modulations, ϕ and $\Delta\phi$, has never been given attention so far I know. Section 3.3.2 will unveil why this information is useful though. n -fold frequency mixing has been reported for $n = 1$ [1] and $n = 2$ [2]. Section 3.3.2 shall complete this series with a novel approach for $n = 4$.

The low-frequency component of the current modulation of equation (3.3) can be isolated either by filtering, or by mixing the signal with another one, at the offset frequency $\Delta\omega$ and with phase $\Phi = \Delta\phi - \phi$, as suggested in Figure 3.2. Such an approach is very convenient, as first, it circumvents the lowpass readout challenges encountered at higher frequencies, and second, can long-term integration in the lock-in amplifier filter a large part of the off-frequency off-phase noise. This makes mixing a very selective characterization technique. On the other side of the coin, are the down-mixing to $\Delta\omega$ and the long-term integration, which are detrimental for fast retrieval of the information about resonance and disqualify such an approach for fast sensor applications. Instantaneous information about the oscillation is entirely lost, and one cannot infer the position of the tube at any time. This can be seen from equation (3.3), where

Inherent
trade-off

terms in $n\omega$ have disappeared. The implications are that mixer operation does not allow to enclose CNT-NEMS in a direct feedback loop. A final disadvantage of mixing is the feeble signal strength, which directly scales with the conductance modulation and the drain-source bias. The latter is constrained to few tens of millivolts to ensure linear regime operation, while the former finds its maximum in the saturation regime, as has been shown in chapter 2. The reported mixing currents, of tens [1] [2] to hundred [32] picoamperes, reflect consequently not maximal device performance and shall not discourage incentives towards direct readout.

Gang of mixers The setup of Figure 3.2 allowed to present the concept of mixing in a generic way, but it is far from being the only constellation. [1], [32] and [33] used it indeed with $n = 1$ to demonstrate resonance with a 10kHz offset and 100ms lock-in time. [19] holds the speed record for an offset frequency of 6MHz and 780ns lock-in time. A bit slower was the detection for [2] and [28] with a 7kHz and 9kHz offset and 300ms lock-in for the $n = 2$ technique. A frequency modulated (FM) signal, applied at the source, may replace the need for modulation of the gate signal. When the modulation frequency is smaller than the resonator's bandwidth ($\Delta\omega \ll \frac{\omega_0}{Q}$), the sidebands drive the CNT to motion. This FM mixing is praised for the absence of any electrical contribution at the lock-in frequency, but the spectral constraint is rather restrictive, and an offset frequency of 616Hz in combination with a 100ms integration, were necessary for [29] to detect resonance. [34] mixed the motional information even down to DC, by using the CNT-NEMS as a Coulomb blockade rectifier at cryogenic 20mK. A more practical DC readout consists in averaging and has been proposed by [15]. Although DC readout neatly solves the readout problems, it has to struggle with $1/f$ noise, and is inherently slow and void of phase information. For completeness, the amplitude modulation technique of [79] shall be mentioned. It used cantilever CNTs and voltages beyond availability in IC technology. This extensive survey of CNT-NEMS mixer setups underlines the popularity of mixing. The coming section adds a new entry to this listing.

3.3.2 Stepping onto the virgin soil of mixers



Categorization Despite the versatility of the proposed mixer setups, which allow to prove mechanical motion, the theoretical support of the observations is only served in piecemeal fashion. A systematic categorization of the observability of the effects may be beneficial in order to interpret the measurements. Such a classification requires information on the frequency and phase of the capacitive, field effect and piezoresistive phenomena, knowledge that has been established in chapter 2. The phase and frequency dependence of equations (2.60), (2.61), (2.62), (2.65), (2.66) and (2.69) allows to indicate in Table 3.3 which phenomena can be observed for a mixer setup with parameters n and $\Delta\phi$.

State-of-the-art revisited All $n = 1$ mixing experiments have supposedly observed the motional field effect ($\omega_g = \omega_0$, $n = 1$, $\Delta\phi = \frac{\pi}{2}$), given the reported tunability on frequency and the relative strength of the field and capacitive effects. The weaker capacitive motional effect (for $\Delta\phi = 0$) would indeed be overshadowed by the electrical field effect, which is not tunable over frequency. A side-

3.3. The Dementia and Latency of Mixers

$\omega_g = \omega_0$			$\omega_g = \frac{\omega_0}{2}$		
$\Delta\phi = 0$	$\Delta\phi = \frac{\pi}{2}$		$\Delta\phi = 0$	$\Delta\phi = \frac{\pi}{2}$	
$n = 1$	fet, elec capa, motion	fet, motion capa, elec	$n = 1$	fet, elec	capa, elec
$n = 2$	-	piezo, motion	$n = 2$	fet, motion	capa, motion
$n = 4$	-	-	$n = 4$	-	piezo, motion

Table 3.3: Observable mixing phenomena at $\Delta\omega$ for full frequency actuation (left) and half frequency actuation (right). (hyp. $\Phi = 0$)

observation of the motional field effect is the capacitive electrical effect, which is weaker only below GHz and for careful electrode design, as reported by Table 3.2. The parasitical outgrowth may consequently hinder mixer readout of the motional information for trans-GHz frequencies or poor NEMS design. This limitation justifies the use of the narrow-bandwidth and slow FM modulation mixing, which suppresses this electrical side effect. Reported $n = 2$ techniques claim to have observed the motional piezoresistive effect ($\omega_g = \omega_0$, $n = 2$, $\Delta\phi = \frac{\pi}{2}$). This is plausible, but they may just as well have observed the motional capacitive effect ($\omega_g = \frac{\omega_0}{2}$, $n = 2$, $\Delta\phi = \frac{\pi}{2}$), or even the motional field effect ($\omega_g = \frac{\omega_0}{2}$, $n = 2$, $\Delta\phi = 0$). The choice $n = 2$ makes the observability of the effects indeed not unique, and hypothesizing the wrong effect leads to a factor 2 error in the estimation of the eigenfrequency, which is ω_g if the observed effect is piezoresistive, and $2\omega_g$ if it is capacitive or field effect. This uncertainty could be resolved by checking whether another resonance peak is observed at half the driving frequency, which is the case only if the first peak was based on the piezoresistive component.

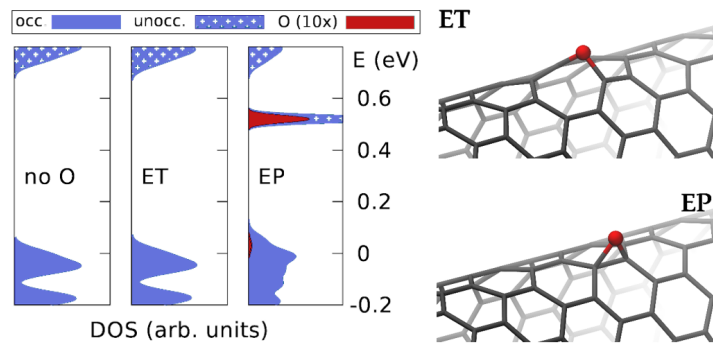
Another neat bypass is the use of a fourfold frequency factor ($n = 4$), which allows to determine the eigenfrequency uniquely via the piezoresistive effect. No purely electrical component would interfere either. This novel mixing strategy shall henceforth complete the state-of-the-art, but still requires a practical demonstration. While being just another mixer technique, this one comes with two benefits:

Novel 4ω technique

- The fourfold frequency between actuation and readout allows easier spectral signal separation in direct readout topologies.
- Once detected, all other components may be characterized uniquely. The motional capacitive and field effects occur by decreasing n to two and adding a $\frac{\pi}{2}$ phase delay, while the purely electrical counterparts appear for $n = 1$.

This 4ω mixing technique and the resultant characterization of all the single electrical and motional transport phenomena, is a beneficial contribution to CNT-NEMS characterization

Figure 3.3: Chemisorption of oxygen on CNTs is more likely to happen in ether (ET) configurations, than in epoxy (EP) configurations. Hence no perturbing effect on the bandgap may be expected. Simultaneous observation of the electrical and mechanical implications of oxygen adsorption may be monitored by the ($\omega_g = \omega_0, n = 1$) mixing technique. [by courtesy of [6]]



techniques. The main limitation is the required actuation strength, leading to a strong electrical field effect and limiting the use of such a half frequency actuation technique to sub-GHz bands. Inert to the field effect, metallic zigzag CNTs form an exception by defying these odds, and offer seamless piezoresistive readout up to GHz, as Figure 2.34 affirms.

Electrical & mechanical sensing

Another precious corollary from Table 3.3 is that the electrical and mechanical parts of the field effect can be obtained by solely switching one parameter, either the phase for full frequency actuation, or the ratio for half frequency actuation. The former is especially practical, as it allows to observe both components simultaneously on the two X and Y outputs of the lock-in amplifier, delayed by $\Phi = \frac{\pi}{2}$. Such a simultaneous observation may be of interest when studying the electrical and mechanical impacts of tube functionalization. Oxygen is for instance found to adsorb either in an ether (ET) or an epoxy (EP) configuration [6]. While the former has no impact on the CNT band structure, the latter creates gap induced states, as can be seen in Figure 3.3, and changes the electronic transport properties in addition to the mechanical dynamics [47]. The binding configuration may consequently be determined in a mixing setup, without the need of scanning tunneling spectroscopy (STS). Density functional theory (DFT) calculations show that oxygen is preferentially chemisorbed in ET configurations on CNTs, which allow for mechanical sensing without electrical perturbation. Besides characterization of functional groups, the technique also allows to infer second order information in mass sensing applications, presented in chapter 4. While motional information brings insight on the adsorbed particle's mass and hence nature, the additional electrical impact informs about the adsorbate configuration.

3.4 The Versatility of Direct Readout



Why direct readout?

Mixing may be retained as an ingenious technique to circumvent high-frequency issues when demonstrating CNT-NEMS motion. Major drawbacks are, however, the inherent latency and phase information loss, meaning that motion of CNTs, resonating at hundreds of MHz or GHz, may not be detected faster than within a microsecond, and often it takes even seconds to locate the lorentzian resonance peak. Direct readout, at the frequency ω_e of the effect of interest, would speed up the detection by several orders of magnitude and bring a hundred- to thousand-fold improvement with respect to the fastest reported mixer. Such a speed-up would

lead to faster frequency stabilization loops and sensing with higher temporal resolution, down to hundreds of nanoseconds. One should also bear in mind that the maximal transduction gain and signal strength are obtained in the saturation regime, which was inaccessible to mixers.

Hitherto failure of direct readout does not mean it is impossible, but might be partially explained by the following reasons: Assessment

- The absence of an urgent large-scale need for closed-loop CNT-NEMS oscillators, given that graphene sheets [17] and nanowire [18] could perform these tasks.
- The ignorance of the full potential and opportunities that reside in CNT-NEMS. It is not by pure accident that the here newly reported mixing scheme has remained undiscovered during a full decade.
- The ligation on 50Ω lab equipment and RF components, coupled to the insufficiency of PCBs. The interconnect parasitics of direct readout may be circumvented for systems-in-package, as shown in Figure 1.3, or possibly with the use of custom designed printed circuit boards, but not necessarily with the standard bulky lab equipment, due to the interconnects.
- The lack of transdomain collaboration. CNT-NEMS are a rare article, generally in possession of process engineers or physicists, while circuit designers could contribute the necessary knowledge for the interface design. Hand in hand collaboration of both parties may be a key step forward.

The major challenges for direct readout are twofold. On the one hand, the spurious background signals due to the competing capacitive, field and piezoresistive effects have to be attenuated. The required attenuation expresses as a signal-to-background ratio (SBR), expressed for the effect's sub- and super harmonics. On the other band, do the electronic circuit components cause some noise, which, integrated over the readout's bandwidth, perturbs the motional information. A signal-to-noise ratio (SNR) is defined for quantification of this purpose. Background & noise

3.4.1 Eliminating spurious signals



Contrariwise to mixing, are dephased signals, with identical frequency, not distinguishable under direct readout. Only spectral filtering may be used to isolate the different motional effects of interest. This entails that the weak capacitive effect, overshadowed by the field effect, cannot be observed at all. Observability of the motional field and piezoresistive effects is assessed in Table 3.4 for eigenfrequencies around 100MHz and in Table 3.5 for NEMS oscillating at GHz. These tables are derived from Figure 2.33 and 2.34. So it becomes apparent that under full frequency actuation and around 100MHz, the motional field effect is 40.8dB Spurious signals

Chapter 3. Electrical Detection of Mechanical Motion in Carbon Nanotubes

Motional effect	$\frac{1}{4}\omega_e$		$\frac{1}{2}\omega_e$		ω_e		$2\omega_e$	
	-	dB	-	dB	-	dB	-	dB
fet ($\omega_g = \omega_0$)		∞		∞	40.8	fet,e	54.4	piezo,m
piezo ($\omega_g = \omega_0$)		∞	-54.4	fet,m 16.4	capa,e	∞	∞	
fet ($\omega_g = \frac{\omega_0}{2}$)		∞	0.4	fet,e	84.0	capa,m	54.4	piezo,m
piezo ($\omega_g = \frac{\omega_0}{2}$)	-54.0	fet,e	-54.4	fet,m	∞	∞	∞	
	-18.0	capa,e	29.6	capa,m				

Table 3.4: @ $\omega_0 = 100\text{MHz}$: Direct comparison between the motional effects, occurring at frequency ω_e , and competing effects at surrounding frequencies. Positive SBR entries reflect dominance of the desired motional effect.

Motional effect	$\frac{1}{4}\omega_e$		$\frac{1}{2}\omega_e$		ω_e		$2\omega_e$	
	-	dB	-	dB	-	dB	-	dB
fet ($\omega_g = \omega_0$)		∞		∞	-4.8	fet,e	31.6	piezo,m
piezo ($\omega_g = \omega_0$)		∞	-36.4	fet,e	∞	∞	∞	
			-26.4	capa,e				

Table 3.5: @ $\omega_0 = 1\text{GHz}$: Direct comparison between the motional effects, occurring at frequency ω_e , and competing effects at surrounding frequencies. Positive SBR entries reflect dominance of the desired motional effect.

stronger than the competing electrical counterpart. The piezoresistive contribution at twice this frequency is 54.4dB weaker, and no further spurious signals exist. This predominance of the motional field effect, should allow for a seamless direct readout in terms of SBR.

If, under the same conditions, readout is based on the piezoresistive effect, then a high-pass filter with roll-off higher than $54.4 \frac{\text{dB}}{\text{oct}}$ is necessary to attenuate the competing motional field effect sufficiently. Zigzag metallic tubes, free of field effects, are a welcome exception. Implementing this filter in a Butterworth topology, having a roll-off of $6 \frac{\text{dB}}{\text{oct}}$ per section, would require a tenth order filter. Lower orders are achieved when following a Chebyshev (5th order) or an elliptic filter implementation, but at the price of an higher ripple and nonlinear phase response. Ripple may not be so much of a problem, but phase nonlinearities may complicate the design of closed-loop applications, as will be shown in chapter 4. Specifically must the filter phase be less sensitive to frequency than the CNT-NEMS phase. This condition is met if the filter quality factor is lower than the NEMS quality factor. Filter design is not pushed further here, but it may be mentioned that a tenth order Butterworth filter can be designed with individual stage quality factors of 3.2 and below, which is considerably smaller than typical CNT quality factors around 100. Filter design for elimination of spurious signals should hence not be problematic. Further note that the filter cut-off frequency is determined in one of three ways: Ideally the circuit designer decides on the desired operation frequency, which becomes possible via tensile frequency tuning, and designs the filter accordingly. Alternatively, a third of the CNTs present no field effect, and precise cut-off design is not necessary. Else, the NEMS eigenfrequency needs to be measured first via the field effect, requiring no filter, before the cut-off frequency is carefully placed at that same frequency.

Filter design

At 100MHz, the motional information should be inferred from the field effect, either under full or half frequency actuation. This is statistically possible for $2/3^{\text{rd}}$ of the tubes. Another $1/6^{\text{th}}$ are metallic zigzag tubes and can be sensed directly via the piezoresistive effect at full frequency, and in combination with a $9 \frac{\text{dB}}{\text{oct}}$ filter under half-frequency actuation. The situation is different at 1GHz, where the electrical field effect turns 4.8dB stronger than the motional field effect. As both phenomena appear at the same frequency, motion cannot be extracted by the field effect anymore. At this point, one shall switch to the piezoresistive effect, which gains in amplitude, as a function of frequency, with respect to the competing electrical parasitics at half the frequency. A $36.4 \frac{\text{dB}}{\text{oct}}$ filter roll-off is necessary though for semiconducting tubes, while a $26.4 \frac{\text{dB}}{\text{oct}}$ is sufficient for metallic zigzag tubes. A half-frequency actuation scheme may be envisioned at the absence of the field effect, reducing the filter constraint to $21 \frac{\text{dB}}{\text{oct}}$ (see Figure 2.34) to sufficiently attenuate the electrical capacitive effect at one fourth the frequency.

Optimal effect

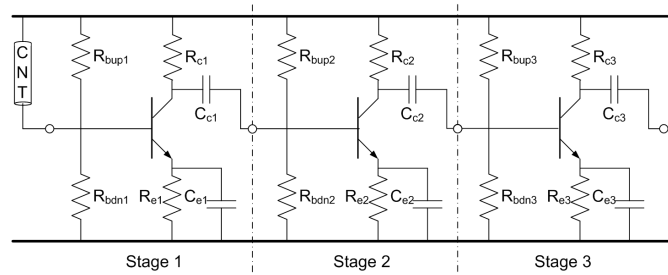
3.4.2 Low-noise front-end design



It has been shown above that the signal-to-background-ratio (SBR) is good enough for filters to be able to clean the motional information from the spurious electrical perturbations. This

Coming soon

Figure 3.4: CNT-NEMS connected to a 3-stage biased CE low-noise amplifier. The interconnect parasitics of Figure 3.1 are not represented and the noise contributions of the base bias resistors is negligible for sufficiently large resistors.



section investigates on the best front-end design so to amplify the CNT signal under minimal addition of noise. The important role of the first stage, for achieving a sound signal-to-noise-ratio (SNR), is illustrated for a bipolar junction transistor (BJT) common emitter (CE) topology. Noise analyses follow for alternative BJT common base (CB), metal oxide semiconductor (MOS) common source (CS) and common gate (CG) topologies, and allow to identify the ideal front-end. Minimisation of the noise figure with sufficient gain, is presented as a constrained optimisation problem, and allows to determine the minimal number of stages. The section condenses in the relation between the minimal detectable signal and circuit bandwidth. The former is to be compared against the CNT signal strength of Table 3.1 and 3.2, while the latter provides the speed constraints for closed-loop applications of chapter 4.

CNT interface The interface, between the CNT-NEMS and the front-end, was shown (see Figure 3.1) to hold several parasitics, out of which the CNT output impedance $R_{CNT} \approx 1\text{M}\Omega$ [80], and the TSV capacitance $C \approx 200\text{fF}$ (for a system-in-package integration of Figure 1.3) or the pad capacitance $C \approx 2\text{pF}$ (for a printed circuit board interface), are retained as most relevant. With these in mind, a circuit view of the interface is shown in Figure 3.4, where the CNT, including the parasitics, is connected to a three-stage CE front-end.

Decisive 1st stage Motivated by Friis' formula (equation (3.1)), the analytical noise study is shown to be sufficiently accurate, if limited to single-stage front-ends, loaded by a noisy resistance R_L . At sufficient gain, the first stage virtually defines the whole circuit's noise factor $F = \frac{\text{SNR}_{\text{in}}}{\text{SNR}_{\text{out}}}$ and its design merits special care. The illustrative topology uses a bipolar junction transistor (BJT) in a common emitter (CE) configuration. Its small signal schematic, including all white noise sources, is shown by the inset of Figure 3.5. As CNT-NEMS resonate in the MHz to GHz frequency range, hypothesizing operation above the device $1/f$ -corner frequency [81] is reasonable, and one may thus safely neglect Flicker noise. The circuit's noise contributions come from the BJT's shot noise at base and collector, completed by the load's thermal noise. Connecting this front-end to the CNT as suggested in Figure 3.5, leads to the following noise

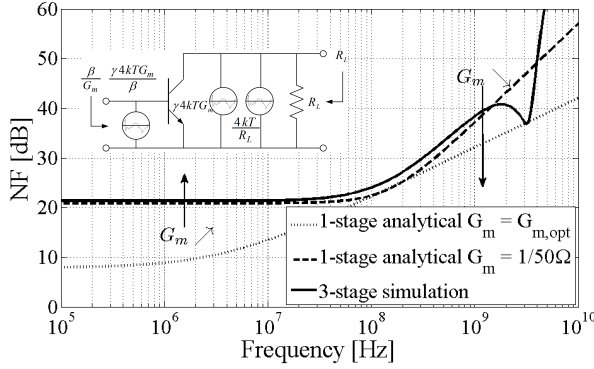


Figure 3.5: 3-stage (simulated with ADS) and 1-stage (analytical expression of equation (3.4)) NF of CE front-end with $C=2\text{pF}$, $R_{CNT}=1\text{M}\Omega$, $R_L=1\text{k}\Omega$. The inset shows the base and collector white noise sources along with the load noise. Flicker noise may be neglected for operation above the corner frequency.

factor expression

$$\begin{aligned}
 F_{CE} = & \quad 1 & \quad \text{by CNT} & \quad (3.4) \\
 & + \frac{\gamma}{\beta^2} R_{CNT} G_m \left[1 + \left(\omega \frac{\beta C}{G_m} \right)^2 \right] & \quad \text{by collector} \\
 & + \frac{\gamma}{\beta} R_{CNT} G_m & \quad \text{by base} \\
 & + \frac{R_{CNT}}{\beta^2 R_L} \left[1 + \left(\omega \frac{\beta C}{G_m} \right)^2 \right] & \quad \text{by load,}
 \end{aligned}$$

where G_m is the transconductance, γ the noise excess factor, β the current gain, and C is the parasitic interconnect capacitance, overshadowing any base-emitter coupling. These expressions are based on the assumption that the electrical CNT noise, in the diffusive saturation regime, may be modelled by a noise current density

$$S_{i^2, \text{CNT}} = \frac{4k_B T}{R_{CNT}} \quad \left[\frac{\text{A}^2}{\text{Hz}} \right] \quad (3.5)$$

On a side note, it may be recalled that all signal strengths in this chapter exceed the thermo-mechanical noise floor, which has been estimated in chapter 2 as the least upper bound of all possible noise sources, summarized in [53]. The noise figure

$$\text{NF} = 10 \log F = 10 \log \left(\frac{\text{SNR}_{\text{in}}}{\text{SNR}_{\text{out}}} \right) \quad [\text{dB}] \quad (3.6)$$

is plotted against frequency in Figure 3.5. The continuous line corresponds to the NF of the 3-stage CE front-end (simulated with ADS), designed to operate at 100MHz with a parasitic capacitance $C = 2\text{pF}$. One can observe that the 3-stage simulation follows rather well the 1-stage analytical prediction of equation (3.4), given by the dashed line. This portends that the noise contribution of stages 2 and 3 remains negligible with respect to the first stage's noise. The dotted line has been obtained by optimizing the bias current for each frequency and gives the absolute best NF for CE topologies. We here conclude that single-stage NF expressions, such as the one of equation (3.4), represent the overall circuit noise with sufficient accuracy.

Best topology The previous conclusion allows to significantly simplify the noise analysis and leads to precious insights from analytical expressions. Four candidate first stage topologies are presented and their respective advantages are discussed.

BJT - common emitter (CE) The noise factor of the CE topology was given by equation (3.4) and is presented in Figure 3.6a for $C = 2\text{pF}$ (—) and $C = 200\text{fF}$ (- - -). The important NF values result from the combination of the CNT's large output impedance and the non-negligible interconnect capacitance. It becomes apparent that this capacitance shall be kept to a minimum. Transistor bias varies the transconductance G_m , and the noise figure for optimal bias is given by the red curves. The analytical expression of $G_{m,\text{opt}} = \frac{I_{C0,\text{opt}}}{U_t}$, with $I_{C0,\text{opt}}$ the collector current and $U_t = \frac{k_B T}{q} \approx 26\text{mV}$, will be provided by equation (3.11). Transistor transconductances around 20mS are close to optimal for PCB front-ends around 100MHz and integrated TSV connected chips around 1GHz . For both situations, CE front-ends yield $\text{NF} \approx 22\text{dB}$. Given that CE topologies possess enough power gain to subvert the load's noise contribution, the NF is limited by the base noise at low frequencies and by the collector noise at high frequencies.

BJT - common base (CB) The CB front-end, represented in the inset of Figure 3.6b, also relies on bipolar technology, but has a lower input impedance than the CE. Compared to the CE, it presents a larger pass-band at the cost of a unity current gain. This implies a stronger noise contribution from the load, as emanates from

$$\begin{aligned}
 F_{CB} = & \quad 1 & \quad \text{by CNT} & \quad (3.7) \\
 & + \frac{\gamma}{\beta^2} R_{CNT} G_m \left[1 + \left(\omega \frac{\beta C}{G_m} \right)^2 \right] & \quad \text{by collector} \\
 & + \gamma R_{CNT} G_m & \quad \text{by base} \\
 & + \frac{R_{CNT}}{R_L} \left[1 + \left(\omega \frac{C}{G_m} \right)^2 \right] & \quad \text{by load.}
 \end{aligned}$$

At low frequencies, the NF is limited by load and base shot noise, while the collector shot noise dominates at high frequencies, where the performance equals the one of the CE. Although a large load enhances gain and noise performance at low frequencies, the performance of a CB front-end remains inferior to the CE in terms of noise. The $1\text{k}\Omega$ load resistance is a placeholder for an amplification stage, typically a CE, which has an input impedance of $R_{\text{in,CE}} = \frac{I_{C0}}{\beta U_t}$, on the order of several $\text{k}\Omega$. The NF for frequencies up to GHz , and interconnect capacitances up to picofarad, is of 42dB .

MOS - common source (CS) The noise of metal-oxide-semiconductor (MOS) front-ends can be summarized to the channel thermal noise, with negligible gate-induced noise in the considered frequency range. Its immense input impedance makes the common source (CS) an ideal candidate for low NF at relatively low frequencies, as arises from

3.4. The Versatility of Direct Readout

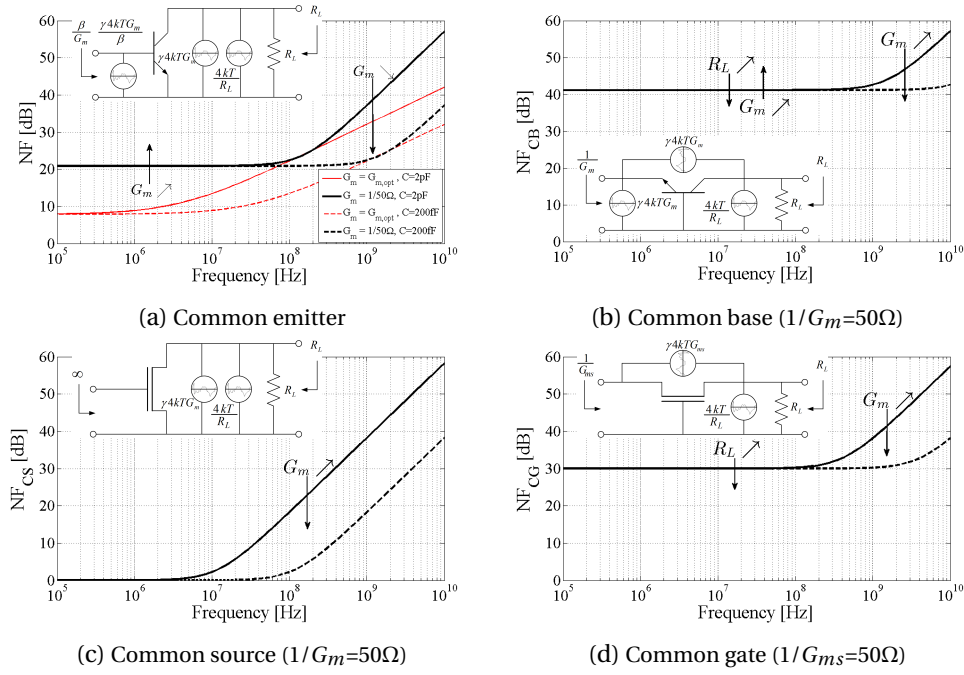


Figure 3.6: Noise figure for front-ends with $C=2\text{pF}$ (—) and $C=200\text{fF}$ (- -), $R_{CNT}=1\text{M}\Omega$, $R_L=1\text{k}\Omega$

Figure 3.6c. The NF, given by

$$\begin{aligned}
 F_{CS} = & \quad 1 & \quad \text{by CNT} & \quad (3.8) \\
 & + \frac{\gamma}{R_{CNT}G_m} [1 + (\omega R_{CNT}C)^2] & \quad \text{by channel} \\
 & + \frac{1}{G_m^2 R_{CNT} R_L} [1 + (\omega R_{CNT}C)^2] & \quad \text{by load,}
 \end{aligned}$$

can be enhanced at any frequency at the cost of a larger biasing current. At low frequencies, the SNR is limited by the CNT noise, while the channel noise is responsible for the increasing NF at high frequencies. 19dB NF are achieved at 100MHz for PCB and 1GHz for IC front-ends, and the IC front-end would add only 3dB of noise at 100MHz.

MOS - common gate (CG)

A large load and hence large voltage gain is beneficial to a common gate (CG) topology at low frequencies. As for the CS front-end, at high frequencies, increased bias current enhances the NF

$$\begin{aligned}
 F_{CG} = & \quad 1 & \quad \text{by CNT} & \quad (3.9) \\
 & + \frac{\gamma}{R_{CNT}G_{ms}} [1 + (\omega R_{CNT}C)^2] & \quad \text{by channel} \\
 & + \frac{R_{CNT}}{R_L} \left[1 + \left(\omega \frac{C}{G_{ms}} \right)^2 \right] & \quad \text{by load.}
 \end{aligned}$$

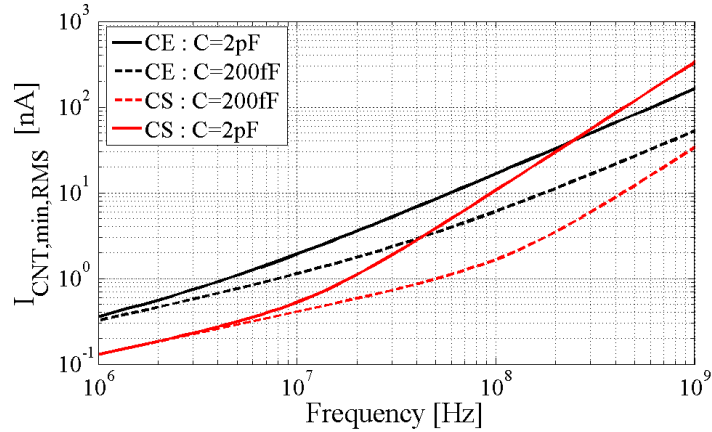


Figure 3.7: Minimum detectable current from CNT with $R_{CNT} = 1M\Omega$, by an optimally biased CE ($\beta = 100$) and CS front-end at ambient temperature for $SNR_{out} = 1$. The represented curves may be pessimistic in the sense that the noise integration has been approximated conservatively.

The unity gain, however, confronts the CNT signal unamplified with the drain and load noise, which leads to lesser performance than for a CS topology.

From the previous analysis, it is retained that a common emitter outperforms a common base, and that a common source outperforms a common gate. The reason was the larger current gain. Further is MOS retained as the better technology when interfacing high impedance devices such as CNT-NEMS. It is noteworthy that the fastest mixer [19] used a high electron mobility transistor (HEMT), with high input impedance, to read the CNT signal at MHz. It has to be admitted nevertheless, that the analyses supposed transistor operation well below the unity gain frequency. This hypothesis is acceptable for integrated technologies, featuring transition frequencies of 90GHz (130nm), 140GHz (90nm), 180GHz (65nm) and 250GHz (40nm)¹. As a guideline, CMOS common source front-ends are best for frequencies up to GHz, but if discrete components are used, then BJT common emitters are on a par for the 100MHz-1GHz frequency range of interest.

Minimum detectable signal

With knowledge on the maximal signal out of the CNTs (see Table 3.1 and 3.2) and on front-end noise figures, we have at disposal all ingredients to assess the ability of standard electronic devices, such as bipolar junction (BJT) or field effect (FET) transistors, to sense and amplify the CNT signal. The minimum detectable signal (MDS) depends on the signal-to-noise ratio (SNR) necessary for subsequent signal processing, the front-end's noise figure (NF), and the circuit's bandwidth B , defined by the bandpass filter. Overestimating the noise power by multiplying the noise figure NF by the bandwidth, leads to a conservative upper bound of the minimum detectable signal:

$$I_{CNT,RMS} \geq \sqrt{\frac{4k_B T B}{R_{CNT}} \cdot 10^{NF} \cdot SNR_{out}} \quad [A] \quad (3.10)$$

Considering a CE front-end, the optimal transconductance $G_{m,opt} = \frac{I_{C0,opt}}{U_T}$ and collector current

¹Transition frequencies for Toshiba's RF-CMOS technology, available under http://www.toshiba-components.com/ASIC/data/Toshiba_ASIC&Foundry_RFCMOS_flyer.pdf

are obtained by differentiation of equation (3.4) with respect to G_m , leading to

$$I_{C0,opt} = \sqrt{2\beta} \frac{kT}{q} \omega C, \quad (3.11)$$

with q the elementary positive charge. The bias of the subsequent stages may be chosen as to provide maximum stable gain, as their impact on the NF is less significant. Figure 3.7 shows two important facts:

- At 100MHz, a PCB CE front-end can detect the motional 100nA field effect with $\text{SNR}_{\text{out}} \approx 100$.
- This same effect becomes unfortunately masked by a spurious electrical signal of identical frequency at 1GHz (see Table 3.2), but a TSV-connected on-chip CE front-end can detect the piezoresistive 1nA component with $\text{SNR}_{\text{out}} \approx 4$, if used in combination with a filter quality factor $Q = 10^4$. Although such aggressive filtering enables direct readout, it somehow sacrifices all the benefits related to high-speed readout. $Q = 10^4$ is indeed very likely to exceed the CNT-NEMS quality factor, which means that closed-loop systems would converge to the filter's eigenfrequency, instead to the NEMS eigenfrequency. Hence a tedious frequency scan is necessary to center the narrow-band filter at the CNT's eigenfrequency. The same signal strengths and front-end performance would, however, allow to sense resonating graphene ribbons with quality factors of 10^4 [17]. It is retained that direct readout is possible at GHz, but only with aggressive filtering, blocking the extension to closed-loop operation with its benefits for VCO and sensor applications.

3.5 Implementation & Characterization



The previous analyses did not account for practical limitations on transistor transconductance, current gain and transition frequency (unity-gain frequency). Such limits entail that minimal noise cannot necessarily be combined with maximal gain up to arbitrary frequencies. This section illustrates how the performance limits may be reached by the use of multi-stage front-ends and shows a common emitter and common source implementation.

Practical issues

The front-end, being a cascade of stages, its noise figure is expressed via Friis' formula

Number of stages

$$\text{NF}_{\text{total}} = \log_{10} \left(F_1 + \sum_{i=2}^n \frac{F_i - 1}{\prod_{j=1}^{i-1} G_j} \right) \quad (3.12)$$

where F_i and G_i denote the noise factor and power gain of stage i . NF_{total} shall be minimized under the constraint of overall sufficient gain. The resulting minimum detectable signal (MDS) shall be lower or equal to the signal provided by the CNT as reported in Table 3.1 and 3.2. Considered candidate circuits operate the BFP750, a high linearity low noise Silicon-Germanium-Carbon NPN transistor, in a common emitter configuration. The reasonable

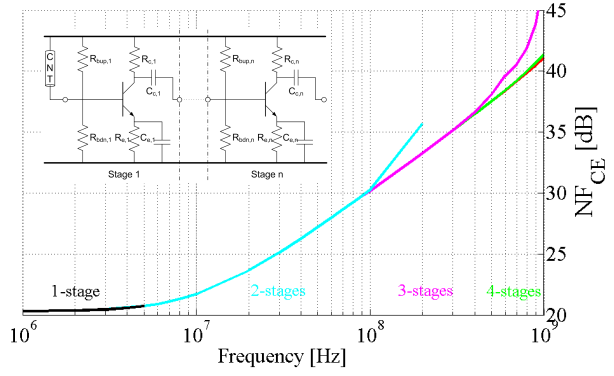


Figure 3.8: Gain-constrained minimum NF as a function of frequency and number of stages for real CE front-end with bias-dependent current gain and transition frequency. (hyp. $SNR_{out}=1$).

assumption, that bias resistors exceed the transistor's base impedance up to GHz frequencies, making their noise contributions negligible, is made. The CNT is interfaced by the discrete component front-end [16]. Hence the interface capacitances are on the order of $C = 2\text{pF}$. The front-end's transimpedance, as a function of the first stage input impedance $\frac{1}{1+s\frac{h_{fe,1}\cdot C}{g_{m1}}}$, the transconductances g_{mi} , the subsequent stage input impedances $\frac{h_{fe,i}}{g_{mi}}$ and the final load, supposed to be a pad, identical to the input pad $\frac{1}{sC}$, writes

$$A_{\Omega,CE} = \frac{1}{1+s\frac{h_{fe,1}\cdot C}{g_{m1}}} \cdot \prod_{i=1}^n h_{fe,i} \cdot \frac{1}{sC} \quad [\Omega] \quad (3.13)$$

and must be able to convert a 100nA current variation into a 1V stimulus for the digital CMOS IC (presented in chapter 4), hence exceed 10M Ω . The DC current gain β decreases with bias from 365 ($I_{C0} = 1\text{mA}$) to 185 ($I_{C0} = 100\text{mA}$) and the small-signal current gain frequency dependence is modelled as

$$h_{fe} = \frac{\beta}{\sqrt{1+\left(\frac{\omega}{\omega_T}\right)^2}} \quad (3.14)$$

with ω_T being the bias-dependent transition frequency - $\omega_T = 4.85\text{GHz}$ at $I_{C0} = 1\text{mA}$ and $\omega_T \approx 40\text{GHz}$ for $I_{C0} \geq 60\text{mA}$. Given the CNT's thermal current noise density $\frac{4k_B T}{R_{CNT}}$ and the transistors' base and collector shot noise, equation (3.12) writes

$$NF_{CE} = \log_{10} \left(1 + \gamma R_{CNT} \cdot \sum_{i=1}^n \left(\frac{g_{m,i}}{\left(\prod_{j=1}^i h_{fe,j}\right)^2} \right) \cdot \left(\left| 1 + s \frac{h_{fe,1}\cdot C}{g_{m1}} \right|^2 + h_{fe,i} \right) \right) \quad [\text{dB}] \quad (3.15)$$

Equation (3.15), evaluated for a single unloaded stage, reduces to the CNT, base and collector contributions of equation (3.4). The effect of the load R_L is added by cascading a second stage, which makes appear the load term of equation (3.4) for the second stage input impedance $R_L = \frac{h_{fe,2}}{g_{m2}}$, completed by the second stage collector noise. Completing equations (3.14) and (3.15) by further constraints for acceptable transistor bias (1mA to 100mA), the constrained

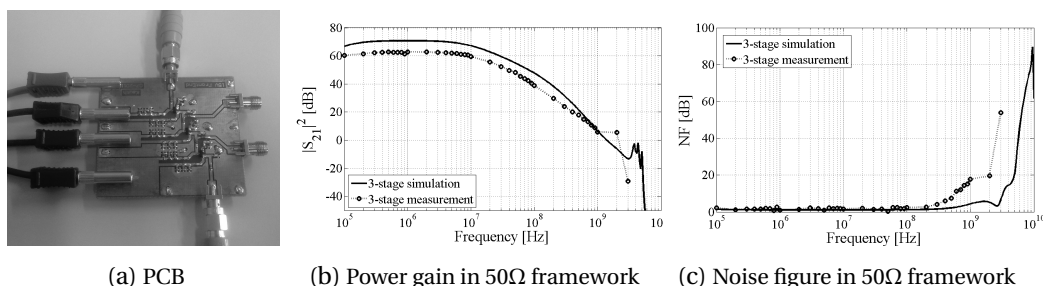


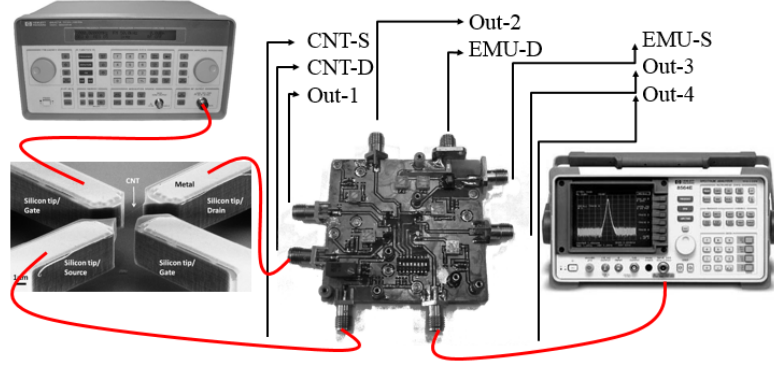
Figure 3.9: 3-stage discrete component CE front-end

optimization problem is solved via sequential quadratic programming (SQP) and leads to the minimal NF for practical multi-stage inputs, shown in Figure 3.8. Practice shows that all but 1dB comes from the most noise-critical first stage. While a single stage can provide the necessary gain up to few MHz, cascading is necessary for higher frequencies. Although 2 stages work out up to 200MHz, the use of 3 stages allows to relax the gain constraint and provide notably better noise figures. Close to optimal noise figures can be achieved by 4 stages up to GHz. The optimal bias, with sufficient number of stages to ensure gain, lies around the lower bound of 1mA for the BFP750. Given that the SNR degradation is due to the first stage, the addition of supplementary stages does not compromise the NF and an optimally biased 4-stage front-end will perform nearly-optimal for any signal frequency from MHz to GHz. The previously discussed noise filter (see section 3.4.1), can interlace the front-end's stages. This avoids transistor saturation without noise performance loss, given the negligible SNR degradation due to all but the first stage.

The 3-stage CE front-end of Figure 3.4 is subsequently implemented on a PCB. Insensitive to the transistors' current gain β , the bias networks of each stage are decoupled via capacitors C_{ci} . The base potential is a free design variable and hence presents a degree of freedom that, in the case of the first stage, can be exploited to adjust the base voltage as to properly set the CNT's DC bias to the on-state ($\sim 2V$). The emitter capacitance C_{ei} grounds the bias resistor R_{ei} over the widest feasible bandwidth to avoid noise contributions and negative feedback. Choosing R_{up1} and R_{dn1} larger than the BJT's input impedance $\frac{\beta}{G_m}$, renders their contribution to the noise figure insignificant. To keep the biasing independent from the current gain β , current through the base biasing resistors shall render the BJT base current negligible. The last two constraints can be achieved simultaneously by providing sufficient voltage supply. With the objective of validating the previous conclusions for the CE front-end interfacing a CNT-NEMS, exclusively based on analytical analyses and simulations, the simulations are confronted with measurement results for the 3-stage CE front-end in the common 50Ω RF framework. Although the absolute values of gain and NF happen to be very different from what they would be in the CNT MΩ framework, the mere fact that the measurements match the simulation (see Figure 3.9b & 3.9c), provides the necessary provisional faith into the previously drawn conclusions on noise figure (see Figure 3.5) and minimal detectable signal from the CNT-NEMS (see Figure 3.7). No working CNT-NEMS, however, was available during the lifetime

3-stage CE

Figure 3.10: 4-stage discrete component CS front-end interfaced with CNT-NEMS. The 27.72dB SNR, achieved over a 1Hz bandwidth, requires the use of a selective filter under direct readout. The test-conditions with the CNT biased to the linear regime, however, were not optimal.



of this circuit and a demonstration of CNT signal readout capabilities is not available. The low-pass cut-off is due to the pole defined by $\omega_{p1} = \frac{G_m}{C_e}$. Although it is possible to extend the passband to lower frequencies, a second pole limits this endeavour at $\omega_{p2} = \frac{1}{(R_{in} + R_c)C_c}$, R_{in} being the input impedance of the next stage, speak $\frac{\beta}{G_m}$. While the measured pass-band frequencies were accurately predicted by the simulation, its gain presents a discrepancy, which is partially ascribed to the absence of impedance matching, given that 50Ω is not the final target and the front-end is primarily meant for M Ω NEMS interfaces. . The power gain in the passband, writing

$$|S_{21}|^2 = 20 \log \frac{2\beta G_m R_c}{\beta + G_m R_c}, \quad (3.16)$$

the difference between measured and simulated current gains β accounts for twice 1.9dB and the cabling losses for 0.4dB. More importantly does the NF, shown in Figure 3.8, confirm that the simulation predicts the measurement trend up to the front-end's gain decay. By this validation principle, we can prognosticate for the CE front-end a NF similar to the simulated one of Figure 3.5 when interfacing the CNT-NEMS, implying an upper bound on signal sensitivity provided by Figure 3.7.

4-stage CS A 4-stage CS front-end, based on the dual gate BF998, was designed on demand when a resonating CNT was evidenced. The resonance frequency was found via a mixer setup at 10.45MHz, and the quality factor estimated to 50. This rather low resonance frequency may be attributed to the existence of slack, as in [1]. The PCB, shown in Figure 3.10, biases the NEMS and amplifies the signal, before sending it to a spectrum analyzer. Actuation is done by an RF signal generator. On board is also a floating tunable resistance, which allows to calibrate the circuit for the specific needs of the CNT. The owner of the CNT-NEMS was little adventurous and imposed bias limits of $V_g = 1V$ and $V_{ds} \leq 110mV$, standing for a 92nA drain bias. These values clearly lie below the requirements for direct readout, which shall interface a tube biased to saturation ($V_{ds} \geq 2V$) and with μA -drain current at DC ($V_g \approx 2V$). The experiment was conducted nevertheless, and resulted in a signal at 20.9MHz with 27.72dB SNR when integrated over a 1Hz bandwidth and driven at its eigenfrequency. The observed effect was the motional piezoresistive effect, according to Table 3.1. If the entire signal strength is due to the amplified

CNT signal, then the 27.72dB SNR stands for a peak 592 times stronger than the noise in 1Hz of bandwidth. Hence, for the noise power to equal the signal, the bandwidth may be enlarged to 592Hz. In other terms, for direct readout to succeed under the mentioned conditions and for the device under test, a filter with quality factor $Q = \frac{20.9e6}{592} \approx 35'000$ would be necessary. This is considerably larger than the CNT quality factor, and no closed-loop operation is imaginable. Whether the tube under test could have performed better under higher bias, remains a secret, as it has been blown to kingdom come, ironically not via carbonization by the front-end circuit, but by a probe, that slipped away, when cooling the setup to cryogenic temperatures.

3.6 Summary



The underlying question of the chapter was to assess whether CNT-NEMS can be sensed at high bandwidth or not. High-bandwidth readout would allow the design of sensors offering unprecedented speed and sensitivity (subsequently presented in chapter 4), but low-bandwidth mixing techniques are the workhorse nowadays. So the chapter set out on the quest of high-bandwidth interfaces and allowed to enlighten the limitations faced by such circuits. CNT-NEMS motion may be inferred by three effects, namely a strong field effect, a moderate piezoresistive effect, and a weak capacitive effect. Typical eigenfrequencies range from 100MHz to 1GHz, but lower frequencies may be caused by slack.

To be or not to be

Electronic circuits were confronted with the challenge of sensing and amplifying these carbon nanotube signals, extracted in chapter 2. Spurious signals and electronic component noise were shown to impede the detection of the motional information. More specifically, two techniques, mixing and direct readout, were analysed, assessed and related state-of-the-art has been completed by precious insights. The chapter is rounded off by a practical experiment, which allowed to read CNT-NEMS motion via a PCB front-end.

Survey

Among the interconnect RLC parasitics, the capacitance was identified as the most critical element. Picofarad pad PCB capacitances, in combination with the megaohm CNT output impedance, were found to limit direct readout of the 100nA motional field effect to hundreds of megahertz, while the nanoampere piezoresistive effect becomes blurred already at few megahertz. The interconnect capacitance is reduced by an order of magnitude when the front-end sits on an integrated circuit, connected to the NEMS chip via TSVs, as has been shown in Figure 1.3. It has been retained that IC front-ends are favoured over custom PCB interfaces, which still perform better than 50-Ω RF lab equipment. The key performance factor was high front-end impedance, and with the advent of always smaller and highly resistive NEMS, there may be a market niche for high impedance characterization setups.

Interconnect parasitics

Best front-end noise figures were observed for high-impedance front-ends with small input noise. Common source MOSFETs perform best up to 100MHz, but they are outperformed by common emitter BJT front-ends in GHz vicinity. The minimum detectable CNT current modulation is reported on Figure 3.7 and sets this limit to roughly 10nA at 100MHz and 100nA at 1GHz for both topologies, if implemented on a PCB. Their integrated versions can reach

Minimum detectable signal

down to 1nA at 100MHz and few tens of nA at 1GHz.

- Direct readout @100MHz These values enable direct NEMS readout around 100MHz, if the CNT performance is optimized according to the guidelines of chapter 2. The 100nA motional field effect (Table 3.1) comes indeed with an SNR \approx 20dB over a 100MHz bandwidth for discrete component front-ends and SNR \approx 30dB for integrated chips (Figure 3.7). This field effect being present in all semiconducting tubes, 2/3rd of the tubes can be sensed with high-bandwidth readout in terms of SNR. Under full frequency actuation, no spurious signal would mask the motional information either (Table 3.4), which has an edge over half frequency actuation. The use of a bandpass filter, with high-frequency cut-off above the CNT-NEMS eigenfrequency and low-frequency cut-off around MHz, is recommended, to limit the noise integration bandwidth and avoid the $1/f$ flicker noise below the corner frequency. Another 1/6th of the tubes (metallic zigzag) present a 1nA piezoresistive current and are void of the field effect. These can be sensed by integrated front-ends with a SNR equal to the quality factor of the noise filter and spurious signals are negligible under full frequency actuation. The filter's quality factor must not exceed the one of the NEMS, and is hence restricted to around 100, and an SNR \approx 20dB. The motion of a final sixth of the CNT-NEMS remains obfuscated by either spurious signals, or because the noise level exceeds the 10pA weak motional capacitive effect.
- Direct readout @1GHz While the 100nA strong motional field effect component still lies in the realm of integrated front-ends for GHz eigenfrequencies, it is the NEMS device itself, which makes such an approach impracticable by masking the motional component by a stronger electrical spurious signal at the identical frequency (Table 3.2). The electronic interface can circumvent this limitation by focusing on the 1nA piezoresistive component with $SNR_{out} \approx 4$, if used in combination with a filter quality factor $Q = 10^4$. Although such aggressive filtering enables direct readout, considering CNT Q-factors around 100, it somewhat sacrifices all the closed-loop perspectives related to high-speed readout.
- In practice It is also the front-end's mission to provide sufficient amplification for the CNT signal to be suitable for the subsequent signal processing blocks. It has been shown that practical implementations, with 3 or 4 amplification stages, are recommended in the 100MHz to 1GHz range. A 3-stage common emitter and a 4-stage common source front-end have been implemented on a printed circuit board. The latter demonstrated observation of a resonating CNT-NEMS. The SNR was however not sufficient for full-bandwidth operation and a filter quality factor of 35'000 would be necessary for closed-loop operation. It has to be conceded that instructions were given to operate the CNT in its linear region, definitely a suboptimal situation for readout, and that no other working CNT-NEMS was available.
- New realms of mixing Another approach consists in reading the CNT-NEMS signal at an intermediate frequency. Such mixer setups circumvent the high-bandwidth challenges and they do without custom PCB or IC design. This advantage for device characterization comes at the price of losing instantaneous motional information. Not knowing the exact instantaneous position of the CNT, makes it impossible to insert the NEMS into a self-calibrating direct feedback loop. The

known mixing methods were reviewed and completed by a novel mixing method with a 4-fold frequency ratio between actuation and readout. This new mixing technique allows to identify the capacitive, field-effect and piezoresistive motional and electrical current modulation phenomena individually and without interference. The necessary setup parameters for each component are summarized in Table 3.3. Besides offering complete CNT-NEMS characterization, it has been brought forward that electrical and motional properties can be observed simultaneously on lock-in amplifiers, and may be of avail for characterization of adsorbate configurations.

While the novel mixing method roots in the half-frequency actuation scheme, it is suggested to use a full frequency actuation in consideration with direct readout. At 100MHz, such a scheme eliminates the need for aggressive filtering of spurious signals, while at 1GHz, its performance is equivalent to the half frequency actuation, given that the SNR constraints become more stringent than the SBR requirements. Actuation

While the utility of the novel mixing technique is restrained to systematic characterization of CNT-NEMS and adsorbate configurations, the direct readout technique, operational up to CNT-NEMS eigenfrequencies of few hundreds of megahertz, allows to operate CNT-NEMS in high-speed closed loop systems and applications like voltage controlled oscillators, force, pressure and mass sensors. Utility

The important thing in science is not so much to obtain new facts as to discover new ways of thinking about them.

— William Bragg

4

Electromechanical Oscillators and Sensors

After assisting to the eclosion of carbon nanotube NEMS into electronically measurable resonators in chapter three, the present chapter treats of their operation as voltage controlled electromechanical oscillators (VCO) and sensor systems. The common denominator of these applications is the ability to continuously operate the CNT-NEMS as a quantitatively controllable oscillator and feedback plays a major role. VCOs & Sensors

With higher quality factors than integrated LC tanks and wider tuning ranges than quartz crystals, tunable CNT-NEMS have the potential to complement these omnipresent electronic blocks in their roles as oscillators. Joint circuit and NEMS integration in the system-in-package concept of Figure 4.1, brings the further advantage of reduced size. CNT-NEMS operation as a VCO, forms also a milestone towards high-speed mass sensing. Today's mass sensors evolved along the direction of sensitivity and reached atomic resolution, while neglecting the potential importance of high temporal resolution. The used, intrinsically slow, mixing techniques cannot extend towards high-speed. The VCO topology, on the other hand, can metamorphose into a high-speed sensor, and a novel *in situ* calibration technique, enables unbiased high-precision mass sensing. Such precise and fast mass detection allows observation of phenomena that so far are not observable because they are either too subtle (insufficient sensor resolution) or happen too fast (insufficient sensor speed), like chemical and biochemical reactions. Rationale

Although the presented figures of merit are related to the exceptional CNT properties, are the presented system-level concepts not restricted to the realm of carbon nanotube NEMS, but remain applicable to other electromechanical resonators, at micro- and nanoscales, made of Generalization to MEMS

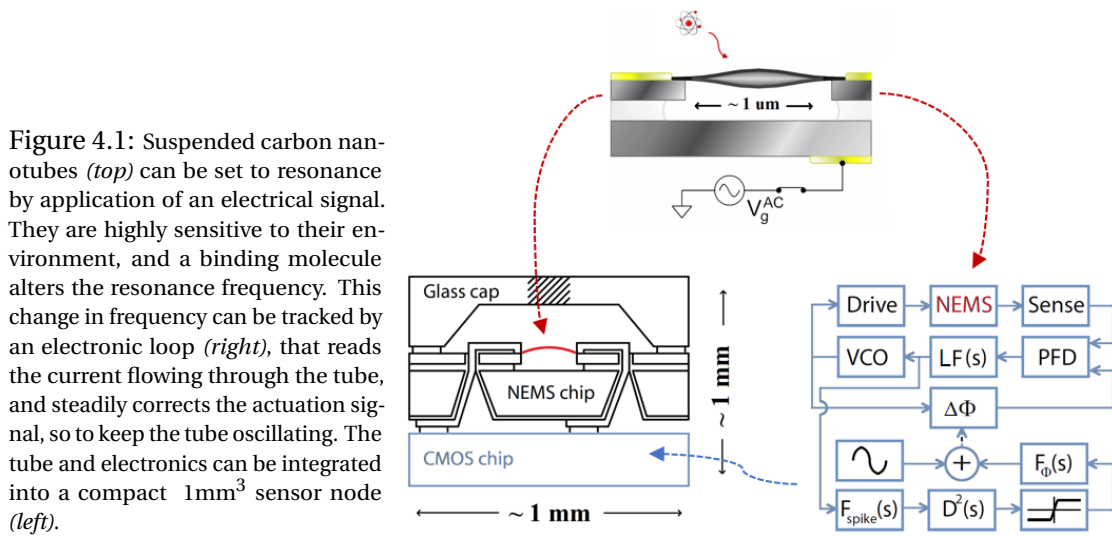


Figure 4.1: Suspended carbon nanotubes (*top*) can be set to resonance by application of an electrical signal. They are highly sensitive to their environment, and a binding molecule alters the resonance frequency. This change in frequency can be tracked by an electronic loop (*right*), that reads the current flowing through the tube, and steadily corrects the actuation signal, so to keep the tube oscillating. The tube and electronics can be integrated into a compact 1mm^3 sensor node (*left*).

semiconducting or piezoresistive materials.

- Overview The chapter first presents the potential target applications, with focus on electromechanical VCOs, force and pressure sensors, and mass balances, in section 4.1. Section 4.2 then sets out on the quest of an appropriate oscillator topology, which forms the common ground of all considered applications. NEMS-based phase-locked loops are retained for their high-frequency closed-loop operation and self-sufficient open-loop testing possibilities. Once conceptual functionality is established, efforts strive towards the optimisation of closed-loop system performance in section 4.3, leading to NEMS oscillator design guidelines. Section 4.4 compares the VCO-based high-speed sensors with the mixer-based high-precision mass balances, and proposes an *in situ* calibration technique to combine high-speed and high-resolution into a single sensor system, forming the world’s fastest mass sensor with molecular scale sensitivity. A succinct summary of the highlights concludes the chapter in section 4.5. Circuit implementation and characterization, as well as a performance assessment of the system, follow in chapter 5.
- Novelty

4.1 Ingredients to Electromechanical VCOs and Sensors



- Greatest common divisor Whether operated as VCO or as sensor, electromechanical resonators reveal their full potential when integrated into a closed-loop oscillator. Such a feedback system allows to stabilize the oscillation around the NEMS eigenfrequency, providing optimal signal to noise (SNR) and signal to background (SBR) ratios. Fast responsivity is achieved when the NEMS information is read at the eigenfrequency, rather than at an intermediate mixed frequency. The dynamic mode sensitivity to the environment is boosted by the NEMS quality factor, with respect to static mode operation. These factors endorse the design of oscillators, based on an electromechanical resonator. This challenge will be addressed in the subsequent sections. The coming paragraphs hypothesize it as solved, and illustrate how such an electromechanical oscillator

4.1. Ingredients to Electromechanical VCOs and Sensors

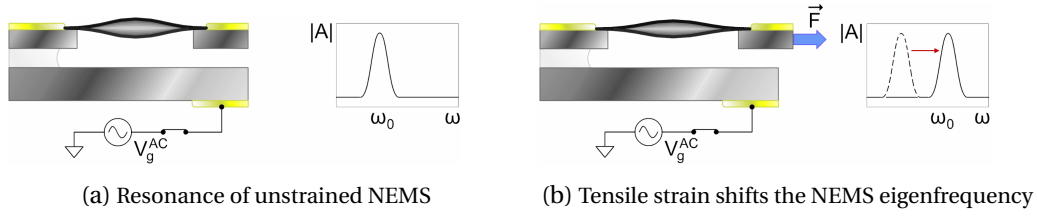


Figure 4.2: NEMS eigenfrequency tunability and strain sensitivity.

may be customized into different applications, mentioned in chapter 1.

4.1.1 Frequency tunability for VCOs



Frequency tunability may be obtained by controlling the NEMS eigenfrequency, as suggested by equation (2.9) for the case of CNT-NEMS

VCO
tunability

$$\omega_0 = \sqrt{\frac{k'}{m'}} = \left(\frac{\pi^2}{L^2}\right) \sqrt{\frac{8EI}{\rho A} \left(1 + \frac{T_0 L^2}{4\pi^2 EI}\right)} \quad \left[\frac{\text{rad}}{\text{s}}\right] \quad (4.1)$$

The two single parameters, which may alter during operation, are the tensional force T_0 [N] and the mass density ρ $\left[\frac{\text{kg}}{\text{m}^3}\right]$. While the latter is reserved to mass sensor operation, the former may be controlled either mechanically or electrically. Direct mechanical application of a longitudinal tensional force through displacement of the source electrode by an actuator MEMS is shown by Figure 4.2. A similar straining effect can be obtained indirectly by changing the DC gate voltage, which induces strain via a lateral electrostatic force, given by equation (2.51). It has been brought forward in section 2.2.4, that the DC gate bias has a considerable impact on the CNT conduction properties. It is consequently advisable to keep this one unchanged, to ensure optimal NEMS bias, and rely on the mechanical force of a MEMS to shift the eigenfrequency. Those may for instance be piezoelectric, magnetic, thermal or electrostatic actuators [55], as pictured in Figure 5.12b. A noteworthy final remark on electromechanical VCO applications is that the closed-loop system must lock on a frequency which depends on the NEMS eigenfrequency to assure tunability. This frequency must not mandatorily be the NEMS eigenfrequency itself, but any frequency within the NEMS's lorentzian peak, providing sufficient signal strength, may do.

4.1.2 Strain sensitivity for force and pressure sensors



Instead of imposing the oscillation frequency by application of a tuning force, this straining force can reciprocally be inferred from the resonance frequency, transforming the system of Figure 4.2 into a force sensor. Such longitudinal forces can be detected with a resolution of

Force
sensitivity

$$\Delta F_{\text{long}} = 2 \frac{\Delta \omega_0}{\omega_0} \cdot \left(\frac{4\pi^2 EI}{L^2} + T_0\right) \quad [\text{N}] \quad (4.2)$$

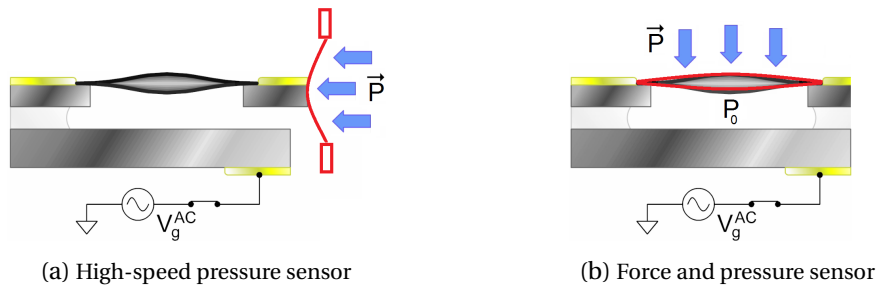


Figure 4.3: NEMS-VCO extension to force and pressure sensing.

reaching down to piconewton [78].

Novel pressure sensor Pushing the reasoning a step further, one could attach the movable source electrode to a thin membrane, shown in red in Figure 4.3a. The differential pressure on both sides of the diaphragm determines the strain on the tube, and sets consequently its eigenfrequency. Tracking of the latter transforms the system into a high-speed pressure sensor.

Standard pressure sensor The price to pay for this high-speed pressure sensing is the supposedly challenging fabrication process. Pressure sensing via a standard approach would stick the nanotube onto the diaphragm, as shown in Figure 4.3b. Such operation causes however considerable changes to the device properties and requires a separate study. The transverse pressure sensitivity

$$\frac{\Delta P_{\text{trans}}}{P_{\text{trans}}} = 2 \frac{\Delta \tilde{\omega}_0}{\tilde{\omega}_0} \quad (4.3)$$

depends indeed on the membrane's lower eigenfrequency, as the dynamics of the diaphragm are likely to dominate the ones of the NEMS. The resulting hybrid system, inherits the mechanical dynamics of the diaphragm and the electronic properties of the CNT-NEMS.

4.1.3 Adsorption sensitivity for particle detectors & mass balances

Mass sensitivity Adsorption of a particle of mass Δm onto the CNT surface, or a functionalized site, locally alters the density ρ , causing a shift in the resonance frequency, as suggested by Figure 4.4. The amplitude of the shift is simultaneously influenced by the change in mass and the position of binding. For a shift in the resonance frequency to provide quantitative information on the adsorbed particle's mass, the binding site must be known.

Functionalization If quantitative weighing is the aim, it is consequently beyond question not to functionalize the tube with a receptor, in order to determine the ligand's binding site in advance. Today's state-of-the-art lithography allows to place such a receptor with a 1% precision along the tube length. Preciser information on the binding locus can be obtained via scanning tunneling microscopy [46]. If the particle binds at mid-length of the NEMS, the observed change in frequency is maximal, while it would be nil at the tube's ends.

4.1. Ingredients to Electromechanical VCOs and Sensors

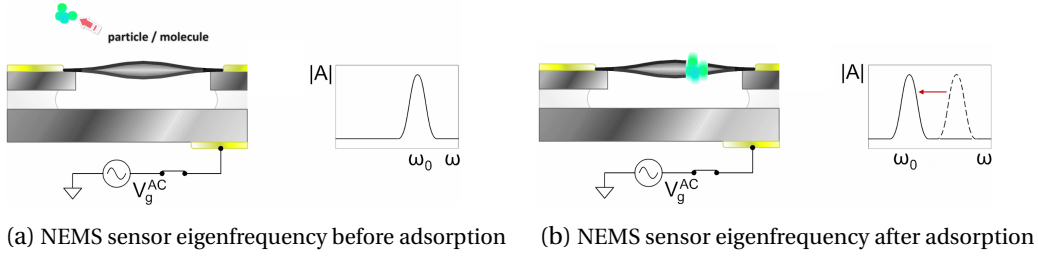


Figure 4.4: Sensitivity of NEMS eigenfrequency to adsorption.

In the absence of functionalization, and for particles with affinity to CNTs, the binding may occur anywhere along the tube. Although this situation is not suitable for quantitative mass sensing, the system can still serve as particle detector. Hypothesizing a uniform adsorption position probability distribution along the NEMS, is equivalent to a binding at \bar{x} , where $\psi(\bar{x}) = 1$ (see equation (2.5)). Hence the expectation of the particle's mass, to be used in combination with any equation from chapter 2, is also Δm . Differentiation of equation (4.1) with respect to the mass $\partial_m \omega_0$, leads to the smallest detectable particle mass in expectation

Sensitivity
in expecta-
tion

$$\frac{\Delta m}{m} = -2 \frac{\Delta \omega_0}{\omega_0} \quad (4.4)$$

where $m = m' L = \rho A L$ is the NEMS's mass. The resolution for optimally mid-length functionalized tubes is given by multiplying the right hand side of equation (4.4) by $\sqrt{\frac{3}{8}}$, in accord with equation (2.5).

An upper bound on sensitivity is set by the NEMS dynamics and defined by thermomechanical and adsorption-desorption noise, temperature fluctuations and momentum exchange [82]. A practical limit is set by the sensor circuitry noise and is assessed in chapter 5, via the recorded jitter $\tilde{\sigma}$ at a given observed oscillation period \tilde{T}_0 . Under the hypothesis that crossover fluctuations follow a normal distribution, the oscillator's output signal's period is a random variable, following a gaussian distribution of mean μ and variance σ^2

Resolution

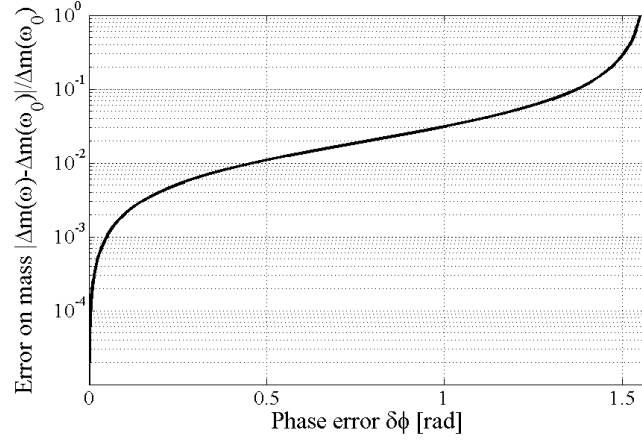
$$T \sim \mathcal{N}(\mu, \sigma^2) \sim \mathcal{N}\left(T_0, \left(\sqrt{\frac{T_0}{\tilde{T}_0}} \tilde{\sigma}\right)^2\right) \quad [\text{s}] \quad (4.5)$$

The estimation error on a NEMS eigenfrequency ($\omega_0 = \frac{2\pi}{T_0}$) via the electronic interface, decreases consequently with the square root of the number of observed periods N , resulting in a relative frequency error of

$$\frac{\Delta \omega_0}{\omega_0} \approx \frac{\Delta t}{T_0} = \alpha \cdot \frac{\sigma}{T_0} \cdot \frac{1}{\sqrt{N}} \quad (4.6)$$

where α represents the desired certainty, which amounts to 99.7% for $\alpha = 3$. Defining an observation time t_{meas} , during which crossovers are counted, the number of observations writes $N = \frac{t_{\text{meas}}}{T_0}$. Feeding equation (4.4) with these expressions leads to a 3σ confidence mass

Figure 4.5: Closed-loop systems enable unbiased quantitative mass sensing if they lock precisely onto the NEMS eigenfrequency. Failure of doing so leads to a bias in the measurement and a relative error, increasing with the frequency offset from the eigenfrequency, expressed here as an error in phase with respect to Table 3.1.



resolution

$$\left| \frac{\Delta m}{m} \right|_{3\sigma} = 6 \cdot \frac{\tilde{\sigma}}{\sqrt{T_0}} \cdot \frac{1}{\sqrt{t_{\text{meas}}}} \quad (4.7)$$

that improves with the square root of measurement time. The expression of equation (4.7) is valid only for sufficiently short integration times, before the $1/f$ flicker noise dominates, which, for CNT-NEMS biased to microamperes, is on the order of $100\mu\text{s}$ [81] [83].

Sensor bias Although convergence occurs with the square root of time, it is even more important that the asymptotic value is correct. A closed-loop system infers the adsorbed particle's mass from an observed difference in oscillation frequencies. If the system locks exactly on the NEMS eigenfrequency, then the inferred particle mass is indeed given by equation (4.4). If on the other hand, the system locks on a frequency ω slightly off the NEMS eigenfrequency ω_0 , then translation of the observed shift in frequency into a particle mass, carries an error of

$$\left| \frac{\Delta m(\omega) - \Delta m(\omega_0)}{\Delta m(\omega_0)} \right| = \frac{2}{Q} \cdot \tan(\delta\Phi) \quad (4.8)$$

derived from the NEMS equation of motion (2.11). Q is the NEMS quality factor and $\delta\Phi$ the difference between the NEMS phase at resonance (provided by Table 3.1) and the real NEMS phase, as imposed by the feedback loop. The relative error of equation (4.8) is shown for a CNT-NEMS with typical quality factor $Q = 100$. Taking the example of a blood analysis, a loop phase error of 1 radian would for instance mistake a lactic acid [$\text{CH}_3\text{CH}(\text{OH})\text{COOH}$] molecule, weighing 90.08Da, for a glycerol [$\text{C}_3\text{H}_8\text{O}_3$] molecule of 92.09Da. It is concluded that quantitative mass sensing is more demanding than voltage controlled oscillation, in the sense that it requires the closed-loop system to lock precisely on the NEMS eigenfrequency. Given the circuit component delays, an *a priori* compensation of the phase offset is infeasible and calibration via feedback becomes necessary.

Speed The novel design aspect in sensor applications is speed. Mass balances shall not only be precise, but shall sense also rapidly. It has previously been shown (equation (4.7)) that the

4.2. The Quest of the Ideal Oscillator Topology

estimate of the sensed mass improves with the square root of time. But for such an estimate to be unbiased, the observed frequency has to correspond to the NEMS eigenfrequency. So a second ingredient to fast sensing is the time it takes to locate the eigenfrequency. If the lorentzian peak is located via a frequency sweep, then it may take seconds. Today's fastest technique uses a computer-aided feedback loop and locates the eigenfrequency within tens of milliseconds. This chapter proposes an approach locating the eigenfrequency within a few oscillations of the NEMS, which is on the order of 100ns and 10^5 times faster than the existing state-of-the-art.

The performance achieved by the voltage controlled electromechanical oscillator and the mass balance are assessed in chapter 5. The present chapter continues on the analysis of an appropriate oscillator topology, able to metamorphose into the previously described applications.

Case study

4.2 The Quest of the Ideal Oscillator Topology



The ideal oscillator topology shall be tunable in frequency and sensitive to the environment, in prospect of its operation as voltage controlled oscillator (VCO) and high-speed high-resolution mass balance. If CNT-NEMS oscillators had already reached industrial production levels, then yield, compactness and power consumption were further design criteria. But today, a mere proof of concept of closed-loop operation would already be a sound achievement. So criteria like testability and the ease of debugging come to the fore.

Selection criteria

4.2.1 The sobriety of self-sustained oscillation



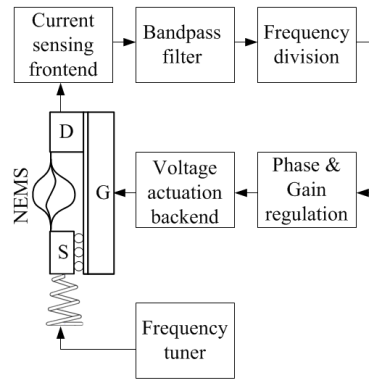
The pursuit of VCO applications hints at the desire to create an observable tunable frequency generator at the limits of nanoelectromechanical systems. Obtaining observability only at a lower, intermediate frequency, would probably not meet the desires of NEMS VCO designers. Exploiting the NEMS below its eigenfrequency in high-speed mass sensors, would be perceived as just as suboptimal by particle balance designers. The prospects of maximal performance, strongly motivate the use of direct readout techniques, rather than CNT mixer operation.

Direct readout is trump

The sparsest oscillator topology for industrial application, using direct readout, would probably resemble the self-sustained oscillator of Figure 4.6. It is formed by a single feedback loop and contains no functional redundancy. The oscillating NEMS's current modulation is sensed by the biasing front-end, presented in chapter 3. A bandpass filter attenuates spurious, non-motional information, and enhances the signal-to-noise ratio, just as discussed in chapter 3. If the motional information is inferred above the eigenfrequency (e.g. by the piezoresistive effect), or if a half-frequency actuation scheme is used, then the signal's frequency needs to be reduced by a factor two or four, according to Table 3.1. The gain and phase need to be adjusted to ensure steady-amplitude oscillation at the NEMS's eigenfrequency, before the signal is fed back onto the gate electrode, to close the loop. A tensile actuator can be used

Topology

Figure 4.6: Self-sustained single-feedback oscillation loops offer minimal component count. They need to be augmented by a starter circuit, to ensure the loop locks onto the NEMS's motion and not on a spurious signal. The NEMS signal is amplified and relieved from noise and spurious signals. Frequency division reverses the optional frequency multiplication of the NEMS, while gain and phase regulators ensure loop-lock on the NEMS eigenfrequency.



to pull the movable source electrode, and tune the eigenfrequency by straining the tube, as illustrated by Figure 2.9a.

Barkhausen phase criterion It is a considerable challenge to make such minimalistic self-sustained loops oscillate precisely on the NEMS eigenfrequency. The first Barkhausen criterion states that oscillation will occur at the frequency at which the overall loop phase delay is congruent modulo 2π radians. This is very likely to happen at a frequency close to the NEMS eigenfrequency, as the NEMS phase inflects here and sweeps over π radians, shown by Figure 1.7, while being quasi constant otherwise. A sweep over π radians is admittedly not enough to satisfy the Barkhausen criterion, which requires flexibility in a 2π interval. This is without considering the fact that the actuating electrostatic force (equation (2.51)) is purely attractive and invariant with respect to a phase shift of π . Hence this relaxed Barkhausen criterion will be satisfied by a frequency close to the NEMS's eigenfrequency. The closer it gets, the stronger the motional signal is, and the less stringent are the constraints on the noise filter. The phase compensation block must hence supplement to π the NEMS's phase delay at resonance, summarized in Table 3.1, by accounting for the phase delay of all individual circuit components. If the phase is nearly correctly compensated, then the NEMS signal is strong enough to allow operation as a VCO. For quantitative unbiased mass sensing, absolute compensation is necessary. Section 4.3 presents a technique which learns a phase that is good enough to sustain closed-loop oscillation, and section 4.4 unveils a calibration technique cancelling phase errors ($\delta\Phi \rightarrow 0$).

Barkhausen gain criterion The second Barkhausen criterion requires that, at the oscillation frequency, the feedback loop complements the NEMS gain to unity at steady-state. Gain regulation becomes subsequently necessary, as high gain is required in the start-up phase, where the weak NEMS signal requires heavy amplification, while low gain is necessary once the signal exceeds the target oscillation amplitude. This target oscillation amplitude has a lower bound set by the thermomechanical noise (equation (2.12)), and an upper bound given by the inset of Duffing nonlinearities (equation (2.10)), which entail hysteretic behaviour (Figure 2.7) and may ultimately result in dynamic pull-in and NEMS destruction.

Open-loop start-up The requirement for large gain at start-up, has a more profound implication. Large gain and reduced filter bandwidth would indeed help a purely electrical oscillator to start. Contrariwise,

4.2. The Quest of the Ideal Oscillator Topology

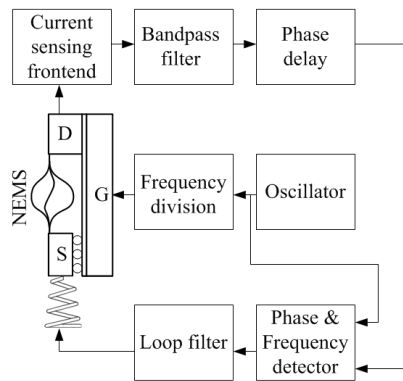
do electromechanical resonators come with additional electrical, non-motional signals. These spurious signals are present even at rest, where the motional signal is absent. As a consequence, if the motional and spurious signals are expected to appear at an identical frequency, as it is the case for field-effect readout under full frequency actuation (Table 3.4), then the initially stronger spurious signal will lead to a purely electrical oscillation at a frequency defined by the loop filter's phase, instead of the NEMS eigenfrequency. Different from the eigenfrequency, mechanical resonance will not build up. If, on the other hand, a frequency divider is used in the loop, because motional and spurious signals are expected at different frequencies, as for piezoresistive readout (Table 3.4), then no electrical signal can satisfy the first Barkhausen criterion either, and no oscillation builds up at all. For both scenarios, the situation requires the use of an open-loop start-up, which could be a slowly varying frequency ramp. Once mechanical oscillation is detected, the loop can be closed to lock on the NEMS eigenfrequency.

Another important design decision is whether analog or digital feedback is preferable. It has been shown in section 2.2.4, that only analog drive allows to perform half frequency actuation. While the tricks, related to this scheme, were judged to be useful for the novel mixing technique (section 3.3.2), it has been concluded (section 3.6), that a full-frequency actuation is recommended for closed-loop applications. So the only remaining disadvantage of digital feedback is the existence of odd harmonics, with order-decreasing strengths. These are not problematic, as the steady state motional information strength always exceeds the spurious signal: If field-effect readout is used, the effect is stronger than the same-frequency spurious effect at the fundamental frequency (Table 3.4), hence the same must hold for the weaker odd harmonics. If piezoresistive readout is considered, readout happens at an even harmonic, and odd harmonics can be filtered within the attenuation requirements of the fundamental. It may thus be concluded that analog and digital feedback loops lead to equivalent system performance, and that the decision is up the designer's choice.

Testing of this closed loop relies on simultaneous correct performance of each and every component, because, if the loop is interrupted at any point, the signal decays with a time-constant $\frac{Q}{\omega_0}$ within less than a microsecond. This leaves little time to identify the failing component, or chain of events that lead to failure, and makes debugging extremely difficult. At times where oscillating CNT-NEMS are still in their fledgling stages, few rare success stories have reported their exclusive operation as mixers, at times where optimization of their design for signal strength is still a dream of the future, the prospect of a CNT-NEMS and a newly developed feedback loop, merging seamlessly into an operational closed-loop VCO or mass balance, seems highly utopic.

So, even though the direct feedback-loop of Figure 4.6, augmented by a start-up mechanism, has the potential to become the future work horse, this approach was judged too risky. An alternative topology, larger, more power-hungry, but self-sufficient for testing, has been devised. The single joint CNT-circuit measurement, reported in chapter 3, certified that this decision was appropriate. Insights gained from this alternative topology may nevertheless

Figure 4.7: Forced actuation ensures incessant oscillation of the NEMS. The actuation efficiency depends on the distance between the forced frequency and the NEMS eigenfrequency. A feedback-loop adjusts the NEMS eigenfrequency accordingly via tensile stiffening. For this adjustment to converge towards the eigenfrequency, the phase delay must complement the NEMS and circuit delays to π .



contribute beneficial findings for self-sustained loop design.

4.2.2 The indefatigability of forced actuation



Additional features The desirable additional features of a versatile robust and debug-capable feedback topology crystallize into:

Self-sufficient testing stands for the option to fully characterize and debug the loop in absence of a CNT-NEMS.

Open-loop NEMS operability is desirable, as it allows to characterize the NEMS in terms of signal strength, frequency and phase delay.

Closed-loop NEMS operability should be possible once the loop and the NEMS have been characterized individually. This aspect will be treated in section 4.3.

Fault tolerance to sporadic obfuscation of the NEMS signal allows to render the oscillator robust to transient noise and perturbations.

Amplitude control shall avoid signal loss due to amplitude degradation or nonlinear hysteresis with subsequent NEMS destruction.

Phase control must ensure oscillation at the NEMS eigenfrequency. This aspect will be treated in section 4.4.

Start-up shall set the NEMS into motion in an open-loop configuration and allow to switch towards closed-loop operation.

Operation principle A candidate topology, offering most of the above features, is shown in Figure 4.7. The NEMS is driven at a given frequency by an oscillator, and a feedback loop is in charge of adjusting the tensile strain in the NEMS so to align its eigenfrequency with the drive frequency. The current out of the NEMS, having experienced a one- to fourfold multiplication inside the NEMS, which is neutralized by the frequency divider block, is sensed just as for the previous topology. Its

4.2. The Quest of the Ideal Oscillator Topology

phase delay is then compared against the actuating drive, to decide whether the NEMS is currently oscillating below or beyond its eigenfrequency. This information is averaged and used to smoothly adjust the command of the tuning MEMS actuator.

This certainly less compact feedback system offers several considerable advantages, and the most prominent one is the drive's independence from the sensed NEMS output signal, rendering the system fault tolerant. Given the constant actuation amplitude, the need for amplitude control vanishes. Closed-loop operation has been described above, and the NEMS can be characterized in open-loop by controlling the tensile actuator externally, sweeping the NEMS eigenfrequency, and reading the loop filter's output, to establish the transfer function. If no NEMS is available, this loop can functionally be tested for debugging purposes, by substituting the NEMS and its tuning MEMS by an electrical VCO for instance. Such a test shows whether the loop can adjust the VCO in accord with the oscillator's frequency, while a big chunk of loop dynamics, related to the NEMS and MEMS transfer functions, are neglected. The utility of such a self-sufficient test is consequently limited to the detection of conceptual design errors, but delivers little information on the true loop performance within the presence of a real NEMS.

Improvements

The phase delay in the two feedback paths, arriving at the phase detector, must be adjusted correctly, to ensure the loop locks as close as possible to the eigenfrequency, just as for self-sustained oscillation. Although steady amplitude actuation is guaranteed, a start-up mechanism is necessary. This could be a voltage ramp, controlling the tuning MEMS through in-/decreasing strains and hence sweeping the eigenfrequency. When sweeping the NEMS's lorentzian past the drive frequency, the second track of the phase detector registers a signal, and the loop can be closed to perform the final adjustment.

Open issues

The system of Figure 4.7 bears the heavy load of operating the tuning MEMS within its feedback path. This does not only complicate the system's dynamics, but it also limits its bandwidth. MEMS are by their size more inert than NEMS, and in the proposed constellation sets an upper limit to the settling speed of the loop. A better topology would combine the forced actuation of the present system with a feedback path excluding the frequency tuning MEMS, as it was the case in section 4.2.1.

Disadvantage

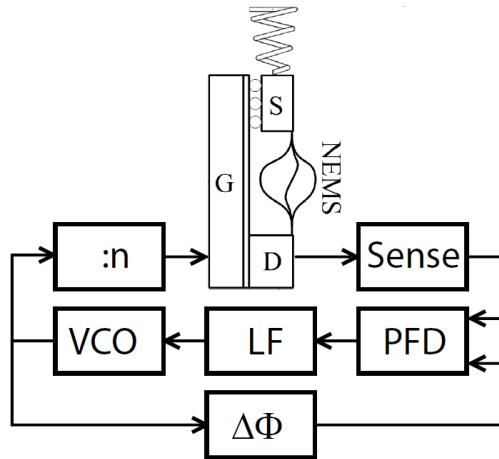
4.2.3 The memory effect of phase-locked loops



The proposed system that can satisfy the previous wish list of features, embeds the CNT-NEMS into a phase-locked loop (PLL). The blocks, ensuring the core functionality, are shown in Figure 4.8. The PLL is formed by a phase frequency detector (PFD), a loop filter (LF) and a voltage controlled oscillator (VCO). It detects and maintains the NEMS motion at a frequency defined by the loop phase $\Delta\Phi$ and the NEMS eigenfrequency. The latter is sensitive to the environment and shifts when a particle binds onto the NEMS, which enables sensor operation of the proposed topology. Further does an actuator offer frequency tuning by straining the NEMS and enables operation as a VCO.

Core topology

Figure 4.8: NEMS operated within a PLL. Oscillation is forced at a frequency that corresponds to a NEMS phase delay of $\Delta\Phi$. A tensile actuator allows to adjust oscillation frequency by tuning the NEMS eigenfrequency. Although open-loop start-up is necessary, this topology comes with built-in amplitude control. Phase control (of $\Delta\Phi$) can be added via a second feedback loop, as shown in section 4.4.



Readout The NEMS signal is sensed via a low-noise front-end, amplified and filtered with respect to the spurious signals and noise, just as for the direct feedback loop of section 4.2.1. The PLL blocks are subsequently analysed in a meet-in-the-middle approach.

PFD The PFD receives two signals. One is the VCO signal $\phi_{VCO}(s)$, arriving with a constant delay $\Delta\Phi$, the other is the NEMS signal $\phi_{NEMS}(s)$, arriving with a frequency-dependent delay. Both signals have the same frequency, as both root in the VCO's signal. The optional frequency divider in the NEMS branch compensates for potential frequency multiplication by the NEMS, depending on the desired readout effect. The PFD can be imagined as a rising/falling edge detector. If such an edge is detected, the internal signal of the respective track goes to logical one. Once both signals are high, they are reset instantly. On the long, this yields signals whose high-time is proportional to their phase advance with respect to the other. Their subtraction is then a square signal that is positive when the NEMS has phase advance ($\phi_{NEMS}(s)$ rises/falls before $\phi_{VCO}(s) + \Delta\Phi$), negative when it leaks phase, and has a time-average value proportional to the phase difference $\delta\phi(s) = \phi_{NEMS}(s) - (\phi_{VCO}(s) + \Delta\Phi)$, with proportionality factor K_ϕ .

$$V_{PFD}(s) = K_\phi \cdot \delta\phi(s) \quad [V] \quad (4.9)$$

VCO On the actuation side, the VCO generates a frequency K_V -proportional to its steering voltage,

$$\omega_{VCO}(s) = K_V \cdot LF(s) \cdot V_{PFD}(s) \quad \left[\frac{\text{rad}}{s} \right] \quad (4.10)$$

where $LF(s)$ is the loop filter transfer function. The simple fact that the VCO drives the NEMS with a constant amplitude, which does not depend on the response amplitude of the NEMS, substitutes the need for any further amplitude control. The constant VCO amplitude has to be chosen within the linear dynamic range, given by Figure 2.26. The phase being the integral of the angular frequency $\omega_{VCO}(s) = s \cdot \phi_{VCO}(s)$, equations (4.9) and (4.10) combine into the PLL

4.2. The Quest of the Ideal Oscillator Topology

$\phi_{\text{NEMS}}(s) - \Delta\Phi$	Type 1	Type 2	Type 3
Phase step $\sim \frac{1}{s}$	zero	zero	zero
Frequency step $\sim \frac{1}{s^2}$	constant	zero	zero
Frequency ramp $\sim \frac{1}{s^3}$	increasing	constant	zero

Table 4.1: PLL phase error as a function of the NEMS sensor event and the PLL type.

transfer function

$$H_{\text{PLL}}(s) = \frac{\phi_{\text{VCO}}(s)}{\phi_{\text{NEMS}}(s) - \Delta\Phi} = \frac{1}{1 + \frac{s}{K_V K_\phi \text{LF}(s)}} \quad (4.11)$$

If the right-hand side of equation (4.11) equals unity, then the VCO follows the NEMS with identical frequency and a constant phase delay of $\Delta\Phi$, which are the perfect conditions for oscillation. The proper choice of $\Delta\Phi$ is consequently essential in the determination of the oscillation frequency. Resonance, precisely at the eigenfrequency, is indeed obtained if, and only if, the loop delay $\Delta\Phi$, augmented by the electronic component delays, equals the NEMS delay at resonance, as reported in Table 3.1. The adjustment of the loop phase $\Delta\Phi$ merits a separate treatment in section 4.4.

Inserted in-between the PFD and the VCO, the loop filter averages the PFD's output, and the way of doing this, has a major impact on the loop dynamics and performance. For the NEMS to oscillate properly, the VCO frequency must closely follow the NEMS output frequency, and equal it at steady-state, $\omega_{\text{VCO}} = \omega_{\text{NEMS}}$. This condition is necessary, but not sufficient. Also must the phase delay between both signals be constant at steady state, and equal $\Delta\Phi$. Before commenting on transients and loop stability, it is essential to provide the necessary conditions on the filter, for the loop to converge towards an appropriate steady state. The phase difference $\delta\phi$ between the two entries to the PFD, may be expressed by rearranging the transfer function (4.11), to express the error function

Loop filter

$$\delta\phi(s) = \frac{1}{1 + \frac{s}{K_V K_\phi \text{LF}(s)}} \cdot (\phi_{\text{NEMS}}(s) - \Delta\Phi) \quad [\text{rad}] \quad (4.12)$$

The PLL's ability to stabilize after phase or frequency jumps and ramps of the NEMS, upon chemisorption of molecules or drift, highly depends on the type of the filter. *Type* is indeed the keyword, and it is defined as the number of the filter's DC poles. A low-pass filter has for instance no pole at DC and is of type 0, and combined with the DC pole already present in

Steady state
& LF type

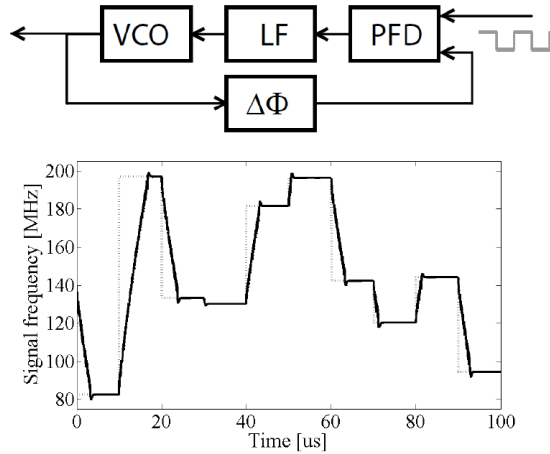


Figure 4.9: PLL tracking of random frequency jumps in open-loop configuration, for loop parameters $\omega_n = 1\text{MHz}$ and $Q_n = \frac{1}{2}$. This simulation uses the parameterset of the PCB implementation of section 5.1.

the denominator term $\frac{K_V K_\phi \text{LF}(s)}{s}$ of the error function, yields a type 1 PLL. Similarly would a first-order integrator filter be of type 1 and yield a PLL of type 2. The notion of *type* shall not be confounded with the notion of *order*, which expresses the order of the polynomial in the denominator of $\frac{K_V K_\phi \text{LF}(s)}{s}$. The steady state error, with respect to an adsorption event, is found via the final-value theorem

$$\delta\phi(t = \infty) = \lim_{s \rightarrow \infty} (s \cdot \delta\phi(s)) \quad [\text{rad}] \quad (4.13)$$

PLL type selection It emanates from Table 4.1, summarizing the steady state errors for different perturbations of the NEMS and PLL types, that a lowpass filter (type 1 PLL) can follow phase jumps. A frequency jump, however, would be followed with an offset. If this offset is larger than the NEMS peak bandwidth $\frac{\omega_0}{Q}$, then oscillation will stop and the NEMS must be restarted. Otherwise oscillation continues, but the observed frequency shift does not reflect the sensed phenomenon. A first order integrator (type 2 PLL) is necessary to quantitatively extract the frequency step, associated with adsorption of a molecule. Such type 2 PLLs can follow drift, which may be caused by a change in temperature for instance, only with a steady latency. This means that a sensor, based on a type 2 PLL, can deliver accurate sensor information only during time intervals where the temperature is constant and the NEMS does not experience drift. It is here conjectured that this assumption can generally be made, given that the microsecond sensing speed (see section 5.4) exceeds the rate of temperature fluctuations in most environmental and *in vivo* neighbourhoods. For unstable environments, where rapid drifts, faster than the sensing rate, may be expected, a type 3 PLL should be used.

Open-loop transients Settling for a type 2 PLL, implemented via a first order intergrator filter,

$$\text{LF}(s) = \frac{1 + \tau_2 s}{\tau_1 s} \quad (4.14)$$

allows to follow phase and frequency jumps. Substituting equation (4.14) in (4.11), yields the

4.2. The Quest of the Ideal Oscillator Topology

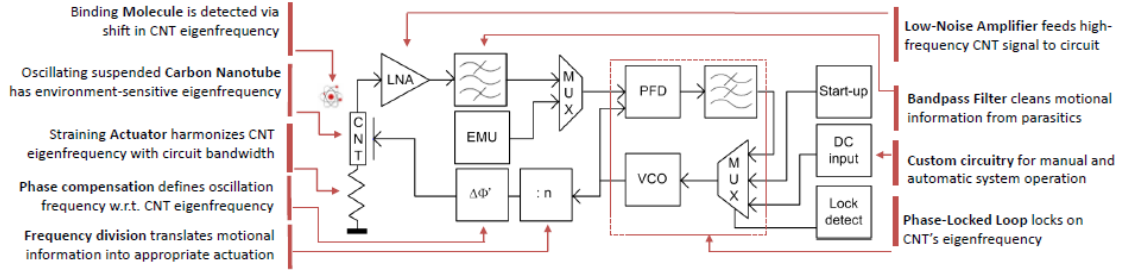


Figure 4.10: CNT-NEMS operated within a PLL with peripheral control and start-up blocks, and NEMS emulator.

type 2 PLL transfer function

$$H_{\text{PLL,t2}} = \frac{\phi_{\text{VCO}}}{\phi_{\text{CNT}}} = \begin{cases} \frac{s\omega_n + \omega_n^2 Q_n^2}{s^2 + s\omega_n + \omega_n^2 Q_n^2} & \text{if } Q_n \leq 1 \\ \frac{s\omega_n + \omega_n^2}{s^2 + s\omega_n + \omega_n^2} & \text{else} \end{cases} \quad (4.15)$$

where $Q_n = \sqrt{\frac{\tau_1}{K_V K_\phi} \frac{1}{\tau_2}}$ is the loop quality factor and ω_n (equal to $\sqrt{\frac{K_V K_\phi}{\tau_1}}$ if $Q_n \geq 1$ and $K_V K_\phi \frac{\tau_2}{\tau_1}$ if $Q_n \leq 1$) is the loop natural frequency. For stability to be guaranteed, the loop natural frequency ω_n must not exceed the oscillation frequency and hence the NEMS eigenfrequency. The loop quality factor expresses the PLL's nervousity. A low Q_n entails slow convergence of the VCO towards the NEMS eigenfrequency, while high Q_n enables higher reactivity, resulting in overshoot and an oscillatory stabilization. In between, and for $Q_n = \frac{1}{2}$, the PLL is critically damped, meaning that the VCO converges to the NEMS frequency as fast as possible without oscillating. Figure 4.9 shows how a critically damped PLL tracks frequency jumps of a resonating NEMS, caused by tensile actuation, with a loop natural frequency of 1MHz, in an open-loop configuration. This setup allows to characterize the loop's performance independently of the NEMS characteristics, and reflects the typical operation of signal tracking by a PLL. It has however to be conceded that, in a NEMS-VCO, the NEMS signal cannot be considered as a given reference signal, but it strongly depends on the VCO's driving, and hence the PLL's tracking capabilities under closed-loop operation. Closed-loop performance is assessed in section 4.3.

Figure 4.10 shows how the peripheral blocks are grafted onto the core topology in order to provide the desired additional functionalities. Open-loop circuit performance can be assessed by substituting the NEMS by an emulator, which can be a simple VCO. Closing the loop around the NEMS, but opening it within the PLL, provides a handy setup, which allows to spectrally characterize the NEMS by feeding a DC input voltage and reading a lowpass filtered average NEMS output. It is noteworthy that this way of characterizing the NEMS provides information equivalent to mixing topologies. The difference is that, in the case of Figure 4.10, mixing happens outside of the NEMS. This has the great advantage that the NEMS can be biased to the saturation regime, which, after all, is the regime of interest. Given that the NEMS is driven by a VCO, the actuation amplitude is constant and supersedes the need of amplitude control. A voltage ramp allows to perform a spectral frequency sweep, and a lock detector block can be

Peripheral blocks

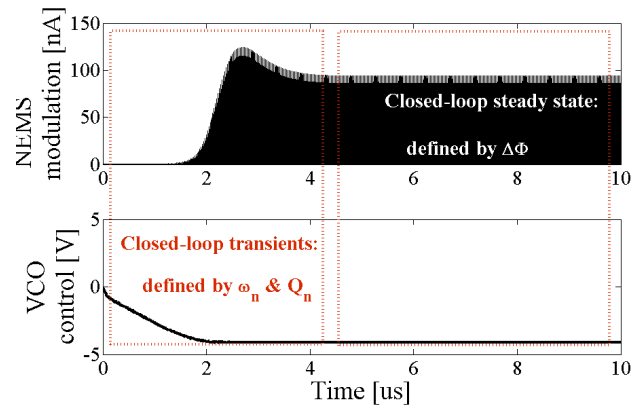


Figure 4.11: In closed-loop, the PLL tracks the NEMS signal, and the NEMS is stimulated by the PLL. The system's transient response depends on the PLL's reactivity (section 4.3), while the system's steady state is defined by the loop phase delay (section 4.4).

used to switch from open- to closed-loop operation when a motional signal is detected during the frequency ramp.

Assessment It has been shown that the embedding of the NEMS into a PLL entails some beneficial features, out of which self-sufficiency for testing is the major improvement over the self-sustained oscillator. Furthermore does the topology of Figure 4.10 offer a handy way to characterize the NEMS in any operation regime. Start-up is performed by a simple frequency ramp and a lock-detector automatically closes the loop. If the NEMS happens to skip a beat, and no signal is measured at the PFD, the VCO continues indefatigably to stimulate the NEMS, and the signal may be retrieved. Closed-loop operation has not yet been addressed and will form the topic of the subsequent sections. Optimal design of PLL parameters, like the natural loop frequency ω_n and quality factor Q_n , which define the closed-loop transients, are examined in section 4.3 and the adjustment of the loop phase $\Delta\Phi$ for eigenfrequency-centered resonance, is discussed in section 4.4. The impact domain of these parameters is illustrated by Figure 4.11, showing a closed-loop start-up of a noiseless system.

Heavy molecules caveat The previous paragraphs showed that NEMS can be embedded into PLLs to form highly sensitive sensors, with minimal mass detection thresholds, given by equation (4.7). Also has the need for open-loop start-up been brought forward. Arises hence the legitimate question on what happens when a heavy molecule binds to the CNT-NEMS, shifting the eigenfrequency further than the NEMS bandwidth $\Delta\omega_0 \gg \frac{\omega_0}{Q}$. In this case, the NEMS signal becomes obfuscated and the PLL would lose lock. Examining the PLL topology of Figure 4.8, shows that this scenario corresponds to the extreme case of the situation where the NEMS leaks phase, which forces the PLL to slow down. Equation (4.4) brings now the relieving insight that a binding particle decreases the eigenfrequency, meaning that the new eigenfrequency lies on the path of the PLL, and can be detected seamlessly. Desorption of heavy particles, on the other hand, requires a new start-up. Whether this is an inconvenience or not, depends on the sensor application, and needs to be assessed in the future.

Design variations For completeness, it may be mentioned that the frequency division block, placed on the actuation side in Figure 4.10, could also be shifted to the readout side. The implication would

be that the PLL can run at a lower frequency. This may be beneficial to avoid challenges arising at GHz NEMS frequencies, but may be a disadvantage for low frequency NEMS in terms of chip area, when an LC tank implementation is chosen for the VCO. In addition has the PLL division factor, on the feedback path from the VCO to the PFD, been chosen to unity. Higher ratios are also acceptable, and lead to higher VCO operation frequencies with respect to the NEMS eigenfrequency. The division factor n in the NEMS feedback path must be adjusted in accordance with the PLL division ratio. A printed circuit board (PCB) and an integrated circuit (IC) implementation of the presented topology are provided in section 5.1 and 5.2 respectively.

4.3 Closed-loop System Optimisation



Limited above-threshold NEMS observability and closed-loop NEMS-controller interaction put PLL design in a new perspective, beyond the usual tracking of a reference signal and concepts like settling time, overshoot and phase margin. In closed-loop oscillator setups, the PLL not only needs to track the NEMS signal, but it also needs to steer this NEMS and keep it resonating. This reciprocal interdependence of the PLL and the NEMS leads to complex system dynamics, which are studied subsequently. A purely analytical study of the system is not possible, because the NEMS transfer function operates on a signal (the drain current), while the PLL transfer function acts on the phase of this signal. Numerical simulations are used to allow inspection of the impact of PLL design criteria.

Chicken
or
the egg?

The system architecture, as well as simplified NEMS and controller models, are presented in section 4.3.1. Section 4.3.2 covers the start-up of the NEMS oscillation under the existence of a detectability threshold. Robustness to noise, phase lag and circuit delays, is assessed in section 4.3.3. A practical design strategy is finally proposed in section 4.3.4.

Overview

4.3.1 Models and system design



The closed-loop system of interest is formed by a NEMS which is tracked and driven by a PLL as illustrated by Figure 4.12a. The signal out of the NEMS is characterized by its amplitude A and phase ϕ , writing $Ae^{i\phi}$. If the signal strength A exceeds the sensitivity threshold of the front-end circuitry (chapter 3), the signal is transmitted to the PLL, whose task it is to follow the signal's phase. The output of the PLL is a signal of constant amplitude and a phase that depends on the history of the NEMS phase. This signal stimulates the NEMS then. Depending on how accurately the PLL is able to follow the NEMS phase, resonance may build up or not.

Principle

The dynamics of the NEMS, a CNT suspended over a trench, may be approximated by the ones of a damped second order harmonic oscillator [84] with eigenfrequency ω_0 and damping factor $\zeta = \frac{1}{2Q}$. A nearby electrode allows to electrostatically drive the NEMS to resonance, while the motion of the tube may be inferred from the field effect (at ω_0) or piezoresistive (at $2\omega_0$) modulation of the current flowing through it, as has been concluded in section 3.6. For the

Simplified
NEMS
model

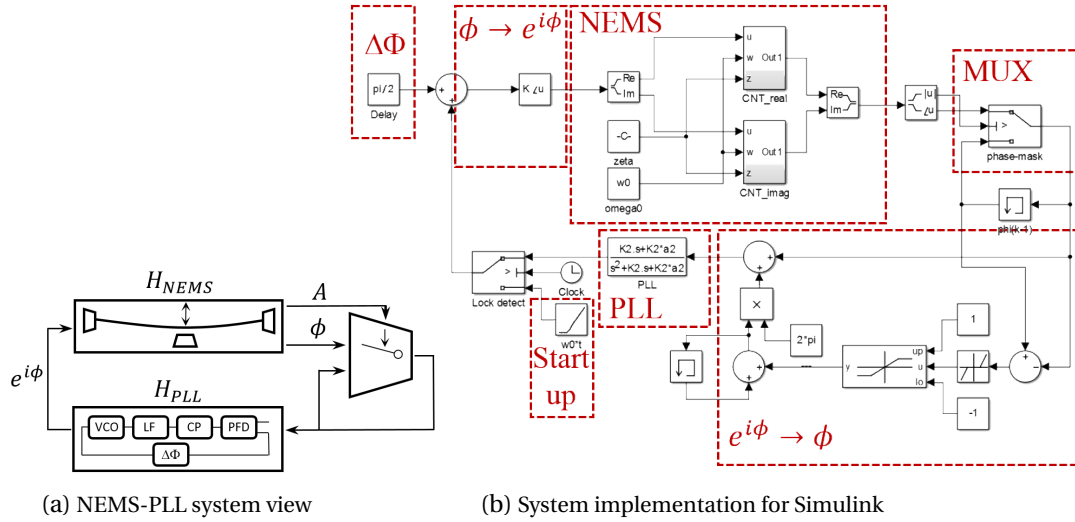


Figure 4.12: Closed-loop interplay between NEMS and PLL

sake of clarity and without loss of generality, NEMS actuation and readout are hypothesized to happen at the same frequency for the subsequent analyses. Additionally has the CNT transfer function been normalized to yield a unity oscillation amplitude at resonance, writing

$$H_{\text{NEMS}}(s) = \frac{2\omega_0\zeta(1-\zeta^2)}{s^2 + 2\zeta\omega_0s + \omega_0^2} \quad (4.16)$$

It has a maximal response at frequency $\omega_r = \omega_0\sqrt{1-2\zeta^2}$ with a phase lag of $\arctan\sqrt{\frac{1}{\zeta^2}-2}$ (taken in $[-\pi..0]$). CNT-NEMS eigenfrequencies appear to range from several MHz [1] up to the GHz [85] domain, and their ambient temperature damping factor generally lies around $\frac{1}{100}$ [1], implying $\omega_r \approx \omega_0$ where the phase lag is $\sim \frac{\pi}{2}$ in the case of equation (4.16). In reality this value depends on the actuation and readout schemes, and may be looked up from Table 3.1. Furthermore does the maximal oscillation amplitude A generally not exceed the circuit detection threshold and noise floor by orders of magnitude for these CNT-NEMS, as emanates from Figure 3.7. This implies that the signal is not visible to the PLL through the front-end during start-up, a design constraint to be accounted for.

PLL model The PLL is composed of a phase-frequency detector (PFD) of proportional gain K_ϕ , followed by a charge pump (CP), a loop filter $LF(s)$ and a voltage controlled oscillator (VCO) with integral gain K_V . The optional divider ratio is taken as unity and the loop delay is $\Delta\Phi$. Given that the PLL dynamics are largely imposed by the loop filter, and that it has been concluded in section 4.2.3 that a second order type two PLL is widely adequate for VCO and mass balance applications, two first order filters are considered henceforth, leading to second order PLLs of types 1 and 2 with open-loop $G_{\text{PLL}}(s)$ and closed-loop $H_{\text{PLL}}(s)$ transfer functions in terms of signal phase, summarized in Table 4.2.

System design The Simulink implementation of the system topology of Figure 4.12a, is provided by Fig-

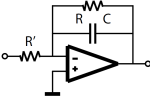
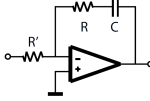
Filter LF (s)	$-\frac{R}{1+sRC}$	$-\frac{1+sRC}{sR'C}$
Sample implementation		
$G_{PLL}(s)$	$\frac{K}{s(s+a)}$	$\frac{K(s+a)}{s^2}$
	$K = \frac{K_\phi K_V}{R'C}$	$K = \frac{K_\phi K_V R}{R'}$
	$a = \frac{1}{RC}$	$a = \frac{1}{RC}$
$H_{PLL}(s)$	$\frac{K}{s^2+as+K}$	$\frac{Ks+Ka}{s^2+Ks+Ka}$
Damping	$Q_n = \frac{\sqrt{K}}{a}$	$Q_n = \sqrt{\frac{a}{K}}$
Bandwidth	$\omega_n = \begin{cases} \frac{K}{a} & , Q_n \leq 1 \\ \sqrt{K} & , Q_n \geq 1 \end{cases}$	$\omega_n = \begin{cases} K & , Q_n \leq 1 \\ \sqrt{Ka} & , Q_n \geq 1 \end{cases}$

 Table 4.2: Type 1 (left) and type 2 (right) second order PLL open $G(s)$ and closed-loop $H(s)$ transfer functions.

ure 4.12b. It shall allow to analyse the performance of these PLLs in a NEMS steering context, in order to make a selection of good and poor parameter value choices. To start with, it is important to realize that H_{NEMS} acts on a signal, while H_{PLL} operates on that signal's phase! The implementation of the NEMS transfer function, as described by equation (4.16), is presented in [84]. The NEMS is driven by a complex signal (voltage) of unity amplitude and a phase as chosen by the PLL. Both, the signal's real and imaginary parts, pass the same purely real implementation of the CNT-NEMS transfer function, before combining again (drain current) into a signal of amplitude A and phase ϕ . If the amplitude is sufficient for the front-end of chapter 3 to detect the signal, ϕ is transmitted, and its precedent value otherwise. The following blocks unwrap the phase that was folded so far onto the interval $[-\pi.. \pi]$. Next the PLL generates a phase in response to ϕ and its history, according to H_{PLL} . A final adjustment compensates for the NEMS's phase lag at resonance, given by Table 3.1 and equal to $\frac{\pi}{2}$ for the case of the simplified model of equation (4.16).

4.3.2 From open- to closed-loop



Given that noise processes, such as thermomechanical fluctuations, are not strong or coherent enough to induce the NEMS into spontaneous detectable motion, the system needs a starter Loop closure

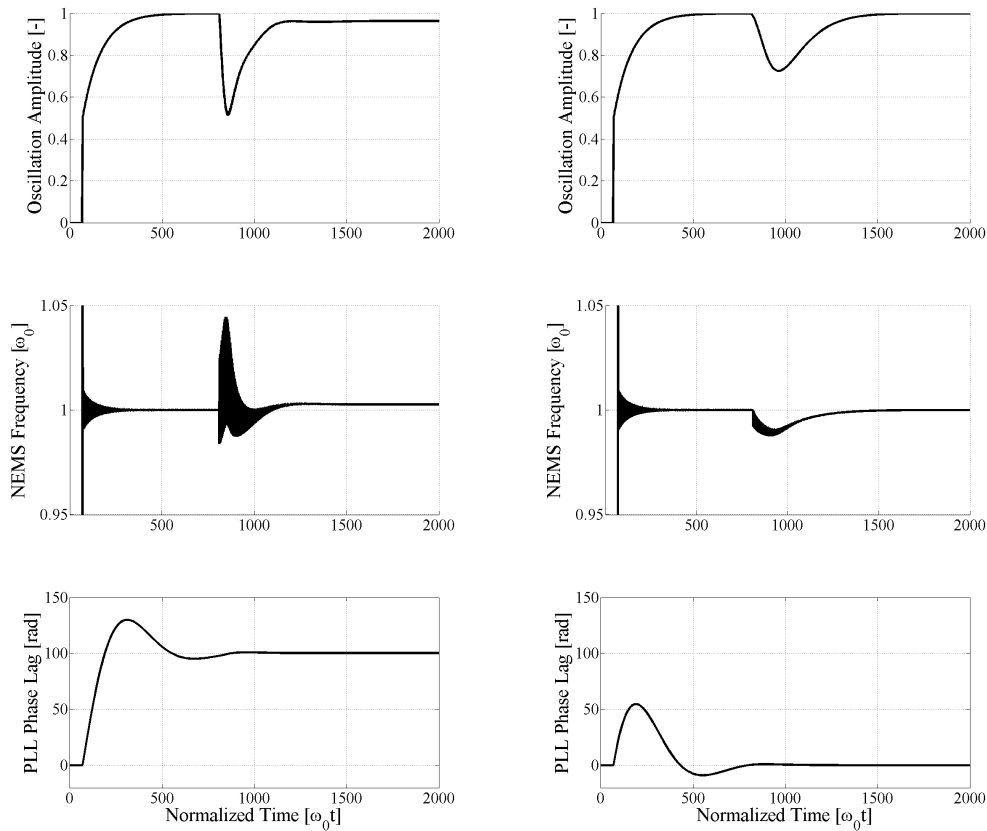


Figure 4.13: Loop closure system transients with type 1 (left) and type 2 (right) second order PLLs with $\omega_n = \frac{\omega_0}{100}$ and $Q_n = 1$

mechanism. This could be an open-loop frequency sweep in combination with a lock detection circuit, as proposed in [86]. Figure 4.13 shows the start-up and locking behaviour of the system with slightly underdamped ($Q_n = 1$) PLLs of types 1 and 2 and identical natural frequency $\omega_n = \frac{\omega_0}{100}$. The NEMS is gradually brought to motion via a start-up ramp and the front-end detection threshold set to half the maximum signal amplitude at resonance. As soon as a signal is detected, the PLL sets to its pursuit. After $N = 130$ oscillations of the NEMS, occurring in a time of $\frac{2\pi}{\omega_0}N$, not all of which were visible to the PLL, the loop is closed and the PLL henceforth drives the NEMS. Though a steady state is reached in both cases, only type 2 PLLs reach full amplitude oscillation, which stands for zero frequency error and compensated phase lag. This result has been expected by Table 4.1. Type 1 PLLs do not fully compensate for oscillations they slipped through, and finally lock on a frequency close to, but not precisely at, ω_0 . This steady-state frequency error translates into oscillation at reduced amplitude. It may thus be concluded that, under the settings of Figure 4.12b, with delay- and noiseless loop components and a loop phase adjusted according to Table 3.1, any second order PLL may successfully maintain NEMS oscillation, but solely type 2 PLLs lock on a frequency that is exclusively imposed by the NEMS itself, unobstructed from PLL-related artefacts.

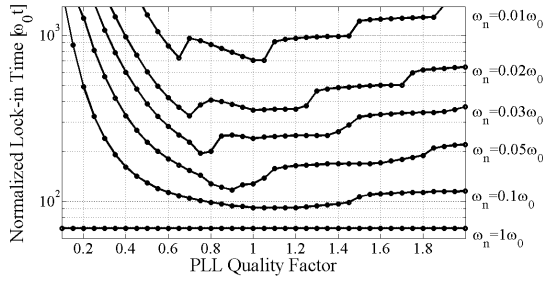


Figure 4.14: Lock-in time as a function of Q_n for several ω_n for type 2 PLLs. The minimal time a PLL needs to observe an oscillating NEMS in open-loop, before the loop can be closed successfully, decreases with the PLL speed ω_n and is minimal for slightly underdamped $Q_n \approx 1$. Loop closure is defined as successful when no transient signal fallback below the 50% threshold occurs. This arbitrary criterion causes discontinuities in the result graph, because the memory effect of PLLs could revive a signal which temporarily dived below the threshold.

With the scope of designing a system capable of quantitative sensing, for which the NEMS eigenfrequency needs to be detected precisely, focus lies on type 2 PLLs. Section 4.3.3 shows how to handle phase lag of type 1 PLLs, and amplitude- and phase-noise in sensing setups. On the quest of the ideal PLL parameters for fast lock-in, Figure 4.14 provides the precious insight that fast PLLs, with natural frequency ω_n scraping the NEMS eigenfrequency ω_0 , provide the shortest lock-in times. The number of observable oscillations necessary to ensure loop closure, without transient fallback below the 50% signal threshold, is presented as a function of the eigenfrequency ratio $\frac{\omega_n}{\omega_0}$ between PLL and NEMS. It is noteworthy that critical damping ($Q_n = 0.7$) ensures fastest lock-in only in relatively slow PLLs, while the PLL nervousness, powered by higher Q_n , provides faster system lock-in when ω_n starts approaching ω_0 .

Optimal
 ω_n & Q_n

4.3.3 Robustness to circuit noise and delays



Once oscillation is established, whatever the purity of the mechanical NEMS oscillation is, the input signal to the PLL will always be immersed in some electrical noise, from the NEMS or the circuit front-end. Hypothesizing NEMS operation above the devices' corner frequency, the noise may be modeled as a white distribution up to ω_0 that modulates the oscillation amplitude. For the purpose of analytical accessibility, further suppose the noise process to have a uniform distribution with zero mean and width $\Delta = 2\sqrt{3}\sigma$. Parseval's identity tells that such a noise's power is σ^2 . It is assumed that the PLL's PFD samples the noisy signal $(A + \delta(t))e^{i\phi}$, $\delta(t) \in [-\Delta, \Delta]$, at its zero-crossing, where the signal's slope is $A\omega_0$ at resonance. Under the above uniform white noise, this zero-crossing may happen in the time window $\left[-\frac{\Delta}{2A\omega_0}, \frac{\Delta}{2A\omega_0}\right]$ around the noiseless crossing moment, as shown in Figure 4.15a. Sampling this interval at N uniformly spaced instants $t_{k \in [1, N]} = -\frac{\Delta}{2A\omega_0} + \frac{k}{N} \frac{\Delta}{A\omega_0}$, each sample's mean amplitude is $A\omega_0 t_k = -\frac{\Delta}{2} + \Delta \frac{k}{N}$, which leads to a probability $p_k = \frac{k}{N}$ that the sample's amplitude exceeds the zero-crossing threshold. Consequently, the probability that the zero-crossing happens exactly at time t_k is the probability that none of the previous samples triggered the PFD $\prod_{j=1}^{k-1} (1 - p_j)$ times the probability that the k^{th} sample triggers it, p_k . The cumulative probability is plotted in Figure 4.15a for large $N = 10^4$. In continuous reality, the cumulative probability function converges to the unit step function. One may thus expect the crossing to happen close to t_1 , which means that the amplitude noise translates into a phase advance of $-\frac{\Delta}{2A\omega_0}$.

From
amplitude-
to phase-
noise

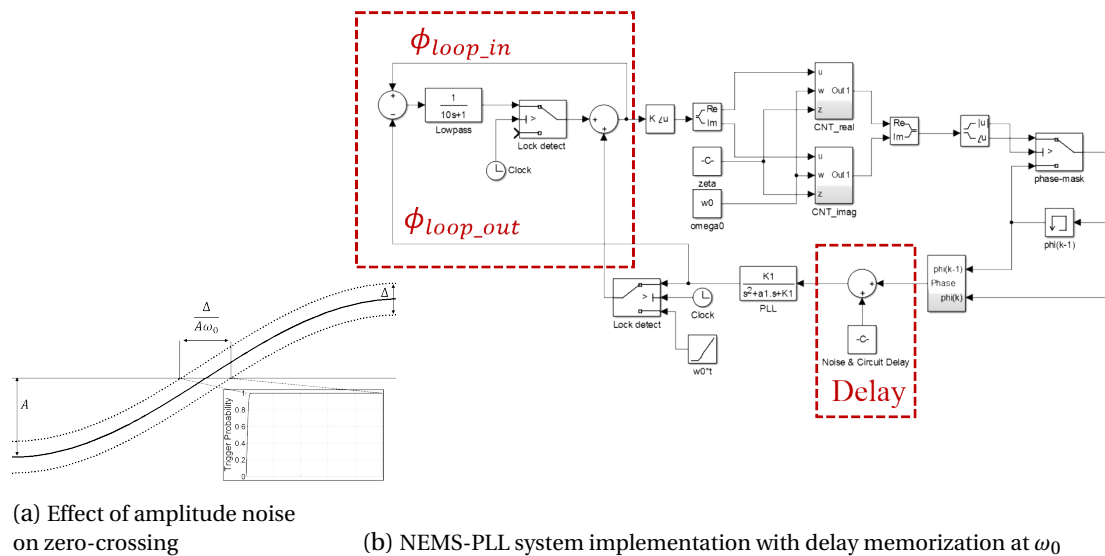


Figure 4.15: Loop delays and their compensation by memorization.

Delay This phase advance does not make type 2 PLLs any better than type 1 PLLs, as the observed memorization overall loop delay at NEMS resonance now deviates from the ideal value, tabulated in Table 3.1. The delay caused by the front-end circuitry, so far neglected, would also contribute to this same phenomenon. So need for a solution urges. The topology presented in Figure 4.12b is flexible enough to permit a simple modification that allows to memorize the overall open-loop loop delay, and to compensate for it, so to create an overall loop phase delay congruent modulo 2π or π (relaxed Barkhausen criterion). A low-pass filter may be used as a leaky memory that remembers the loop delay during start-up precisely at ω_0 . This delay, accounting for amplitude noise, component delays and PLL lag, is then compensated for, instead of the ideal value of Table 3.1. A system implementation is given in Figure 4.15b, where the memorized loop delay is injected as soon as the loop locks. It may be noted that the compensated value in open-loop configuration is irrelevant and may be grounded. For this memorized loop delay to be correct, the system must be given the time to fully settle during start-up at ω_0 , which consequently requires longer start-up times than the earliest stable lock-in times provided by Figure 4.14.

Assessment The efficiency of this adaptive phase compensation is depicted by Figure 4.16, showing the system dynamics for a noisy type 1 PLL, with fixed $\frac{\pi}{2}$ versus adaptive compensation. It becomes apparent that, if started at ω_0 , this slight change in the system puts type 1 and type 2 PLLs again on a par with respect to closed-loop oscillator operation. If the oscillator shall be tunable (VCO), then this system extension allows type 2 PLLs, but not type 1 PLLs, to follow the frequency shift without loss in amplitude. If the start-up frequency, at loop closure, corresponds exactly to ω_0 , then unbiased quantitative mass sensing becomes possible by noisy systems thanks to delay memorization. The memorized phase loop corresponds indeed to the frequency at which the lock-detector is triggered. If a start-up is performed through a frequency sweep, loop closure is likely to happen already on the rising slope to the lorentzian amplitude peak, which makes the system lock close to, but off the eigenfrequency. It

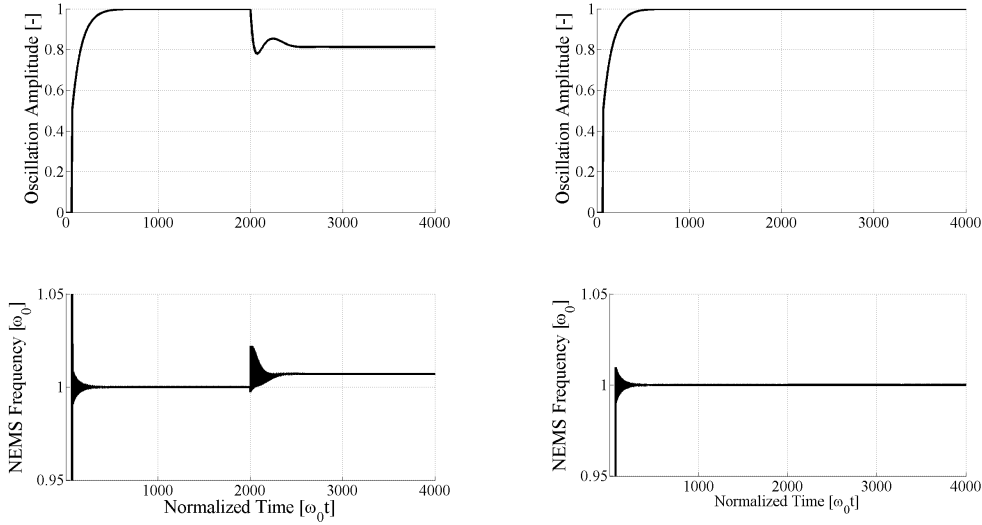


Figure 4.16: System dynamics for noisy type 1 PLL without (left) and with (right) delay correction, with $\omega_n = \frac{\omega_0}{100}$ and $Q_n = 1$

is concluded that the proposed phase memorization technique may reduce the offset from the eigenfrequency, and guarantees loop closure without oscillation loss. Unbiased quantitative sensing can nevertheless not be guaranteed. An enhanced loop-phase calibration technique is presented in section 4.4. Whatever the frequency at loop closure is, this technique regulates the loop delay so to ensure oscillation at the NEMS eigenfrequency, enabling unbiased mass sensing.

4.3.4 Optimal PLL design under limited bandwidth



On the way to a practical system implementation, it is instructive to enlighten the impact of the physical constraints onto the choice of ω_n and Q_n . The closer ω_n gets to ω_0 , the better the partial observability is handled by the loop, as has been shown by Figure 4.14. The open-loop gain Bode plot of type 2 PLLs is illustrated by Table 4.3. The limit of how close ω_n can get to the NEMS eigenfrequency, is imposed by the unity gain frequency ω_T of any amplification stage in the feedback path, which may for instance be the operational amplifier used in the filter implementation (see Table 4.2). It introduces a pole in the filter transfer function and consequently the PLL open-loop transfer function $G_{PLL}(s)$, at $\omega_T \frac{R'}{R}$. It seems wise to require the parasitical pole to lie a decade above the loop's natural frequency, in order not to influence the PLL's phase margin by more than 5 degrees.

Bandwidth limitation

$$10\omega_n \leq \omega_T \frac{R'}{R} \quad \left[\frac{\text{rad}}{\text{s}} \right] \quad (4.17)$$

The maximum obtainable PLL bandwidth within this constraint is given by Table 4.3, along

Optimal PLL design

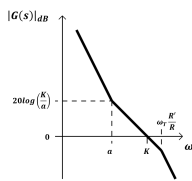
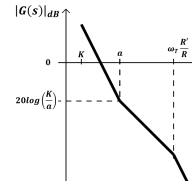
	$Q_n \leq 1$	$Q_n \geq 1$
$ G(s) $		
$\frac{R}{R'}$	$\sqrt{\frac{\omega_T}{10K_{\text{PFD}}K_{\text{VCO}}}}$	$\sqrt{\frac{\omega_T}{10QK_{\text{PFD}}K_{\text{VCO}}}}$
$\frac{1}{RC}$	$\sqrt{\frac{1}{10}\omega_T K_{\text{PFD}}K_{\text{VCO}}Q^4}$	$\sqrt{\frac{1}{10}\omega_T K_{\text{PFD}}K_{\text{VCO}}Q^3}$
ω_n	$\sqrt{\frac{1}{10}\omega_T K_{\text{PFD}}K_{\text{VCO}}}$	$\sqrt{\frac{Q}{10}\omega_T K_{\text{PFD}}K_{\text{VCO}}}$
$\frac{\omega_n}{\omega_0} \Big _{\text{max}}$	$\frac{1}{10} \sqrt{\frac{\omega_T}{\omega_0}}$	$\frac{\sqrt{Q}}{10} \sqrt{\frac{\omega_T}{\omega_0}}$

Table 4.3: Second order type 2 PLL design limitations and optimal sizing

with the corresponding sizing of the filter gain and cut-off. The VCO free running frequency shall be chosen close to ω_0 . Given that 10% tuning range VCOs are available, one can expect the VCO gain as high as $K_{\text{VCO}} = \frac{\omega_0}{10}$. The PFD, mapping a 2π phase range onto a window of few volts in modern integrated technologies, K_{PFD} is on the order of 1. This leads to the maximum conceivable $\frac{\omega_n}{\omega_0}$ ratio. Looking at the latter's expression, high-performance commercially available $\omega_T=100\text{MHz}$ operational amplifiers allow this ratio to hit the 0.01 to 1 interval for NEMS with typical eigenfrequencies spanning from 1MHz to 10GHz, and the results, presented in section 4.3, are applicable in practice.

Settling time Table 4.3 and the previously mentioned component limits, provide an upper bound on the system bandwidth, which is approximately $\omega_n \leq \frac{\sqrt{\omega_T \omega_0}}{10}$. This means that a 100MHz NEMS can be followed with a 10MHz bandwidth, and a 1GHz NEMS can be followed with a 30MHz bandwidth. This bandwidth translates into settling time, estimated from the exponential behaviour of the transient step response

$$t_s = \frac{Q_n}{\omega_n} \cdot \ln\left(\frac{\omega_0}{\Delta\omega_0}\right) \quad [\text{s}] \quad (4.18)$$

4.4. Merging High-Speed & High-Resolution Mass Sensing

and is on the order of $\frac{Q_n}{\omega_n}$, meaning that the above optimal design criterion leads to settling times on the order of 100ns.

4.4 Merging High-Speed & High-Resolution Mass Sensing

State-of-the-art mass sensing is predicated on the detection of a shift in a resonator's eigenfrequency when an additional mass binds to its surface. Evaluation of the theoretical ultimate limits to such inertial mass sensing [82] suggests that single proton weighing is feasible at room temperature. This yoctogram mass resolution has been achieved [31] at liquid-helium temperature with an ultrasensitive carbon nanotube resonator, operated in a mixer setup [29]. The equivalent room-temperature record ranges at a hundredfold worse resolution [30]. These high-resolution sensors find applications in atomic physics, biology and life science as molecule identifiers, gas detectors and cell weighing to name but a few.

State-of-the-art mass resolution

In contrast to this impressive mass resolution, the temporal resolution of such sensors appears unspectacular. Frequency sweeps that last several seconds [1] and computer-aided feedback loops of tens of milliseconds [31] set the benchmark hitherto. By comparing this sensing speed to the quasi gigahertz NEMS eigenfrequency, it becomes apparent that there is immense potential to improve sensing speed by several orders of magnitude.

Slow sensor response

A novel approach to simultaneous high-speed and high-resolution nanomechanical mass sensing is presented in this section. Today's state-of-the-art mass sensors do not combine these two desirable properties yet: High-resolution methods [31] rely on frequency sweeps or mixing, which makes them inherently slow, while high-speed methods [47] as proposed in section 4.2.3, were shown to present non-quantifiable offsets (see Figure 4.5), which lead to erroneous mass inference. An auto-calibrating system, grafted onto the NEMS-embedding PLL of Figure 4.8, is shown to compensate offsets and hence enables high-resolution high-speed sensing. Such precise and fast mass detection allows observation of phenomena that so far are not observable because they are either too subtle (insufficient sensor resolution) or happen too fast (insufficient sensor speed), like chemical and biochemical reactions.

2-in-1

Section 4.4.1 brings forward the key elements for high-speed and high-resolution mass sensing, and presents a novel topology combining both features. The physical phenomenon at the basis of this self-calibrating sensor topology is investigated in section 4.4.2. Section 4.4.3 demonstrates that this nonlinear phenomenon can indeed be exploited in practice for calibration and the operation principle of the resulting high-resolution high-speed mass sensor is explained in section 4.4.4.

Overview

4.4.1 Fast and precise oscillators

Fast and precise identification of the NEMS eigenfrequency ω_0 may be modelled as a search

Search problem

problem. A questioner interrogates a comparator oracle

$$O: \omega \mapsto \begin{cases} -1 & \text{if } \omega \leq \omega_0 \\ +1 & \text{else} \end{cases} \quad (4.19)$$

on whether the unknown eigenfrequency ω_0 equals an arbitrary guess ω . The oracle answers with -1 or $+1$ as a function of the relative position of ω and ω_0 . Two key parameters to high-speed high-resolution mass sensing crystallize from this formal description of the eigenfrequency search. First must the oracle provide fast and trustworthy responses, and second shall the questioner interpret the answer quickly and rapidly improve the quality of the guess.

Resonance indicators The fastest way to determine a periodic signal's frequency is to measure exactly one period, as suggested in section 4.1. Hence high NEMS eigenfrequencies are beneficial for the first criterion, and suspended carbon nanotubes could be a neat choice. Noise may distort the oracle's answer, but can be countervailed by averaging over several periods, as explained by equation (4.7). The resulting speed-precision trade-off is assessed in section 5.4. The current section's emphasis lies on the inspection of techniques to rapidly observe the oracle's answer and formulate a precise guess on ω_0 . The following observations are independent of the exact NEMS nature and averaging-time. Expressing equation (4.16) as a function of the NEMS quality factor Q , a generic dynamic NEMS may be modelled as a normalized damped harmonic oscillator

$$H_{\text{NEMS}}(s) = \frac{\frac{\omega_0}{Q} \left(1 - \frac{1}{4Q^2}\right)}{s^2 + \frac{\omega_0}{Q}s + \omega_0^2}, \quad \begin{cases} |H(s)| & = A \\ \arg(H(s)) & = \phi \end{cases} \quad (4.20)$$

The eigenfrequency is observable via detection of the amplitude A peak at ω_p or the phase ϕ inflection at ω_i , shown in Figure 2.7,

$$\omega_p = \omega(\phi_p) = \omega_0 \sqrt{1 - \frac{1}{2Q^2}}, \quad \omega_i = \omega(\phi_i) = \omega_0 \sqrt{\sqrt{4 - \frac{1}{Q^2}} - 1} \quad (4.21)$$

$\omega_p \approx \omega_i \approx \omega_0$ for sufficiently large Q . Adsorption of a particle onto the oscillating NEMS, causes a change in the oscillator's effective mass, defined by the particle's weight and the binding position [87], and shifts the resonance characteristics, according to equation (4.4), as $(\omega_0, Q) \rightarrow (\frac{\omega_0}{\sqrt{\alpha}}, \sqrt{\alpha}Q)$, with $\alpha = 1 + \frac{\Delta m}{m}$. This shift in eigenfrequency is to be detected as fast and precisely as possible.

Sensing techniques Today's techniques of doing so may be systematically categorized into

ω -controllable techniques drive the NEMS at a given frequency ω and observe its amplitude A or phase ϕ response. Such approaches benefit from a reduced noise bandwidth when operating the NEMS as a mixer [1]. The mixed signal out of the NEMS, however, has a

4.4. Merging High-Speed & High-Resolution Mass Sensing

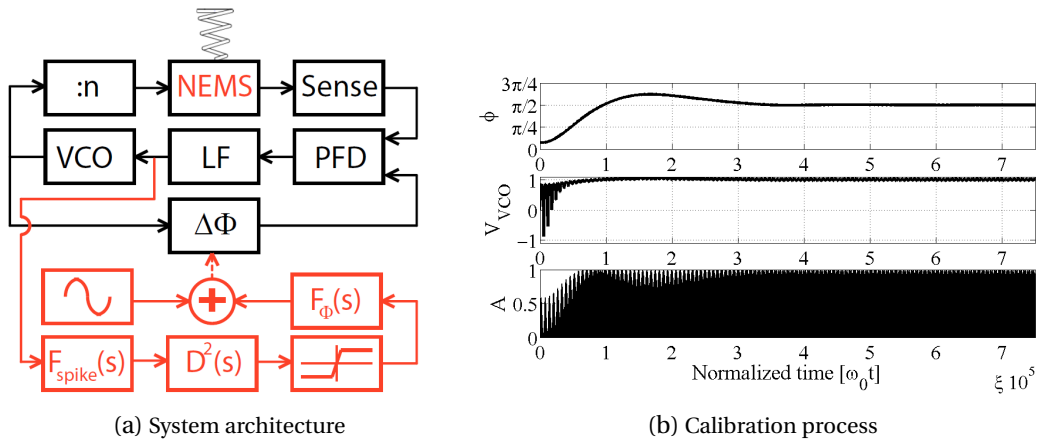


Figure 4.17: Auto-calibrating mass balance, derived from the NEMS-embedding PLL of Figure 4.8.

much lower frequency than ω_0 , 1MHz at best [19]. This makes mixing incompatible with the high-speed detection exigence, and feedback loops take tens of milliseconds [31] to improve the estimation of ω_0 . High-resolution weighing is enabled by the simultaneous extraction of ω_p or ω_i and Q from a response plot around the resonance peak [31], which takes seconds. It is concluded that ω -controllable methods, are precise, but slow.

ϕ -controllable techniques embed the NEMS into a phase locked loop (PLL) and feed its output back to the input [30],[88], with a controllable phase shift $\Delta\Phi$, which forces the NEMS to oscillate at a unique frequency ω . An adsorption-related shift in ω is directly observable, enabling high-speed weighing, but the error in the observed $\Delta\omega_0$ scales as $\frac{1}{Q} \tan(\delta\Phi)$, illustrated by Figure 4.5. If $\delta\Phi = 0$, meaning that the loop delay $\Delta\Phi$ and the noisy component delays sum to the selected entry of Table 3.1, the error vanishes. This ideal hypothesis is hard to satisfy in practice, where component delays are *a priori* hardly entirely corrigible. It is concluded that ϕ -controllable methods, are fast, but have limited resolution.

As a matter of fact could the high-resolution and high-speed sensing hitherto be combined yet. An novel approach is shown in Figure 4.17a, where in-situ calibration of the NEMS phase ϕ via a nonlinear technique, adds precision to ϕ -controllable methods and opens the gate to high-speed high-resolution mass sensing. The NEMS is embedded into a phase locked loop, formed by a phase-frequency detector (PFD), a loop filter (LF) and a voltage controlled oscillator (VCO). At steady state, the VCO oscillates at a frequency for which both feedback paths, one formed by the NEMS and the readout electronics, the other by a simple phase shifter, have exactly the same delay. Hence the NEMS is forced to oscillate at a precise frequency, at which ϕ satisfies the above constraint. This frequency depends consequently on the loop delay $\Delta\Phi$. The additional feedback adjusts $\Delta\Phi$ so to center resonance at ω_i , quasi equal to ω_0 for NEMS with decent Q . Figure 4.17b illustrates how the auto-calibration circuit adjusts the loop phase so to bring the NEMS phase ϕ to $\frac{\pi}{2}$, its ideal value from Table 3.1, which reflects maximum amplitude oscillation at ω_0 and error-free sensing. Once the NEMS has been calibrated, $\Delta\Phi$

Loop phase
regulating
topology

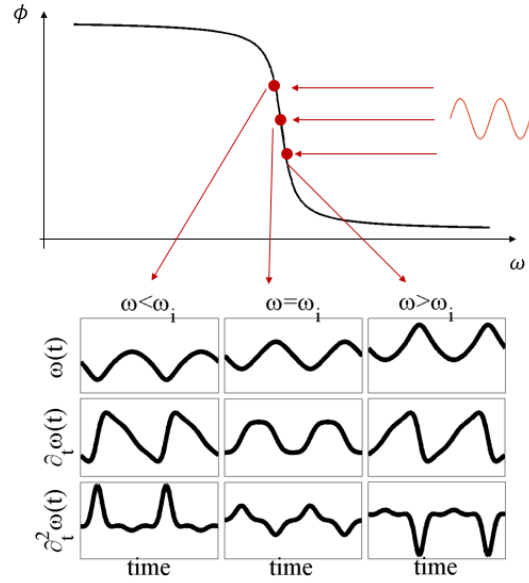


Figure 4.18: The calibration technique, proposed in Figure 4.17a, introduces small variations onto the loop phase $\Delta\Phi$, and hence the NEMS phase ϕ . The NEMS's nonlinear phase-frequency relation translates the variation of ϕ into a variation of ω , which gives away the loop's oscillation frequency with respect to the NEMS eigenfrequency. The impact of the phase shift on ω is illustrated for a sinusoidal phase variation, centered in $\bar{\phi} \in \{\phi_i \pm \frac{\pi}{8}, \phi_i\}$ and of amplitude $\Delta\phi = \frac{\pi}{5}$

may simply be memorized and sensing happens precisely at the speed of ϕ -controllable methods. The underlying hypothesis for this memorization to work out, is that the NEMS phase is far more sensitive to the oscillation frequency than is any other circuit component. This condition is tacitly met in ϕ -controllable methods, as the PLL locks onto a frequency imposed by the circuit component with the highest quality factor, speak phase sensitivity, which must be the NEMS, if sensor operation is envisioned.

4.4.2 The nonlinear physical phenomenon



Perturbation theory The technique to enable calibration of the feedback loop phase shift $\Delta\Phi$, such that NEMS oscillation at ω_i is enforced, roots in the nonlinearity of the NEMS phase-frequency relation

$$\omega = \begin{cases} \frac{\omega_0}{2Q \tan(\phi)} \left[1 + \sqrt{1 + (2Q \tan(\phi))^2} \right] & \text{if } \phi \in]-\pi, -\frac{\pi}{2}[\\ \frac{\omega_0}{2Q \tan(\phi)} \left[1 - \sqrt{1 + (2Q \tan(\phi))^2} \right] & \text{if } \phi \in]-\frac{\pi}{2}, 0[\end{cases} \quad (4.22)$$

derived from equation (4.20). The reasonable hypothesis, that the NEMS presents the highest Q among all loop elements, makes a sinusoidal modulation of the loop phase $\Delta\Phi$ cause an identical modulation of the NEMS phase ϕ , which results in a variation of its frequency ω , as Figure 4.18 reveals. The key observation is that the frequency's inflection points, distinguishable as the extrema of its time derivative $\partial_t \omega$ or zeros of $\partial_t^2 \omega$, are spread over a period with an irregularity defined by the signed average distance between ϕ and ϕ_i , speak $\delta\Phi$. When the NEMS oscillates below ω_i , then the down-time of $\partial_t^2 \omega$ exceeds its up-time, while the reverse is true for frequencies above ω_i , and equilibrium is obtained at ω_i .

4.4. Merging High-Speed & High-Resolution Mass Sensing

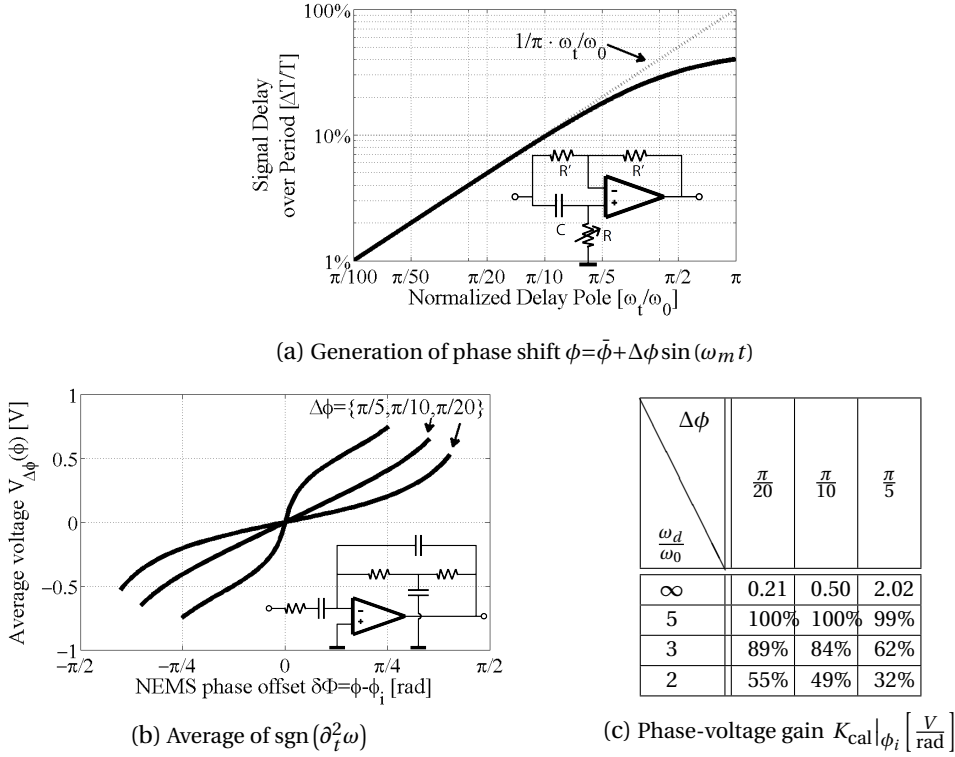


Figure 4.19: Phase modulation for controllability and signal differentiation for observability

4.4.3 Controllability & observability



Practical implementation of the calibration-loop consequently requires $\Delta\Phi$ to be controllable and $\partial_t^2\omega$ to be observable.

The phase modulation can be performed by inserting the circuit of Figure 4.19a

$$T(s) = \frac{\frac{s}{\omega_t} - 1}{\frac{s}{\omega_t} + 1}, \text{ with } \omega_t = \frac{1}{RC} = \frac{1}{(R_0 + \Delta R \sin(\omega_m t))C} \quad (4.23)$$

Controllability of $\Delta\Phi$

into the NEMS signal path. A sinusoidal control of R at a frequency $\omega_m \ll \omega_0$ introduces a highly linear delay $2 \arctan\left(\frac{\omega_0}{\omega_t}\right) \approx 2 \frac{\omega_0}{\omega_t}$ with variational amplitude $\Delta\phi = 2\omega_0\Delta RC$ and no impact on the signal amplitude $|T(s)|=1$.

Information on the NEMS frequency is available through the control voltage of the VCO in the topology of Figure 4.17a, which consists of the ϕ -controllable technique of Figure 4.8, completed by the calibration loop of $\Delta\Phi$. If the phase modulation frequency ω_m is chosen such that $\omega_m \ll \omega_n \ll \omega_0$, then the impact of $\Delta\Phi$ on the NEMS frequency is retrievable from the low-pass filtered VCO control voltage, which unveils $\partial_t^2\omega$ after two differentiations, performed

Observability of $\partial_t^2\omega$

by the second order bandpass filter of Figure 4.19b

$$D(s) = \frac{\omega_d^2}{\omega_L} \frac{s}{s^2 + 2\zeta\omega_d s + \omega_d^2} \quad (4.24)$$

that amplifies signals above ω_L , differentiates till ω_d and integrates above ω_d . The choice of $\zeta = 0.65$ stands for maximally accurate derivation at minimal noise bandwidth performance loss [89]. Saturation of $\partial_t^2 \omega$ yields a bipolar digital signal (± 1) with phase-dependent average voltage $V_{\Delta\phi}(\phi)$, depicted in Figure 4.19b, negative below, positive above and zero at ϕ_i , which is notably independent of the NEMS quality factor. The phase-to-voltage conversion gain $K_{\text{cal}} = \partial_\phi V_{\Delta\phi}$ depends on the modulation amplitude and is given by Figure 4.19c, in absolute terms for ideal differentiators ($\frac{\omega_d}{\omega_0} = \infty$) and relatively to this ideal value for the limited bandwidth differentiator of Figure 4.19b.

Feasibility It is concluded that the phase-calibration technique, proposed in Figure 4.17a, can indeed be implemented in practice, and with only minor noise overhead with respect to the non-calibrating system of Figure 4.8.

4.4.4 NEMS mass balance system

System analysis The proposed auto-calibrating mass balance of Figure 4.17a omits frequency division, necessary to lock on the field effect or the piezoresistive NEMS signal, for the sake of clarity. A periodic modulation of the delay $\Delta\phi$ modulates the NEMS frequency nonlinearly. PFD-spikes are removed via a lowpass filter $F_{\text{spike}}(s)$ and $D^2(s)$ differentiates the nonlinearity twice, before saturating it. The calibration-loop is closed by a filter $F_\phi(s)$, which adjusts the NEMS phase ϕ to ϕ_i , reducing $\delta\Phi$ to zero. This phase calibration loop acts hence as a PLL, tracking the unknown value of ϕ_i . ϕ_i is implicitly defined by the NEMS and is made observable through the injected phase modulation. Given the involved frequencies, the PFD and LF(s), of the primary PLL, are transparent to this secondary loop, and $T(s)$ has unity gain.

Nested PLLs For the calibrating secondary PLL not to perturb the operation of the primary, NEMS-embedding PLL, the phase modulation (ω_m) must be slower than the primary PLL's natural frequency ω_n . For stability, the secondary PLL's natural frequency (ω_{cal}) must be lower than the injected modulation (ω_m), leading to the condition

$$\omega_{\text{cal}} \ll \omega_m \ll \omega_n \ll \omega_0 \quad (4.25)$$

This condition guarantees stable regulation, without interference between the injected phase modulation and the resulting compensation of $\delta\Phi$. The secondary PLL's calibration process is transparent to the primary PLL, tracking and driving the NEMS.

PLL order The secondary PLL needs to track continuous phase modulations. So it must be able to follow phase accelerations. In accord with section 4.2.3, this secondary PLL shall hence be of type 3. The calibration loop filter $F_\phi(s)$ may consist of a zero-order integrator (unity gain at $\frac{K}{K_\phi\beta}$),

a first-order integrator (zero at α) and a lowpass filter (pole at β), forming the closed-loop transfer function

$$H_{\text{cal}}(s) = \frac{\phi}{\phi_i} = \frac{K(s + \alpha)}{s^3 + \beta s^2 + Ks + K\alpha} \quad \begin{cases} K &= (2\pi\omega_{\text{cal}})^2 \sqrt{\frac{1+\sin\varphi}{1-\sin\varphi}} \\ \alpha &= 2\pi\omega_{\text{cal}} \frac{1-\sin\varphi}{\cos\varphi} \\ \beta &= 2\pi\omega_{\text{cal}} \frac{\cos\varphi}{1-\sin\varphi} \end{cases} \quad (4.26)$$

where ω_{cal} reflects the calibration loop bandwidth and φ is its the phase margin. The graphs of Figure 4.17b illustrate the settling of a critically damped third order ($\omega_c=10^{-5}\omega_0$, $\varphi=50^\circ$) calibration loop for a NEMS embedded in a critically damped second order PLL ($\omega_n=10^{-1}\omega_0$, $Q_n = \frac{1}{2}$), presented in section 4.2.3. The VCO center frequency is $0.9 \cdot \omega_0$, the gain $0.1 \cdot \omega_0$, and the injected variation ($\Delta\phi=\frac{\pi}{20}$, $\omega_m=10^{-3}\omega_0$). Upon convergence, the calibration loop may be disconnected to remove the modulation-induced residual ripple.

The calibration system of Figure 4.17a enables unbiased high-speed high-resolution mass sensing by NEMS, which are embedded into PLLs, such as of Figure 4.8. A start-up mechanism first sets the NEMS to motion in open-loop. The open-loop phase can be memorized by the add-on of Figure 4.15b, so to ensure seamless closure of the loop. The calibration system of Figure 4.17a then calibrates the loop delay so to ensure oscillation at the NEMS eigenfrequency. The loop phase delay $\Delta\Phi$ is then frozen, and the core topology of Figure 4.8 is now able to follow the NEMS precisely at its eigenfrequency. If this eigenfrequency shifts due to adsorption of a molecule, then the loop oscillation frequency changes with the exactly same amount, provided that the NEMS is the most selective loop element, and the added mass may be inferred precisely if its binding position is known.

Assessment

4.5 Microelectromechanical VCOs & Sensors in a Nutshell



The vision of chapter 1, the analyses of chapter 2 and the feasibility study of chapter 3, empowered the present chapter to explore new application areas for CNT-NEMS. Focus was set on voltage controllable electromechanical resonator operation and mass sensing. Both applications have the potential to excel by their combination of unique performance. CNT-VCOs combine high quality factors and tunability, while CNT mass balances are simultaneously fast and offer high sensitivity.

Breaking
new
ground

A feedback system, embedding the CNT-NEMS into a phase-locked loop, has been devised and its versatility was demonstrated by showing its mutability for self-testing without CNT-NEMS (Figure 4.20a), for open-loop characterization of CNT-NEMS (Figure 4.20b) and its closed-loop operation. An additional calibration loop can be grafted (Figure 4.20c) to ensure maximum amplitude oscillation and unbiased mass sensing. Two alternative loop topologies have been discussed, amongst which the self-sustaining direct feedback oscillator has attractive feats for industrial scale design, once CNT-NEMS resonators are more mature.

Survey

A phase-locked loop, operating the NEMS as its resonator, has been identified as the greatest

Core
oscillator
system

Chapter 4. Electromechanical Oscillators and Sensors

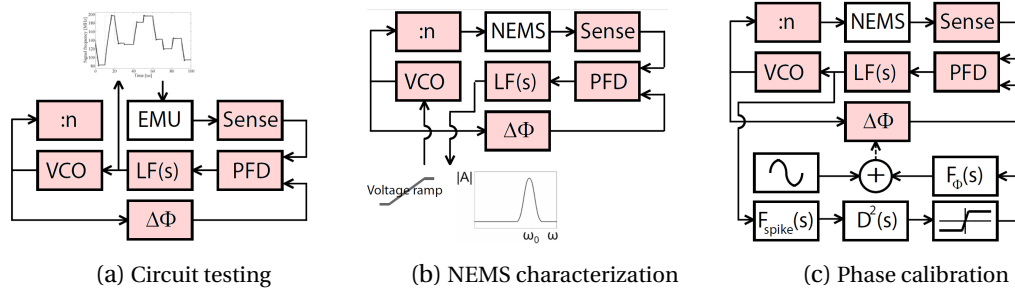


Figure 4.20: An all-in-one system for circuit and NEMS characterization, VCO and mass balance operation.

common divisor of NEMS-VCOs and high-speed high-resolution mass sensing. Tuning ranges, wider than a decade, date back to chapter 2, and mass sensitivity is predicted to reach down to atomic scales, and this with unprecedented speed thanks to high-frequency direct readout and large bandwidth PLL settling. NEMS actuation via a VCO makes amplitude control obsolete and it has been concluded that the feedback system presents equivalent performance for analog and digital implementations. The memory effect of PLLs provides temporary robustness to obfuscated NEMS oscillations. Finally second order type 2 PLLs crystallized as the minimal requirement to properly operate the NEMS in a VCO or sensor context.

Novel sensing approach Unbiased quantitative mass sensing was shown to require NEMS operation precisely at its eigenfrequency. While the state-of-the-art approach consists in sweeping through frequencies in search of the resonance peak of mixer NEMS, the present chapter proposes a faster approach, without penalty in terms of resolution. It uses the high-speed PLL core topology, depicted in Figure 4.8, and equips it with a calibration loop, cancelling possible offsets. While being as precise as state-of-the-art sweeping mixers, the novel approach operates up to the NEMS eigenfrequency and settles in large PLL bandwidths. Once calibrated, sensing happens at the NEMS eigenfrequency, and may start as soon as the PLL settled, which can be within a few NEMS oscillations. Sensing for previous attempts was limited in speed to the lower intermediate mixer frequency, and could only start after a feedback loop had localized the lorentzian peak at the eigenfrequency, which typically takes milliseconds.

Design optimisation Fastest transients and settling to steady state have been shown to be obtained for slightly underdamped PLLs with maximal natural frequencies. Practical implementation guidelines under limited bandwidth are given, and state that lock-in can be obtained at 30MHz with settling times of 100ns, for a NEMS oscillating at 100MHz or 1GHz (Table 4.3). Quality of the measurement improves with the square root of the 100MHz or 1GHz sampling time. This is a sound improvement over existing mass balances. The best of breed solutions converge within 15ms via a computer-controlled feedback loop [31] and the fastest sampling has been reported to 6MHz and microsecond integration time [19]. So the novel approach reduces the time to locate the eigenfrequency by a factor 10^5 and improves the estimate 5 times faster than today's state-of-the-art approaches.

Start-up Necessity for a start-up mechanism has been claimed and a lock detector allows to switch from

4.5. Microelectromechanical VCOs & Sensors in a Nutshell

open-loop start-up to closed-loop operation. Memorization of the loop phase at the moment of lock-in ensures a smooth transition towards closed-loop operation. While adsorption of heavy molecules, of mass $\Delta m = \frac{2m}{Q}$, is unproblematic, does their desorption require a system restart.

The here presented concepts find their implementation in chapter 5. Although the only available CNT-NEMS had been shown in chapter 3 not to be compliant with direct readout, a semi-theoretical, semi-practical case study will allow to load the present chapter's equations with numbers and provides a taste of the system's expected performance in mass balance applications. Outlook

*In science the credit goes to the man who convinces the world,
not the man to whom the idea first occurs.*

— Francis Darwin

5

Implementation, Characterization & Assessment

The so far largely theoretical and system-level analysis of electronic interfaces for carbon nanotube electromechanical oscillators and sensors, finds its practical circuit-level counterpart in the present chapter. Striving towards a system-in-package concept, presented in Figure 1.1, the core oscillator topology, for NEMS-based VCOs and mass balances, is now implemented on silicon. A visual summary of all the presented circuits and their interconnection is given by Figure 5.1. The power supplies for the chip are provided by its host PCB. The signal from the CNT-NEMS is read by the front-end, implemented in chapter 2. An actuator controller is used to tune the CNT-NEMS eigenfrequency and to remove slack from not taut tubes.

The big picture

The outcome of the joint CNT-NEMS and front-end measurement of chapter 3 fulminates the hope to test the feedback system of chapter 4 with a device scraping the ultimate performance predictions of chapter 2. The situation can be antagonized by incorporating an electrical emulator of the CNT-NEMS onto the chip, to illustrate its conceptual operation principle. Characterization of the complete loop dynamics must however wait the availability of a mature CNT-NEMS in order to become observable. The semi-theoretical semi-practical summary of Table 5.1 foretells the expected implemented circuit's performance for an optimally designed CNT-NEMS, as described in section 2.2.

A drop of bitterness

Following its analysis of section 4.2.3, the debug-capable oscillator feedback loop's implementation and characterization are presented here. A straight-forward implementation of a minimal functional topology on a printed circuit board (PCB), proves the feedback concept in section 5.1. Enhanced performance, in terms of frequency and noise, is obtained by an integrated circuit (IC) version in section 5.2. This chip's frequency range is used in section 5.3

Survey

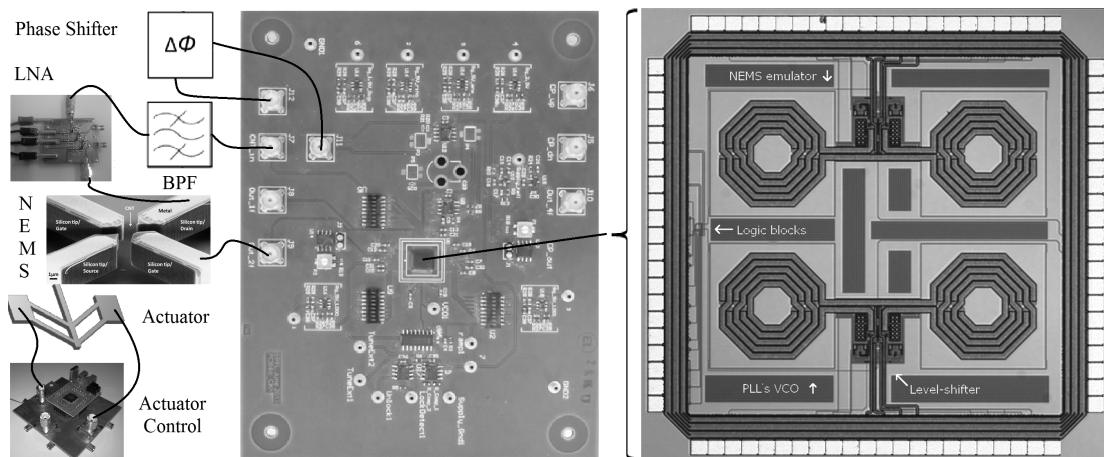


Figure 5.1: Partially integrated NEMS oscillator for VCO and mass balance applications

to evaluate its compatibility with the typical CNT space in terms of frequency range and an actuator controller is shown to improve the system yield. Its noise performance finally allows in section 5.4 to assess the sensor resolution achievable by the system implementation, before section 5.5 summarizes the results.

5.1 Functional Proof of Concept on PCB



Loop parameters A digital implementation of the NEMS-embedding PLL, presented in section 4.2.3, has been realized on PCB, and demonstrates successful locking on an emulated NEMS. The design decision was to infer motion via the piezoresistive signal, which explains the presence of the frequency divider block in Figure 5.2a. Expecting NEMS eigenfrequencies between 10MHz and 100MHz, and hence piezoresistive signals up to 200MHz, a natural loop frequency of $\omega_n = 1\text{MHz}$ is chosen and critical damping is achieved for $Q_n = \frac{1}{2}$. It is recalled that this quality factor provides fastest possible open-loop tracking of the emulator without overshoot (see section 4.2.3). Optimal closed-loop performance would, however, be obtained for a slightly underdamped PLL, with $Q_n \approx 1$ (see section 4.3). The PLL is designed to have a free-running frequency of 140MHz and can be tuned by 15MHz per volt over a $\pm 4\text{V}$ range.

Testing & start-up The emulator, allowing to test the circuit in absence of a NEMS, is implemented via a VCO, with identical parameters as the loop VCO, and its measured transfer function is shown in Figure 5.3a. As the NEMS is not expected to yield a detectable signal when merely driven by thermal noise, a start-up circuit becomes indispensable for practical applications. This one consists of a voltage ramp (green trace), sweeping the VCO through decreasing frequencies. Its practical operation is illustrated in Figure 5.3b. As long as the frequency is above the NEMS resonance, no signal is detected by the LNA, and the floating loop filter (LF) output (blue trace) indicates phase advance of the VCO. Once the drive approaches the NEMS eigenfrequency, a signal is detected from the NEMS, which is compared with the steadily decreasing VCO

5.1. Functional Proof of Concept on PCB

frequency. The LF output changes polarity to indicate that the VCO now leaks phase. This edge is used to trigger a monostable lock detector, which switches the multiplexer (MUX) (red trace) from the start-up ramp to the loop filter (LF) output and hence closes the oscillator loop, which now continues working according to the principles highlighted in section 4.2.

The shaded area of Figure 5.2a has been implemented on an FR-4 printed circuit board, shown in Figure 5.2b. The chosen PFD has unlimited capture range and its voltage excursions of twice 750mV must cover 360° of phase advance or delay, resulting in a PFD gain of $K_\phi = 239 \frac{\text{mV}}{\text{rad}}$. The inductance and tunable capacitance in the VCO's LC tank were chosen to cover a frequency range from 80 MHz to 200 MHz via a 8 V control voltage excursion, which translates into a VCO gain of $K_V = 15 \frac{\text{MHz}}{\text{V}}$. The LF has been implemented as a differential active first-order filter and the RC time-constants for equation (4.14) were chosen as $\tau_1 = \frac{K_V K_\phi}{\omega_n^2}$ and $\tau_2 = \frac{1}{Q\omega_n}$. An additional pole is integrated into the LF at $5\omega_n$ to inhibit the pulse transients while causing acceptable further overshoot. Finally the start-up ramp is generated with a Deboo integrator for unipolar non-inverting designs, based on a Howland current source [90]. The excursion covers 12 V, within 1.2 s, sweep the PLL range $\Delta\omega_{\text{range}} = 120\text{MHz}$ within $\Delta T_{\text{sweep}} = 800\text{ms}$. The drive consequently stimulates the NEMS within its bandwidth $\frac{\omega_0}{Q} \approx \frac{100\text{MHz}}{100}$ during a time ΔT_{start}

Design & implementation

$$\Delta T_{\text{start}} = \Delta T_{\text{sweep}} \cdot \frac{\omega_0/Q}{\Delta\omega_{\text{range}}} \approx 6.6\text{ms} \gg 10\mu\text{s} \approx \frac{10^3}{\omega_0} \geq \Delta T_{\text{start,min}} \quad (5.1)$$

which is considerably longer than the minimal required lock-in time $\Delta T_{\text{start,min}} \leq \frac{10^3}{\omega_0} \approx 10\mu\text{s}$, even for slow PLLs with $\omega_n = \frac{\omega_0}{100}$, according to Figure 4.14. Frequency division is finally obtained by the use of JK flip-flops.

This implementation is adequate for oscillators around piezoresistive NEMS that have eigen-frequencies in the 40 MHz to 100 MHz range. PLL control signals and the actuation to be sent to the NEMS are shown in Figure 5.4. While being smooth at mid-range (68MHz), control

Performance

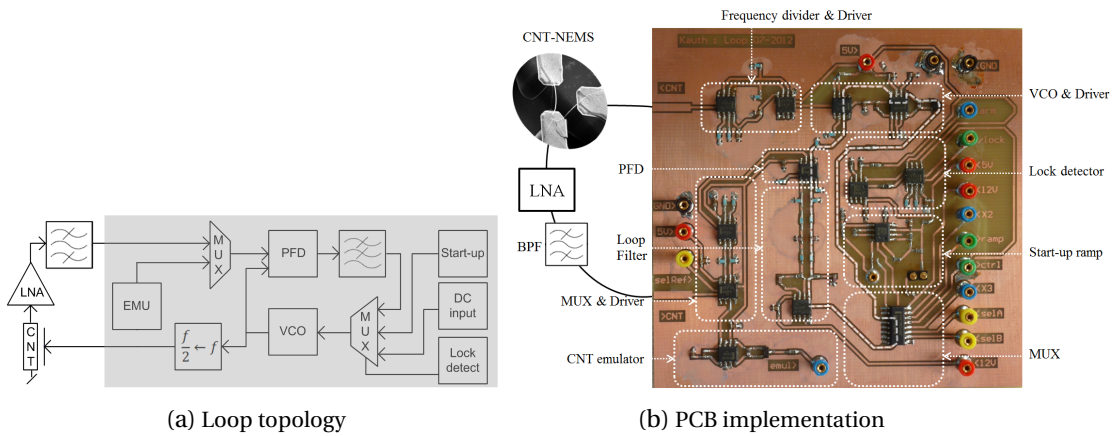


Figure 5.2: Oscillator feedback loop topology and PCB implementation (shaded area)

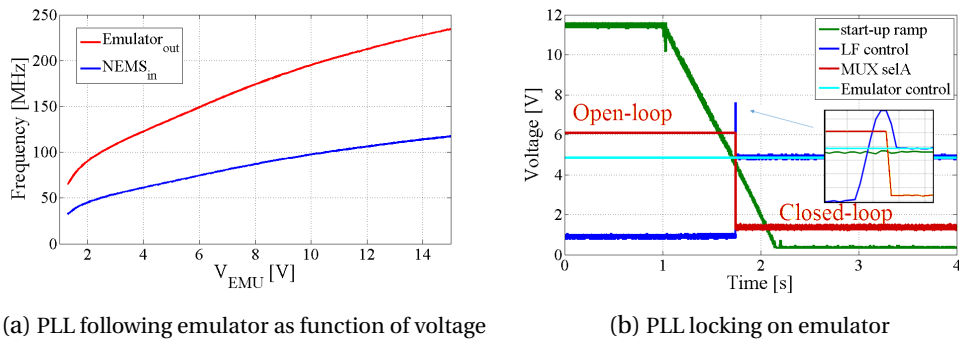


Figure 5.3: Printed circuit board PLL performance

voltage peaks arise at the varactor’s low-frequency end (35MHz). The upper frequency limit (102MHz) is set by the filtering of the rectangular signal’s odd harmonics. Adaptation of the range to lower frequencies is uncomplicated and achieved by replacing the inductor of the LC tank, while higher ranges are inaccessible due to frequency limitations of the PCB components and require integration of the circuit [88].

5.2 Performance on IC



Essentials An integration step followed the proof of concept delivered by the previously presented PCB circuit implementation. Integrated in a 180nm CMOS technology were first and foremost the sensible high frequency blocks forming the PLL (indicated by the grey area of Figure 5.5a). The resulting 4.5mm² chip hosts two 3-bit programmable LC-tank VCOs, one for the PLL, the other as a NEMS emulator, able to span frequencies from 600MHz to 770MHz, as measurements report in Figure 5.10a. This frequency range is sufficiently high to integrate the inductor coil with reasonable surface overhead, and low enough to prevent challenging RF layout issues. Level-shifters saturate the sinusoidal VCO signal into a digital signal and frequency dividers allow to extend the operation range of the chip to the 300MHz-385MHz, 150MHz-192MHz and 75MHz-96MHz bands. The union of these frequency ranges covers a considerable part of the CNT-NEMS oscillation spectrum, and may address even more CNT-NEMS resonators

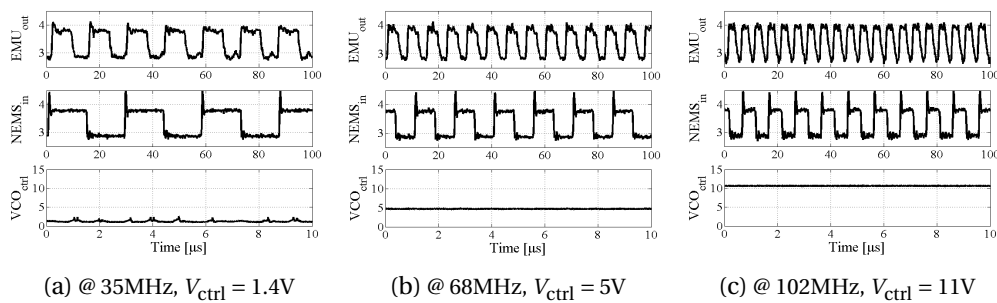


Figure 5.4: PLL trackig of emulator

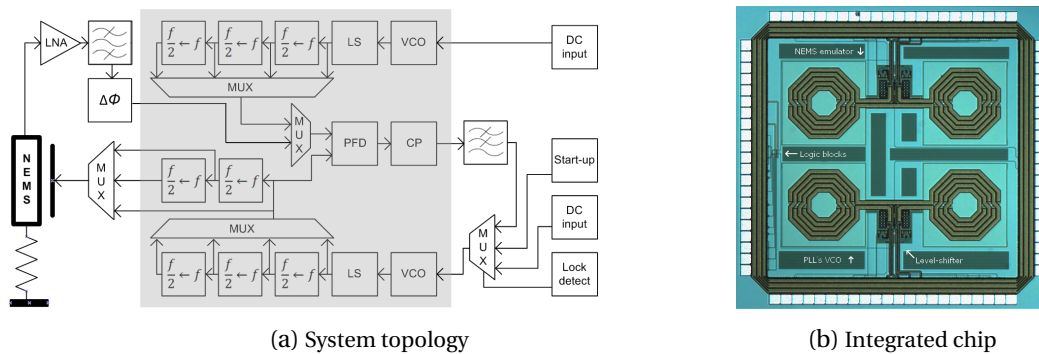


Figure 5.5: NEMS oscillator for VCO and mass balance

thanks to a tuning tensile actuator, as will be shown in section 5.3. A detailed chip description will follow. Worth mentioning are the three chip outputs that allow to drive the CNT-NEMS at a quarter, half and full its electrical signal frequency, meaning that capacitive, field-effect and piezoresistive phenomena may be exploited in the oscillator, as explained in section 3.2. The loop filter has been kept off-chip, in order to allow flexible tuning of the system dynamics [91]. The piecewise integrated system is shown in Figure 5.1 and is composed of a PCB, hosting the integrated circuit (IC), pictured in Figure 5.5b, the PLL filter, start-up and lock-detection blocks, as well as current and voltage references. A microcontroller, presented in section 5.3, controls the actuator that strains the CNT-NEMS in order to oscillate at the desired frequency, which makes this system a voltage controllable electromechanical oscillator. The NEMS motion is read by a low-noise amplifier (see chapter 3) and the motional information is extracted by the bandpass filter, briefly addressed in chapter 3 as well. Best signal strength out of the CNT-NEMS is obtained when the loop phase $\Delta\Phi$ is set in accord with the electronic block delays, to make the NEMS oscillate close to its eigenfrequency, where it exhibits a phase shift as reported in Table 3.1. This delay in the signal path may be generated by a long cable, a programmable counter, or the phase shifter of Figure 4.19a, either manually or by the calibration loop of section 4.4.

Given the large spread in NEMS eigenfrequencies (10MHz – 1GHz), depending on their nature, shape and material, programmability and tuning range of the VCO is a major design criterion. Though ring oscillators are the most flexible in frequency tuning and are easy to integrate, preference was given to a harmonic LC oscillator. Given their better phase noise, this is a conservative and safe choice for the design of NEMS oscillators with all its unknowns. The VCO is powered by a 5 V supply, designed for frequencies from 600 MHz to 770 MHz (Figure 5.10a) and an average gain of $-40 \frac{\text{MHz}}{\text{V}}$ (Figure 5.10b). The frequency span can be divided down to the NEMS eigenfrequency. This VCO design at higher frequencies has the twofold advantage of being beneficial to the phase noise and allows integration of the inductance. The inductor is of octagonal shape, approaching to the best the maximum quality factor Q under the 45° layout constraint (see Figure 5.5b), and hosted in the least resistive top metal layers, which have minimal capacitance to the substrate. Its value is 17.2nH (8.6nH per coil) with $Q_L=7.3$. The subsequent level-shifter's input transistors constitute a fixed load of 2.4 pF, and set the upper

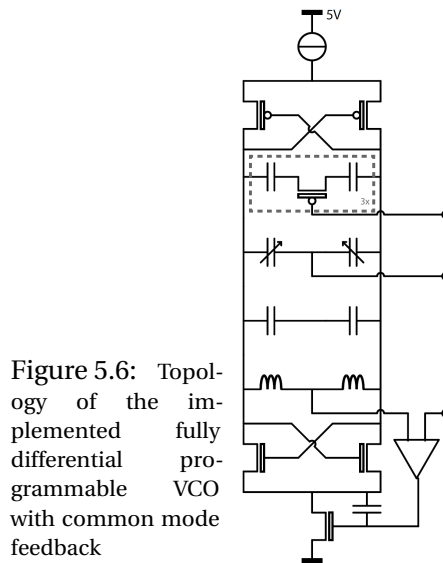


Figure 5.6: Topology of the implemented fully differential programmable VCO with common mode feedback

bound of the tuning range. The fully differential VCO structure, represented in Figure 5.6, is biased to 1mA by a cascoded current source. Three bits allow to program the VCO's free-running frequency (the least significant bit corresponds to a capacitance of 205 fF) and an analog input allows for frequency tuning via control of a 410 fF capacitor. The common mode is regulated via feedback through a fully differential folded cascode transconductance amplifier and stabilized via Miller effect. Measured performance of the tuning range, gain and phase noise are reported on Figure 5.10.

Level-shifter design The sinusoidal differential output of the VCO is loaded by the structure of Figure 5.7. The first, high-voltage stage is a resistively loaded differential pair. This stage generates proper logical zeros and the resistors allow to pull the output voltage high enough to properly serve the input transistors of the second, low-voltage stage, without risk of destruction. The second stage is supplied by 1.8V, as are all low-voltage downstream blocks. A comparator, with a cross-coupled active load, produces proper logical signals in the 600 MHz to 770 MHz range. An inverter buffers the stage.

Frequency division Frequency division by powers of two is achieved by cascading several compact and high speed true-single-phase-clock (TSPC) flip-flops [92], as illustrated in Figure 5.8, for which the

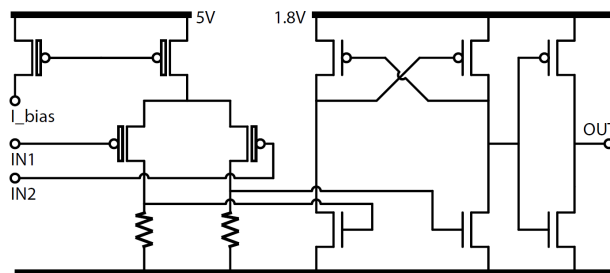


Figure 5.7: 5V to 1.8V level-shifter for saturated full-swing signals

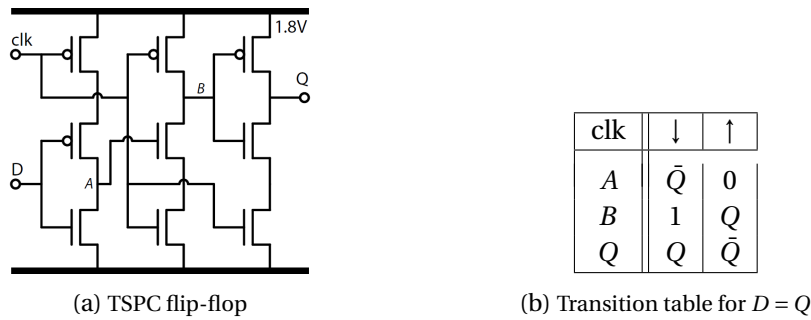


Figure 5.8: TSPC flip-flop based frequency division circuit

output Q toggles at half the input clk frequency if fed back to the second input D . Buffers have been introduced between the stages to avoid overloading the feedback node. The full-swing clock, necessary to proper operation, is guaranteed, for the first divider by the level-shifter's buffer, and then intrinsically by the structure's output stage for all downstream dividers. The frequency division works as follows. When the clk signal is low, the internal node B is precharged to 1, Q is at high impedance and cannot change, while A is the inverted value of Q , that is $A \leftarrow \bar{Q}$. Rise of the clk signal makes of B a frail state on gate capacitances that remains at 1 if A is low, but can be swiftly toggled to 0 if A is high, summarizing to $B \leftarrow Q$. At high clk , Q is the inversion of B , that is to say $Q \leftarrow \bar{Q}$. Note that A was at this same value already before the rise in clk and that topologically A could now be pulled down by Q . Hence if Q is low after the rise in clk , A must be low since some time. Otherwise Q is high after the rise in clk and pulls A low then. Both scenarios summarize to $A \leftarrow 0$. The cycle now starts over again, with a toggled value of Q , which indicates frequency division.

In order to extend the PLL's capture range up to the VCO's complete frequency span, a PFD with unlimited frequency range is designed. This PFD takes the NEMS and VCO signals as inputs and generates outputs whose high-time is proportional to the phase or frequency advance of the respective signal. Figure 5.9b shows how these outputs drive a charge pump (CP) that consequently steers the voltage at its output node according to the relative phase and frequency of the NEMS and VCO signals. The CP is implemented as two transistors with matched conductance, each loaded by a $1\text{ k}\Omega$ resistor, having a limiting effect on short-circuit currents and acting as equalizer of the CP's sourcing and sinking behaviour. A passive lowpass

PFD, charge pump & filter

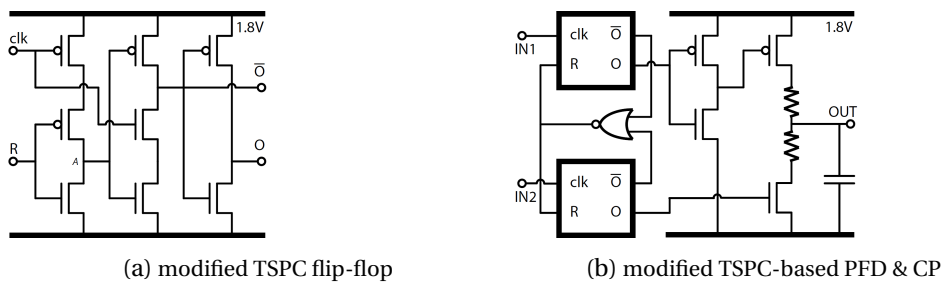


Figure 5.9: Phase frequency detector and charge pump

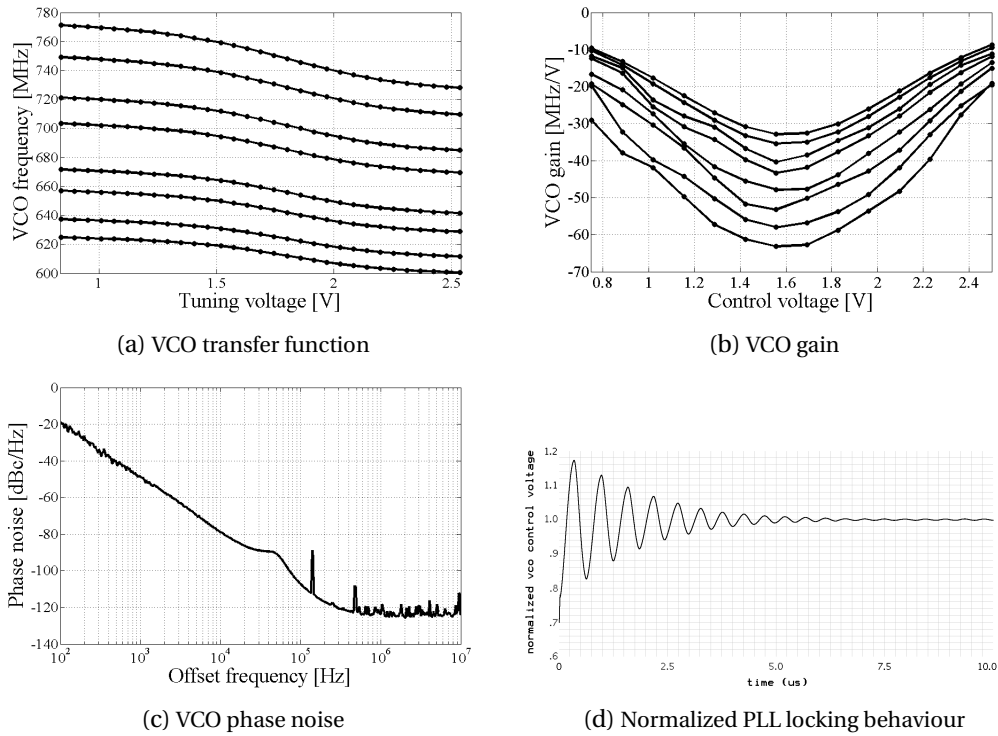


Figure 5.10: Measured chip characteristics

filter is formed when loading the output node by a capacitor, be this the 1 pF pad capacitance or a PCB-mounted external capacitor. The implemented high-speed and low-power PFD is based on a modified TSPC positive edge triggered D flip-flop with unlimited phase and frequency detection range [93]. The 360° range of phase advance or delay are reflected via a 1.8 V voltage excursion, resulting in a gain of $K_{\phi} = 286 \frac{\text{mV}}{\text{rad}}$. Depicted in Figure 5.9a, its operation principle is as follows. When reset R and clock clk are low, the internal node A is pulled up and output \bar{O} is in high impedance, consequently freezing also its inverted output O . A rising edge of the clock will now ground \bar{O} and pull its inversion O high. This output will stay high until a reset signal is applied and shall be used to drive the CP. Reset shall be triggered as soon as the sourcing and sinking CPs are active, which is expressed via a logical NOR on the \bar{O} s and has the effect of pulling A down via the NMOS, which consequently pulls \bar{O} high, setting the reset signal low again. The PMOS transistor on the R terminal merely reduces the short-circuit current when clk is low but R is high. Figure 5.10d shows the simulated normalized PLL locking behaviour on the emulator for an LF load of 100pF, corresponding to a closed-loop time-constant on the order of $\omega_n = 1\text{MHz}$. The PLL reaches steady-state within a 10 μs time lap with acceptable overshoot. The 0V to 1.8V output range of the CP was shifted upward by 0.7V to cover the most sensitive tuning range of the VCO, located between 0.75V and 2.5V (see Figure 5.10b).

Realm of possibility If PLL settling within ten microseconds (see Figure 5.10d) is obtained for a 100pF filter capacitance loading the charge pump, then settling within 100 nanoseconds is envisionable

5.3. NEMS versus Circuit Compatibility

VCO gain	$32 - 62 \left[\frac{\text{MHz}}{\text{V}} \right]$
PFD gain	$286 \left[\frac{\text{mV}}{\text{rad}} \right]$
PLL range	$600 - 770 \text{ [MHz]} \times \left(1, \frac{1}{2}, \frac{1}{4}, \frac{1}{8} \right)$
1σ jitter	0.2%
Minimal settling	100 [ns]

Table 5.1: Performance summary of the integrated PLL. The most important figures of merit for fast sensor operation are

Settling time: It defines the minimal time it takes the PLL to lock onto the NEMS frequency and corresponds consequently to the earliest time a quantitative assessment can be made.

Frequency range: The PLL frequency range determines which CNT-NEMS can be used in combination with it (see Table 5.11a for details). High-frequency NEMS improve sensor resolution faster (see equation (4.4)).

Jitter: The lower the jitter, the better the sensor resolution (for a fixed integration time) (see equation (4.7)).

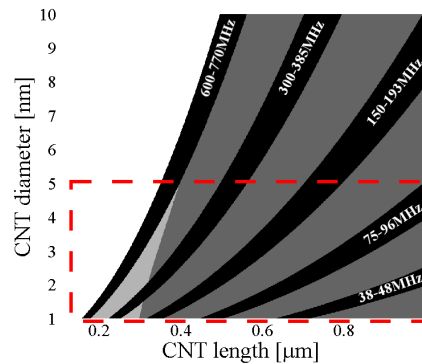
for the ultimate lower bound of 1pF capacitance. Such low capacitance requires the signal ideally not to leave the chip, as any PCB pad would already be of this magnitude (see Figure 3.1). Connecting the CP output directly to the 410fF tuning gate of the VCO leads to such fast settling. This is not foreseen in the integrated topology of Figure 5.5a, but the minor change could be made in a future version. All in all, it is retained that settling times of hundreds of nanoseconds lie in the realm of possibility.

A photograph of the chip unveils its layout in Figure 5.5b. The two VCOs, one for the PLL, the other as emulator of the NEMS, occupy most of the $2.085 \times 2.165 \text{ mm}^2$ surface. Dummy structures are introduced to keep the layout fully symmetrical, while conductances of the NMOS and PMOS transistors have been equalized to reduce the phase noise. The level-shifter saturates the small-swing VCO signals as close as possible to the VCO output and conveys the 1.8V rail-to-rail signals then to the logic blocks, situated close to the left edge of the chip. All digital outputs are buffered and equipped with an enable bit, which are set to either allow readout of signals on internal nodes in debug mode, or to reduce the capacitive load, which creates spikes on the power supply, under normal operation. Layout

The measured frequency tuning ranges are reported on Figure 5.10a. The complete frequency spectrum from 600MHz to 770MHz is covered for tuning voltages in the 0V to 5V range. The maximum VCO gain is achieved around 1.8V and reaches $-62 \frac{\text{MHz}}{\text{V}}$ in the high frequency range (728MHz-771MHz) and $-32 \frac{\text{MHz}}{\text{V}}$ in the low frequency range (600MHz-625MHz), as can be seen in Figure 5.10b. This gain decays to $-10 \frac{\text{MHz}}{\text{V}}$ at the extremes of the reported 0.75V to 2.5V tuning range. The phase noise, measured at a carrier frequency of 190MHz, is reported in Figure 5.10c and presents a corner frequency at an offset of around 300kHz for a noise density of $-123 \frac{\text{dBc}}{\text{Hz}}$. The associated root mean square jitter was found to be $\bar{\sigma} = 10.55\text{ps}$. The measured characteristics and their implications, presented in this section, are summarized in Table 5.1. Measurements

ω_0 [MHz]	Field effect	Piezoresistive
37.5 – 48.1	-	✓
75.0 – 96.3	✓	✓
150.0 – 192.5	✓	✓
300.0 – 385.0	✓	✓
600.0 – 770.0	✓	-

(a) NEMS eigenfrequencies accessible to IC



(b) CNT-space accessible to IC

Figure 5.11: Compatibility between the designed IC and CNT-NEMS, in terms of frequency.

5.3 NEMS versus Circuit Compatibility



- Frequency range** The IC's VCO base operation frequency was found to range from 600MHz to 770MHz. In combination with the three frequency dividers, lower ranges are accessible. These ranges correspond to NEMS eigenfrequencies which the presented IC can handle, if a field effect readout, occurring at ω_0 , is used. Under piezoresistive readout, occurring at $2\omega_0$, the adequate eigenfrequency ranges are to be divided by two. Table 5.11b summarizes the NEMS eigenfrequencies accessible to the presented IC.
- CNT space** These eigenfrequencies depend on the CNT dimensions, which are length and diameter, as by equation (2.9). Figure 5.11b shows in black the 30.3% of the $L \times d = [100\text{nm}; 1\mu\text{m}] \times [1\text{nm}; 5\text{nm}]$ CNT space, corresponding to NEMS eigenfrequencies within the IC's range. Reminding that two thirds of the tubes are semiconducting, having a field effect, and an additional sixth is piezoresistive, the presented IC is, statistically speaking, able to sense a quarter of all the tubes.
- System yield** This 25.3% system yield may be enhanced by targeting appropriate CNT dimensions. On the one hand, the suspension length can be controlled by lithography with a precision of tens of nanometers: the International Technology Roadmap for Semiconductors (ITRS) estimates the 14 nm technology to be reached by semiconductor companies in the 2014 timeframe. On the other hand, the tube growth techniques lead to a nanometer spread in diameter [94]. These tolerances make it rather difficult to considerably increase the yield through specific tube selection, given the narrowness of the five black bands.
- Tensile tuning** The yield may nevertheless be increased by tuning the NEMS eigenfrequency with prestrain. The use of a MEMS actuator with an appropriate set of levers may serve to stretch the CNT by pulling on its movable source, thereby tuning its eigenfrequency. Such an approach extends the IC's compatibility to a large portion of the CNT parameter space, indicated by the grey zones in Figure 5.11b. The displacement resolution required to shift the CNT's eigenfrequency into the IC's range varies from 100 picometer (for a 60%-yield) down to 10 picometer (65.15%-

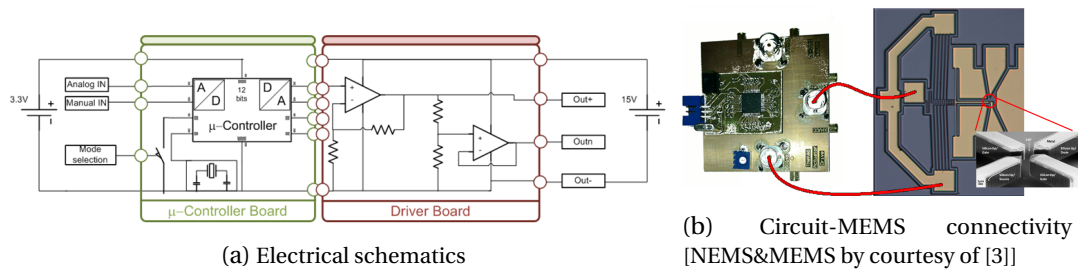


Figure 5.12: Tensile MEMS actuator and its driver electronics

yield).

Though piezoelectric macro actuators reach picometer resolution, their integrated MEMS versions achieve only a 100pm resolution [55]. In optional combination with a simple lever ratio of 1:10, they could tune a substantial part of the CNTs to the IC's operating range. These piezoelectric MEMS are low-power, exhibit high forces and present large travel under robust operation. Their actuation voltage exceeds standard IC supply, and CMOS compatibility of the process may be an issue. Though alternatively magnetic MEMS trade resolution for lower actuation voltage, is simple CMOS process compatibility achieved only by electrostatic and thermal actuators, at the cost of an insufficient 10nm resolution. If high actuator resolution for frequency tuning is an objective, then CMOS compatible aluminum nitride (AlN) MEMS [95] can be used. If, on the contrary, the tensile MEMS shall merely tauten slack tubes, then silicon thermo or electrostatic MEMS are good enough and easier to integrate into the process flow.

Actuator
MEMS

Not appropriate for tuning purposes, but still useful to tauten CNTs, which present slack, a thermoactuator [3] can control the source electrode. The candidate thermo-MEMS has a $300 \frac{\mu\text{m}}{\text{V}}$ sensitivity, a $1\mu\text{m}$ excursion range and presents a 100pF load. Driver electronics have been developed to allow characterization of the MEMS. The modular system is formed by a programmable microcontroller board atop a driver board, schematically depicted in Figure 5.12a. With an output swing of 14.3V, a resolution of 3.5mV LSB, limited by the 12-bit DAC, and a load drive capability of 330pF, the PCB, shown in Figure 5.12b, is able to control the actuator with diverse patterns. 5Hz motion has been observed under the optical microscope, and no circuit noise contribution to motion could be detected by the in-plane motion analyzer.

Actuator
driver

5.4 Mass Resolution & Sensor Speed

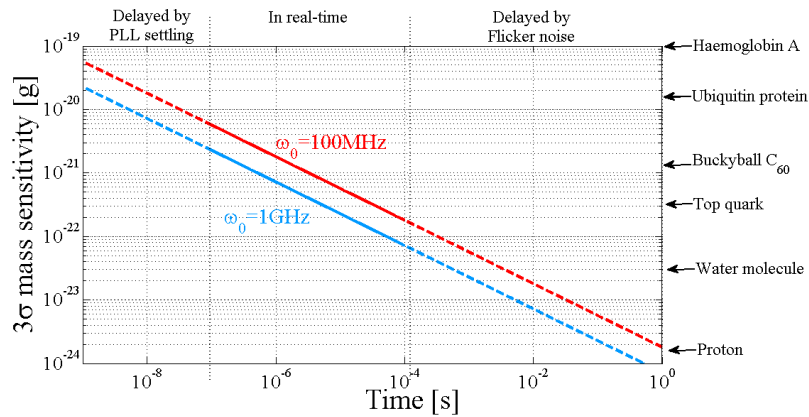


The measured jitter of the IC ($\sigma = 10.55\text{ps} @ \tilde{T}_0 = 5'263\text{ps}$) translates into mass sensitivity by equation (4.7). Using CNT-NEMS optimized for signal strength, according to Figure 2.11, the 100MHz NEMS shall be a $1\mu\text{m}$ -long unstrained tube of mass $m = 2.1\text{ag}$, while the 1GHz-CNT shall be a slightly prestrained 400nm-long tube, weighing $m = 820\text{zg}$. These tubes' sensor performance is reported on Figure 5.13 and reveals zeptogram resolution within a microsecond, which compares favorably to the 1s averaging time necessary in [30] to achieve

Sensor
resolution

Figure 5.13:

CNT-NEMS sensor sensitivity and 3σ -detection speed limits imposed by the integrated PLL. The indicated mass-time resolution is obtained once the PLL has settled. Once Flicker noise starts, the slope smoothens.



the same resolution.

Speed limit The measurement resolution was found in equation (4.7) to improve with the inverse of the square root of time. Before this averaging process can start, the PLL needs to settle, which was predicted in section 4.3.4 to occur after roughly 100ns. The IC demonstrates that 10 μ s are possible (Figure 5.10d) under a condition, which can be extrapolated towards 100ns in an optimal but realistic scenario (Table 5.1). This settling time sets an absolute upper bound on the sensing speed. It is noteworthy to point out that these 100ns considerably undercut conventional frequency sweeps (~ 1 s) and state-of-the-art computer-aided feedback (15ms [31]). This means that for any weighing faster than ten milliseconds, the here proposed mass balance, embedded into a calibrated PLL topology, would hold the record, making it the fastest weight detector almost down to single protons.

NEMS limit It has been assumed previously that the circuit noise limits the sensing performance. This is true within the white noise range of CNT-NEMS [82], but the situation may toggle at long integration times, where the CNT-NEMS start showing important Flicker noise [83]. With corner frequencies around 10kHz [81], the sensitivity slope of Figure 5.13 is expected to slab beyond 100 μ s sensing time. This phenomenon is to be attributed to the NEMS and occurs independently of the readout technique.

Maximum tolerable weight In connection with the evaluation of the maximum tolerable desorbed single particle mass, of section 4.2.3, the heaviest detectable particle able to ad- and desorb without requiring a NEMS restart, must weigh less than $\Delta m_{\max} = \frac{2m_{\text{NEMS}}}{Q} > 10\text{zg}$. This corresponds approximately to the mass of ubiquitin (see Table 5.13), a small regulatory protein in eukaryotic organisms. Heavier particles can still be sensed, as explained in section 4.2.3, but their desorption causes the PLL to lose the signal and converge towards the wrong direction in the frequency spectrum, calling for a restart. These heavy particles can still be sensed, and if their adherence is permanent, they are unproblematic anyway.

5.5 Summary



The previously discussed system topologies have been partially implemented, with the goal of delivering a proof of concept via practical demonstration of joint closed-loop CNT-NEMS and circuit operation. From a circuit point of view, no immediate obstacles occurred, but the absence of an operational CNT-NEMS did not allow to push the endeavour through. A semi-practical, semi-theoretical assessment of the expected system's performance could be performed nevertheless.

Theory
meets
practice

A printed circuit board (PCB) and an integrated CMOS circuit (IC) implementation of the core PLL topology, being at the basis of NEMS-VCOs and sensors, have been presented. The 4.5mm² IC system can operate on different frequency bands, ranging from 37.5MHz to 770MHz, covering 30.3% of the typical CNT-NEMS space. Operated in combination with a high-resolution frequency tuning actuator MEMS, the IC has a 60% probability to be able to operate on a randomly selected CNT-NEMS. The underlying condition is that the CNT-NEMS shall be operated optimally (section 2.2), or at least sufficiently close to optimality, for the front-end to be able to detect the signal (section 3.4). PLL settling times of hundred nanoseconds were found to lie in the realm of possibility, meaning that the system can provide quantitative sensor information hundreds of nanoseconds after a particle was adsorbed. This is orders of magnitude faster than what state-of-the-art sweeping (seconds) or computer-aided feedback loops (tens of milliseconds) can perform.

NEMS-
VCO

The IC's jitter was measured to 0.2% of the period, translating into a high-speed mass resolution, out of reach for state-of-the-art mixing and sweeping mass balances. Zeptogram detection would be possible within a microsecond, which is four orders of magnitude faster than any reported mass balance system. The system must however be shielded from parasitic particles, heavier than 10zg, to prevent the need of an unwanted restart at their desorption.

Mass
balance

The resulting findings raise hope for prospective faster mass balances, without however consistently integrating all the previously discussed systems. This decision rooted in the perceived improbability to obtain a high-performance CNT-NEMS within the time constraints. For the not implemented blocks, circuit schematics have nevertheless been provided in chapter 4, which shall allow to inspire their implementation once CNT-NEMS are more mature. All in all, the potential, for the presented system topology, to be on a par with state-of-the-art sensors in terms of resolution, while undercutting them in terms of speed, is considerable.

Assessment

*A conclusion is the place,
where you got tired thinking.*

— Martin H. Fischer

Conclusion

This thesis systematically unveiled the full potential residing in carbon nanotube electromechanical resonators and proposed strategies both for their characterization and for exploitation of their desirable qualities within electronic applications. Adequate electronic interfaces, enabling the CNT-NEMS' advance to high-speed oscillator and high-resolution sensor applications, have been devised. A system, prone to becoming the world's fastest, high-precision mass balance, with resolution down to molecular scale within a microsecond, has ultimately been developed and was partially integrated into hardware.

Citius
Altius
Fortius

To achieve these results, a number of advancements in diverse domains were made. In-depth electromechanical analyses of CNT-NEMS, at the physical level, were followed by the study of low noise electronic interfaces at circuit level, allowing exploitation of the ultrasensitive high-frequency properties of CNT-NEMS at system level, in particular for voltage controlled oscillators and mass balance applications, offering unprecedented temporal resolution.

Multi-
domain
progress

A recursion through the highlights of this thesis would point out the self-calibrating NEMS mass balance, orders of magnitude faster than any previously known equally sensitive particle detector, and the exhaustive electromechanical and solid state analysis of CNT-NEMS resonators, quantifying once and for all the electromechanical signals in amplitude, frequency and phase. Notable is also the novel 4ω mixing technique, allowing to individually characterize the motional and electrical capacitive, field and piezoresistive effects in CNT-NEMS, as well as the simultaneous electrical and mechanical characterization of CNT adsorbate configurations. The compiled optimal CNT-NEMS and circuit design guidelines may foster their transfer from research to application level. Furthermore, the discovery of potential third harmonic frequency tuning via amplitude control, and the high-speed pressure sensor system concept, can be mentioned.

Stars &
starlets

The benefits of the tunable, high frequency, moderate quality factor and high sensitivity of CNT-NEMS resonators is found to be accessible to electronic systems, if the NEMS is

Application
maturity of
CNT-NEMS

Conclusion

designed and operated in accordance with circuit requirements and vice versa. To perform the successful leap out of their promising-property-investigating ivory tower, towards beneficial system applications, CNT-NEMS underwent a thorough, in-depth electromechanical analysis, which confronted them with the requirements of electronic circuit interfaces. A theoretical analysis showed that doubly-clamped single-walled CNT-NEMS resonators yield maximal signal-to-noise ratio when biased to their diffusive saturation regime, sustaining a DC current of several microamperes. For two thirds of the CNT-NEMS, their motion can be detected by the 100nA strong field effect current modulation. Another sixth is measurable via the medium-strength 1nA piezoresistive current modulation, while a final sixth only offers the tens of picoampere weak capacitive modulation. These values presume optimal CNT-NEMS selection, which crystallized into clear guidelines as a function of the target operation frequency. Narrow, possibly prestrained, tubes of lengths between 100nm to 1 μ m cover eigenfrequencies from tens of megahertz to low gigahertz, and the optimal parameter set has been determined by maximisation of the electromechanical transduction efficiency under the constraint of state-of-the-art CNT-NEMS process limitations. The transduction mechanism has been retraced to an oscillating Euler-Bernoulli beam with von Kármán strains, discretized by a Galerkin procedure. Solid state investigations showed how resonating tubes experience potential fluctuations (capacitive effect), carrier state repopulation (field effect) and density of state variations (piezoresistive effect).

Prospective motion detection The quality of the first electronic interface stage was shown to be the crucial factor for the overall system signal-to-noise ratio. Operating the CNT-NEMS as a mixer (inferring motion from a lower frequency), was the state-of-the-art solution to circumvent the challenges involving noise, spurious electrical signals and high-frequency attenuation. The present work contributed in this characterization aspect by categorizing the different current modulation effects in CNT-NEMS, for the first time ever, by their strength, frequency and phase. Instructions on how to experimentally detect each and every effect via the mixing technique have been provided. Their experimental verification would allow to systematically evaluate the true CNT-NEMS potential for applications. The 4ω half-frequency detection of the piezoresistive component is new and offers as its corollary the ability to infer not just CNT-NEMS adsorbates' mass, but also to inform on their binding configuration. The contributions of the present dissertation extend beyond the mere characterization of NEMS. The true benefits of CNT-NEMS reside at their high sensitivity and eigenfrequencies, which can be exploited only through direct readout, while mixing techniques would sacrifice these potential high-speed benefits. In this context, high-frequency common source MOS front-ends were found to have an edge over common emitter BJT interfaces in terms of SNR. This convenience is attributed to their higher input impedance and lasts up to hundreds of megahertz, after which the situation toggles. Four-stage front-ends were shown to allow direct readout and offer sufficient amplification for NEMS eigenfrequencies until hundreds of megahertz, with a full bandwidth SNR reaching 30dB for the motional field effect. At even higher, gigahertz frequencies, the spurious electrical NEMS signal starts obfuscating the motional field effect, which requires evasion towards the less efficient piezoresistive readout strategy. The latter requires aggressive filtering, resulting

in unfeasibility of closed-loop oscillator operation. Hundreds of megahertz are consequently the limit for wideband direct readout and closed-loop NEMS operation for the case of CNTs. Beyond this limit, graphene ribbons and nanowire resonators may be an option.

Several closed-loop systems, regulating the NEMS oscillation, have been proposed. For speed, robustness and testability reasons, a feedback system, embedding the NEMS into a phase-locked loop, has been retained. It allows to characterise NEMS in an open-loop setup and can lock on unknown NEMS characteristics, to form a closed-loop oscillator. With wider tunability than quartz crystals and larger quality factors than LC tanks, system-in-package NEMS-VCOs can complement these ubiquitous electronic blocks. The oscillation frequency is imposed by the NEMS and is tunable over a decade. Reversely, high-speed force and pressure sensing has been shown to be feasible. Second order PLLs are required and fastest settling is obtained for slightly underdamped PLLs with maximal, sub-eigenfrequency bandwidth. PLL settling times as short as 100ns can be obtained at NEMS eigenfrequencies of hundreds of megahertz. Integrated in a 180nm technology, the 4.5mm² PLL can operate on different frequency bands, ranging from 37.5MHz to 770MHz. This range makes the system statistically compatible with a third of the CNT-NEMS, grown by state-of-the-art processes.

Conceiving
NEMS-
VCOs

Precise tracking of the eigenfrequency has been shown to be a necessary condition for unbiased quantitative sensing. Unprecedented high-speed high-resolution mass sensitivity is obtained after calibration of the NEMS-VCO through a novel approach. The *a priori* unknown NEMS phase is made observable through a nonlinear technique and is corrected via a third-order PLL-like feedback. Sensing can start as soon as the PLL settled, which was shown to be possible within hundreds of nanoseconds. From then on, the sensor resolution was found to improve with the inverse of the square root of observed oscillation periods. High-frequency direct readout is especially beneficial at this point. All in all, evaluation of the IC's noise predicts zeptogram resolution within a microsecond. This is immensely fast in comparison to equivalently precise state-of-the-art weighing techniques, which are hampered by an equivalent settling time of tens of milliseconds. It is claimed that the novel system has the potential to improve speed performance of high-resolution mass balances by several orders of magnitude.

Precise &
fast sensing

In retrospect, the present dissertation offers a systematic study of NEMS and CNT-NEMS in particular, bringing forward beneficial insights on their maximal performance expectations. With the hidden agenda of providing the world's most sensitive devices with a boost in speed, direct readout circuitry has been proposed and was shown to be possible, although the CNT-NEMS under test was not exactly brilliant. Novel system topologies, within the realm of CNTs and semiconducting or piezoresistive NEMS in general, have been developed and were partially integrated, accompanied by design guidelines. Their semi-experimental, semi-theoretical assessment offers bright prospects onto high-speed electromechanical VCO and sensing applications. With these insights, know-how, design guidelines, implementations and a twinge of regret for the half-way case study, the availability of a proficient CNT-NEMS can be eagerly awaited.

Sparkling
prospects

Conclusion

An outlook From theoretical, circuit and system points of view, no show-stopper has been described up to application frequencies of hundreds of megahertz, allowing to conclude the thesis on a positive note. In hindsight, this contribution may come too early, with respect to the actual maturity status of CNT-NEMS fabrication processes, far from being batch production. Confident about future progress on this aspect, the contributions of the present thesis shall be used in a first phase to systematically characterize CNT-NEMS by their electrical and motional capacitive, field and piezoresistive effects. This would be done through a mixer setup in their linear regime and by direct readout, in combination with the proposed open-loop PLL, under saturation. In a second phase, the loop shall be closed in order to verify the semi-theoretical, semi-experimental speed and resolution projections. Alternative resonators, such as graphene ribbons or silicon nanowires, may as well be considered for the proposed system applications.

Revisiting Depending on the experimental outcomes, CNT-NEMS may experience a boost in popularity
Utopia for system designers, bringing the smart dust utopia from section 1.1 a step closer to reality. Concretely, the high-speed sensors may be used as fast microscopic cameras, monitoring biological reactions and benefiting health applications. Whether one fine day they become part of systems instantly disassembling viruses or mutated cells, is still written in the stars. The sensor could just as well become part of a large scale environmental monitoring system... Research trees are indeed infinite, and "prediction is very difficult, especially about the future",
— Niels Bohr.

*Publication has been extended far beyond
our present ability to make real use of the record.*

— Vannevar Bush

Bibliography

- [1] V. Sazonova, Y. Yaish, H. Ustunel, D. Roundy, T. A. Arias, and P. L. McEuen, “A tunable carbon nanotube electromechanical oscillator,” *Nature*, vol. 431, no. 7006, pp. 284–287, Sep. 2004.
- [2] H. Peng, C. Chang, S. Aloni, T. Yuzvinsky, and A. Zettl, “Ultrahigh frequency nanotube resonators,” *PRL*, vol. 97, p. 087203, Aug 2006.
- [3] S.-W. Lee, “Integration platform for tunable carbon nanotube electromechanical resonators,” *PhD Dissertation ETH Zurich No 21508 Switzerland*, 2013.
- [4] A. Svizhenko and M. P. Anantram, “Effect of scattering and contacts on current and electrostatics in carbon nanotubes,” *Phys. Rev. B*, vol. 72, p. 085430, Aug 2005.
- [5] J. Park, S. Rosenblatt, Y. Yaish, V. Sazonova, H. Ustunel, S. Braig, T. Arias, P. Brouwer, and P. McEuen, “Electron-phonon scattering in metallic single-walled carbon nanotubes,” *Nano Letters*, vol. 4, no. 3, pp. 517–520, 2004.
- [6] J. M. H. Kroes, F. Pietrucci, A. Curioni, R. Jaafar, O. Gröning, and W. Andreoni, “Atomic oxygen chemisorption on carbon nanotubes revisited with theory and experiment,” *The Journal of Physical Chemistry C*, vol. 117, no. 4, pp. 1948–1954, 2013.
- [7] T. Durkop, S. A. Getty, E. Cobas, and M. S. Fuhrer, “Extraordinary mobility in semiconducting carbon nanotubes,” *Nano Letters*, vol. 4, no. 1, pp. 35–39, 2004.
- [8] P. Avouris, Z. Chen, and V. Perebeinos, “Carbon-based electronics.” *Nat Nanotechnol*, vol. 2, no. 10, pp. 605–615, Oct 2007.
- [9] G. Katti, M. Stucchi, K. De Meyer, and W. Dehaene, “Electrical modeling and characterization of through silicon via for three dimensional ics,” *Electron Devices, IEEE Transactions on*, vol. 57, no. 1, pp. 256–262, 2010.

Bibliography

- [10] F. Leonard and J. Tersoff, "Role of fermi-level pinning in nanotube schottky diodes," *Phys. Rev. Lett.*, vol. 84, pp. 4693–4696, May 2000.
- [11] Z. Chen, J. Appenzeller, J. Knoch, Y. Lin, and P. Avouris, "The role of metal-nanotube contact in the performance of carbon nanotube field-effect transistors." *Nano Lett*, vol. 5, no. 7, pp. 1497–1502, Jul 2005.
- [12] L. Jeong, C. Park, K. JuJin, K. Jinhee, W. Jong, and H. Kyung, "Formation of low resistance ohmic contacts between carbon nanotube and metal electrodes by a rapid thermal annealing method," *Journal of Physics D*, vol. 33, no. 16, p. 1953, 2000.
- [13] C. Yang, A. Hazeghi, K. Takei, C. Hong-Yu, P. Chan, A. Javey, and H. Wong, "Low-resistance electrical contact to carbon nanotubes with graphitic interfacial layer," *Electron Devices, IEEE Transactions on*, vol. 59, no. 1, pp. 12–19, 2012.
- [14] H. S. Kim, G. I. Lee, H. S. Kim, J. K. Kang, and Y.-H. Kim, "Intrinsically low-resistance carbon nanotube-metal contacts mediated by topological defects," *MRS Communications*, vol. 2, pp. 91–96, 9 2012.
- [15] H. Chandralalim, C. Roman, and C. Hierold, "Analytic modeling and piezoresistive detection theory of acoustic resonances in carbon nanotubes," in *10th conf. IEEE-NANO*, aug. 2010, pp. 778 –781.
- [16] C. Kauth, M. Pastre, and M. Kayal, "Wideband low-noise rf front-end for cnt-nems sensors," *Mixed Design of Integrated Circuits and Systems conference proceedings*, pp. 289–293, May 2012.
- [17] Y. Xu, C. Chen, V. Deshpande, F. DiRenno, A. Gondarenko, D. Heinz, S. Liu, P. Kim, and J. Hone, "Radio frequency electrical transduction of graphene mechanical resonators," *Applied Physics Letters*, vol. 97, p. 243111.
- [18] T. Abhilash, J. Mathew, S. Sengupta, M. Gokhale, A. Bhattacharya, and M. Deshmukh, "Wide bandwidth nanowire electromechanics on insulating substrates at room temperature," *Nano Letters*, vol. 12, p. 6432, 2012.
- [19] H. Meerwaldt, S. Johnston, H. Van der Zant, and S. G, "Submicrosecond-timescale readout of carbon nanotube mechanical motion," *Applied Physics Letters*, vol. 103, p. 53121, 2013.
- [20] M. Eckert and W. Zhao, "Opening windows on new biology and disease mechanisms: development of real-time in vivo sensors," *Interface Focus*, vol. 3, 2013.
- [21] E. Pop, D. Mann, J. Cao, Q. Wang, K. Goodson, and H. Dai, "Negative differential conductance and hot phonons in suspended nanotube molecular wires," *Phys. Rev. Lett.*, vol. 95, p. 155505, Oct 2005.
- [22] S. Frank, P. Poncharal, Z. Wang, and W. Heer, "Carbon nanotube quantum resistors," *Science*, vol. 280, no. 5370, pp. 1744–1746, 1998.

- [23] R. Landauer, "Conductance determined by transmission: probes and quantised constriction resistance," *Journal of Physics: Condensed Matter*, vol. 1, no. 43, p. 8099, 1989.
- [24] S. J. Tans, A. R. M. Verschueren, and C. Dekker, "Room-temperature transistor based on a single carbon nanotube," *Nature*, vol. 393, no. 6680, pp. 49–52, May 1998.
- [25] S.-W. Lee, S. Truax, L. Yu, C. Roman, and C. Hierold, "Carbon nanotube resonators with capacitive and piezoresistive current modulation readout," *Applied Physics Letters*, vol. 103, no. 3, pp. –, 2013.
- [26] M. Radosavljevic, S. Heinze, J. Tersoff, and P. Avouris, "Drain voltage scaling in carbon nanotube transistors," *Applied Physics Letters*, vol. 83, p. 2435, Sep. 2003.
- [27] A. W. Orbaek, A. C. Owens, C. C. Crouse, C. L. Pint, R. H. Hauge, and A. R. Barron, "Single walled carbon nanotube growth and chirality dependence on catalyst composition," *Nanoscale*, vol. 5, pp. 9848–9859, 2013.
- [28] H. B. Peng, C. W. Chang, S. Aloni, T. D. Yuzvinsky, and A. Zettl, "Microwave electromechanical resonator consisting of clamped carbon nanotubes in an abacus arrangement," *Phys. Rev. B*, vol. 76, p. 035405, Jul 2007.
- [29] V. Gouttenoire and et al., "Digital and fm demodulation of a doubly clamped single-walled carbon-nanotube oscillator: towards a nanotube cell phone," *Small*, pp. 1060–1065, 2010.
- [30] Y. T. Yang, C. Callegari, X. L. Feng, K. L. Ekinici, and M. L. Roukes, "Zeptogram-scale nanomechanical mass sensing," *Nano Letters*, vol. 6, no. 4, pp. 583–586, 2006.
- [31] J. Chaste, A. Eichler, J. Moser, G. Ceballos, R. Rurali, and A. Bachtold, "A nanomechanical mass sensor with yoctogram resolution," *Nature Nanotechnology*, vol. 7, pp. 301–304, 2012.
- [32] B. Witkamp, M. Poot, and H. S. J. van der Zant, "Bending-mode vibration of a suspended nanotube resonator," *Nano Letters*, vol. 6, no. 12, pp. 2904–2908, 2006.
- [33] B. Lassagne, D. Garcia-Sanchez, A. Aguasca, and A. Bachtold, "Ultrasensitive mass sensing with a nanotube electromechanical resonator," *Nano Letters*, vol. 8, no. 11, pp. 3735–3738, 2008.
- [34] A. K. Hüttel, G. A. Steele, B. Witkamp, M. Poot, L. P. Kouwenhoven, and H. S. J. van der Zant, "Carbon nanotubes as ultrahigh quality factor mechanical resonators," *Nano Letters*, vol. 9, pp. 2547–2552, June 2009.
- [35] J. Moser, J. Guttinger, A. Eichler, M. Esplandiu, D. Liu, M. Dykman, and A. Bachtold, "Ultrasensitive force detection with a nanotube mechanical resonator," *Nat Nano*, vol. 8, pp. 493–496, 2013.
- [36] S. Iijima, "Helical microtubules of graphitic carbon," *Nature*, vol. 354, no. 6348, pp. 56–58, Nov. 1991.

Bibliography

- [37] T. Guo, P. Nikolaev, A. Thess, D. Colbert, and R. Smalley, "Catalytic growth of single-walled nanotubes by laser vaporization," *Chemical Physics Letters*, vol. 243, no. 1–2, pp. 49 – 54, 1995.
- [38] K. S. Kim, G. Cota-Sanchez, C. T. Kingston, M. Imris, B. Simard, and G. Soucy, "Large-scale production of single-walled carbon nanotubes by induction thermal plasma," *Journal of Physics D: Applied Physics*, vol. 40, no. 8, p. 2375.
- [39] M. José Yacamán, M. Miki Yoshida, L. Rendón, and J. G. Santiesteban, "Catalytic growth of carbon microtubules with fullerene structure," *Applied Physics Letters*, vol. 62, no. 2, pp. 202–204, 1993.
- [40] S. Purcell, P. Vincent, C. Journet, and V. Binh, "Tuning of nanotube mechanical resonances by electric field pulling," *Physical Review Letters*, vol. 89, no. 27, p. 276103, 2002.
- [41] S. K. Youn, N. Yazdani, J. Patscheider, and H. G. Park, "Facile diameter control of vertically aligned narrow single-walled carbon nanotubes," *RSC Adv*, vol. 3, pp. 1434–1441, 2013.
- [42] Y. H. Yang and W. Z. Li, "Radial elasticity of single-walled carbon nanotube measured by atomic force microscopy," *Applied Physics Letters*, vol. 98, no. 4, 2011.
- [43] M. Dresselhaus, G. Dresselhaus, A. Jorio, A. S. Filho, and R. Saito, "Raman spectroscopy on isolated single wall carbon nanotubes," *Carbon*, vol. 40, p. 2043–2061, 2002.
- [44] J. Lehman, M. Terrones, E. Mansfield, K. Hurst, and V. Meunier, "Evaluating the characteristics of multiwall carbon nanotubes," *Carbon*, vol. 49, no. 8, pp. 2581 – 2602, 2011.
- [45] P. Ruffieux, O. Groning, M. Biemann, P. Mauron, L. Schlapbach, and Groning.
- [46] G. Buchs, A. Krasheninnikov, P. Ruffieux, P. Groning, A. Foster, R. Nieminen, and O. Groning, "Creation of paired electron states in the gap of semiconducting carbon nanotubes by correlated hydrogen adsorption," *New Journal of Physics*, vol. 9, no. 8, p. 275, 2007.
- [47] C. Kauth, M. Pastre, and M. Kayal, "On-chip mass sensing at the physical limits of nano-electromechanical systems," *Advances in Sensors and Interfaces conference proceedings*, pp. 131–135, June 2013.
- [48] M. Dequesnes, Z. Tang, and N. R. Aluru, "Static and dynamic analysis of carbon nanotube-based switches," *Journal of Engineering Materials and Technology*, vol. 126, no. 3, pp. 230–237, 2004.
- [49] L. Forro, J.-P. Salvetat, J.-M. Bonard, R. Bacsá, N. Thomson, S. Garaj, L. Thien-Nga, R. Gaal, A. Kulik, B. Ruzicka, L. Degiorgi, A. Bachtold, C. Schonenberger, S. Pekker, and K. Hernadi, "Electronic and mechanical properties of carbon nanotubes," pp. 297–320, 2002.
- [50] S. Gupta, F. Bosco, and R. Batra, "Wall thickness and elastic moduli of single-walled carbon nanotubes from frequencies of axial, torsional and inextensional modes of vibration," *Computational materials science*, vol. 47, pp. 1049–1059, 2010.

- [51] S. Senturia, *Microsystem Design*. Kluwer academic publishers, 2001.
- [52] S.-W. Lee, S. Truax, L. Yu, C. Roman, and C. Hierold, “Carbon nanotube resonators with capacitive and piezoresistive current modulation readout,” *Applied Physics Letters*, vol. 103, no. 3, 2013.
- [53] A. N. Cleland and M. L. Roukes, “Noise processes in nanomechanical resonators,” *Applied Physics*, vol. 92, no. 5, pp. 2758–2769, sep 2002.
- [54] R. S. Ruoff, D. Qian, and W. K. Liu, “Mechanical properties of carbon nanotubes: theoretical predictions and experimental measurements,” *Comptes Rendus Physique*, vol. 4, no. 9, pp. 993–1008, 2003.
- [55] D. Bell, T. Lu, N. Fleck, and S. Spearing, “Mems actuators and sensors: observations on their performance and selection for purpose,” *J. Micromech. Microeng.*, vol. 15, pp. 153–164, 2005.
- [56] E. A. Laird, F. Pei, W. Tang, G. A. Steele, and L. P. Kouwenhoven, “A high quality factor carbon nanotube mechanical resonator at 39 ghz,” *Nano Letters*, vol. 12, no. 1, pp. 193–197, 2012.
- [57] S. Reich, J. Maultzsch, C. Thomsen, and P. Ordejón, “Tight-binding description of graphene,” *Phys. Rev. B*, vol. 66, no. 3, p. 035412, 2002.
- [58] J. Chaste, L. Lechner, P. Morfin, G. Feve, T. Kontos, J. Berroir, D. Glattli, H. Happy, P. Hakonen, and B. Placais, “Single carbon nanotube transistor at ghz frequency,” *Nano Letters*, vol. 8, no. 2, pp. 525–528, 2008.
- [59] J. Kong, E. Yenilmez, T. W. Tombler, W. Kim, H. Dai, R. B. Laughlin, L. Liu, C. S. Jayanthi, and S. Y. Wu, “Quantum interference and ballistic transmission in nanotube electron waveguides,” *Phys. Rev. Lett.*, vol. 87, p. 106801, Aug 2001.
- [60] Z. Yao, C. L. Kane, and C. Dekker, “High-field electrical transport in single-wall carbon nanotubes,” *Phys. Rev. Lett.*, vol. 84, no. 13, pp. 2941–2944, Mar 2000.
- [61] X. Zhou, J.-Y. Park, S. Huang, J. Liu, and P. L. McEuen, “Band structure, phonon scattering, and the performance limit of single-walled carbon nanotube transistors,” *Phys. Rev. Lett.*, vol. 95, no. 14, p. 146805, 2005.
- [62] S. Datta, *Electronic Transport in Mesoscopic Systems*. Cambridge University Press, May 1997.
- [63] S. Rosenblatt, “Pushing the limits of carbon nanotube transistors,” *Ph.D Thesis, Connel University*, 2006.
- [64] C. L. Kane and E. J. Mele, “Size, shape, and low energy electronic structure of carbon nanotubes,” *Phys. Rev. Lett.*, vol. 78, no. 10, pp. 1932–1935, Mar 1997.

Bibliography

- [65] W. Harrison, *Electronic structure and the properties of solids*. New York, Dover, 1989.
- [66] L. Yang and J. Han, "Electronic structure of deformed carbon nanotubes," *Phys. Rev. Lett.*, vol. 85, no. 1, pp. 154–157, Jul 2000.
- [67] P. Zhao and G. Shi, "Study of poisson's ratios of graphene and single-walled carbon nanotubes based on an improved molecular structural mechanics model," *cmc-computers materials & continua*.
- [68] C. Nisoli, P. Lammert, E. Mockensturm, and V. Crespi, "Carbon nanostructures as an electromechanical bicontinuum," *PHYSICAL REVIEW LETTERS*, vol. 99, p. 045501, 2007.
- [69] M. Huang, Y. Wu, B. Chandra, H. Yan, Y. Shan, T. F. Heinz, and J. Hone, "Direct measurement of strain-induced changes in the band structure of carbon nanotubes," *Phys. Rev. Lett.*, vol. 100, p. 136803, Apr 2008.
- [70] P. K. Valavala, D. Banyai, M. Seel, and R. Pati, "Self-consistent calculations of strain-induced band gap changes in semiconducting $(n, 0)$ carbon nanotubes," *Phys. Rev. B*, vol. 78, p. 235430, Dec 2008.
- [71] A. Javey, J. Guo, Q. Wang, M. Lundstrom, and H. Dai, "Ballistic carbon nanotube field-effect transistors," *Nature*, vol. 424, no. 6949, pp. 654–657, Aug. 2003.
- [72] M. Anantram and F. Leonard, "Physics of carbon nanotube electronic devices," *Reports on Progress in Physics*, vol. 69, no. 3, p. 507, 2006.
- [73] H. Ago, T. Kugler, F. Cacialli, W. Salaneck, M. Shaffer, A. Windle, and R. Friend, "Work functions and surface functional groups of multiwall carbon nanotubes," *The Journal of Physical Chemistry B*, vol. 103, no. 38, pp. 8116–8121, 1999.
- [74] S. Jones and J. Greer, "Formation of contacts between doped carbon nanotubes and aluminum electrodes," *Journal of Applied Physics*, vol. 114, no. 15, 2013.
- [75] Y. Yaish, J. Park, S. Rosenblatt, V. Sazonova, M. Brink, and P. McEuen, "Electrical nanoprob- ing of semiconducting carbon nanotubes using an atomic force microscope," *Physical Review Letters*, vol. 92, no. 4, p. 046401, Jan 2004.
- [76] K. Milowska and J. Majewski, "Functionalization of carbon nanotubes with -chn, -nhn fragments, -cooh and -oh groups," *jcp*, vol. 138, no. 19, p. 194704, May 2013.
- [77] D. Kang, N. Park, J. Ko, E. Bae, and W. Park, "Oxygen-induced p-type doping of a long individual single-walled carbon nanotube," *Nanotechnology*, vol. 16, no. 8, p. 1048, 2005.
- [78] C. Kauth, M. Pastre, J. Sallese, and M. Kayal, "System-level design considerations for carbon nanotube electromechanical resonators," *Journal of Sensors*, vol. 23, p. Article ID 384643, 2013.

- [79] K. Jensen, J. Weldon, H. Garcia, and A. Zettl, "Nanotube radio," *Nano Letters*, vol. 7, no. 11, pp. 3508–3511, 2007.
- [80] *Carbon Nanotubes: Properties and Applications*. CRC, 2006, p. 93.
- [81] P. G. Collins, M. S. Fuhrer, and A. Zettl, "1/f noise in carbon nanotubes," *Applied Physics Letters*, vol. 76, no. 7, pp. 894–896, 2000.
- [82] K. L. Ekinici, Y. T. Yang, and M. Roukes, "Ultimate limits to inertial mass sensing based upon nanoelectromechanical systems," *Journal of Applied Physics*, vol. 95, no. 5, pp. 2682–2689, 2004.
- [83] H. Postma, T. Teepen, Z. Yao, and C. Dekker, *XXXVIth Rencontres de Moriond : "Electronic Correlations: From Meso- to Nano-Physics"*.
- [84] C. Kauth, M. Pastre, and M. Kayal, "Closed-loop oscillator circuit for piezoresistive carbon nanotube nems resonators," *Mixed Design of Integrated Circuits and Systems proceedings*, pp. 365–368, June 2013.
- [85] H. Peng, C. Chang, S. Aloni, T. Yuzvinsky, and A. Zettl, "Microwave electromechanical resonator consisting of clamped carbon nanotubes in an abacus arrangement," *Phys. Rev. B*, vol. 76, p. 035405, 2007.
- [86] C. Kauth, M. Pastre, and M. Kayal, "Low-noise wideband circuit for closed-loop rf cnt-nems sensors," *International Journal of Microelectronics and Computer Science*, vol. 3, pp. 67–72, 2012.
- [87] H.-Y. Chiu, P. Hung, H. W. C. Postma, and M. Bockrath, "Atomic-scale mass sensing using carbon nanotube resonators," *Nano Letters*, vol. 8, no. 12, pp. 4342–4346, 2008.
- [88] C. Kauth, M. Pastre, and M. Kayal, "A self-regulating oscillator for sensor operation of nanoelectromechanical systems," *New Circuits and Systems conference proceedings*, pp. 1–4, June 2013.
- [89] D. Nordlund, "High accuracy analog differentiator," *Rev. Sci. Instrum.*, vol. 43, no. 11, p. 1699, 1972.
- [90] G. J. Deboo, "A novel integrator results by grounding its capacitor," *Electronic Design*, vol. 15, 1967.
- [91] C. Kauth, M. Pastre, and M. Kayal, "Robust control of oscillating nems sensors," *IEEE International Conference on Electronics, Circuits and Systems*, pp. 185–188, December 2013.
- [92] J. Yuan and C. Svensson, "High-speed cmos circuit technique," *Solid-State Circuits, IEEE Journal of*, vol. 24, no. 1, pp. 62–70, feb. 1989.

Bibliography

- [93] W.-H. Lee, J.-d. Cho, and S.-D. Lee, "A high speed and low power phase-frequency detector and charge-pump," in *Design Automation Conference Proceedings*, 1999, pp. 269–272 vol.1.
- [94] C. Cheung, A. Kurtz, H. Park, and C. Lieber, "Diameter-controlled synthesis of carbon nanotubes," *The Journal of Physical Chemistry B*, vol. 106, no. 10, pp. 2429–2433, 2002.
- [95] S. Trolier-McKinstry and P. Muralt, "Thin film piezoelectrics for mems," *Journal of Electroceramics*, vol. 12, no. 1-2, pp. 7–17, 2004.

*There is no form of prose more difficult to understand
and more tedious to read than the average scientific paper.*

— Francis Crick

Publications

Journal Articles



- C. Kauth, M. Pastre, M. Kayal, "A Novel Approach to High-Speed High-Resolution On-Chip Mass Sensing", submitted to *Microelectronics Journal*, 2013.
- C. Kauth, M. Pastre, M. Kayal, "Electromechanical System-in-Package Carbon Nanotube VCO", *International Journal of Microelectronics and Computer Science*, vol. 4, no. 4, pp. 153-158, 2013.
- C. Kauth, M. Pastre, J-M. Sallese, M. Kayal, "System-Level Design Considerations for Carbon Nanotube Electromechanical Resonators," *Journal of Sensors*, vol. 2013, Article ID 384643, 2013.
- C. Kauth, M. Pastre, M. Kayal, "Low-noise Wideband Circuit for Closed-loop RF CNT-NEMS Sensors", *International Journal of Microelectronics and Computer Science*, vol. 3, no. 2, pp. 67-72, 2012.

Conference Proceedings & Talks



- C. Kauth, M. Pastre, M. Kayal, "Robust Control of Oscillating NEMS Sensors", in proceedings of *20th IEEE International Conference on Electronics, Circuits and Systems*, United Arab Emirates / Abu Dhabi, 2013, pp. 185-188.
- C. Kauth, M. Pastre, M. Kayal, "Closed-Loop Oscillator Circuit for Piezoresistive Carbon Nanotube NEMS Resonators", in proceedings of *20th International Mixed Design of Integrated Circuits and Systems Conference*, Poland / Gdynia, 2013, pp.365-368.
- C. Kauth, M. Pastre, M. Kayal, "A Self-Regulating Oscillator for Sensor Operation of NANOelectromechanical Systems", in proceedings of *11th IEEE International New Circuits*

Publications

and Systems Conference, France / Paris, 2013, pp. 1-4.

- C. Kauth, M. Pastre, M. Kayal, "On-chip Mass Sensing at the Physical Limits of Nanoelectromechanical Systems", in proceedings of 5th *IEEE International Workshop on Advances in Sensors and Interfaces*, Italy / Bari, 2013, pp. 131-135.
- C. Kauth, M. Pastre, M. Kayal, "Wideband Low-Noise RF Front-End for CNT-NEMS Sensors", in proceedings of 19th *International Mixed Design of Integrated Circuits and Systems Conference*, Poland / Warsaw, 2012, pp. 289-293.

Posters Presentations



- C. Kauth, M. Pastre, M. Kayal, "Quomodo Nano-fistulis e Carboneo factis Rerum primordia ponderare possimus", *Nano-Tera Annual Plenary Meeting*, Switzerland / Bern, 2013.
- C. Kauth, M. Pastre, M. Kayal, "A Carbon Nanotube Based NEMS Oscillator", *Nano-Tera Annual Plenary Meeting*, Switzerland / Zurich, 2012.
- C. Kauth, M. Pastre, M. Kayal, "Low-noise sensor front-end for carbon nanotube based oscillators", *Nano-Tera Annual Plenary Meeting*, Switzerland / Bern, 2011.
- C. Kauth, M. Pastre, M. Kayal, "A circuit-level modeling approach for Carbon Nanotube based NEMS resonators", *Nano-Tera Annual Plenary Meeting*, Switzerland / Bern, 2010.

Technical Press Articles



- C. Kauth, "La machine à loisirs", *Flash Informatique*, no. 5, p. 6, 2013.
- C. Kauth, "hc2.ch, a success story made in EPFL", *Flash Informatique*, no. 3, p.1 & 9-10, 2013.
- C. Kauth, "Ingéniosité en ingénierie", *Flash Informatique*, no. 9, pp. 27-28, 2012.
- C. Kauth, "Tour de magie pour la pause-café", *Flash Informatique*, no. 4, pp. 27-28, 2012.
- C. Kauth, J. Wagner, "Savoir et savoir-faire en algorithmique", *Flash Informatique*, no. 10, pp-24-26, 2011.
- C. Kauth, "Le problème le plus populaire de l'hc2 2011 passé au crible", *Flash Informatique*, no. 4, pp-7-9, 2011.

- C. Kauth, "Médaille au SWERC = justesse x efficacité",
Flash Informatique, no. 1, pp-10-11, 2011.
- C. Kauth, "La Suisse a trouvé ses meilleurs programmeurs",
Flash Informatique, no. 4, pp. 11-13, 2010.

International Competition Task



- C. Kauth, "Rice Hub", 23rd *International Olympiad in Informatics*, Thailand / Pattaya, 2011.

Curriculum Vitae



Christian Kauth

born in Luxembourg on October 17th, 1984
may be contacted at christian.kauth@a3.epfl.ch
preferably in English, French, German, Italian or Luxembourgish

My way to the PhD

2009 – 2014	PhD in Microsystems and Microelectronics Ecole Polytechnique Fédérale de Lausanne (EPFL), Switzerland
2007 – 2009	MSc in Micro- and Nanotechnologies for Integrated Systems EPFL (Switzerland), INP Grenoble (France), Politecnico di Torino (Italy)
2004 – 2007	BSc in Electrical Engineering , EPFL, Switzerland
1997 – 2004	Diplôme de fin d'études secondaires , Athénée de Luxembourg

Precious professional experiences

2014 – ...	Software Development Engineer Microsoft, Redmond, WA, USA
2009 – 2014	Research & teaching assistant Electronics Laboratory, EPFL, Switzerland
2009 – 2013	Trainer in advanced algorithms & programming Freelance for Centre de Technologie de l'Education, Luxembourg
2008	Research assistant , Electronics Laboratory, EPFL, Switzerland
2006	Software Developer General Engineering, Paul Wurth S.A. Luxembourg

Some of my favourites

2011	Scientific committee member & medallist International Olympiad in Informatics, Thailand/2011 & Greece/2004
2010 – 2012	Co-founder & head of the Helvetic Coding Contest Switzerland's biggest algorithmic challenge, hc2.ch
2009 – 2012	Co-founder & president of PolyProg EPFL's association training students in algorithms, polyprog.epfl.ch
2008	Full Ironman , is to the body what a PhD thesis is to the brain